



**HAL**  
open science

# Modelling thermal effects on starch granule suspension

Arnesh Palanisamy

► **To cite this version:**

Arnesh Palanisamy. Modelling thermal effects on starch granule suspension. Chemical and Process Engineering. Université Paris-Saclay, 2022. English. NNT : 2022UPASB009 . tel-03853229

**HAL Id: tel-03853229**

**<https://pastel.hal.science/tel-03853229>**

Submitted on 15 Nov 2022

**HAL** is a multi-disciplinary open access archive for the deposit and dissemination of scientific research documents, whether they are published or not. The documents may come from teaching and research institutions in France or abroad, or from public or private research centers.

L'archive ouverte pluridisciplinaire **HAL**, est destinée au dépôt et à la diffusion de documents scientifiques de niveau recherche, publiés ou non, émanant des établissements d'enseignement et de recherche français ou étrangers, des laboratoires publics ou privés.

# Modélisation des effets thermiques sur une suspension de granules d'amidon

*Modelling thermal effects on starch granule suspension*

## Thèse de doctorat de l'université Paris-Saclay

École doctorale n° 581, Agriculture, alimentation, biologie,  
environnement et santé (ABIES)  
Spécialité de doctorat : Génie des Procédés  
Graduate School : BioSphERA, Référent : AgroParisTech

Thèse préparée dans l'**UMR SayFood**  
(Université Paris-Saclay, INRAE, AgroParisTech),  
sous la direction de **Denis Flick**, Professeur,  
la co-direction de **Marco Ramaioli**, Directeur de Recherche,  
le co-encadrement de **Paul Menut**, Professeur,  
et de **Artemio Plana-Fattori**, Ingénieur de Recherche

Thèse soutenue à Paris-Saclay, le 08 Avril 2022, par

**Arnesh PALANISAMY**

### Composition du jury

<b>Patrick PERRE</b> Professeur, CentraleSupélec, Université Paris-Saclay	Président
<b>Guy DELLA VALLE</b> Ingénieur de recherche, INRAE, Nantes	Rapporteur et Examineur
<b>Stefan LUDING</b> Professeur, University of Twente, Netherlands	Rapporteur et Examineur
<b>Jean-Yves DELENNE</b> Directeur de Recherche, INRAE, Montpellier	Examineur
<b>Anne MATIGNON</b> Docteure/Food scientist, Roquette	Examinatrice
<b>Denis FLICK</b> Professeur, AgroParisTech, Université Paris-Saclay	Directeur de thèse
<b>Marco RAMAIOLI</b> Directeur de Recherche, INRAE, Université Paris-Saclay	Co-directeur de thèse
<b>Paul MENUT</b> Professeur, AgroParisTech, Université Paris-Saclay	Co-encadrant

**Titre :** Modélisation des effets thermiques sur une suspension de granules d'amidon

**Mots clés :** CFD, Amidon, DEM, Rhéologie de suspensions, Transfert de chaleur, Nanoindentation

**Résumé :** L'amidon est un matériau présent dans de nombreuses plantes et une source de nourriture pour la plupart des animaux sur terre. Les grains d'amidon, lorsqu'ils sont chauffés en présence d'eau, gonflent en s'imbibant d'eau. Ce processus est également connu sous le nom de gélatinisation de l'amidon. L'amidon en tant que matériau a fait l'objet de nombreuses recherches au fil des décennies. Cependant, on manque encore de certaines connaissances sur ce matériau intéressant et une meilleure compréhension de certains phénomènes pourrait conduire à d'importantes économies lors de son traitement et aider au développement de nouveaux produits amylicés. Ainsi, dans cette thèse, nous visons à caractériser expérimentalement le gonflement d'un amidon de maïs cireux modifié chimiquement et à modéliser la cinétique de gonflement au niveau des granules alors que les modèles rapportés précédemment dans la

littérature modélisent ce gonflement au niveau de l'ensemble d'une population de granules. Dans un second temps, nous caractérisons la variation des propriétés mécaniques d'un granule d'amidon à différents degrés de gonflement. Nous montrons ensuite comment par des simulations DEM (méthode des éléments discrets) on peut prédire la viscosité effective d'une suspension d'amidon en utilisant les propriétés caractérisées précédemment. Enfin, nous simulons également, à l'aide d'un modèle CFD-DEM entièrement couplé, l'écoulement du fluide et des particules avec transfert de chaleur lors de gélatinisation de l'amidon à l'intérieur d'un rhéomètre de Couette à petit entrefer. Ces résultats nous rapprochent d'une meilleure compréhension des suspensions granulaires en général, d'une conception améliorée des équipements de traitement thermique des produits à base d'amidon et de leur contrôle dans les industries alimentaires.

**Title :** Modelling thermal effects on starch granule suspension.

**Keywords :** CFD, Starch, DEM, Suspension Rheology, Heat Transfer, Nanoindentation

**Abstract :** Starch is one of the most omnipresent materials found in plants. It is a direct food source for most animals on earth. Starch suspensions when heated in presence of water undergoes starch swelling by imbibing water. This process is also known as starch gelatinization. Starch as a material has been a subject of perennial research over the decades. However, this interesting material still hides a lot of knowledge, a better understanding of which could lead to huge savings in processing and also aid in the development of novel products for consumption. Thus, in this thesis, we aim to decipher experimentally swelling of chemically-modified waxy maize starch and model swelling kinetics at the inter-granular level compared to earlier reported efforts in the literature

that model the starch swelling at the broad population level. Secondly, we decipher the variation of mechanical properties of the starch granule at different swelling degrees. We further show through DEM simulations the viscosity predictions of the overall suspension using the characterized material properties. We finally, also simulate, using a fully coupled unresolved CFD-DEM model, fluid and particle flow with heat transfer for starch gelatinization inside a small gap Couette rheometer. These results take us one step closer to understanding better the granular suspension systems in general and also in designing better process equipment and model-based control systems for starch gelatinization in food industries.

யாதும் ஊரே யாவரும் கேளிர்

*"Yaadhum Oore Yaavarum Kelir"- To us all towns are our own, everyone is our kin*

*Pour nous, toutes les villes sont les nôtres, tout le monde est de notre famille.*

*- Kaniyan Pungundranar (6th century BCE)*

*This thesis is dedicated to my parents and the city of Visakhapatnam (India).*

*Cette thèse est dédiée à mes parents et à la ville de Visakhapatnam (Inde).*

# Acknowledgements

When I arrived in Paris to start this PhD thesis without speaking a word of French, I did not know what to expect. These years have reached beyond expectations both professionally and personally despite the pandemic. These years have been very transformative. All this would not have been possible without the unconditional support of various people I encountered during this project.

First of all, I would like to thank all my supervisors Denis Flick, Marco Ramaioli, Paul Menut and Artemio Plana-Fattori. It was a pleasure working with all of you. Thanks for systematically dividing the advisory role and secondly, allowing me a free hand to explore the project. I thank all of you for your generosity, forgiveness and patience. I appreciate our discussions. I consider myself extremely lucky to have you as my advisors.

Denis Flick, thanks a lot for the extra effort to communicate in English during this thesis. I am amazed at the level of organization and ability to adapt quickly to situations. Thanks for all the technical inputs and I do plan to take a couple of leaves out of your book in terms of consistency.

Marco Ramaioli, I can't thank you enough for all the innovative research ideas you keep producing. Your ability to think outside the box and design simple systems along with your technical expertise is amazing. Thanks again for sparing time for this thesis despite your overwhelmingly busy schedule. I can't thank you enough for suggesting and encouraging the MePhy summer school.

Paul Menut, you are one of the kindest and gentle people I have encountered in my life. You inspire me to be humble and stay grounded. Thanks a lot for handling all the administrative chores right from the first interview to managing me in the Gépro group especially when I faced language problems.

Artemio Plana-Fattori, Thanks a lot not only for your help to design and carrying out the experiments but also for your reactivity. This thesis wouldn't have looked the same if not for the countless amount of your previous work on this starch. Even beyond the technical aspects you were always there and happy to help out in any way possible especially during the pandemic.

I thank the member of the thesis committee, Pierre Jop and Graciela Alvarez. Thanks a lot for making yourself available and for your valuable inputs and questions during the review meetings. They played an important role in shaping this thesis.

I would also like to take this opportunity to thank both members and ex-members of Gepro. Especially Brigitte Deau, Giana Almeida Perre, Gabrielle Moulin.

Brigitte, I still miss the slow practice french conversations with you during the tea breaks and the lab is not the same without you. we miss you.

I thank all the members involved in MATHEGRAM-ITN including the coordinator Chuan-Yu Wu and Ling Zhang.

I thank my secondment supervisors at the University of Surrey: David Cox, Tan Sui and Chuan-Yu Wu and DCS computing: Andreas Aigner and Christoph Goniva. Thanks for taking me under your wing and helping produce results despite the pandemic constraints.

Special thanks to Stefan Radl for the brief exchanges concerning LIGGGHTS over email and in person.

---

I also thank the members of my thesis jury for their many comments and suggestions. improvement, I enjoyed our discussions. Special thanks to Guy Della Valle, Anne Matignon, Jean Yves Delenne and Stefan Luding for agreeing to evaluate my work.

# Contents

<b>List of Figures</b>	<b>4</b>
<b>List of Tables</b>	<b>7</b>
<b>Context of MATHEGRAM</b>	<b>11</b>
<b>Context and objective of the PhD (Early Stage Researcher 8 in Mathegram)</b>	<b>14</b>
<b>Structure of PhD work</b>	<b>18</b>
<b>Outcomes</b>	<b>20</b>
<b>1 Literature review- State of the Art</b>	<b>23</b>
1.1 Suspension classification in terms of dimensionless numbers . . . . .	24
1.2 Rheology of granular suspensions . . . . .	27
1.3 Starch . . . . .	30
1.3.1 Structure of starch . . . . .	30
1.3.2 Starch gelatinization . . . . .	33
1.4 DEM . . . . .	37
1.4.1 Soft-particle method (Molecular dynamics method) . . . . .	38
1.4.2 Contact-dynamics method . . . . .	39
1.5 CFD-DEM . . . . .	39
1.6 Heat transfer coupling . . . . .	41
1.6.1 Conduction . . . . .	43
1.6.2 Convection . . . . .	44
1.6.3 Radiation . . . . .	44
1.7 Summary and thesis objectives . . . . .	45
<b>2 Kinetic modelling of individual starch granule swelling</b>	<b>47</b>
2.1 Introduction . . . . .	49
2.2 Materials and methods . . . . .	51
2.2.1 Experimental method . . . . .	51
2.2.2 Image data analysis and notation . . . . .	51
2.3 Experimental results and observation . . . . .	53
2.3.1 Observation at constant temperature between 55 °C and 62 °C . . . . .	53
2.3.2 Diameter increase during temperature ramp . . . . .	53
2.4 Model formulation and results . . . . .	55

2.4.1	Kinetic model development . . . . .	55
2.4.2	Calibration of model parameters and model predictions . . . . .	58
2.4.3	Monte Carlo simulation and results . . . . .	58
2.4.4	Model application and validation . . . . .	61
2.4.5	Possible explanation of variability and model limitations . . . . .	63
2.5	Conclusion . . . . .	64
2.6	Acknowledgments . . . . .	64
<b>3</b>	<b>Starch granule material properties characterization</b>	<b>67</b>
3.1	Determination of the mechanical properties of gelatinized starch granule from bulk suspension characterization . . . . .	68
3.1.1	Introduction . . . . .	70
3.1.2	Materials and methods . . . . .	72
3.1.3	Results and discussion . . . . .	75
3.1.4	Conclusion . . . . .	81
3.1.5	Acknowledgments . . . . .	82
3.2	Estimation of Young's modulus of un-swollen starch granules through nano-indentation . . . . .	83
3.2.1	Materials and Methods . . . . .	85
3.2.2	Results and discussion . . . . .	86
3.2.3	Raw data and images . . . . .	89
3.2.4	Young's modulus calculation . . . . .	90
3.2.5	Conclusion . . . . .	93
<b>4</b>	<b>DEM simulations of starch suspensions</b>	<b>97</b>
4.1	Transient DEM simulation of starch granule suspension undergoing thermal treatment . . . . .	98
4.1.1	Introduction . . . . .	100
4.1.2	Methods . . . . .	101
4.1.3	Results . . . . .	103
4.1.4	Conclusion . . . . .	105
4.1.5	Future work . . . . .	107
4.2	Shear flow DEM simulations of fully swollen starch granule suspension . . . . .	109
4.2.1	Introduction. . . . .	111
4.2.2	Materials and methods . . . . .	115
4.2.3	Results and discussion . . . . .	119
4.2.4	Conclusion . . . . .	126
<b>5</b>	<b>Multiscale modelling of flow, heat transfer and swelling during thermo-mechanical treatment of starch suspensions</b>	<b>129</b>
5.1	Introduction . . . . .	131

5.1.1	Coupling starch swelling, flow and heat transfer . . . . .	131
5.1.2	Starch swelling modelling . . . . .	132
5.1.3	Starch suspension rheology . . . . .	133
5.2	Modelling . . . . .	135
5.2.1	Starch swelling modelling . . . . .	135
5.2.2	CFD-DEM modelling . . . . .	136
5.2.3	Numerical solving . . . . .	140
5.2.4	Results and discussion . . . . .	141
5.3	Conclusion . . . . .	150
5.4	Acknowledgments . . . . .	151
<b>6</b>	<b>General conclusion and outlooks</b>	<b>153</b>
6.1	Take away from this thesis (Everything that remains) . . . . .	153
6.2	Future prospects . . . . .	154
6.2.1	Starch swelling . . . . .	155
6.2.2	Methods to characterize materials . . . . .	155
6.2.3	DEM shear flow simulations . . . . .	155
6.2.4	Coupling simulations . . . . .	155
6.3	Final word . . . . .	155
<b>A</b>	<b>Appendix: Transient DEM simulation of starch swelling (MATLAB script)</b>	<b>159</b>
<b>B</b>	<b>Appendix: Thermo-mechanical treatment of starch suspensions in small gap Couette rheometer (MATLAB)</b>	<b>165</b>
<b>C</b>	<b>Appendix: LIGGGHTS files</b>	<b>177</b>
C.1	Lubrication contact model . . . . .	177
C.2	Swelling model . . . . .	177
C.3	Variable Young's modulus based on swelling degree . . . . .	177
<b>D</b>	<b>Appendix: Effect of particle size on DEM shear flow simulations</b>	<b>179</b>
<b>E</b>	<b>Bibliography</b>	<b>181</b>

# List of Figures

1	Overview of structure/plan of the thesis . . . . .	20
1.1	Conceptual classification of rheo-physical regimes of a suspension. Courtesy: [Cousot and Ancey, 1999] . . . . .	26
1.2	Flow curves for a typical time-independent fluids. Courtesy: [Steffe, 1996]. . . . .	28
1.3	Biochemical pathway of starch biosynthesis from sucrose. Enzymes are represented with alphabets they are (a) sucrose synthase; (b) UDPglucose pyrophosphorylase; (c) ADPglucose pyrophosphorylase; (d) phosphoglucomutase; (e) starch synthase (GBSSI); (f) starch synthase and starch-branching enzyme; (g) ADPglucose transporter; (h) hexose phosphate transporter. PPI: inorganic pyrophosphate. Courtesy: [Smith et al., 1997] . . . . .	31
1.4	Amylose polymer skeletal structure. Courtesy: [Khandelwal et al., 2020] . . . . .	31
1.5	Amylopectin polymer skeletal structure. Courtesy: [Khandelwal et al., 2020] . . . . .	31
1.6	Maize starch granules viewed under polarized light (Magnification X50). . . . .	32
1.7	Schematic diagram of starch granule structure. Courtesy: [Donald et al., 1997] . . . . .	33
1.8	Methods of starch modifications. Courtesy: [Nawaz et al., 2020] . . . . .	34
1.9	Loss of birefringence of starch granules during gelatinization process. (A) Individual starch granule from normal maize; (B),(C) and (D) individual, aggregate and elongated granules from high-amylose maize, respectively. Courtesy: [Cai and Wei, 2013] . . . . .	35
1.10	DSC measurements of starch suspensions. Courtesy: [Chen et al., 2007] . . . . .	35
1.11	Flour Rapid Visco Analyser (RVA) pasting curves. Courtesy: [Guo et al., 2003] . . . . .	36
1.12	Spring and dashpot analogy of contact deformation in soft-particle method. . . . .	38
1.13	Modeling scales in fluid-solid systems. Courtesy: [Norouzi et al., 2016] . . . . .	39
1.14	CFD-DEM coupling methods. Courtesy: [Kanitz and Grabe, 2021] . . . . .	40
1.15	Flow chart of unrevolved CFD-DEM coupling. Courtesy: [Norouzi et al., 2016] . . . . .	42
1.16	Heat exchange mechanisms in fluid-solid system. Courtesy: Golshan et al. [2020] . . . . .	43
2.1	Time-Temperature profiles imposed on starch suspensions and typical diameter evolution of a starch granule during gelatinization. . . . .	52
2.2	Starch granules at the beginning and after 1 hour at different temperatures . . . . .	54
2.3	Experimental delay times for swelling onset at 62 °C . . . . .	55
2.4	Non dimensional diameter evolution . . . . .	56
2.5	Model prediction of non dimensional diameter evolution . . . . .	59
2.6	Model prediction of diameter evolution . . . . .	60
2.7	Cumulative particle size distribution of different cases at different times and temperatures . . . . .	61
2.8	Validation of kinetic swelling model for non-linear temperature profiles . . . . .	62

3.1	Suspension shear modulus as a function of volume fraction. Triangles[△], Squares[□], circles[○] represent samples prepared via centrifugation, limited water swelling and osmotic compression respectively( $\gamma = 0.01$ , $f = 1$ Hz). The solid dotted line represents the polynomial fit of overall experimental data ( $G_{suspension} = -352\phi^2 + 1229\phi - 330$ ). The purple continuous line represents the power-law fit for volume fractions $\phi < \phi_{rcp}$ , Green dashed line represents the best fit from the <a href="#">Evans and Lips [1990]</a> model for $0.8 < \phi < 1$ , Pink continuous line represents the power law fit for volume fractions $\phi > 1$ . . . . .	77
3.2	Confocal stack images of starch granule suspension. Blue Boxes (□) correspond to the contact of the traced granule with the neighbouring granule. Image slice number starting from left to right [30, 39, 46, 69, 78, 92]. Each slice corresponds to a depth of $0.422 \mu\text{m}$ . . . . .	78
3.3	Suspension bulk modulus as function of volume fraction. Asterisks[*] correspond to experimental data. . . . .	79
3.4	Storage modulus of suspension at different temperatures. Asterisks[*], circles[○], boxes[□] and triangles[△] correspond to volume fractions $\phi$ of 0.42, 0.63, 0.83 and 1.03 respectively. Error bars correspond to one standard deviation. The dashed line is the mean value of all the measurements across temperatures. . . . .	80
3.5	Dispersed starch on silicon substrate mounted on a SEM stub. . . . .	85
3.6	Nano-indenter alignment inside the SEM chamber . . . . .	85
3.7	Illustration of pile-up and sink-in material behaviour at maximum indentation depth (a) side profile of indentation, (b) geometry of projected contact areas for each case. Courtesy: [ <a href="#">Hardiman et al., 2016</a> ] . . . . .	87
3.8	Schematic of load-displacement curve for an instrumented nanoindentation test . . . . .	87
3.9	Particle indentation depth illustration . . . . .	88
3.10	SEM images of starch . . . . .	89
3.11	Raw data from the indenter . . . . .	90
3.12	SEM imaging during nano-indentation. . . . .	91
3.13	Stress-strain curve obtained via nano-indentation. . . . .	92
3.14	Initial portions of the loading curve and Hertzian model fits. . . . .	92
3.15	Initial portions of the unloading curves and linear fits for applying Oliver-Pharr method. . . . .	93
4.1	Granules contours at every 30 seconds . . . . .	104
4.2	Contour comparison of different runs . . . . .	104
4.3	Time evolutions of parameters . . . . .	106
4.4	Interactions energy vs volume fraction . . . . .	107
4.5	Different modes of near field lubrication interactions on particles in a suspension. . . . .	114
4.6	Aspect ratio . . . . .	116
4.7	Particle contacts of ellipsoidal particles. . . . .	117
4.8	Discretization of particle size distribution in simulations. . . . .	117

4.9 Newtonian to shear thinning transition of fully swollen starch suspensions. . . . . 119

4.10 Flow-curves of fully swollen starch granules. . . . . 121

4.11 Shear dependency of lubrication and contact contributions to virial stresses at  $\phi \approx 30\%$  (45%) and  $\phi \approx 23\%$  (35%). . . . . 123

4.12 Shear stress evolution with shear stress for  $\phi \approx 23\%$ (35%) (*Insert: Shear stress evolution with number of timesteps*) . . . . . 124

4.13 Scheme illustrating the different rheology in hard particle and soft particle limits . . . . . 125

5.1 Simulation domain . . . . . 140

5.2 Temperature of granules and fluid . . . . . 142

5.3 velocity of granules and fluid . . . . . 143

5.4 xy cross section of the simulation domain . . . . . 144

5.5 Time evolution of suspension parameters at different regions of the simulation domain . . . . . 145

5.6 Sample granule properties evolution during simulation . . . . . 146

5.7 Granule population properties evolution with time . . . . . 147

5.8 cumulative distributions of distance from neighbors . . . . . 150

D.1 Impact of Particle size distribution on Flow-curves of fully swollen starch granules. . . . . 179

# List of Tables

1.1	Proportion of amylose and amylopectin in common starch sources. Courtesy: [Thomas and Atwell, 1999]. . . . .	32
1.2	Common solid-state reaction kinetic model used to model starch gelatinization in Malumba et al. [2013]	37
2.1	Summary of Experimental conditions and swelling data with sigmoid fits . . . . .	53
3.1	Evolution of the sample volume fraction during osmotic compression, at two different PEG concentrations . . . . .	75
3.2	Equilibrium osmotic pressure and volume fractions . . . . .	80
3.3	Indentation program . . . . .	86
3.4	Data summary of Hertz and Oliver-Pharr fits to the data. . . . .	93
4.1	Granule material properties used in the simulation. . . . .	117
4.2	Simulations summary. . . . .	118
4.3	Summary of samples tested for flow-curves . . . . .	118
4.4	Rheometer program to measure flow-curves . . . . .	118
4.5	Volume fraction estimates using viscosity data and krieger-Dougherty equation . . . . .	120
4.6	Ellis model fit summary . . . . .	120
4.7	Contribution of lubrication and contact forces to the viscosity of suspension. . . . .	123
5.1	Variability between runs . . . . .	145



**INTRODUCTION GÉNÉRALE**

**GENERAL INTRODUCTION**

# Contexte du projet MATHEGRAM

L'acronyme MATHÉGRAM signifie Analyse multi-échelle du comportement thermomécanique des matériaux granulaires. Les matériaux granulaires tels que les sols, les semences agricoles et les poudres pharmaceutiques sont très courants et ont de nombreuses applications industrielles. Ils possèdent des propriétés physiques uniques et un comportement d'écoulement complexe. MATHEGRAM est un réseau de formation innovant financé dans le cadre du programme Marie Skłodowska-Curie Actions (Horizon 2020). Il s'agit d'un consortium multidisciplinaire et intersectoriel composé de 10 principaux bénéficiaires universitaires et non universitaires de six pays de l'UE. Les 15 projets de thèse financés par MATHEGRAM abordent des défis expérimentaux et de modélisation relatifs au comportement thermomécanique des matériaux granulaires. Les principales questions de recherche posées sont distribuées en trois tâches.

1. Comment la température augmente-t-elle dans les matériaux granulaires en l'absence de sources de chaleur externes ?
2. Comment la température affecte-t-elle les propriétés physiques des matériaux granulaires ?
3. Comment les propriétés thermomécaniques des matériaux granulaires peuvent-elles être utilisées efficacement dans diverses applications telles que la fabrication additive, le revêtement de surface à base de poudre, le frittage et la catalyse ?

# Context of MATHEGRAM

MATHEGRAM acronym stands for Multiscale analysis of thermomechanical behaviour of granular materials. Granular materials such as soils, agricultural seeds and pharmaceutical powders are common in nature and have many industrial applications. They possess unique physical properties and complicated flow behaviour. MATHEGRAM is an Innovative Training Network funded as part of Marie Skłodowska-Curie Actions of Horizon 2020 program. It is a multidisciplinary and inter-sectoral consortium consisting of 10 leading academic and non-academic beneficiaries from six EU countries. The 15 PhD projects funded through MATHEGRAM address the experimental and modelling challenges in analyzing the thermomechanical behaviour of granular materials. The core research questions to be answered are respectively divided into their corresponding work packages.

- Work Package 1- How does temperature increase within granular materials without the application of external heating sources?
- Work Package 2- How does temperature affect the physical properties of granular materials?
- Work Package 3- How can the thermomechanical properties of granular materials be effectively utilized in various applications such as additive manufacturing, powder coating, sintering and catalysis?

# Contexte et objectif de la thèse (Early Stage Researcher 8 dans le projet Mathegram)

La thèse (ESR 8 : Early Stage Researcher 8 du projet Mathegram) fait partie de la tâche 2 et se concentre sur l'impact de la température et de l'histoire thermique sur les propriétés physiques des suspensions d'amidon, notamment la rhéologie.

L'amidon est largement utilisé dans l'industrie pour accroître la viscosité, notamment dans l'industrie alimentaire. L'amidon, présent dans la plupart des tubercules et des graines, se présente sous forme de granules denses. Lorsqu'il est soumis à un traitement thermique, il absorbe de l'eau et gonfle en modifiant sa structure physico-chimique. Au cours de ce processus, connu sous le nom de gélatinisation, les propriétés du matériau changent radicalement et à la fin de la gélatinisation, il en résulte des particules molles et déformables. Cela a des effets importants sur une suspension d'amidon, d'une part en raison d'un changement rapide du volume occupé par les granules et d'autre part en raison de changements dans les propriétés mécaniques des granules tels que le module de Young. La caractérisation et la modélisation des phénomènes ayant lieu pendant la gélatinisation dans un système aussi complexe sont importantes d'un point de vue industriel.

Au cours du traitement thermique d'un produit alimentaire liquide contenant de l'amidon, les changements de viscosité doivent être connus pour estimer avec précision des variables telles que la vitesse, la température ou la pression, car le processus est fortement couplé en termes de transfert de chaleur, de transfert de quantité de mouvement et de transformation [Plana-Fattori et al., 2016]. La viscosité est également un paramètre important pour la perception sensorielle en bouche des produits alimentaires [Szczesniak, 1963, Wood, 1968]. La viscosité est fonction de la fraction volumique des granules dans une suspension [Einstein, 1905, Krieger and Dougherty, 1959, Batchelor, 1977, Maron and Pierce, 1956, Quemada, 1977, Shewan and Stokes, 2015b]. Les équations développées par Einstein et Batchelor ne peuvent prédire la viscosité avec précision que pour les suspensions diluées ( $\phi < 0,1$ ). Récemment, Shewan and Stokes [2015b] ont utilisé l'équation proposée par Quemada [1977], Maron and Pierce [1956] en déterminant la fraction volumique critique (random close packing volume fraction) via le modèle de Farr and Groot [2009] pour une distribution granulométrique donnée. Cette méthodologie est empirique et n'est valable que pour des sphères dures. Par ailleurs, même avec cette hypothèse, l'application de tels modèles nécessite la connaissance de la distribution de tailles des particules à un instant donné pour pouvoir prédire la fraction volumique critique et en déduire la viscosité de la suspension.

Comme discuté précédemment, la distribution granulométrique évolue constamment au cours de la gélatinisation. Historiquement, le gonflement de l'amidon a été modélisé comme une sorte de 'réaction' et divers modèles cinétiques ont été rapportés [Anuntagool et al., 2017, Okechukwu and Rao, 1996, Bagley and Christianson, 1982, Bakshi and Singh, 1980a, Suzuki et al., 1976, Doublier et al., 1987, Kokini et al., 1992]. Cependant, tous ces travaux portent sur l'ensemble d'une population de granules et modélisent uniquement l'évolution du diamètre médian ou moyen des granules avec le temps. Ceci est clairement insuffisant pour prédire

la fraction volumique critique. Ainsi, nous avons entrepris de développer un modèle de gonflement cinétique au niveau d'un granule. Ceci sera discuté en détail dans le chapitre 2 de cette thèse.

L'autre inconvénient des approches précédentes (e.g. [Chantoiseau et al., 2012, Plana-Fattori et al., 2016]) est qu'elles considèrent la suspension comme une seule phase équivalente, c'est-à-dire qu'elles ignorent les effets granulaires. Dans de telles simulations, on suppose que les particules suivent les lignes de courant et les collisions de particules ne sont pas prises en compte. Les particules se comportent en quelque sorte comme des particules <<fantômes>>. Ainsi, pour pouvoir mieux modéliser de telles suspensions, les contributions granulaires (interactions particule-particule et particule-fluide) doivent être prises en compte. C'est la deuxième nouveauté et motivation de cette thèse. Dans le chapitre 3, nous caractérisons les propriétés matérielles des granules d'amidon à différents degrés de gonflement. Dans le chapitre 4, nous utilisons ces propriétés pour effectuer des simulations par la méthode des éléments discrets (DEM) pour un écoulement cisailé de suspensions concentrées afin de prédire leur viscosité apparente. Enfin, dans le chapitre 5, nous couplons les 4 aspects : écoulement fluide (CFD), interaction entre particules (DEM), transfert de chaleur et gonflement pour simuler la gélatinisation de l'amidon à l'intérieur d'un rhéomètre de Couette à petit entrefer.

En résumé, les objectifs de la thèse portent à la fois sur la caractérisation expérimentale, la modélisation et la simulation numérique:

- Déterminer expérimentalement le gonflement des particules en fonction de leur historique temps-température et proposer un modèle de cinétique de gonflement à l'échelle d'une particule.
- Caractériser les propriétés mécaniques d'un granule d'amidon telles que le module de Young en fonction du degré de gélatinisation.
- Effectuer des simulations DEM avec ces propriétés pour prédire la viscosité de la suspension et comparer ces prédictions avec des résultats expérimentaux.
- Simuler la gélatinisation de l'amidon à l'intérieur d'un rhéomètre de Couette à petit entrefer en utilisant un modèle couplé CFD-DEM.

# Context and objective of the PhD (Early Stage Researcher 8 in Mathegram)

The present thesis (ESR 8: Early Stage Researcher 8 in Mathegram) is part of work package 2 and is concentrated on the impact of temperature and thermal history on physical properties of starch granule suspensions, most notably rheology.

Starch is largely used in industry as a viscosity enhancer, of which the food industry is a vehement user of this raw material. The starch found in most tubers and grains occurs as dense granules in its native form. When subjected to thermal treatment, it absorbs water and swells changing its physio-chemical structure. During this process, also known as gelatinization, the material properties change drastically and at the end of gelatinization results in soft deformable particles. This has compounded effects on starch suspension, firstly due to rapid change in the volume occupied by the granules and secondly due to changes in granule materials properties such as Young's modulus. Characterizing and modelling such a complex suspension system during gelatinization is of importance from the industrial perspective.

During thermal processing of liquid food products containing starch, viscosity changes must be known to accurately estimate process variables as the process is highly coupled in terms of heat transfer, momentum transfer and transformation [Plana-Fattori et al., 2016]. Sensory perception of viscosity is also an important mouthfeel sensation in food products [Szczesniak, 1963, Wood, 1968]. Viscosity is shown to be a function of granular volume fraction in a suspension [Einstein, 1905, Krieger and Dougherty, 1959, Batchelor, 1977, Maron and Pierce, 1956, Quemada, 1977, Shewan and Stokes, 2015b]. Earlier works of Einstein and Batchelor equations could predict the viscosity accurately only for dilute suspensions ( $\phi < 0.1$ ). Later, Shewan and Stokes [2015b] used the equation proposed by Quemada [1977], Maron and Pierce [1956] which involves the random close packing volume fraction ( $\phi_{\text{rcp}}$ ) determined via Farr and Groot [2009] model for a given particle size distribution. These methodologies are empirical and are only valid for hard particle assumptions. Nevertheless, even with this assumption, application of such models requires the knowledge of particle sizes of the granules in the suspension to be able to predict  $\phi_{\text{rcp}}$  which can be further used to predict the viscosity of the suspension.

As discussed previously, the PSD (particle size distribution) is constantly evolving during gelatinization. Historically, starch swelling is modelled like a reaction and various kinetic models have been reported [Anuntagool et al., 2017, Okechukwu and Rao, 1996, Bagley and Christianson, 1982, Bakshi and Singh, 1980a, Suzuki et al., 1976, Doublier et al., 1987, Kokini et al., 1992]. However, all these works deal with population-scale instead of inter-granular scale and model only granule median or mean diameter evolution with time. This is insufficient for one to predict  $\phi_{\text{rcp}}$ . Thus, we set out to develop a kinetic swelling model at the inter-granular level which will be discussed in detail in chapter 2 of this thesis.

Secondly, the other shortcoming of the earlier approaches is that they consider the suspension as an equivalent single-phase i.e. ignoring the granular effects (e.g. [Chantoiseau et al., 2012, Plana-Fattori et al., 2016]). In such

simulations, one assumes that particles follow the streamlines and particle collisions are not accounted for. In essence, the particle behaves like 'ghost' particles. Thus, to be able to better model such suspensions the granular contributions (particle-particle and particle-fluid interactions) have to be taken into account. This is the second novelty and motivation of this thesis. In chapter 3, we characterize the material properties of granules at different swelling degrees. In chapter 4, we use these properties to perform shear-flow DEM simulations of fairly concentrated suspensions to predict suspension viscosity. Finally, In chapter 5 we couple all 4 aspects: fluid flow (CFD), particle interactions (DEM), heat transfer and swelling to simulate starch gelatinization inside a small gap Couette rheometer.

In summary, the objectives of the thesis involve both experimental characterization, modelling and subsequent simulations. They can be broadly listed as follows

1. To determine experimentally the particle swelling given the time-temperature history and to propose an individual particle swelling kinetic model.
2. To characterize the particle material properties such as Young's modulus as a function of gelatinization degree.
3. To perform DEM simulations with the said material properties to predict suspension viscosity and compare the same with experimental results.
4. To simulate starch gelatinization inside a small gap Couette rheometer using a coupled CFD-DEM model.

# Structuration de la thèse

L'amidon est un biopolymère composé d'amylose et d'amylopectine. C'est la principale source de stockage d'énergie pour les plantes. On le trouve dans une variété de céréales et de tubercules. La forme native de l'amidon se présente sous forme de granules denses. Sa composition en amylose et en amylopectine varie en fonction de l'origine botanique et sa structure dépend du procédé; ceci conduit à une grande variété de propriétés fonctionnelles. Dans ce travail, nous nous concentrons sur l'amidon de maïs cireux chimiquement modifié. Ce type d'amidon est résistant au cisaillement et contient moins de 1% d'amylose. La granulométrie de ce type d'amidon est supérieure à 5  $\mu\text{m}$ , ce qui conduit à classer les suspensions d'amidon de maïs cireux chimiquement modifié dans les suspensions non-colloïdales. L'amidon chauffé en présence d'eau s'imprègne d'eau et subit un gonflement. C'est ce qu'on appelle aussi la gélatinisation de l'amidon. La plupart des amidons se rompent et libèrent de l'amylose à un stade ultérieur de la gélatinisation. Ce n'est pas le cas pour les amidons de maïs cireux chimiquement modifiés. Pour ce type d'amidon, la gélatinisation des granules d'amidon se réduit donc au gonflement. Néanmoins, lors d'un traitement thermique industriel d'une suspension d'amidon même aussi << simple >>, de nombreux phénomènes couplés ont lieu. D'un point de vue macroscopique (la suspension étant considérée comme une phase unique équivalente), le transfert de chaleur et l'écoulement de fluide sont couplés notamment parce que la rhéologie de la suspension dépend du gonflement qui à son tour dépend de l'histoire thermique. Cette approche, largement développée dans la littérature, nécessite d'identifier une relation empirique entre rhéologie et degré de gonflement et suppose généralement que les particules suivent le fluide (même vitesse pour les phases liquide et solide). Dans cette thèse nous essayons de développer une approche multi-échelles, tant par l'expérimentation que par la modélisation et la simulation. Le gonflement est caractérisé pour chaque granule individuel. Les propriétés mécaniques de chaque granule sont également supposées dépendre de son propre degré de gélatinisation. Les granules peuvent interagir directement (par contact/pénétration) ou indirectement, via le fluide, par des forces de lubrification. Plus généralement, les différents transferts de chaleur et de quantité de mouvement de particule à particule, de fluide à particule et de fluide à fluide doivent être pris en compte. Ensuite, en considérant une suspension d'amidon dans un écoulement cisailé, avec un éventuel transfert de chaleur, des propriétés (macroscopiques) effectives peuvent être déduites, comme la viscosité apparente ou la diffusivité des particules (comme émergence des phénomènes microscopiques). La construction pas à pas de ce type d'approche a été la ligne directrice de la thèse.

Le chapitre 1 présente un aperçu de la littérature sur l'amidon, les suspensions et les techniques de modélisation utilisées pour modéliser leur rhéologie en général.

Dans le chapitre 2, nous caractérisons expérimentalement le gonflement individuel des granules d'amidon en suspension diluée à l'aide d'un microscope couplé à une platine chauffante Linkam. L'analyse des images microscopiques prises à intervalles réguliers, permet de déterminer l'évolution du diamètre des granules individuels pour diverses histoires thermiques. Un modèle semi-mécanistique du gonflement de l'amidon à l'échelle du granule individuel est proposé. Ce modèle est vérifié avec des mesures indépendantes de la taille des

particules par diffraction de lumière.

Logiquement, la prochaine question à laquelle il faut répondre est de savoir comment les propriétés du matériau des granules varient avec le degré de gélatinisation. Dans le chapitre 3, nous caractérisons les propriétés mécaniques des granules à différents degrés de gonflement notamment le module de Young et le coefficient de Poisson. Pour les particules entièrement gonflées, nous caractérisons le module d'élasticité volumique et le module de cisaillement des particules par le biais de ceux de suspensions denses (en faisant varier la fraction volumique solide jusqu'à des valeurs très élevées). Nous étudions également la dépendance de ces propriétés avec la température. Pour les granules d'amidon natif, nous utilisons la nano-indentation (avec un poinçon plat) couplée à la microscopie électronique (SEM). Le module de Young est identifié en appliquant le modèle de contact entre une sphère élastique et un plan rigide développé par Hertz. Malheureusement, les essais avec des granules de degrés de gélatinisation intermédiaires n'ont pas été concluants.

Après avoir caractérisé le gonflement et les propriétés mécanique des granules d'amidon, dans le chapitre 4, nous couplons d'abord le modèle de gonflement avec un modèle d'interaction entre particules par la méthodes des éléments discrets (DEM) pour observer l'évolution des indicateurs d'encombrement au fur et à mesure que le gonflement progresse. Par ailleurs, nous utilisons les propriétés mécaniques des granules d'amidon gonflés dans des simulations DEM d'écoulement de cisaillement pour prédire la rhéologie de suspensions d'amidon entièrement gonflées. Ces simulations sont ensuite comparées à des mesures expérimentales.

Enfin, dans le chapitre 5, nous couplons les modèles CFD (mécanique des fluides numérique) et DEM, pour prendre en compte simultanément l'écoulement de cisaillement, le transfert de chaleur et le gonflement des grains d'amidon à l'intérieur d'un rhéomètre de Couette chauffé (à petit entrefer). Cette étude permet de déterminer les phénomènes les plus importants à prendre en compte dans une situation aussi complexe.

# Structure of PhD work

Starch is a bio-polymer consisting of amylose and amylopectin. It is the main source of energy storage for plants. It is found in a variety of grains and tubers. The native form of starch occurs as dense granules. The composition of amylose and amylopectin varies based on the botanical origin and the structure depends on processing, which in turn leads to a wide variety of changes in the functional properties. In this work, we concentrate on chemically-modified waxy maize starch. This type of starch is shear resistant and has less than 1% amylose content. The particle sizes of this type of starch are greater than 5  $\mu\text{m}$ , which leads one to classify chemically-modified waxy maize starch in water suspensions as non-colloidal in nature. Starch when heated in presence of water imbibes water and undergoes swelling. This is also called starch gelatinization. Most starches rupture and release amylose at a later stage of gelatinization. This is not the case for chemically modified waxy maize starches. This way, the modification of starch granules reduces the gelatinization to just swelling. Nevertheless, during industrial heat treatment of such a 'simple' starch suspension, many phenomena are coupled. From a macroscopic point of view (the suspension is seen as an equivalent single-phase), heat transfer and fluid flow are coupled notably because the suspension rheology depends on swelling which in turn depends on thermal history. This approach, largely developed in the literature, needs to identify an empirical relation between rheology and swelling degree and assumes generally that particles follow the fluid (same velocity for liquid and solid phases). In this thesis, we try to develop a multiscale approach, both by experimentation and simulations. The swelling is characterized for each granule. The mechanical properties of each granule are also assumed to depend on its degree of gelatinization. The granules can interact directly (by contact/penetration) or indirectly, via the fluid, through lubrication forces. More generally, the different transfers of heat and momentum from particle to particle, from fluid to particle and from fluid to fluid should be considered. Then, considering a starch suspension in a shear flow with an eventual heat transfer, effective (macroscopic) properties can be deduced, like apparent viscosity or particle diffusivity (as the emergence of the microscopic phenomena). The step by step construction of this kind of approach was the guideline of the thesis. Chapter 1 presents a literature overview of starch, suspensions and modelling techniques used to model their rheology in general. In chapter 2 we characterize the individual starch granule swelling experimentally in dilute suspension through a microscope coupled with a Linkam hot-stage. The microscope images captured at regular intervals were processed which resulted in diameter evolutions of individual granules for various thermal histories. A semi-mechanistic kinetic model for starch swelling at the individual granule scale is proposed. This model is verified with independent particle size measurements using light diffraction. The next logical question to answer is how the granule material properties are varying with gelatinization degree. In chapter 3 we characterize the mechanical properties of granules at different degrees of swelling notably Young's modulus and Poisson's ratio. For fully swollen particles we characterize the bulk modulus and shear modulus of the particle through bulk characterization of dense suspensions (by varying the solid volume fraction up to very high values). We also study the dependence of material properties on the temperature of fully swollen starch. For native starches, we use SEM coupled nano-indentation using a flat punch to estimate Young's modulus with the

application of Hertzian contact theory. Unfortunately, tests with granules of intermediate gelatinization degrees were not conclusive. Now that the swelling and material properties are characterized, in chapter 4 we first couple the swelling model with DEM (discrete element method) to observe the jamming indicators evolution as the swelling proceeds. Further, we use the granule material properties of fully swollen starch and perform NEMD (non-equilibrium 'molecular' dynamics)-shear flow simulations using DEM to predict the rheology of fully swollen starch suspensions. We further validate the same with experimental measurements. Finally, in chapter 5 we couple CFD (computational fluid dynamics) and DEM models, to take into account simultaneously shear flow, heat transfer and starch granule swelling inside a heated small gap Couette rheometer. This study enables one to characterize which phenomena are of appreciable importance in such a complex setup.

# Outcomes

The broad overview and plan of the PhD work are summarized in the figure 1. As described in the previous section the entire PhD could be divided into 4 components or tasks, each of the tasks correspond to each chapter. Task - 1 corresponds to characterizing single starch granule swelling characterization and proposing a kinetic model for the same. Task - 2 is concerned with the characterization of material properties of granules at different swelling degrees. In task - 3, suspension bulk viscosity is predicted through DEM simulations making use of the material properties characterized in the task - 2. Further, the simulation results are compared with experimental data for validation. In task - 4, Heat transfer, swelling model, DEM and CFD are all combined to decipher the important phenomena occurring during thermo-mechanical treatment of starch suspension inside a small gap Couette rheometer.

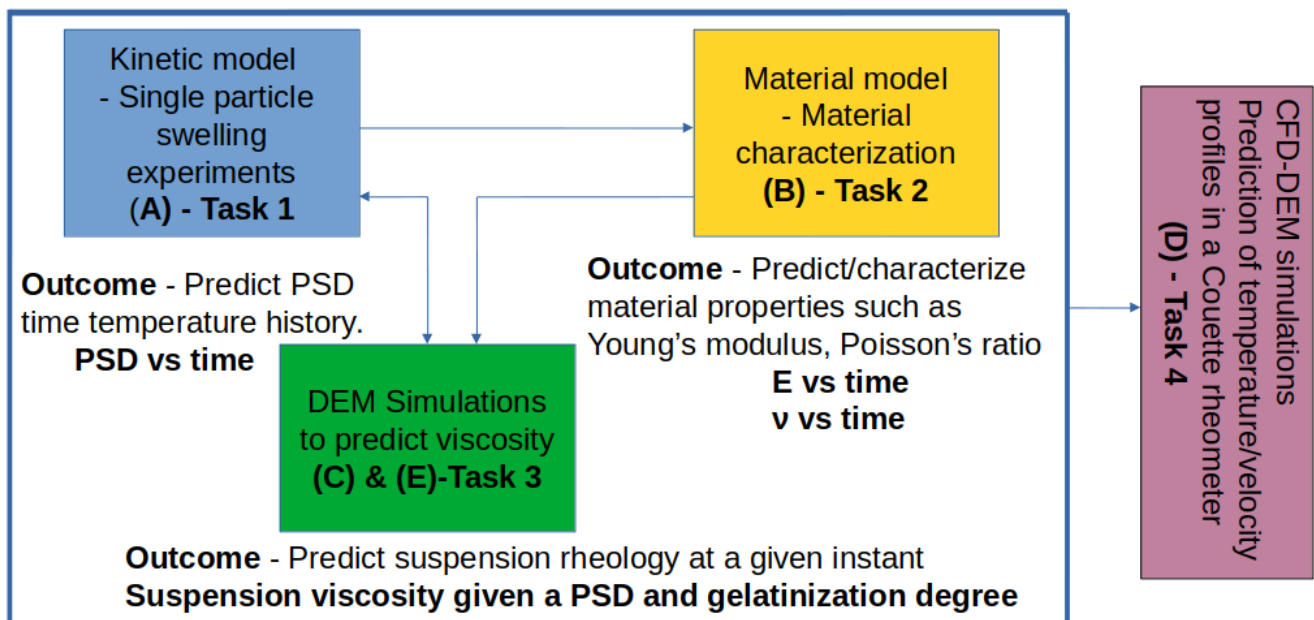


Figure 1: Overview of structure/plan of the thesis

The present PhD work led to the following dissemination, the contribution of each item is marked in capital letters in the figure 1.

## Articles in international journals

- A)– Palanisamy A., Deslandes F., Ramaioli M., Menut P., Plana-Fattori A. and Flick D., 2020. Kinetic modelling of individual starch granules swelling. *Food Structure*, 26, p.100150. See chapter 2
- B)– Palanisamy A., Gabrielle M., Ramaioli M., Plana-Fattori, A., Flick, D. and Menut, P., 2021. Determination of the mechanical properties of gelatinized starch granule from bulk suspension characterization. *Rheologica Acta* (In press). See chapter 3
- C)– Palanisamy A., Plana-Fattori, A., Menut, P., Flick, D. and Ramaioli M., 2021. NEMD-DEM simulations to predict shear-thinning in starch suspensions. (To be submitted). See chapter 4

- D)– Palanisamy, A., Ramaioli, M., Menut, P., Plana-Fattori, A. and Flick, D., 2021. Multiscale modelling of flow, heat transfer and swelling during thermo-mechanical treatment of starch suspensions. *Food Structure*, 29, p.100211. See chapter 5

### *Articles in international conferences*

- E)– Palanisamy A., Plana-Fattori A., Menut P., Ramaioli M. and Flick D., 2020. Transient DEM simulation of starch granule suspension undergoing thermal treatment, In 11th International Conference on Simulation and Modelling in the Food and Bio-Industry (FOODSIM'2020). See chapter 4.

### *Reports*

- F)– Contribution to MATHEGRAM work package 2: Thermal effects on rheology of suspensions. See appendix.

### *Codes: (See in Appendix)*

- Lubrication contact model implementation, along with virial stress computation in LIGGGTHS.
- Kinetic starch swelling model implementation in LIGGGTHS.
- Variable Young's modulus model implementation in LIGGGTHS.
- MATLAB scripts for Transient DEM simulation of starch swelling.
- MATLAB scripts for Thermo-mechanical treatment of starch suspensions in small gap Couette rheometer.



# Chapter 1

## Literature review- State of the Art

Granular materials are broadly defined as a “collection of rigid macroscopic particles, whose particle sizes are typically larger than 100  $\mu\text{m}$ ” [Andreotti et al. \[2013\]](#). The size classification is based on the importance of the inter-particle forces. For size ranges between 1  $\mu\text{m}$  to 100  $\mu\text{m}$ , forces such as Van der Waal or drag become significant and such materials are typically labelled as powders for dry granular materials and suspensions for particles immersed in a liquid. Below 1 $\mu\text{m}$  particles are termed colloidal particles. Thus, the family of granular materials encompasses a large class of materials and are omnipresent. They are disordered at the grain level but behave like a solid or liquid or in-between at the bulk level. Most typically they do have stress memories like solids. Some of the classical phenomena of granular and powder materials are arching, avalanches and segregation.

Suspensions can be defined as a large number of finite-sized, microscopic, solid particles fully surrounded by interstitial fluid. Suspensions are a sub-class of granular materials, which due to the presence of surrounding liquid behave very different compared to dry granular materials. This is due to the presence of particle-fluid forces which are negligible in dry granular materials. The discrete particles can be either hard or soft. Hard particles are the ones that have negligible deformation and have strong repulsion during surfaces collision such as grains of sand, native starch. Soft particles on the other hand deform and exhibit weaker repulsive forces during surface collisions. Some biological cells such as apple cells in puree and fully swollen starch granules are examples of soft particles.

Typically, the rheology of a suspension depends on (a) the suspending medium's viscosity, (b) the granule's volume fraction, (c) the granule's deformability, (d) the imposed shear rate [[Chen et al., 2007](#)]. The relative volume of solid present or the granule's volume fraction is defined as follows.

$$\phi = \frac{V_{\text{particles}}}{V_{\text{particles}} + V_{\text{fluid}}} \quad (1.1)$$

where  $V_{\text{particles}}$  is the total volume of the particles and  $V_{\text{fluid}}$  is the total volume of the fluid.

The volume fraction can vary from 0 to an upper limit defined by the maximum packing limit for hard particles. For soft particles, since particles deform or shrink, it is usually defined as a notional volume fraction defined using  $V_{\text{particles}}$  as the volume of particles in the fully swollen state. Thus, it could exceed 1 if  $V_{\text{particles}}$  change.

For low volume fraction fractions ( $\phi < 0.1$ ) the behaviour of the system will be dominated by the fluid viscosity and fluid-particle interactions. Also in such dilute systems, the particles do not “feel” the presence of other particles. For intermediate volume fractions, particle-particle lubrication interactions are prevailing and contribute significantly to the viscosity of the suspension. At very high volume fractions (close to the jamming transition), the particle-particle contacts govern the material properties of the system.

## 1.1 Suspension classification in terms of dimensionless numbers

In this section, we introduce some non-dimensional numbers which were used by [Coussot and Ancy \[1999\]](#) to explain the regimes in which certain forces are dominant.

The non-dimensional number that characterizes the Brownian and non-Brownian limits compared to sedimentation is called the Peclet number (Pe).

$$Pe = \frac{4\pi r^3(\rho_p - \rho_f)gH}{3k_B T} \quad (1.2)$$

where  $r$  is the radius of the particle,  
 $\rho_p$  is the density of the particle,  
 $\rho_f$  is the density of the fluid,  
 $g$  is the acceleration due to gravity,  
 $k_B$  is the Boltzmann constant,  
 $T$  is the Temperature,  
 $H$  is the height of the vessel,

Peclet number is the ratio of the advection (particle sedimentation) to the diffusion due to Brownian motion. For  $Pe \gg 1$  Brownian motion can be neglected. Non-Brownian suspensions are usually in-homogeneous due to the density difference between the particles and the continuum fluid.

$\rho_p > \rho_f$  -> sedimentation.

$\rho_p < \rho_f$  -> creaming.

where  $\rho_p$  and  $\rho_f$  are the density of the particle and fluid respectively.

Sedimentation can be avoided by the application of external shear. In such a scenario the modified Peclet number is

$$Pe = \frac{6\pi\mu_f\dot{\gamma}r^3}{k_B T} \quad (1.3)$$

where,  $r$  is the radius of the particle,  
 $\mu_f$  is the viscosity of the fluid.  
 $\dot{\gamma}$  is the shear rate.  
 $k_B$  is Boltzmann constant.  
 $T$  is the Temperature.

Stokes number is defined as the ratio of the characteristic time of a particle to a characteristic time scale of the flow. Here, particle characteristic time is nothing but the time required for the particle to adjust its velocity to the changes in the fluid velocities when fluid encounters an obstacle.

$$St = \frac{t_0 v_f}{l_0} \quad (1.4)$$

where,  $t_0$  is the relaxation time,

$v_f$  is the fluid velocity,

$l_0$  is the characteristic dimension of the obstacle.

For spherical particles, the drag force on the particle is given by

$$F_d = 6\pi\mu_f r u_0 \quad (1.5)$$

and the characteristic time

$$t_0 = \frac{\rho_p d_p^2}{18\mu_f} \quad (1.6)$$

Therefore Stokes number becomes

$$St = \frac{\rho_p d_p^2 u_0}{18\mu_f l_0} \quad (1.7)$$

When a suspension is flowing in a device with velocity changing in magnitude and/or direction, the particles follow the fluid streamlines when the viscous forces are dominant and they deviate when the inertial effects are dominant. Particle Reynold's number is used to decipher the same.

$$Re_p = \frac{\rho_p d_p^2 \dot{\gamma}}{\mu_f} \quad (1.8)$$

where

$\rho_p$  is the particle density

$\mu_f$  is the fluid viscosity

$\dot{\gamma}$  is the shearrate

$d_p$  is the particle diameter

The particle Reynolds number is defined as the ratio of the inertial force to the viscous force. For particle Reynolds number  $\ll 1$ , then viscous force dominates and particles follow streamlines. However, if particle Reynolds number  $> 1$ , then particles tend to drift from the streamlines due to inertial force.

The Reynolds number for the whole system is given by

$$Re = \frac{\rho_s L^2 \dot{\gamma}}{\mu_s} \quad (1.9)$$

where

$L$  is the characteristic length of the macroscopic flow over which the time-averaged velocity significantly varies.

$\rho_s$  and  $\mu_s$  are for the suspension density and viscosity.

This is used to estimate the onset of turbulence in the system. The range of  $Re$  at which transition to turbulence occurs varies widely based on the system under consideration and has not been found for many complex fluids.

$N_r$  represents the ratio of interaction energy(due to surface forces, etc.) to the Brownian energy. This interaction potential arises due to the presence of surface charges or polymeric interactions, steric effects, etc.

$$N_r = \frac{\Phi_0}{k_B T} \quad (1.10)$$

where  $\Phi_0$  is the interaction energy due to the neighbouring particles.

$\Gamma$  is the ratio of hydrodynamic dissipation to suspension yield stress( $\tau_c$ ).

$$\Gamma^* = \frac{\mu\dot{\gamma}}{\tau_c} \quad (1.11)$$

$$\Gamma = \frac{K}{b}\Gamma^* \quad (1.12)$$

where,  $b$  is the average inter-particle distance,  $K$  is a coefficient that depends on the shape and size of the particle and the orientation of the particle. For a sphere,  $K$  is equal to  $3\pi r$ .

Leighton number ( $Le$ ) is the ratio of lubrication forces to friction forces.

$$Le = \frac{\mu_f\dot{\gamma}b}{\sigma_f} \quad (1.13)$$

where  $\sigma_f$  is the stress due to friction which occurs when particles are in contact.

and  $b$  is the average inter-particle distance.

The friction between two particles in contact depends on the normal force and the particle surface roughness. When the Leighton number becomes lower than a critical value, frictional forces predominate and there is no more flow in some regions.

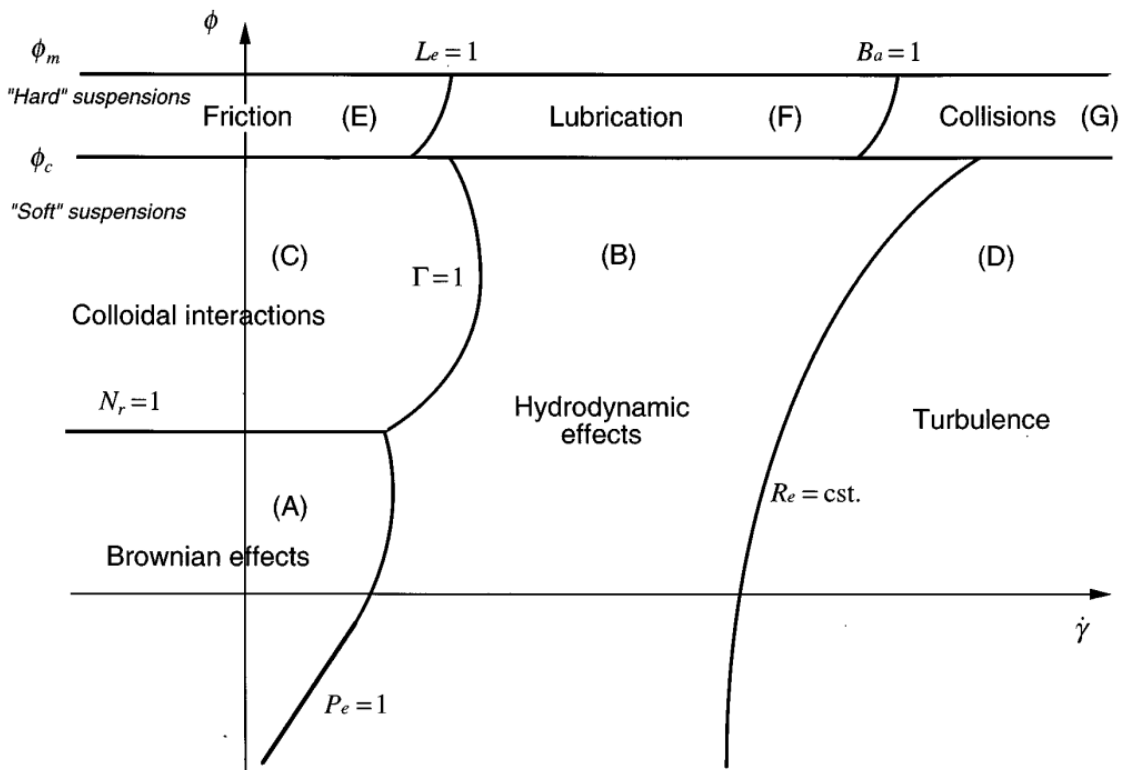


Figure 1.1: Conceptual classification of rheo-physical regimes of a suspension. Courtesy: [Cousso and Ancy, 1999]

Bagnold number(Ba) separates the viscous regime from the inertial regime where particle collisions predominate the rheology at sufficiently large shear rates and/or high volume fractions. For small values of Bagnold numbers, viscous fluid stress are more predominant compared to collision stresses and similarly, when the Bagnold number is very large grain collision stresses dominate the flow. Bagnold number is the ratio of particle kinetic energy to viscous dissipation energy given by

$$\text{Ba} = \frac{\rho_p \dot{\gamma} r^2}{\mu_f} \quad (1.14)$$

Where  $\rho_p$  is the density of the particle.

Suspensions can be theoretically classified based on the predominant phenomena. [Coussot and Ancy \[1999\]](#) proposed the following plot with volume fraction ( $\phi$ ) on the X-axis and shear rate ( $\dot{\gamma}$ ) on the Y-axis for rheo-physical regimes. Different non-dimensional numbers separate the regimes as shown in figure 1.1.

## 1.2 Rheology of granular suspensions

Rheology is defined as the branch of physics which deals with the study of deformation and flow of matter. The classical Navier-Stokes equation is solved with the assumption that for a pure liquid, stress is proportional to strain rate. The fluids for which such a relationship is valid are called Newtonian liquids and the proportionality constant is called viscosity.

$$\tau = \mu \dot{\gamma} \quad (1.15)$$

However, there exists a wide variety of materials with very different stress responses to strain rate. Bingham model fluid is linear but with an intercept called yield stress.

$$\tau = \tau_0 + \mu \dot{\gamma} \quad (1.16)$$

Ostwald-de Waele model fluid can be expressed using the following equation

$$\tau = K \dot{\gamma}^n \quad (1.17)$$

For  $n=1$  the fluid is Newtonian, for  $0 < n < 1$ , the fluid is shear-thinning and for  $n > 1$  the fluid is shear-thickening. Finally, Herschel-Buckley fluid has finite yield stress and non-Newtonian response once it begins to flow.

These different types of rheology could be summarized in the following figure 1.2 by [Steffe \[1996\]](#)

Over the years to describe the rheology of suspensions multiple equations were proposed. Most of them consider Newtonian behaviour, the viscosity depending on the solids volume fraction. Some of which are described in the following subsections.

### **Einstein Equation (1905)**

Einstein was the first to study theoretically the suspension behaviour in the dilute limit (applicable at very low volume fractions:  $\phi < 0.03$ ) [Einstein \[1905\]](#). He analytically derived the solution for the hydrodynamics around an

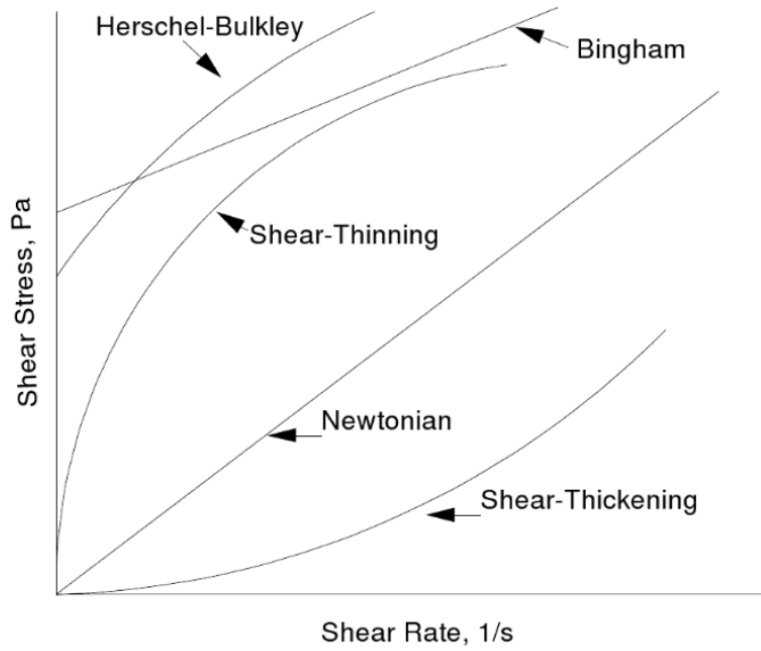


Figure 1.2: Flow curves for a typical time-independent fluids. Courtesy: [Steffe, 1996].

isolated sphere. This can be written as

$$\mu_s = \mu_f(1 + 2.5\phi) \tag{1.18}$$

where  $\mu_s$  is the homogenized viscosity of the suspension and  $\mu_f$  is the viscosity of the fluid.

**Taylor (1932)**

Taylor generalized the Einstein equation and extended it to soft non-rigid spherical particles and droplets [Taylor, 1932].

$$\mu_s = (1 + 2.5\phi * (\frac{\mu_d + \frac{2}{5}\mu_f}{\mu_d + \mu_f}))\mu_f \tag{1.19}$$

where  $\mu_d$  is the viscosity of the dispersed phase.

**Batchelor (1977)**

Batchelor in 1977 modified Einstein’s equation by including the higher order terms and extending the validity to ( $\phi < 0.1$ ) [Batchelor, 1977].

$$\mu_s = \mu_f(1 + 2.5\phi + 5.2\phi^2) \tag{1.20}$$

**Maron-Pierce-Quemada(MPQ) (1956, 1977)**

Maron-Pierce proposed the following model which involves critical volume fraction of the granules in the suspension:  $\phi_c$  [Maron and Pierce, 1956]. It was popularized by Quemada [1977].

$$\mu_s(\phi) = \mu_f \left(1 - \frac{\phi}{\phi_c}\right)^{-q} \quad (1.21)$$

Quemada [1977] obtained the value  $q = 2$  by minimizing the dissipated energy due to viscosity.  $\phi_c$  is considered as the random close packing volume fraction of the granules ( $\phi_{rcp}$ ).

Shewan and Stokes [2015a] have shown that one can predict the viscosity of suspensions using the MPQ model for hard normally distributed poly-disperse spherical particles without any adjustment by estimating the  $\phi_{rcp}$  by the method suggested by Farr and Groot [2009].

### Krieger-Dougherty (1959)

Krieger-Dougherty proposed the following equation which takes into account both the poly-dispersity and shape factor of the granules in the suspension.

$$\mu_s = \mu_f \left(1 - \frac{\phi}{\phi_{\max}}\right)^{-[\eta]\phi_{\max}} \quad (1.22)$$

where  $\phi_{\max}$  is the maximum packing volume fraction and  $\eta$  is the shape factor (2.5 for spheres).

All the above model equations do not describe the non-Newtonian behaviour often observed in dense suspensions such as shear-thickening and shear-thinning [Stickel and Powell, 2005, Chatté et al., 2018]. For the above-derived model, it is assumed that particle-particle interactions are negligible. This assumption is not valid for dense suspensions where hydrodynamic interactions alone are not sufficient to describe the momentum transfer.

Chialvo and Sundaresan [2013] showed that extending kinetic theory allows prediction of dense flows ( $0.5 < \phi < \phi_c$ ) of frictional granular materials. Some micro-mechanical approaches have led to the development of numerous constitutive equations [Johnson and Jackson, 1987, Stickel and Powell, 2005, Seth et al., 2011, Ness and Sun, 2016]

Ness and Sun [2016] showed that particle-particle frictional contacts are at the origin of shear-thickening through DEM shear-flow simulations of bi-disperse spherical particles. Further, they have illustrated that the region at which the onset of shear-thickening occurs could be tuned based on particle parameters.

Shear-thinning in non-Brownian suspensions is an active area of research both experimentally and through simulations. Recently, Lobry et al. [2019] have shown the usefulness of a variable friction model to reproduce the shear-thinning in non-Brownian suspensions using DEM. More and Ardekani [2020] have proposed the plasticity of contact at the scale of particle roughness as yet another possible cause of shear-thinning.

On the experimental front, Chatté et al. [2018] have shown that soft particles which undergo compression at high shear rates could lead to shear-thinning. Vázquez-Quesada et al. [2016] showed that due to high local shear rates experienced by the fluid at the inter-particle gaps, the continuous media (silicon oil in this case) breakdown could lead to overall shear-thinning of the suspension. Papadopoulou et al. [2020] showed via optical rheometer experiments that friction and particle adhesion can play a role in the shear-thinning of suspensions. They have used spherical glass beads in glycerol which showed Newtonian behaviour even for volume fractions as high as 0.5. However, rough silica particles in glycerol (polar solvent) showed shear-thinning behaviour at a volume fraction

as low as 0.25. Also, shear-thinning was observed for both glass-spheres and silica particles in mineral oil (apolar solvent) driven by adhesion even at volume fractions as low as 2%. [Vo et al. \[2020\]](#) showed through simulations combining both particle and viscous effects that, when the apparent friction and packing fraction are normalized by their cohesion-dependent quasistatic values, they are governed by a single dimensionless number that, by virtue of stress additivity, accounts for all interactions.

## 1.3 Starch

Starch is a polysaccharide produced during photosynthesis in plants. It is the principal mode of energy reserves in plants. It is often found in tuber and grains. Worldwide more than 70% of calories consumed by humans originate from starch [Bertolini \[2010\]](#). Thus, starch is one of the most abundant bio-polymer that exists on planet earth [\[Zobel and Stephen, 1995\]](#). Starch also finds many applications as raw materials in biomedical, packaging, paper, textile and pharmaceutical industries. Different types of starch are used as bulking agents, thickeners, stabilizers, viscosity builders and gel formers. Starch is also the key starting material for producing various bio-materials such as maltose, maltodextrins and cyclodextrins.

Worldwide starch production is expected to be around 156 million metric tons by 2025 [\[Reportlinker.com, 2020\]](#). Hence, starch has been a subject of research for many decades and is expected to increase further by a shift away from petroleum-based polymers to meet sustainability challenges.

### 1.3.1 Structure of starch

Starch regardless of the nature of the plant source consists mainly of d-glucopyranose-based polymeric structures [\[Ratnayake and Jackson, 2008\]](#). The size, shape and molecular arrangements, however, depending on the species, cultivar, variety of the source plant and the generic interactions [\[Ratnayake and Jackson, 2008, Trubell, 1944, Zobel et al., 1988\]](#). The starch biosynthesis pathway generally results in the formation of two different kinds of polymers called amylose and amylopectin.

Figure 1.3 shows the biochemical pathway which leads to the formation of amylose and amylopectin in plants. The two polymers have the same monomer and only differ in the glycosidic linkages. Amylose is linear polymer with majorly  $\alpha(1-4)$  glycosidic linkage [and 2-5%  $\alpha(1-6)$  linkages] as shown in figure 1.4 and has molecular weight less than  $100,000 \text{ g mol}^{-1}$ . Amylopectin is a branched polymer which has both  $\alpha(1-4)$  and  $\alpha(1-6)$  bonds with a molecular weight ranging from  $50,000,000 \text{ g mol}^{-1}$  to  $500,000,000 \text{ g mol}^{-1}$  [\[Banks et al., 1974, Thomas and Atwell, 1999\]](#). The amylopectin molecule on average contains 20-25  $\alpha(1-6)$  linkages as shown in figure 1.4, leading to a highly branched structure [Hizukuri \[1986\], Manners \[1989\]](#)

Polymer compositions (amylose and amylopectin ratios) are genetically controlled and mutations occur naturally or via plant breeding techniques to obtain high-amylose or high amylopectin starches [\[Blennow et al., 2001, Bogracheva et al., 1999, Tetlow, 2006\]](#). High-amylopectin starches are called waxy starches. Waxy-maize starches contain less than 1% amylose content. Typical compositions of amylose and amylopectin found in common botanical starch sources are listed in table 1.1.

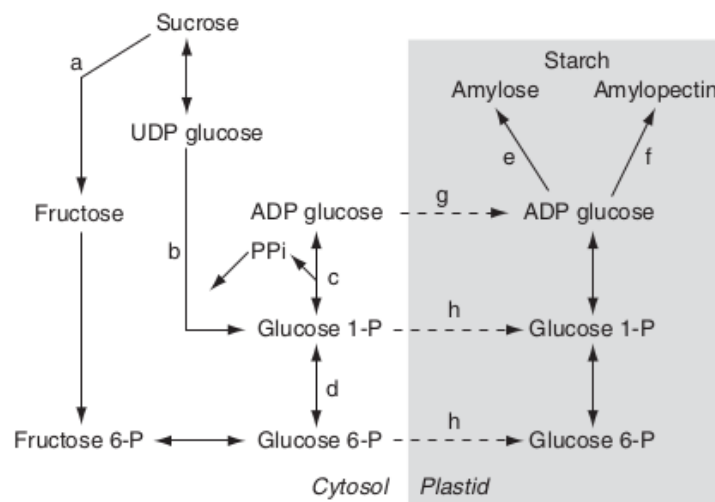


Figure 1.3: Biochemical pathway of starch biosynthesis from sucrose. Enzymes are represented with alphabets they are (a) sucrose synthase; (b) UDPglucose pyrophosphorylase; (c) ADPglucose pyrophosphorylase; (d) phosphoglucomutase; (e) starch synthase (GBSSI); (f) starch synthase and starch-branching enzyme; (g) ADPglucose transporter; (h) hexose phosphate transporter. PPi: inorganic pyrophosphate. Courtesy: [Smith et al., 1997]

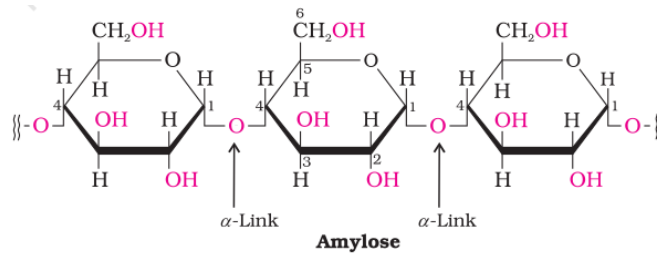


Figure 1.4: Amylose polymer skeletal structure. Courtesy: [Khandelwal et al., 2020]

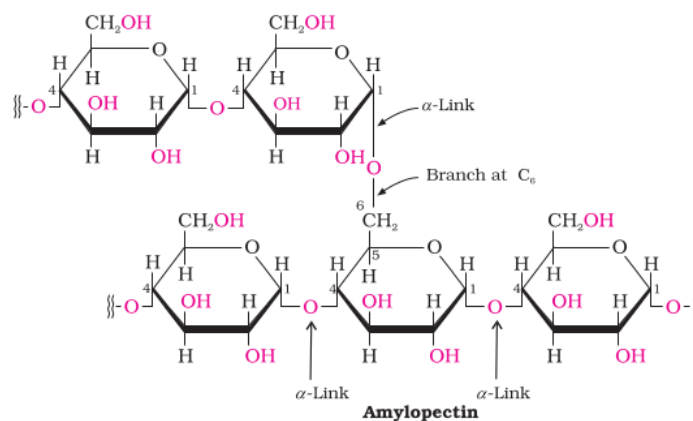


Figure 1.5: Amylopectin polymer skeletal structure. Courtesy: [Khandelwal et al., 2020]

Another important structural feature of starch is the presence of growth rings inside granules. They were first reported by Leach [1913]. Various theories have been proposed to explain the existence of the same [Trubell, 1944,

Type of starch	amylose %	amylopectin %
Maize	25	75
Waxy Maize	< 1	> 99
Amylomaize	55-70	45-30
Tapioca	17	83
Potatoes	20	80
Wheat	25	75
Rice	19	81

Table 1.1: Proportion of amylose and amylopectin in common starch sources. Courtesy: [Thomas and Atwell, 1999].

Pilling and Smith, 2003]. However, it is still not completely understood and is an open research question.

Native unswollen starch shows optical birefringence: when polarized light is shown through starch, a pattern known as “Maltese cross” is observed [Greenwood, 1979] (figure 1.6). This shows that there is a high degree of molecular order within the granule, also known as crystallinity. Birefringence is known to occur only when the material is anisotropic.

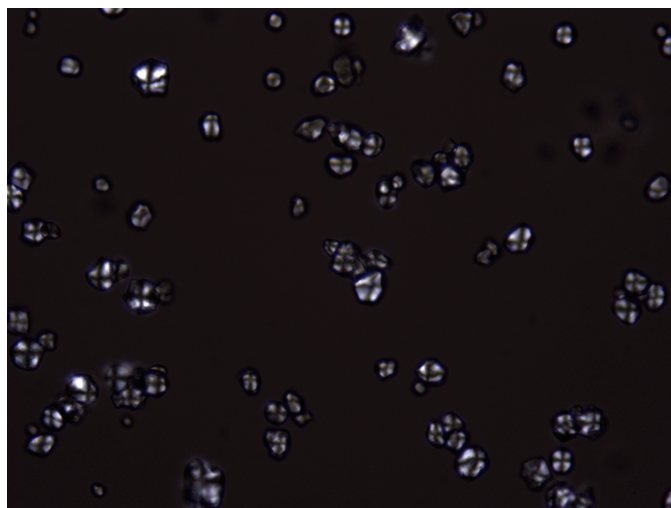


Figure 1.6: Maize starch granules viewed under polarized light (Magnification X50).

In starch, amylose and amylopectin polymers are organized into a radial anisotropic and semi-crystalline unit [Blanshard, 1979]. The crystallinity of starch is caused essentially by amylopectin polymer interactions [Banks et al., 1974, Biliaderis, 1998, Donald et al., 2004, Hizukuri, 1996].

The generally accepted intra-granular structure of starch is shown in figure 1.7. The granule contains alternating layers of amorphous and crystalline domains in concentric rings that create semi-crystallinity. It is known that the crystalline layer is rich in amylopectin and the amorphous layer is rich in amylose with non-crystalline regions of amylopectin. There exist three polymorphs of starches A, B and C based on the pattern of crystallinity [Sarko and Wu, 1978]. Polymorph C is a mixture of polymorph A and polymorph B.

A significant quantity of native starch is processed by subjecting it to various forms of chemical and physical modifications, resulting in starches with greater functionalities [Zobel, 1992]. Physical modification of starch involves changes in morphology and structure with altering parameters such as moisture, temperature, pressure, pH, etc. Typical chemical processing of starch involves oxidation, etherification, etc. [Nawaz et al., 2020].

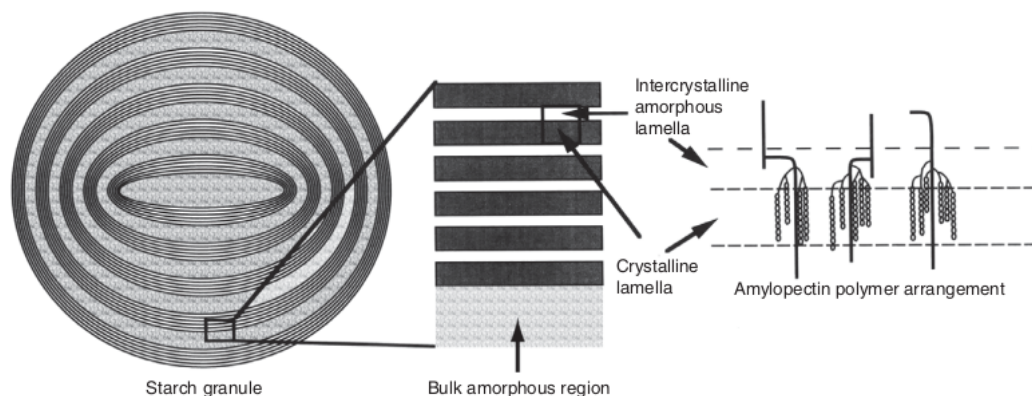


Figure 1.7: Schematic diagram of starch granule structure. Courtesy: [Donald et al., 1997]

Organigram in figure 1.8 encompasses all the types of starch modifications typically employed in the industry. Some of the properties obtained via chemical modification are shear/rupture resistance and lower leaching of amylose. For further details regarding the impact of different modification processes on functional and structural properties of starch, the readers could refer to Nawaz et al. [2020].

### 1.3.2 Starch gelatinization

Starch gelatinization is the process in which starch undergoes an irreversible transformation when subjected to thermal treatment in the excess of water. During gelatinization, the crystalline structures are disrupted resulting in the loss of birefringence [Atwell, 1988, Biliaderis, 1992]. Figure 1.9 shows the in-situ measurements of crystallinity during gelatinization of starch through polarized light microscopy Cai and Wei [2013].

Gelatinization is an endothermic process as shown via DSC measurements Chen et al. [2007]. Figure 1.10 shows the Differential Scanning Calorimetry (DSC) measurements of starch suspensions during gelatinization.

Figure 1.11 shows the rapid visco analyser measurements for different types of starches. The viscosity is measured during the gelatinization process in an arbitrary units (R V U). During gelatinization, starch granules swell by imbibing water. This increases the volume fraction of granules in the suspension thus increasing the viscosity as shown through rapid visco analyser measurements in figure 1.11. However, during later stages of gelatinization for most starches the granule rupture and releases amylose into the continuous phase. This results in loss of viscosity Atwell [1988], Biliaderis [1992]. The granule rupture and loss in viscosity do not occur for some starches such as chemically modified waxy-maize starches. This is primarily because waxy-maize as previously mentioned contains less than 1% amylose and secondly, the introduction of functional groups such as acetylation increases the granule strength. This property enables the use of such starches in a wide range of viscosity-enhancing applications.

The progress of gelatinization has been increasingly quantified based on the increase in diameter of the granules [Anuntagool et al., 2017, Okechukwu and Rao, 1996, Bagley and Christianson, 1982, Bakshi and Singh, 1980b, Doublier et al., 1987, Kokini et al., 1992]. However, alternatives methods to quantify the same such as DSC, change in rheology or loss in birefringence have also been used [Cui et al., 2014, Choi and Kerr, 2004, Dolan and Steffe, 1990, Biliaderis and Prokopowich, 1994, Chang and Liu, 1991, Kohyama and Nishinari, 1991, l'anson et al., 1990,

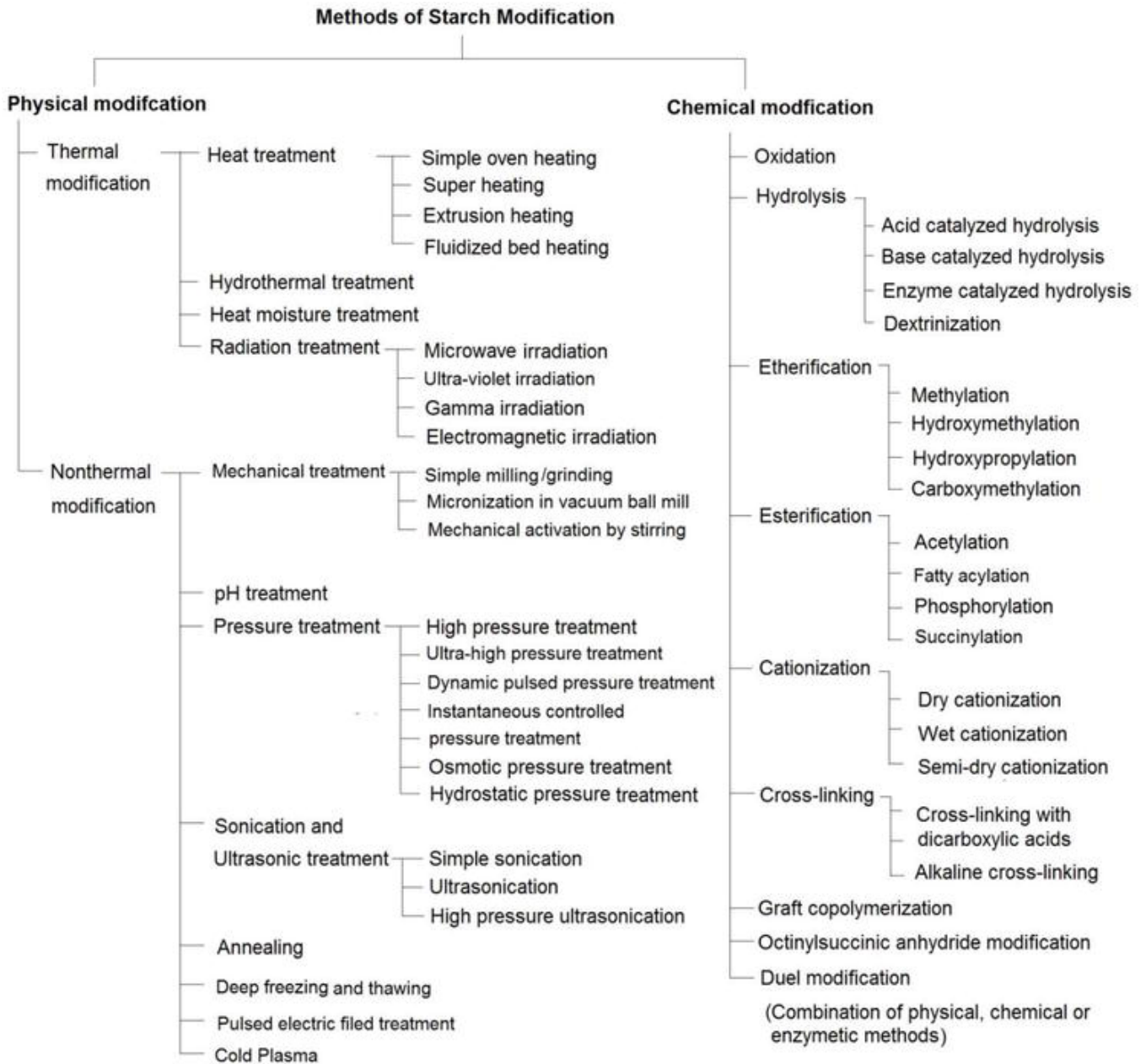


Figure 1.8: Methods of starch modifications. Courtesy: [Nawaz et al., 2020]

Miles et al., 1985, Slade and Levine, 1991].

Various mathematical models based on diameter evolution have been proposed over the decades [Chen et al., 2007, Lagarrigue et al., 2008, Okechukwu and Rao, 1996, Malumba et al., 2013, Desam et al., 2018a, 2020].

Lagarrigue et al. [2008] have defined a non-dimensional parameter called degree of swelling.

$$S = \frac{D_t - D_0}{D_f - D_0} \quad (1.23)$$

where  $D_0$  represents the median diameter of the native starch granules,  $D_t$  is the instantaneous median diameter during gelatinization and

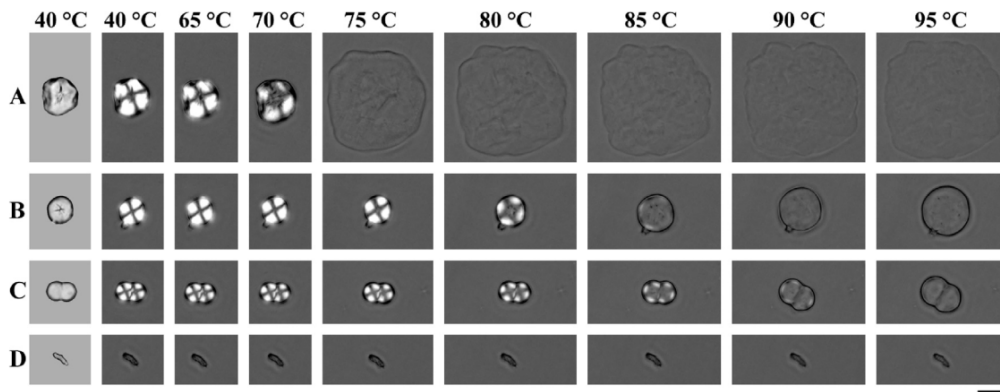


Figure 1.9: Loss of birefringence of starch granules during gelatinization process. (A) Individual starch granule from normal maize; (B),(C) and (D) individual, aggregate and elongated granules from high-amylose maize, respectively. Courtesy: [Cai and Wei, 2013]

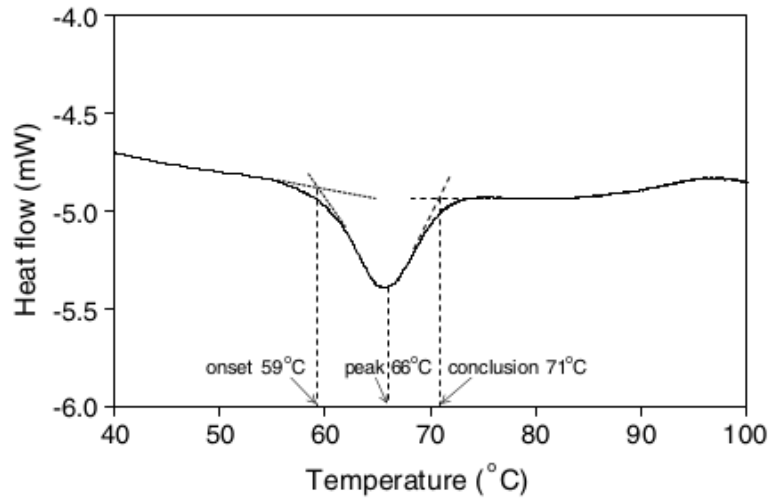


Figure 1.10: DSC measurements of starch suspensions. Courtesy: [Chen et al., 2007]

$D_f$  is the maximum median diameter reached during gelatinization as shown in figure 1.9a.

Further, they proposed a second-order rate equation for gelatinization given by

$$\frac{dS}{dt} = K_0 \times \exp\left(-\frac{E_a}{RT(t)}\right)(1 - S)^2 \quad (1.24)$$

where,  $E_a$  is the energy of activation,  
 $R$  is the universal gas constant,  
 $T$  is the temperature and  
 $K_0$  is the rate constant.

Chen et al. [2007] proposed a Weibullian model to forecast the time-temperature dependence of granules swelling in excess water.

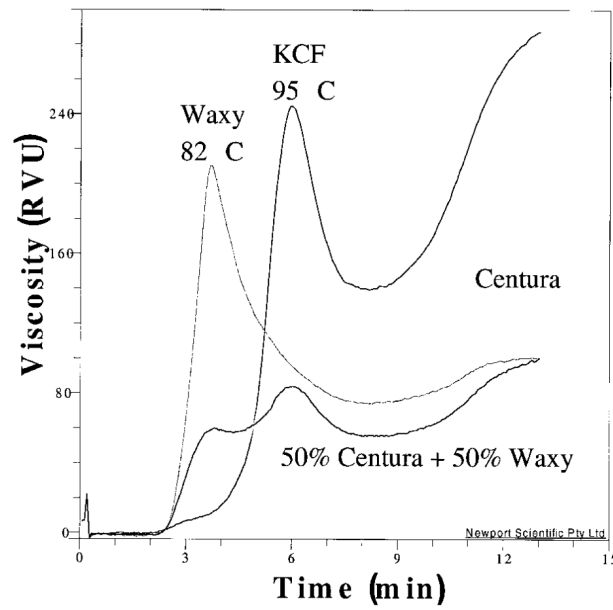


Figure 1.11: Flour Rapid Visco Analyser (RVA) pasting curves. Courtesy: [Guo et al., 2003]

$$S = 1 - 10^{-c_1 t^{c_2}} \quad (1.25)$$

Where  $c_1$  and  $c_2$  are Weibull parameters varying according to the type of starch and experimental conditions.

Peleg [1988] proposed a two parameter empirical model for soaking of rice given by

$$S = \frac{t}{p_1 + p_2 t} \quad (1.26)$$

where  $t$  is the duration of soaking,

$p_1$  and  $p_2$  are constant parameters determined using a non-linear regression.

Okechukwu and Rao [1996] proposed a model to predict the equilibrium median diameter reached by granules using an exponential law. Rao and Tattiyakul [1999] and Chen et al. [2007] for the same prediction used a power-law model given by

$$D_e = BT^{B'} \quad (1.27)$$

Where  $D_e$  is the equilibrium median diameter reached ( $\mu\text{m}$ ) by granules during isothermal treatment

$T$  is the isothermal temperature used to swell the starch granules

$B$  and  $B'$  are power-law parameters respectively.

Malumba et al. [2009] has proposed a generalized two-asymptotic logistic model given by

$$D_{e(T)} = D_f + \frac{D_f - D_0}{1 + \exp\left(\frac{T-T_0}{r}\right)} \quad (1.28)$$

where  $D_{e(T)}$  is the equilibrium median diameter reached ( $\mu\text{m}$ ) by granules during isothermal treatment at  $T$  ( $^{\circ}\text{C}$ ),

$T$  is the temperature considered for isothermal treatment ( $^{\circ}C$ ),

$D_0$  is the median diameter of native granule before any hydro-thermal treatment ( $\mu m$ ),

$D_f$  is the maximum equilibrium median diameter reached during phenomenon ( $\mu m$ ),

$I$  is the temperature at the inflexion point of change on equilibrium median diameter ( $^{\circ}C$ ) and

$r$  is the range of temperature around the inflexion point with significant change on equilibrium median diameter ( $^{\circ}C$ )

[Malumba et al. \[2013\]](#) have used the same definition of non-dimensional parameter for the degree of swelling  $S$  mentioned in equation 1.23, 1.29, 1.30 and fitted a whole array of common kinetic models for gelatinization which are listed in table 1.2.

$$\frac{dS}{dt} = K(T) \times f(S) \quad (1.29)$$

$$\ln(K(T)) = \ln(K_0) - \frac{E_a}{RT} \quad (1.30)$$

Model	$f(S)$
First order	$(1 - S)$
Second order	$(1 - S)^2$
Third order	$\frac{1}{2}(1 - S)^3$
Prout Tompkins	$S(1 - S)$
Two-dimensional phase boundary	$2(1 - S)^{\frac{1}{2}}$
Three-dimensional phase boundary	$3(1 - S)^{\frac{1}{3}}$
One-dimensional diffusion	$\frac{1}{2}S$
Three-dimensional diffusion (Jander)	$\frac{3}{2}(1 - S)^{\frac{2}{3}}[1 - (1 - S)^{\frac{-1}{3}}]^{-1}$
Avrami-Erofeev A2	$2(1 - S)[- \ln(1 - S)]^{(\frac{1}{2})}$
Avrami-Erofeev A3	$3(1 - S)[- \ln(1 - S)]^{(\frac{2}{3})}$
Avrami-Erofeev A4	$4(1 - S)[- \ln(1 - S)]^{(\frac{3}{4})}$

Table 1.2: Common solid-state reaction kinetic model used to model starch gelatinization in [Malumba et al. \[2013\]](#)

[Desam et al. \[2018a\]](#) proposed a model for swelling of single granules based on diffusion kinetics and Flory-Huggins theory of polymer mixing but the model assumes all granules to have similar cross-links, tortuosity and elastic restoring force. In other words the biological variability is not taken into account.

## 1.4 DEM

The discrete element method is a particle-based method that solves Newton's equations of motion with a predetermined timestep. Particle-based simulation techniques often give deeper insights into quantities that may be difficult to determine experimentally such as force between grains, distribution of contacts, etc. Also, the continuous descriptions could be deduced from the particle simulation data through averaging processes to

compute bulk properties such as stress tensor and strain tensor. Despite the growing power of computers, the typical drawback of very high computational intensity for such methods is still a concern. This severely limits the number of particles that could be simulated and often the simulation time ranges from days to weeks.

DEM could be sub-classified based on the methodology used to solve Newton's equations of motion. Some of these sub-types are discussed briefly here.

### 1.4.1 Soft-particle method (Molecular dynamics method)

The soft particle method is by far the most commonly used DEM method owing to its simplicity [Cundall and Strack, 1979]. This method is a branch of traditional molecular dynamics simulations. The motion of each grain is computed from Newton's laws and the contact forces between particles. The particles are assumed to be non-deformable but inter-penetrable as shown in figure 1.12. The interpenetrating distance and the velocity of particles are used to calculate the contact forces between the particles. Various contact models are defined to estimate the normal and tangential forces from the interpenetration distance. Typically, for the normal forces, the interaction is modelled with a spring and a viscous dashpot. The tangential forces are modelled with a combination of spring and a sliding block to imitate the frictional force.

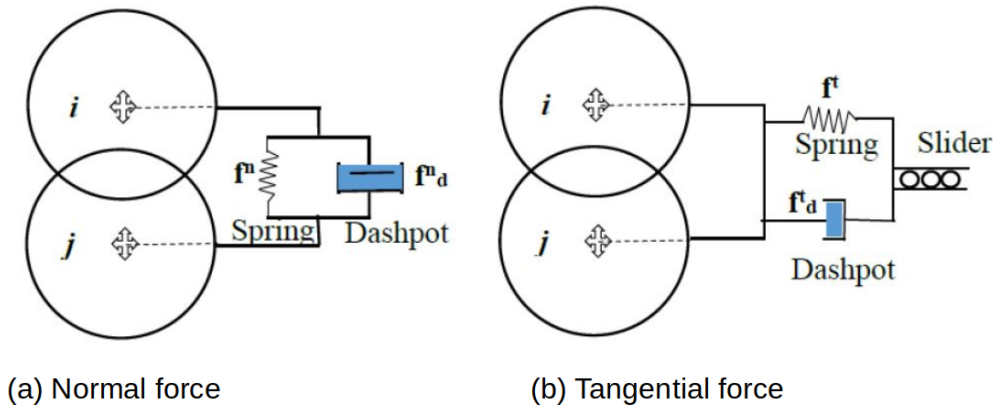


Figure 1.12: Spring and dashpot analogy of contact deformation in soft-particle method.

This method requires that the collision dynamics are accurately resolved, which requires the timestep to be much smaller than the typical time of the collision. A rule of thumb to determine the maximum timestep that can be used without any subsequent reduction in resolution is given by 20% of Rayleigh timestep.

$$t_{\text{rayleigh}} = \frac{\pi * R * \sqrt{\frac{\rho}{G}}}{0.1631 * \nu_p + 0.8766} \quad (1.31)$$

- where  $R$  is the average radius of the particles,
- $\rho$  is the density of particles,
- $G$  is the shear modulus of the particles,
- $\nu_p$  is the Poisson's ratio of particles,

The small timestep results in a very high computational cost for this method. Often this model uses spherical particles for simulations due to the simplicity of the contact detection algorithm employed. Non-spherical particles are modelled either using a multi-sphere approach where particles are glued together to recreate the required non-spherical geometry or through super-quadratics particle shapes. Various interactions such as cohesion, electrostatic forces could be introduced within the framework using a contact model of this method [Ramirez-Aragón et al., 2018]. In this thesis, we use this method owing to this feature and the existence of extensive literature.

### 1.4.2 Contact-dynamics method

The contact dynamics method is based on the idea of perfectly rigid particles and the implementation of Coulomb’s law [Jean and Moreau, 1992, Jean, 1999]. The contact between two particles is described by two non-regular laws, one each for normal and tangential components. This method accounts for both instantaneous collisions and long term contacts as well as multiple collisions. The advantages of the contact dynamics method include the fact that it does not require numerical timesteps as small as those of the soft-particle method and secondly, it could be applied to particles of arbitrary shapes. However, this method only gives the dynamics in the limit of rigid particles which might not be the case in starch particle suspensions.

## 1.5 CFD-DEM

CFD-DEM is a multiscale Eulerian-Lagrangian technique used for the simulation of systems that involve interactive fluid and solid phases. The Lagrangian DEM method is combined with an Eulerian CFD method for fluid motion.

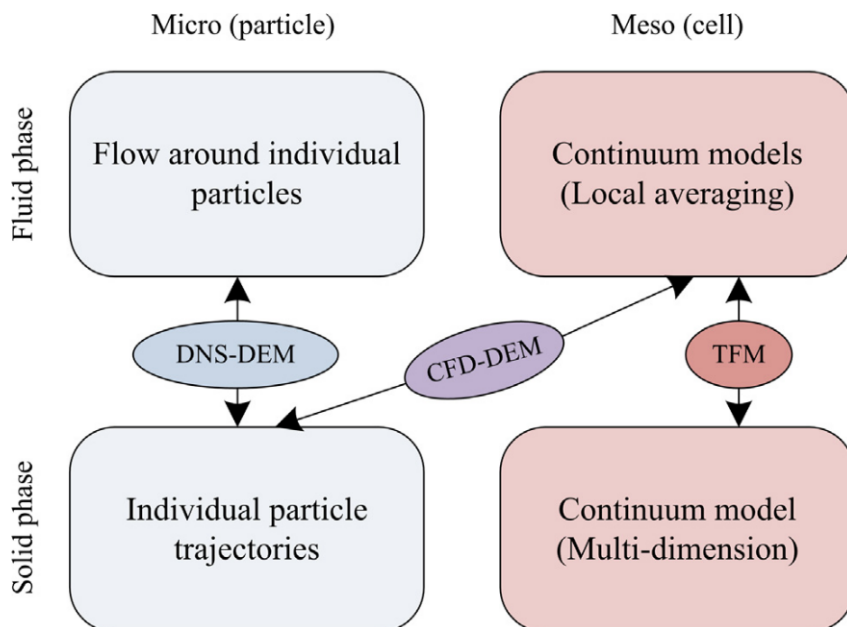


Figure 1.13: Modeling scales in fluid-solid systems. Courtesy: [Norouzi et al., 2016]

Typical simulation techniques which capture different levels of details used for simulating solid-liquid dispersion

are shown in figure 1.13. Direct numerical simulations (DNS) coupled with DEM captures well the micro-scale phenomena in both fluid and solid phases. The two-fluid model (TFM) is a typical Eulerian-Eulerian method that employs continuum assumption to both solid and liquid phases to simulate the averaged macro phenomena. CFD-DEM uses the Lagrangian framework for the solid phase to capture the micro-scale particle data and the Eulerian framework for the fluid phase.

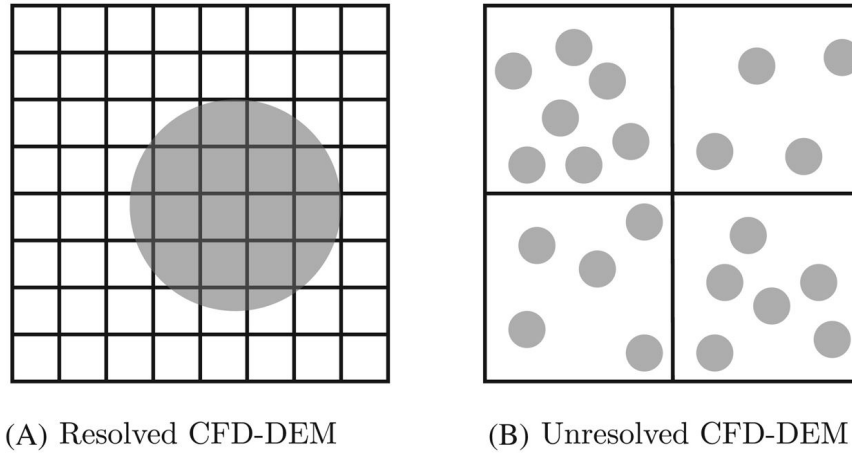


Figure 1.14: CFD-DEM coupling methods. Courtesy: [Kanitz and Grabe, 2021]

Typically two types of CFD-DEM coupling approaches exist: unresolved CFD-DEM and resolved CFD-DEM (Figure 1.14). In unresolved CFD-DEM there are many DEM particles in each CFD cell while in resolved CFD-DEM coupling the size of the CFD cell is much smaller than the particle size of the DEM particle. Most applications in literature use unresolved CFD-DEM coupling owing to its ability to simulate a large number of particles in comparison to resolved CFD-DEM. However, resolved CFD-DEM is useful in analysing applications involving the micro-scale flows around particles. CFD-DEM coupling of non-spherical particles is very complex with many unknown and open research questions. Unresolved CFD-DEM coupling with spherical particles is used in chapter 5 owing to these reasons.

A typical algorithm for unresolved CFD-DEM coupling is shown in figure 1.15. The first step of the coupling process is the calculation of the “porosity” using the volume fraction of the fluid in each CFD cell based on the position (centre of particles) and size of particles.

$$\varepsilon = 1 - \frac{\sum_{i=1}^n \phi_i V_i}{V_{\text{cell}}} \quad (1.32)$$

where  $\phi_i$  is the volume fraction of particle  $i$  in the CFD cell

$V_i$  is the particle volume

$V_{\text{cell}}$  is the fluid cell volume

Methods exist to determine analytically the volume fraction of particles inside the CFD cell. However, it is often complex and computationally intensive, especially for unstructured CFD meshes. The complexity of coupling is

reduced by using the particle centroid method(PCM). Typically, in a particle centroid method, the particle is assumed to belong to one CFD cell if its centre is in the CFD cell. In other words sharing of particles between CFD, cells are not considered. This assumption is valid as long as the ratio of CFD cell size to particle diameter ratio is greater than about 4 as the error associated with PCM is negligible at this resolution [Peng et al., 2014]. The accuracy of the PCM method could be increased up to one order using methods such as the offset method proposed by Alobaid and Epple [2013].

In the second step of the coupling process as shown in figure 1.15, the interaction force on each particle from the fluid is calculated. The typical fluid-particle forces include drag forces, pressure gradient forces, inertial forces, buoyancy forces, viscous forces, etc. To calculate these forces the quantities such as fluid velocity, pressure and temperature are assumed to be uniform and equal to the mean value in a CFD cell. In the next step, using Newton's third law the force of all the particles on the fluid in a CFD cell is calculated. Having all the fluid-solid interaction forces on each particle, then the particle-particle interaction forces are calculated in the DEM step via the contact models. The particle positions are updated through solving Newton's second law of motion. Typically the timestep used for DEM ( $\Delta t_{DEM}$ ) is smaller than the CFD or Coupling timestep. In other words, the fluid particle coupling and CFD flow fields are updated less frequently than particle positions using DEM.

$$m_r = \frac{\Delta t_{CFD}}{\Delta t_{DEM}} \quad (1.33)$$

After the particle positions are integrated  $m_r$  times, the CFD flow fields and pressure are re-calculated. Three coupling schemes have been proposed: model A, model B and simplified model B [Zhou et al., 2010]. Although all the three are shown to be theoretically equivalent, there exist small differences numerically. In model A, the viscous and pressure gradient forces are separated from the fluid-particle interaction force whereas in model B they are included in the fluid-particle interaction force. It was shown that Newton's third law may not hold for model B, unlike model A. The simplified form of model B works with the assumption that fluid flow is steady and uniform [Zhou et al., 2010]. The most commonly used is model A where the pressure gradient and viscous forces are considered in the volume-averaged Navier-Stokes equations.

## 1.6 Heat transfer coupling

Figure 1.16 illustrates the various ways in which heat transfer occurs in fluid-particle systems. Broadly, it can be classified as heat generation and transfer terms. Heat generation can occur both in particles as well as fluid and typical examples of such phenomena are chemical reactions occurring inside the particle and viscous dissipation in fluid respectively. Heat can be transferred from wall to fluid or wall to particle or particle to particle and also from particle to fluid. Heat transfer can occur through conduction, convection and to a much lesser extent in radiation, especially in suspension systems. Heat transfer in granular systems through particle-particle conduction and particle-fluid convection has been developed and made available via fix heat/gran in LIGGGHTS DEM code [Kloss and Goniva, 2011]. However, intra-particle temperature variation is not considered in this implementation as is the case in most CFD-DEM simulations. The temperature of the particle is assumed to be uniform. This assumption is

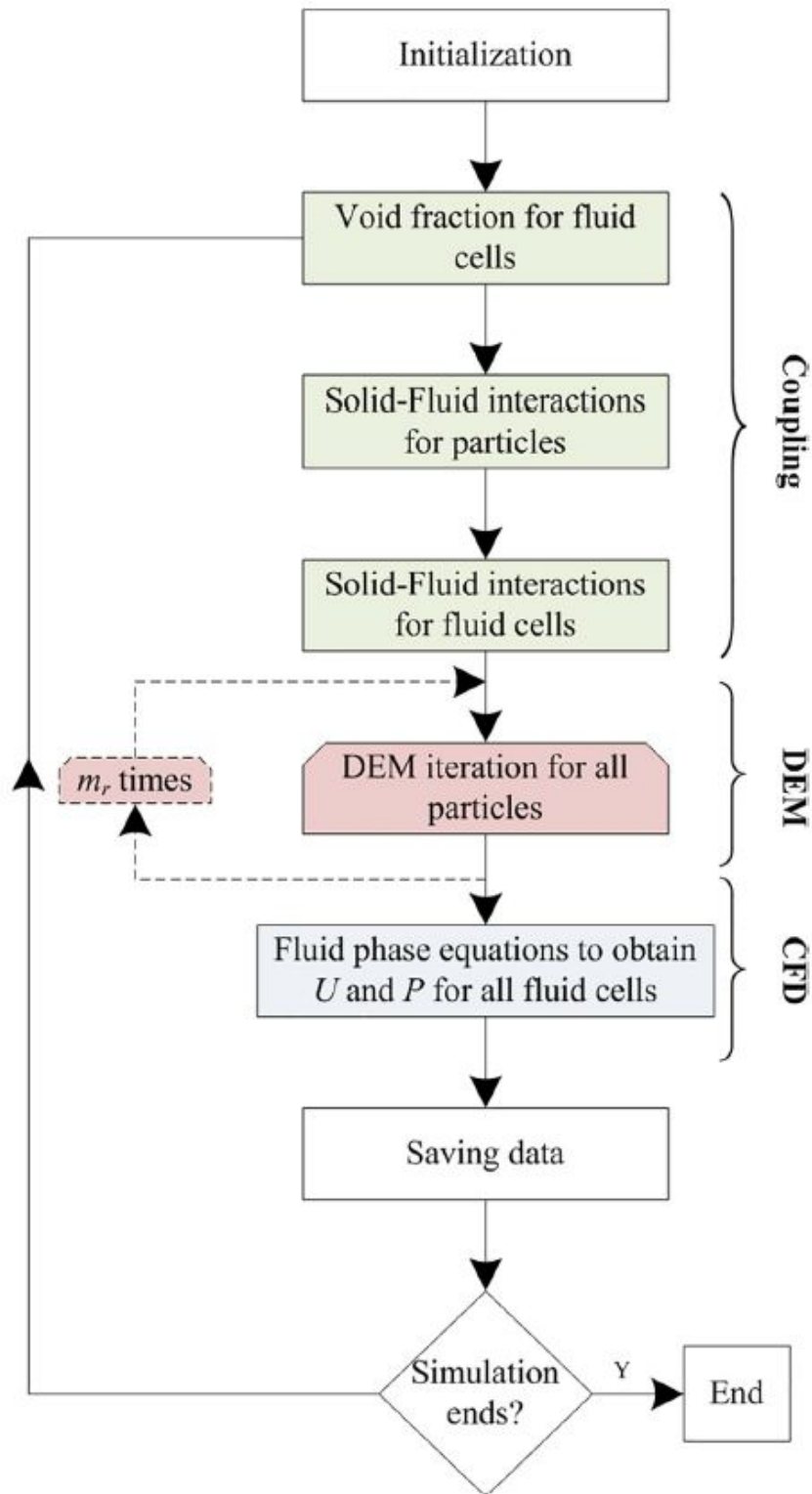


Figure 1.15: Flow chart of unresolved CFD-DEM coupling. Courtesy: [Norouzi et al., 2016]

known as lumped particle assumption and is valid only when the Biot number is less than 0.1. For a spherical particle, the Biot number can be calculated using equation 1.34.

$$Bi = \frac{h_i d_p}{2k_p} \quad (1.34)$$

where  $h_i$  is the heat transfer coefficient between particle surface and surrounding fluid

$d_p$  is the diameter of the particle

$k_p$  is the material thermal conductivity of the particle

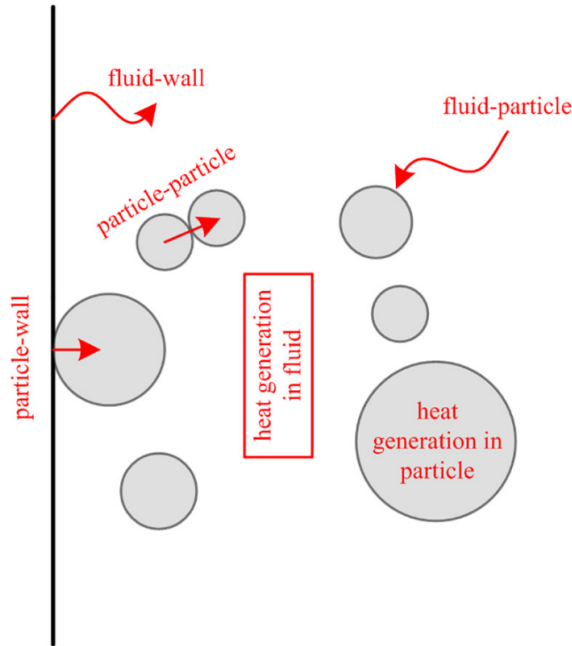


Figure 1.16: Heat exchange mechanisms in fluid-solid system. Courtesy: Golshan et al. [2020]

### 1.6.1 Conduction

Heat conduction between particles in LIGGGHTS during contact is calculated using the equations from Chaudhuri et al. [2006].

$$q_{\text{conduction},i-j} = h_{c,i-j} \Delta T_{i-j} \quad (1.35a)$$

$$h_{c,i-j} = \frac{4k_i k_j}{k_i + k_j} \sqrt{A_{\text{contact},i-j}} \quad (1.35b)$$

$$M_p C_p \frac{dT_i}{dt} = \sum q_{\text{conduction},i-j} \quad (1.35c)$$

where,  $h_c$  is the heat transfer coefficient

$k_i$  and  $k_j$  are the thermal conductivities of particle i and j respectively

$C_p$  is the specific thermal capacity of particle i

$A_{\text{contact},i-j}$  is the particle contact area.

More complex models for particle-particle conduction and particle-fluid-particle conduction have been proposed in the literature. [Zhou et al. \[2009, 2008\]](#) model is also often used to estimate the heat transfer during the collision of particles.

### 1.6.2 Convection

The rate of heat transfer between particles and surrounding fluid is governed by the convective heat transfer mechanism. For a spherical particle suspended in a liquid, the convective heat transfer is given by the equation 1.36.

$$q_{i-f} = h_{\text{conv}} \pi d_p^2 (T_i - T_f) \quad (1.36)$$

where  $T_f$  is the fluid temperature

$h_{\text{conv}}$  is the heat transfer coefficient

$d_p$  is the diameter of the particle.

Convective heat transfer coefficient can be calculated from Nusselt number ( $Nu_i$ ):

$$h_{\text{conv}} = \frac{Nu_i k_f}{d_p} \quad (1.37)$$

where  $k_f$  is the thermal conductivity of the surrounding fluid.

Various correlations exist in literature to calculate the Nusselt number. [Li and Mason \[2000\]](#) proposed the following:

$$Nu_i = \begin{cases} 2 + 0.6\varepsilon^{n1} Re_i^{0.5} Pr^{0.33} & Re < 200 \\ 2 + 0.5\varepsilon^{n1} Re_i^{0.5} Pr^{0.33} + 0.02\varepsilon^{n1} Re_i^{0.8} Pr^{0.33} & 200 \leq Re \leq 1500 \\ 2 + 0.000045\varepsilon^{n1} Re_i^{1.8} & Re > 1500 \end{cases}$$

Where  $n1$  is the model constant equal to 3.5 as chosen by [Wang et al. \[2018\]](#)

Re is Reynolds number

Pr is Prandtl number

### 1.6.3 Radiation

Radiative heat transfer is modelled using Stefan–Boltzmann law for black body radiation [[Zhou et al., 2009](#)].

$$q_{i,\text{rad}} = \sigma_{\text{sb}} \epsilon_i A_i (T_{\text{local}}^4 - T_i^4) \quad (1.38)$$

where  $\sigma_{\text{sb}}$  is Stefan-Boltzmann constant

$\epsilon$  is the emissivity

$A_i$  is the surface area

$T_i$  and  $T_{\text{local}}$  are the temperature of particle and surrounding respectively.

Coupling heat transfer to CFD-DEM is not trivial and the respective heat transfer equations are solved during their respective force calculation steps in figure 1.15. Also, material properties such as Young's modulus are known to be a function of temperature. Thus, simulations of these highly coupled multifaceted phenomena are of interest to the research community from various engineering backgrounds.

## **1.7 Summary and thesis objectives**

To summarize previous modelling starch swelling and rheology evolution needs a multi-pronged approach. Current state of the art lacks principally in modelling swelling taking into account the entire population size distribution and secondly in accurately taking into account granular effects in suspension flow. This thesis aims to address these lacks through answering the following research questions.

- How does one model starch swelling taking into account the entire population evolutions ?
- How does temperature affect the material properties at different scale, especially granule properties ?
- What are the granular effects are important to be considered in the suspensions ?

To answer these research questions we characterize starch swelling at the granule scale in chapter 2. Granule material properties are characterized using various methods in chapter 3. The learnings from chapter 2 and 3 are used in chapter 4 and 5 to perform simulations which provide insights into rheology of this starch suspension.



## Chapter 2

# Kinetic modelling of individual starch granule swelling

Arnesh Palanisamy<sup>a</sup>, François Deslandes<sup>b</sup>, Marco Ramaioli<sup>a</sup>, Paul Menut<sup>a</sup>, Artemio Plana-Fattori<sup>a</sup>, Denis Flick<sup>a</sup>

<sup>a</sup> Université Paris Saclay, INRAE, AgroParisTech, UMR SayFood, 91300, Massy, France

<sup>b</sup> Université Paris Saclay, INRAE, AgroParisTech, UMR MaIAGE, 78350, Jouy-en-Josas, France

### Abstract

A novel kinetic model is proposed for individual starch granule swelling based on swelling kinetics time series data. The data was acquired from time-lapse microscopy observations of starch granules in a dilute suspension and subsequent image analysis. Chemically modified waxy-maize starch was used. The size evolution of many granules, when subjected to various hydro-thermal treatments on a temperature-controlled stage, was determined. Observations showed that swelling is not an instantaneous process and varies from a granule to another. A model has been developed which takes into account the effect of temperature evolution and variability between the granules on their swelling. This model can contribute to a robust multi-scale simulation of industrial processes involving starch suspensions.

*Keywords:* Starch Granule; Image analysis; Swelling kinetics; Time-series data; Modelling.

This article has been published in the Journal *Food structure*

<https://doi.org/10.1016/j.foostr.2020.100150>

## Chapitre 2

# Modélisation cinétique du gonflement individuel de granule d'amidon

Arnesh Palanisamy<sup>a</sup>, François Deslandes<sup>b</sup>, Marco Ramaioli<sup>a</sup>, Paul Menut<sup>a</sup>, Artemio Plana-Fattori<sup>a</sup>, Denis Flick<sup>a</sup>

<sup>a</sup> Université Paris Saclay, INRAE, AgroParisTech, UMR SayFood, 91300, Massy, France

<sup>b</sup> Université Paris Saclay, INRAE, AgroParisTech, UMR MaIAGE, 78350, Jouy-en-Josas, France

### Résumé

Un nouveau modèle cinétique est proposé pour le gonflement individuel de granules d'amidon sur la base de données chronologiques de gonflement. Ces données ont été acquises à partir d'observations microscopiques, à intervalle régulier, de granules d'amidon dans une suspension diluée suivies d'une analyse d'image. De l'amidon de maïs cireux chimiquement modifié a été utilisé. L'évolution de la taille de nombreux granules a été déterminée lors de divers traitements hydrothermaux sur une platine à température contrôlée. Les observations ont montré que le gonflement n'est pas un processus instantané et varie d'un granule à l'autre. Un modèle a été développé qui prend en compte l'effet de l'évolution de la température et de la variabilité entre les granules sur leur gonflement. Ce modèle peut contribuer à une simulation multi-échelles robuste de processus industriels impliquant des suspensions d'amidon.

*Mots clés:* Granule d'amidon; Analyse d'image; Cinétique de gonflement; Séries chronologiques; Modélisation.

## 2.1 Introduction

Starch is the predominant food reserve in plants and provides 70-80% of the calories consumed by humans worldwide in various forms of food products [Bertolini, 2010]. In 2000, the world starch production was estimated to be around 48.5 million tons, including native and modified starches. Hence, starch has been a perennial subject of research through decades. Starch granules majorly consists of two polymers: amylose and amylopectin. Both amylose and amylopectin have  $\alpha$ -glucose as the monomer, however, their difference arises from their linkages. Amylose has  $\alpha(1-4)$  and is linear whereas amylopectin has  $\alpha(1-6)$  and is highly branched. The ratio of amylose and amylopectin in the starch granule depends on its source and botanical origin. This in turn has drastic consequences on the physical properties such as rheology [Banks et al., 1974, Hoover, 2001, Srichuwong et al., 2005, Visser et al., 1997]. Molecular properties such as molecular weight distribution and degree of amylopectin branching are also known to impact the functional attributes at the macro-scale [Blennow et al., 2001, Fredriksson et al., 1998, Singh et al., 2007].

Gelatinization is the process in which starch granules undergo an irreversible transformation when subjected to thermomechanical treatment in the presence of water. During this process starch granules swell by imbibing water and increase the overall viscosity of the suspension. It is also sometimes referred to as starch pasting in literature. Starch granules are semi-crystalline with concentric rings of crystalline and amorphous phases [Ratnayake and Jackson, 2008]. On the microscopic scale, the process corresponds to the melting of crystallites, loss of birefringence, leaching of amylose into the continuous phase and sometimes rupture of the granular structure [Atwell, 1988, Biliarderis, 1992]. During gelatinization, melting of crystalline region in the granule occurs and depending on the origin of the starch, the range for this transition is between 60 and 70 °C [Slade and Levine, 1995]. The evolution of viscosity during gelatinization is also influenced by the process parameters such as concentration, shear rate, thermal history, pH and presence of other ingredients [Thomas and Atwell, 1999, Malumba et al., 2018]. For high amylopectin cereal starches such as waxy maize starch, the granules tend to hydrate with ease, swell rapidly and rupture to a great extent which results in loss of paste viscosity. The rupture of the granules can be avoided by chemically modifying the starch. This involves cross-linking via chemical bonds that act as bridges between the two macromolecules. The introduction of functional groups into the starch molecules such as acetylation results in lower amylose leaching properties of starch. The resulting modified starches have markedly altered physicochemical properties [Ashogbon and Akintayo, 2014]. Waxy maize starch is used in a wide variety of applications in the food industry owing to its stability [Tattiyakul and Rao, 2000].

The sensory perception of viscosity is an important mouthfeel sensation [Szczeniak, 1963, Wood, 1968]. Starch is used as a viscosity enhancer in many food formulations. Hence, it is critical to accurately predict viscosity changes both from a product development standpoint and an engineering design standpoint. During the thermal processing of liquid food product containing starch, viscosity changes must be known to accurately estimate process variables as the process is highly coupled in terms of heat transfer, momentum transfer and transformation [Plana-Fattori et al., 2016]. This warranted decades of research into the sole aspect of viscosity predictions and significant literature exist regarding the chief aspects which dictate the same. They are (a) the suspending medium's viscosity  $\eta_0$ , (b)

the granule's volume fraction  $\phi$ , (c) the granule's deformability, and (d) the imposed shear rate [Chen et al., 2007]. Nayouf et al. [2003] indicated that volume fraction of granules can be estimated if the mean granule size ( $D_t$ ) can be accurately determined.

Increasingly researchers started defining progress of gelatinization in terms of the increase in diameter of granules [Anuntagool et al., 2017, Okechukwu and Rao, 1996, Bagley and Christianson, 1982, Bakshi and Singh, 1980a, Suzuki et al., 1976, Doublier et al., 1987, Kokini et al., 1992]. Alternate methods used to define gelatinization are based on DSC, rheology or birefringence [Cui et al., 2014, Choi and Kerr, 2004, Dolan and Steffe, 1990, Biliaderis and Prokopowich, 1994, Chang and Liu, 1991, l'anson et al., 1990, Kohyama and Nishinari, 1991, Miles et al., 1985, Slade and Levine, 1991]. However these are all equivalent indications of the same process. Granule swelling occurs in two phases, first is the hydration phase where there is a slight reversible increase in the diameter of the granules typically occurring in the temperature range 30–60 °C and a second irreversible phase where there is a large increase in diameter occurring at temperatures above 60 °C [Okechukwu and Rao, 1996]. Some authors reported that mean size and size distribution of swollen granules were correlated with suspension consistency and flow behavior index [Okechukwu and Rao, 1996, Steeneken, 1989, Evans and Lips, 1990]. Thus, there have been multiple attempts at kinetic modelling this phenomena to predict the particle size evolution.

Kubota et al. [1979] attempted to model this phenomena with Arrhenius law and proposed a first order kinetic equation with respect to non-dimensionalised consistency index. Okechukwu and Rao [1995] introduced a similar rate equation with another dimensionless variable called extent of gelatinization based on mean particle diameter of the population. Lagarrigue et al. [2008] used the same formulation but argued that the reaction is second order. Krüger et al. [2003] proposed a kinetic model which suggest the rate of increase in diameter is proportional to the inverse of the mean diameter of the population diameter with Arrhenius behavior and reaching a plateau at maximum diameter. Some authors also suggested a set of reactions to describe gelatinization [Kokini et al., 1992]. Malumba et al. [2013] compared a wide range of rate expressions (Nth order kinetic, Diffusional, Phase boundary and Avrami-Erofeev) to predict the isothermal swelling kinetics at different temperatures and showed that the predictability was best for Nth order reaction models especially second order and third order. They concluded that starch granule gelatinization is not a simple water diffusion or a boundary phenomenon. The heat transferred inside the granules induces phenomena such as melting of the crystallite, interaction between carbohydrate polymers. This includes inter-chain and intra-chain polymer folding and hydrogen bonding proceeding with semi-cooperative swelling of granules. They also argued that activation energy reported in literature must be called apparent activation energy as the same, changed based on the form and order of the rate equation assumed. Plana-Fattori et al. [2016] have used a modified form of rate constant with a cutoff minimum temperature instead of the traditional Arrhenius form, which they substantiated with experiments.

All the above-mentioned works have always been attempts to model the swelling kinetics of the population mean but not at the individual granule scale. Desam et al. [2018a] tried to model the swelling of a single granule based on diffusion kinetics and Flory-Huggins theory of polymer mixing, but the model assumes all granules to have similar cross-links, tortuosity, and elastic restoring force. In this work, we propose a novel kinetic modeling at the individual granule scale rather than the population mean. Time-series data obtained from image processing of

hot stage coupled microscope time-lapse images was used for building and fitting the model. This model captures the inter granule variability of starch swelling in water. This variability has not been quantified and addressed adequately in the previous modeling works. We try to capture these nuances in this work albeit it empirically and thus the parameters obtained are valid for chemically stabilized cross-linked waxy maize starch (acetylated distarch adipate, C\*Tex 06205), provided by Cargill (Baupte, France). The method developed here enables modeling at the granular scale, allowing one to capture the dynamics better for multi-scale modeling translating into wide-reaching consequences in plant equipment design, optimization, differentiated product development, simulation, robust process development and robust model based process control systems.

## 2.2 Materials and methods

### 2.2.1 Experimental method

Chemically stabilized cross-linked waxy maize starch (C\*Tex 06205), provided by Cargill (Baupte, France), cross-linked via adipates, was used in  $0.5g.kg^{-1}$  suspensions of starch in water. This starch is composed of 99 % of amylopectin and less than 1% of amylose. This type of starch does not lead to disruption and no release of amylose content is expected. In terms of functionality, it has notably a good resistance to shear forces, a good storage stability and a high paste clarity. The suspension was preheated to 50°C under gentle stirring with a magnetic pellet. Using a dropper, sampling was performed and sample was transferred to the microscopic glass slides with adhesive spacers of 250  $\mu m$ . Samples were observed under 50X magnification using an Olympus BX-51 microscope (Olympus Optical Co. Ltd., Tokyo, Japan). Images were acquired using a Basler A102fc digital camera (Basler AG, Ahrensburg, Germany). Each observation is an 8 bit image of  $1388 \times 1038$  pixels which represents a  $361 \times 270 \mu m^2$  area. Microscope glass slides with samples were placed on a Linkam LTS120 stage (Linkam Scientific Instruments, Surrey, UK). The temperature was controlled with the Linksys32 software. The samples were subjected to different temperature profiles, starting with a holding at 50 °C for 1 min (figure 2.1a). Some samples were observed under the microscope at different constant temperatures from 55 °C to 62 °C for 1 hour; no image processing was carried out for these experiments as the objective of the same was only to observe if the granules began to swell and to estimate the latency time before swelling.

### 2.2.2 Image data analysis and notation

The Java plugin for ImageJ software developed by [Deslandes et al. \[2019\]](#) was used to process the images. Ferret diameter is a length of an object measured along a specified direction. Thus, along different direction we have different Ferret lengths. We note the minimum and maximum Ferret diameter of a granule ( $\mu m$ ),  $m$  and  $M$  respectively. The diameter of the granule is taken as the geometric mean of the Ferret lengths:

$$D = \sqrt{Mm}. \quad (2.1)$$

Image analysis and subsequent sigmoid curve fitting for the resulting time series data of diameter as a function

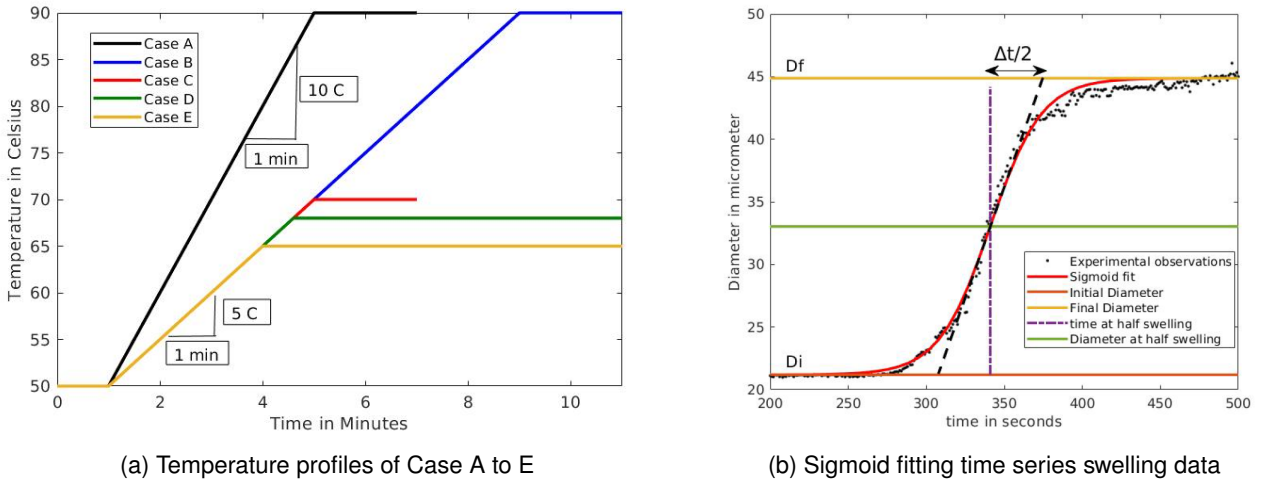


Figure 2.1: Time-Temperature profiles imposed on starch suspensions and typical diameter evolution of a starch granule during gelatinization.

of time was done following the procedure outlined in Deslandes et al. [2019]. The parameters  $D_i$ ,  $D_f$ ,  $\delta$  and  $t_{1/2}$  denote the initial diameter ( $\mu\text{m}$ ), the final diameter ( $\mu\text{m}$ ), the swelling rate ( $\text{s}^{-1}$ ) and the half-swelling time (s) of the granule respectively. These morphological and kinetics parameters are estimated by performing least-squares fitting on the size evolution data obtained from the image processing onto the sigmoid curve given by equation 2.2 [Deslandes et al., 2019]. A typical diameter evolution of a granule with time along the least square fitting of the sigmoid curve is depicted in figure 2.1b.

$$\tilde{D}(t) = \frac{D_f - D_i}{1 + e^{-\delta(t-t_{1/2})}} + D_i \quad (2.2)$$

The beginning of the 1 minute hold time at 50 °C is taken as the origin of time and different temperature profiles as depicted in the figure 2.1a are imposed on the sample. The individual granule swelling duration ( $\Delta t$ ) is estimated by extrapolation of the tangent at the half-swelling time. It can be calculated from the parameter  $\delta$  using the following equation:

$$\Delta t = \frac{4}{\delta}. \quad (2.3)$$

We then define  $t_{\text{onset}}$ , the individual swelling onset time by

$$t_{\text{onset}} = t_{1/2} - \frac{\Delta t}{2}. \quad (2.4)$$

## 2.3 Experimental results and observation

### 2.3.1 Observation at constant temperature between 55 °C and 62 °C

Observing the samples under the microscope at different constant temperatures starting from 55 °C to 62 °C for 1 hour was the objective to determine the minimum temperature at which swelling starts. It was observed, as shown in images of figure 2.2, the gradual increase in fraction of granules swollen as temperature increases from 57 °C to 62 °C. We can safely say that it required at least around 60 °C to observe swelling in majority of the granules, this is consistent with the literature reported values [Slade and Levine, 1995]. However, this may not be entirely true as we saw some granules swell at 58 °C and some granules not swollen at 62 °C even after a duration of 1 hour. Nevertheless, in industrial processes, the maximal temperature is always much greater than 70 °C and residence time in heat exchangers is of some minutes only. In light of the practicality and the relevance to the industrial process, we make this assumption that the minimum swelling temperature is of 60 °C for all the granules.

For the experiments carried for 1 hour (1 image per 5 seconds) at 62 °C, the latency time in the onset of swelling was manually noted from the diameter vs time data obtained after post processing using the plugin developed by Deslandes et al. [2019]. Figure 2.3 shows the experimental cumulative distribution (47 granules) and an exponential curve fit for the same. We use this information in the section 2.4.1 to justify the choice of mathematical formulation.

### 2.3.2 Diameter increase during temperature ramp

The results of the image processing and data analysis during different temperature ramps are summarized in the table 2.1. Note that for the case E with maximum temperature 65°C only the completely swollen granules were used to compute the sigmoid curve parameters. All the reported cases had a lapse rate of 1 image per second. The onset times reported here are from the beginning of the 1 min hold time at 50 °C.

Case	$T_{max} (°C)$	ramp rate ( $°C/min$ )	hold time (min)	Number of granules	$t_{onset}$ (s)		$\Delta t$ (s)		Df/Di	
					mean	std	mean	std	mean	std
A	90	10	2	163	180	18	29	21	2.30	0.32
B	90	5	2	142	276	34	65	46	2.36	0.33
C	70	5	2	48	274	44	51	34	2.38	0.43
D	68	5	15	41	250	37	98	92	2.35	0.25
E	65	5	15	42	293	122	300	169	2.07	0.49

Table 2.1: Summary of Experimental conditions and swelling data with sigmoid fits

Equation 2.5 defines the degree of swelling parameter which is used to track the swelling of an individual granule.

$$S(t) = \frac{D(t) - D_i}{D_f - D_i} \quad (2.5)$$

Thus, S(t) ranges from 0 to 1, where 0 corresponds to no swelling and 1 corresponds to complete swelling. To obtain the dimensionless variable S as function of time for each granule,  $D_i$  and  $D_f$  obtained from the sigmoid fitting are used. Thus one can obtain cloud plots of the non-dimensional diameter evolution for each of the experimental

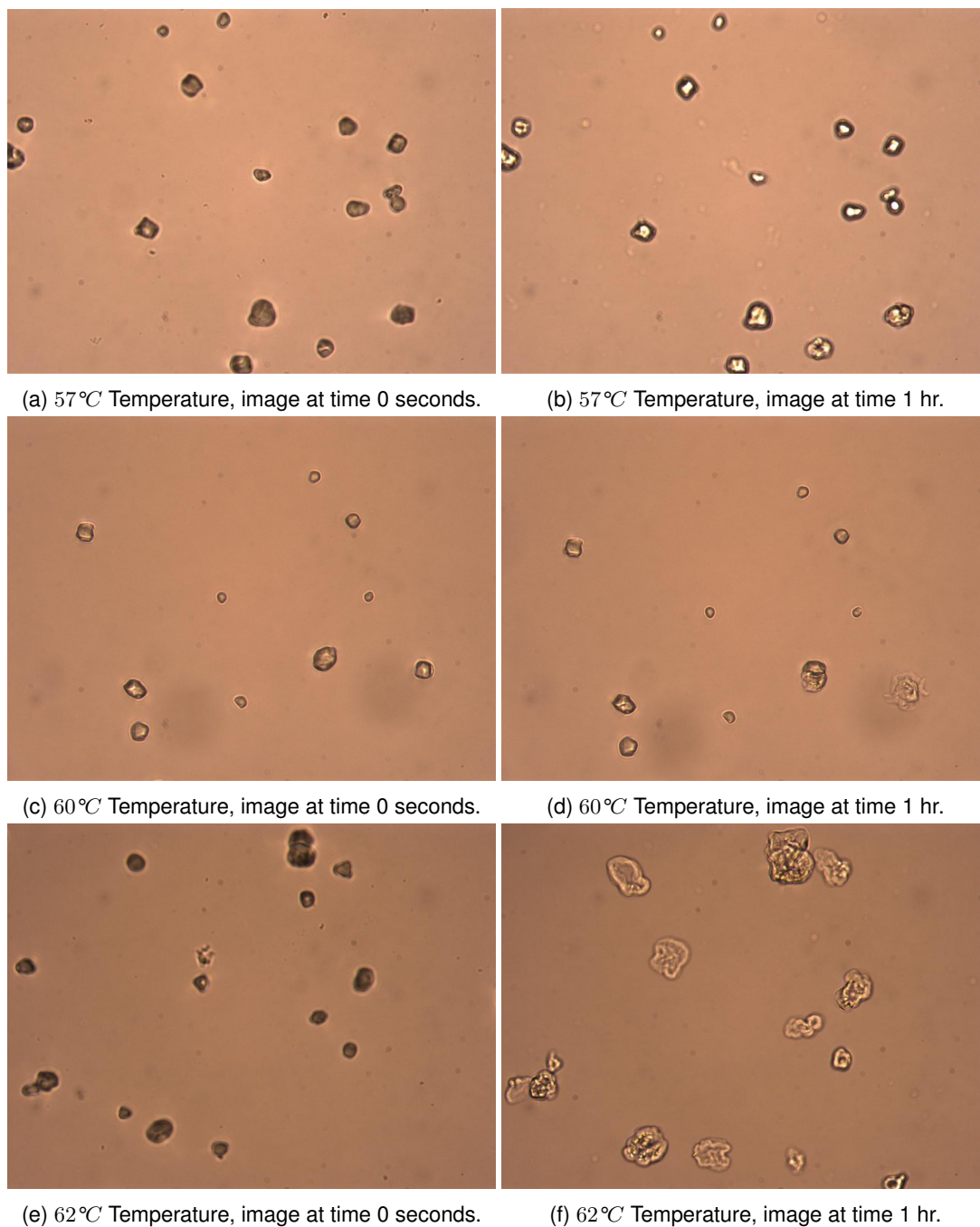


Figure 2.2: Starch granules at the beginning and after 1 hour at different temperatures

cases shown in figure 2.1a. The noise observed in the plots of dimensionless variable  $S$  is the direct result of noise in the diameter of granule estimated through image processing [Deslandes et al., 2019].

From the figure 2.4 and table 2.1 it can be concluded that for a given temperature evolution all granules do not begin to swell at the same time. In fact, there is a latency time or delay in onset time involved in the process. The value of this latency time decreases with increase in temperature and varies from granule to granule as seen from the cloud plots in figure 2.4. Latency time does not depend on the diameter of the granules [Deslandes et al., 2019] and it approximately follows an exponential distribution at a constant temperature as seen in figure 2.3. It is also

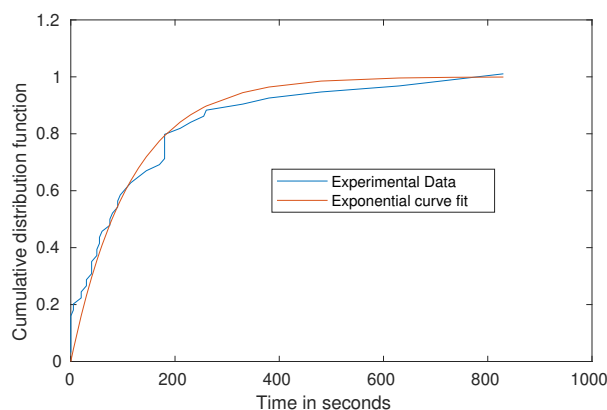


Figure 2.3: Experimental delay times for swelling onset at 62 °C

observed from figure 2.4 that granules with high latency time swell less rapidly than the ones with low latency times.

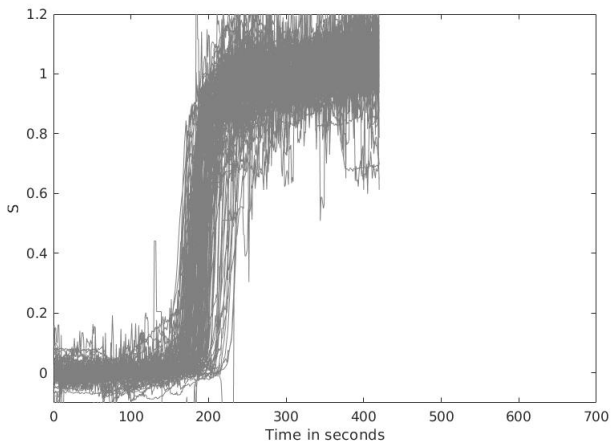
Granule diameter reaches a constant value given sufficient time and temperature. Individual granule characteristics and temperature profile determine the magnitude of time required to achieve this constant value. The ratio of the final diameter to the initial diameter or simply known as the ratio of swelling ( $D_f/D_i$ ) varies from granule to granule. This is also reported by Deslandes et al. [2019]. The mean ratio of swelling practically is almost independent of the temperature history and initial diameter. This is in accordance with mechanistic models (e.g. [Desam et al., 2020, Briffaz et al., 2014, Watanabe et al., 2001, 2007]) in which the final state corresponds to an equilibrium in which the water demand reaches zero. We also did not observe any significant correlation between latency times and swelling ratio ( $D_f/D_i$ ) based on our data. From table 1 for temperatures above 68 °C we have nearly constant ratio of swelling around 2.35 but for lower temperature of 65 °C, the ratio decreases suggesting partial swelling. However, as mentioned in industrial process the temperature used is higher to ensure complete swelling state i.e. swelling ratio of 2.35 in this case. As reported by Deslandes et al. [2019] the ratio of swelling approximately follows a truncated normal distribution.

These observations were used to develop a novel model that captures most of the essential features, which is discussed in detail in the next section.

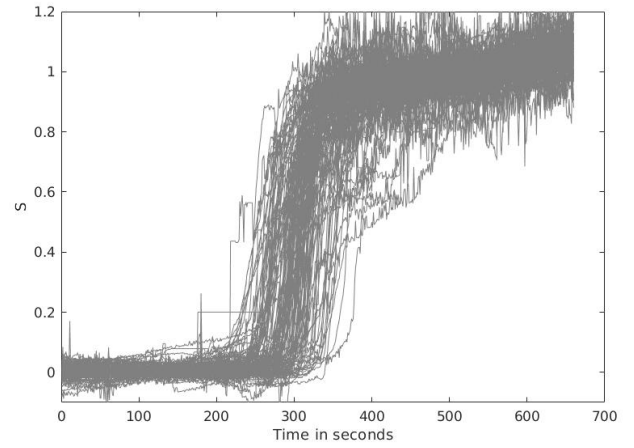
## 2.4 Model formulation and results

### 2.4.1 Kinetic model development

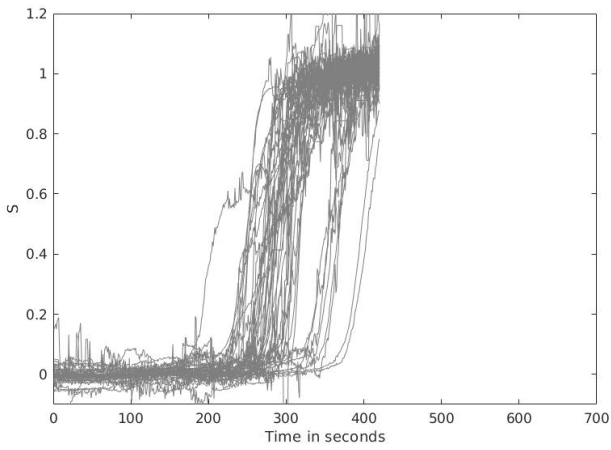
As discussed in the previous section we observed that most granules do not swell at 60 °C even after 1 hour, so we set the minimum temperature of swelling at  $T_{\min} = 60$  °C (i.e. below 60 °C there is no swelling of granules). Based on the microscopic images we observed that each granule has a variable time delay in the onset of swelling which decreases with increase in temperature. To mathematical formulate the same, let at any instant the additional fraction (denoted by  $dF$ ) of granules beginning to swell in next time unit be proportional to the fraction of granules that did not begin to swell yet (denoted by  $1 - F$ ). In equation form it can be expressed as



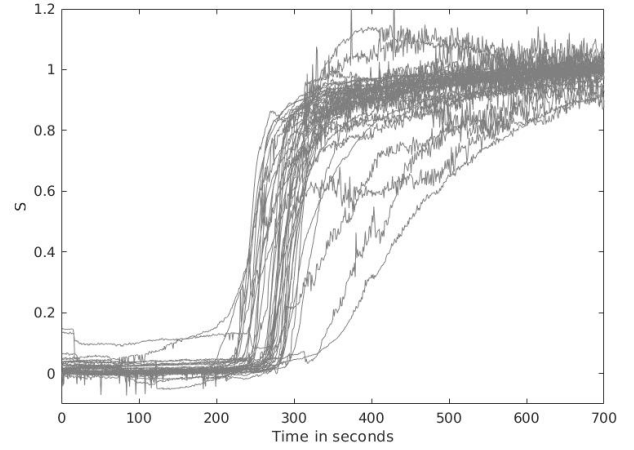
(a) Case A - Max temperature = 90 °C; ramp rate = 10 °C.



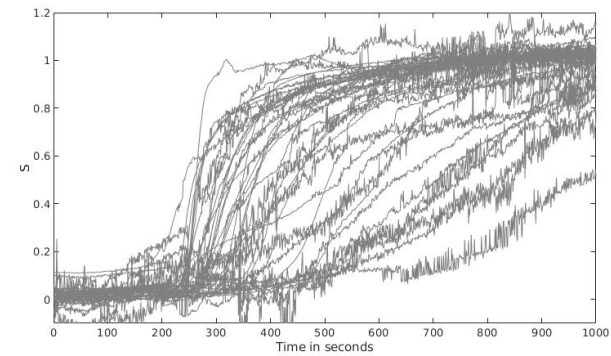
(b) Case B - Max temperature = 90 °C; ramp rate = 5 °C.



(c) Case C - Max temperature = 70 °C; ramp rate = 5 °C.



(d) Case D - Max temperature = 68 °C; ramp rate = 5 °C.



(e) Case E - Max temperature = 65 °C; ramp rate = 5 °C.

Figure 2.4: Non dimensional diameter evolution

$$dF = \frac{(1 - F)}{\tau} dt \tag{2.6}$$

$$\ln(1 - F) = - \int_0^{t_{\text{onset}}} \frac{dt}{\tau} \quad (2.7)$$

Integrating the above requires the knowledge about the characteristic latency time  $\tau$  which depends on temperature  $T$ . When temperature is constant

$$F = 1 - \exp\left(\frac{-t_{\text{onset}}}{\tau}\right). \quad (2.8)$$

Hence in this mathematical formulation we have cumulative density function vs latency time following the exponential function as was observed in figure 2.3.

We propose that the characteristic latency time in function of temperature follows:

$$\tau = \max\left(0, \left(\frac{T_{\text{ref}} - T_{\text{min}}}{T - T_{\text{min}}}\right)\right) \tau_{\text{ref}} \quad (2.9)$$

where  $T_{\text{ref}}$  is arbitrary fixed at  $T_{\text{ref}} = 62^\circ\text{C}$  and  $T_{\text{min}} = 60^\circ\text{C}$  as indicated previously.

Since there is variability of swelling onset between granules, we introduce a parameter called "difficulty of swelling" parameter  $\alpha \in [0, 1]$ . For a granule,  $\alpha$  is selected at random from uniform distribution. Thus during the ramp step of the heat treatment for a granule whose difficulty of swelling is  $\alpha$ ,  $t_{\text{onset}}$  is given by equation 2.10.

$$\ln(1 - \alpha) = - \int_0^{t_{\text{onset}}} \frac{dt}{\tau} = - \int_0^{t_{\text{onset}}} \frac{1}{\tau_{\text{ref}}} \max\left(0, \left(\frac{T - T_{\text{min}}}{T_{\text{ref}} - T_{\text{min}}}\right)\right) dt \quad (2.10)$$

During the temperature ramp  $T = T_{\text{min}} + \beta \times t$ , where  $\beta$  is the ramp rate ( $^\circ\text{C s}^{-1}$ ). Solving equation 2.10 results in

$$t_{\text{onset}} - t_{\text{min}} = \left(\frac{-2 \ln(1 - \alpha)(T_{\text{ref}} - T_{\text{min}})\tau_{\text{ref}}}{\beta}\right)^{1/2} \quad (2.11)$$

where  $t_{\text{min}}$  is the time at which  $T = T_{\text{min}} = 60^\circ\text{C}$ .

Once the granule began to swell ( $t > t_{\text{onset}}$ ), its diameter increases. A first-order reaction rate is assumed inspired from [Kubota et al. \[1979\]](#), [Lund and Lorenz \[1984\]](#) and [Okechukwu and Rao \[1995\]](#).

$$\frac{dS}{dt} = K(1 - S) \quad (2.12)$$

It is assumed the reaction does not proceed below the cut off temperature  $T_{\text{min}}$  similar to the previous work by [Plana-Fattori et al. \[2016\]](#).

Kinetics for swelling also did speed up as temperature increased. Hence we propose the following equation 2.13:

$$K = K_{\text{ref}}(1 - \alpha)^{0.5} \left(\frac{T - T_{\text{min}}}{T_{\text{ref}} - T_{\text{min}}}\right)^2 \quad (2.13)$$

where  $K_{\text{ref}}$  is the rate constant at  $T_{\text{ref}}$  for a granule which has no difficulty to swell ( $\alpha = 0$ ).

Thus now one can solve for  $S$  of a granule given the temperature profile. Moreover from [Deslandes et al. \[2019\]](#) we know that  $D_0$  and  $D_{\text{final}}/D_0$  follow normal distribution.

## 2.4.2 Calibration of model parameters and model predictions

Identification of swelling parameters  $\tau_{ref}$  and  $K_{ref}$  was carried out using the  $S_{50}$  of the data obtained from Case A described in table 1 and figure 2.4. Note that for a median granule by definition the value of  $\alpha$  is 0.5. Non-linear fitting of predicted by the model  $S_{50}$  with the experimental  $S_{50}$  using “fitnlm” function of MATLAB [2018] for the Case A resulted in values  $\tau_{ref} = 190$  s and  $K_0 = 0.0023$  s<sup>-1</sup>. This means the median latency time at the reference temperature of 62 °C is 132 seconds i.e. nearly 2 minutes. In comparison, based on figure 2.3 the median latency time at a reference temperature of 62 °C is 80 seconds.

Thus now we have a calibrated model. Therefore  $S_{10}$ ,  $S_{50}$  and  $S_{90}$  for all the cases can be predicted and compared with the experimental results. Note that the values of alpha for  $S_{10}$  and  $S_{90}$  are 0.1 and 0.9 respectively as previously explained. In the figure 2.5 the predictions of  $S_{10}$ ,  $S_{50}$  and  $S_{90}$  are shown with respect to the experimental data.

It should be noted that due to the noise in the measurement and the value of  $D_i$  derived from fitting the sigmoid curve we have S not beginning exactly at 0 for all the granules at the initial time points. We see the increase in the dispersion between  $S_{90}$  and  $S_{10}$  progressively from cases A to E. These observations are in-line with the model assumptions that rate constant increase with temperature and latency time decreases with temperature. From the plots in figure 2.5, we observe that model predictions overall are close approximations of the experimental data. The discrepancy for  $S_{90}$  in case of D and E could be due to the limited number of observed granules in this case.

## 2.4.3 Monte Carlo simulation and results

Now that sufficient confidence has been established in the kinetic model, we can perform Monte Carlo simulations and predict the population  $D_{10}$ ,  $D_{50}$  and  $D_{90}$  evolution. The following parameters listed here were used for the simulation

$$\begin{aligned} T_{ref} &= 62^\circ\text{C}, T_{min} = 60^\circ\text{C}, \\ \tau_{ref} &= 190 \text{ s}, K_{ref} = 0.0023 \text{ s}^{-1}, \text{ number of granules } I = 1000, \\ D_i &\subset \mathcal{N}(14.77 \mu\text{m}, 4.44 \mu\text{m}), D_f/D_i \subset \mathcal{N}(2.34, 0.33), \end{aligned}$$

The distributions of  $D_i$  and  $D_f/D_i$  were calculated from the pool experimental data of cases A to D. Case E was not considered as we see complete swelling did not always occur in this case. For granule initial diameter the normal distribution was used with truncated tails with minimum diameter as  $0.25 \times$  mean diameter and maximum value  $3 \times$  mean diameter. The ramp rates and hold times were feed into the simulation as per the individual cases as tabulated in table 1. A MATLAB script was written to execute the model, 4<sup>th</sup> order Range Kutta method was used for integration. It can be observed in figure 2.6 that the model predictions are close to the experimental data and the model sufficiently captures the nuances of the process. The slope at the midpoint of granule swelling in case A is twice compared to the same in case B. The rate of swelling is slower progressively with  $D_{50}$  and  $D_{10}$  compared to  $D_{90}$  and this is more pronounced in the lower temperature cases C and D. The deviation in case D can be attributed to the lower sample size and higher dispersion at lower temperatures. The latency time is lower for the higher ramp rate case A compared to the rest of the cases. Finally, both in the model and the experimental data the dispersion in size is higher after swelling compared to initial population.

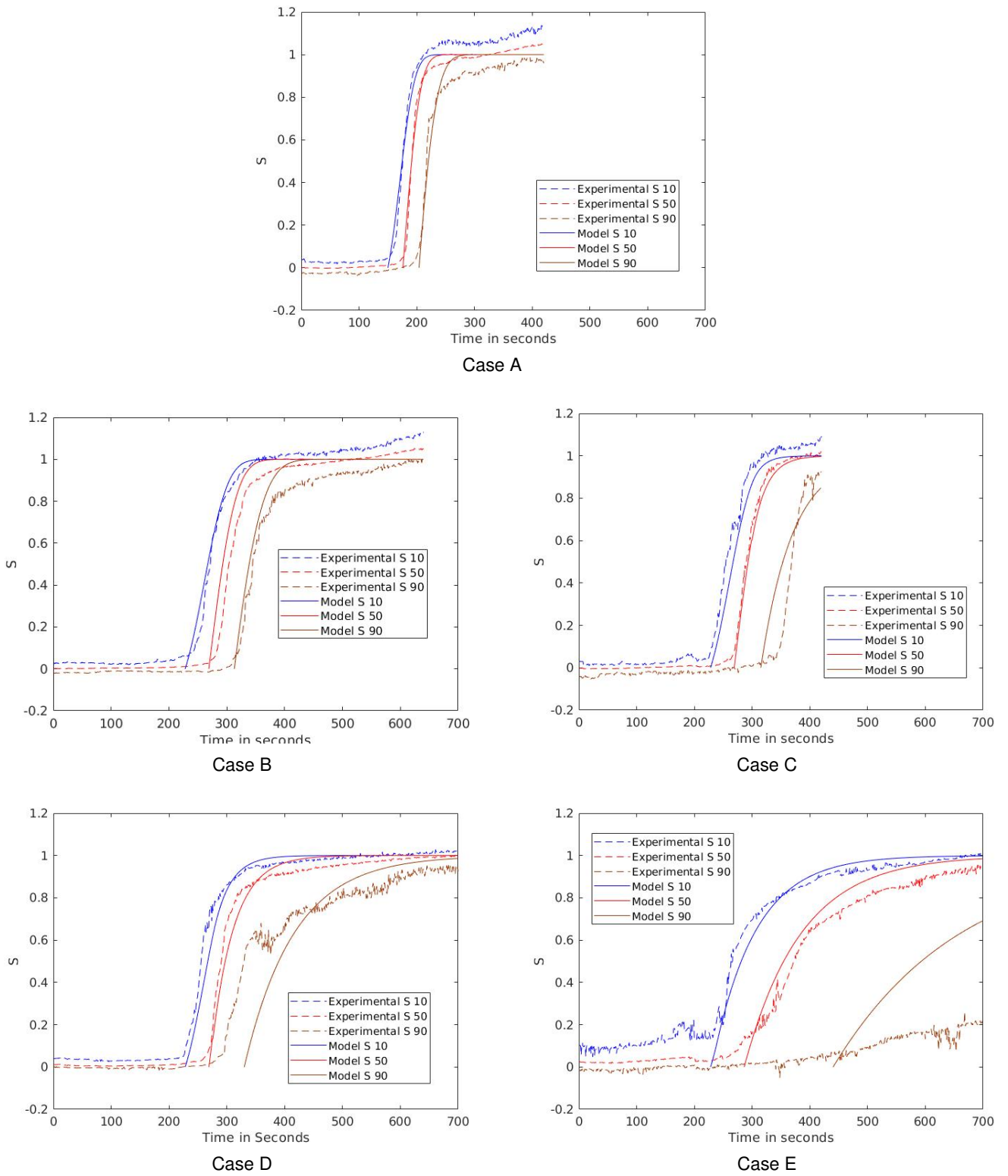


Figure 2.5: Model prediction of non dimensional diameter evolution

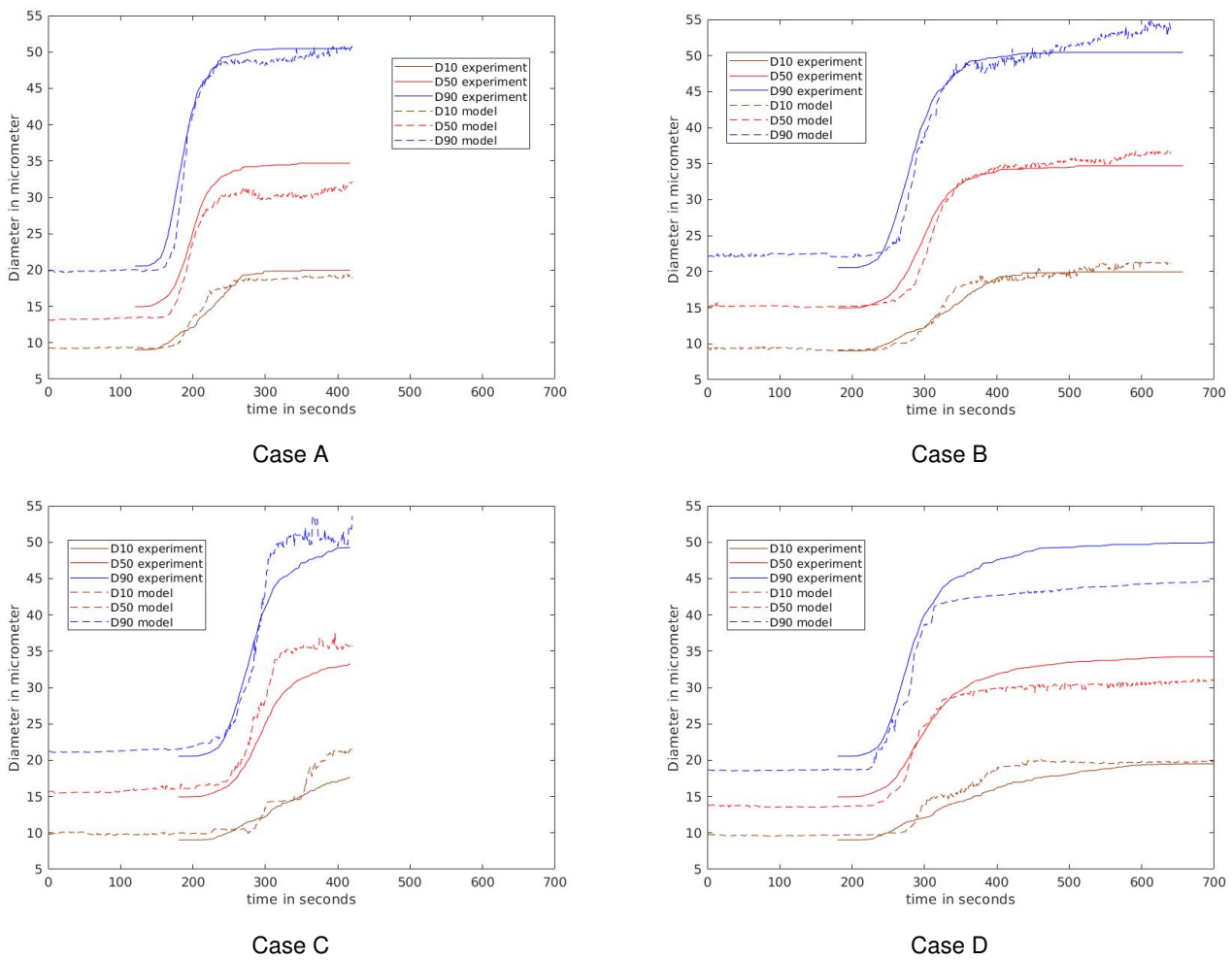


Figure 2.6: Model prediction of diameter evolution

Figure 2.7 presents the cumulative particle size distribution evolution at different time points as the starch granule swelling proceeds. The dashed curves and continuous are the experimentally observed and model predicted particle size distribution respectively. For both the simulation and experiment the curve at 68 °C in case A is much closer to the initial one compared to the same temperature in case B. The difference can be attributed to the difference in latency times (median of 134 s vs 197 s). This means that not only temperature is important but also the temperature history together dictate the swelling of the starch granules. The relative good agreement between predicted and measured size distributions at intermediate starch swelling for different temperature evolution validate the applicability of the model.

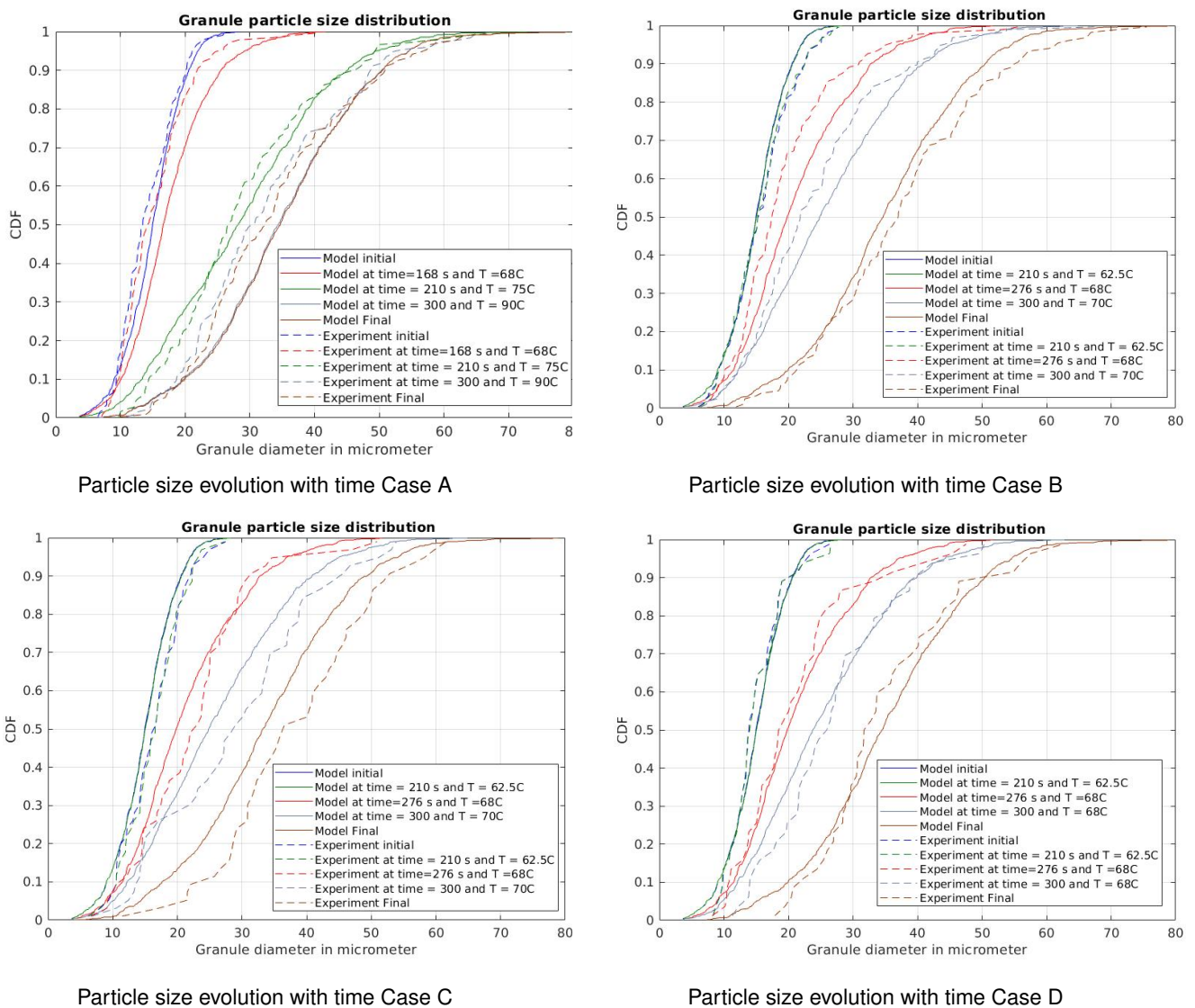
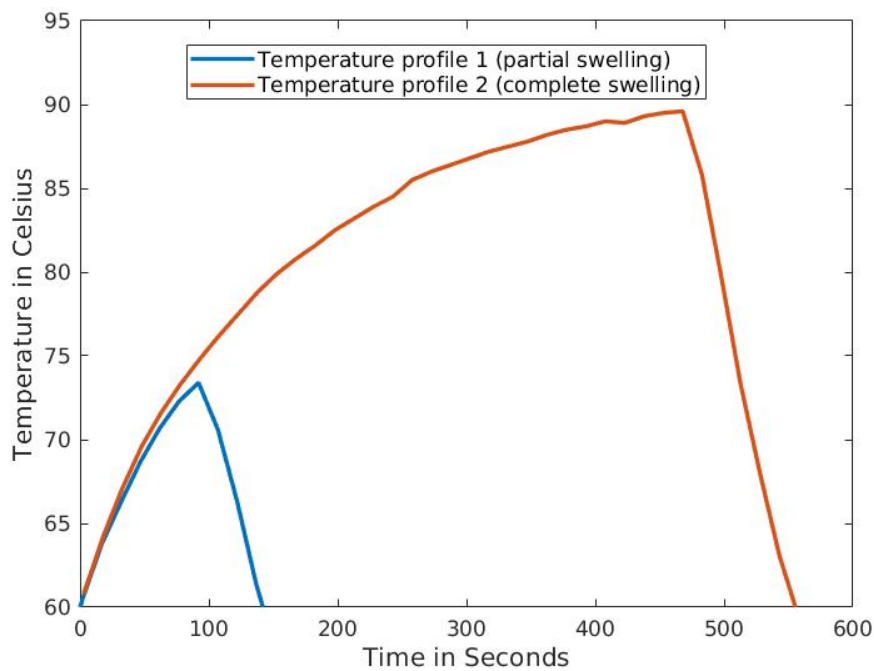


Figure 2.7: Cumulative particle size distribution of different cases at different times and temperatures

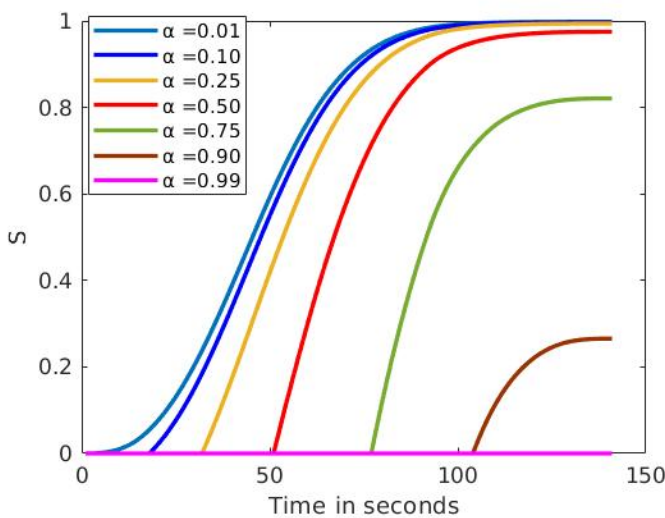
### 2.4.4 Model application and validation

In this section we make predictions using the developed model for the population swelling of the same starch using a completely different setup. [Plana-Fattori et al. \[2016\]](#) observed the volume size distributions of starch suspensions after different time-temperature histories using Malvern Mastersizer. The thermal treatment consisted of a series of three water baths, First the sample was immersed in a 50° C water bath until equilibrium was reached, then it was immersed into a water bath maintained at 92° C. After specified “heating time” the sample was shifted to the third water bath maintained at 4° C. All this while the bulk temperature of the sample was measured and noted at regular time intervals of 15 seconds.

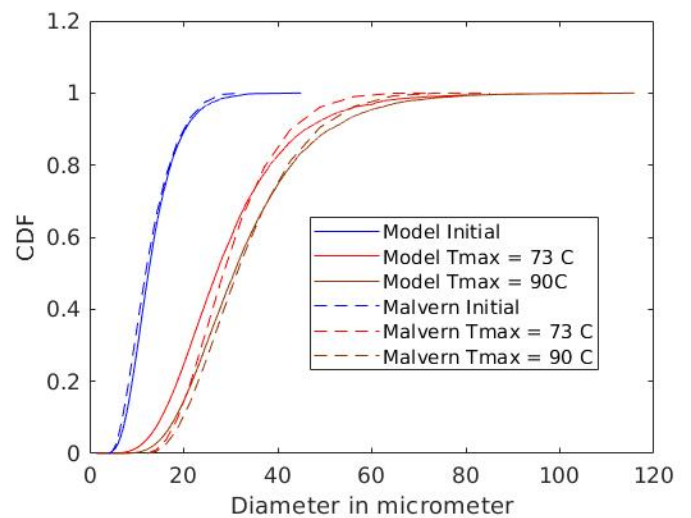
For the sake of simplicity we only consider two cases with maximum temperature of 73° C and 92° C respectively (figure 2.8a). For simulation we only need the bulk temperature profiles above the cut off temperature of 60° C. One should note that swelling can go on even during the cooling step as long as the temperature is above 60° C.



(a) Bulk Temperature profiles recorded for heating times of 2 minutes and 8 minutes (Courtesy of Plana-Fattori et al. [2016])



(b) Non-dimensional diameter evolution temperature profile 1



(c) Cumulative volume distribution

Figure 2.8: Validation of kinetic swelling model for non-linear temperature profiles

Monte Carlo simulations using the same parameters mentioned in section 2.4.3 were performed. The difficulty of swelling parameter ( $\alpha$ ) and the maximum swelling ratio ( $D_f/D_i$ ) are first randomly chosen for each of 100,000 granules. Then the onset times are calculated according to equation 2.10 using piece-wise linear interpolation of the experimental temperature evolution. The swelling degree ( $S$ ) evolution are then calculated. The results of such simulations are shown in figure 2.8b for the first case. Note that because of the decreasing temperature after about 90 s in the first case ( $T_{max}=73\text{ }^\circ\text{C}$ ) the rate at which the granules swell decreases in figure 2.8b. This phenomenon is more evident for  $\alpha \geq 0.5$ . Thus some of the granules are in a frozen state of partial swelling in line with the

interpretations of [Plana-Fattori et al. \[2016\]](#) in this case.

From the diameters of the 1000 granules at the end of the heat treatment for both the cases, the volume size distributions were computed to be compared with results from Malvern Mastersizer assuming spherical particles. Initial diameters from the Malvern Mastersizer were used to perform the simulation. The experimental values and model predictions are overlaid in figure 2.8c. Overall a fairly good prediction is obtained by the model. However, there is discrepancy at lower particle sizes for  $T_{\max} = 73$  °C. Considering the differences in the measuring techniques (microscopy for model fitting, light diffraction for Malvern) and various experimental and model assumptions (spherical particles, temperature uniform across the sample,  $T_{\min} = 60$  °C) the performance of the model on a whole is good, notably to predict the size distribution of partially gelatinized starch which is of practical interest as various functional properties could be obtained with partial gelatinization and  $\beta$ -amylolysis [[Hickman et al., 2008](#)].

### 2.4.5 Possible explanation of variability and model limitations

The presented empirical model is based on individual granules observation and does not explain why different granules submitted to the same temperature evolution begin to swell at different instants ( $t_{\text{onset}}$ ) and with different swelling duration ( $\Delta t$ ). Literature suggests that various mechanisms are involved during starch swelling : melting of crystallites, moisture sorption, water diffusion, fusion of amylose/lipid complexes, leaching of amylose into the continuous phase, rupture of the granular structure [[Briffaz et al., 2013, 2014](#), [Chapwanya and Misra, 2015](#), [Ozturk and Takhar, 2018](#)]. The three last phenomena do not occur in our case as waxy cross-linked maize starch was used for this work. In addition since we consider a very dilute system, there is no water availability limitation as discussed by [Fukuoka et al. \[2002\]](#).

[Debet and Gidley \[2006\]](#) identified three classes of starch granule swelling: (i) rapid swelling, (ii) slow swelling, (iii) limited swelling. For waxy maize starch there is no interaction between amylose, surface proteins and lipids and therefore rapid one-step swelling is observed. For other types of starch, the maximal swelling ratio can be function of the highest temperature reached. Indeed after a first swelling step (typically between 60 and 70 °C), a second step (typically between 80 and 100 °C) is observed, related to amylose/lipid/protein interaction for other types of starches [[Briffaz et al., 2013](#)]. In our case,  $D_f/D_i$  was found to be independent on the maximal temperature (for  $T_{\max} > 65$  °C).

Melting of crystallites and moisture sorption can be affected by different parameters which can vary between granules such as crystallinity, branching of amylopectin, degree of cross linking, etc. [[Debet and Gidley, 2006](#)]. This can explain variability in  $t_{\text{onset}}$  and  $\Delta t$  which was taken into account by a random parameter  $\alpha$  (difficulty of swelling). One could expect that the 'difficulty of swelling' also influences the swelling ratio  $D_f/D_i$ , but no correlation was observed in our case between  $D_f/D_i$  and  $t_{\text{onset}}$  (p value  $\sim 0.95 \gg 0.05$ ).

Diffusion can be assumed as Fickian (based on water concentration gradient), non-Fickian (based on water demand) [[Watanabe et al., 2001](#)] or following Flory-Huggins theory [[Desam et al., 2018a, 2020](#)]. Tortuosity can be considered as function of aqueous volume fraction and can vary between granules depending on the amorphous/crystalline shell structure. If water availability is limited due to diffusion, the smallest granules should

swell more rapidly. However, this was not observed in our case, there is no correlation between  $D_i$  and  $t_{\text{onset}}$ ,  $\Delta t$  or  $D_f/D_i$ . It seems that in our case diffusion is not the limiting factor; different models were tested previously which confirmed that a diffusion based model is not pertinent for this kind of starch [Almeida et al., 2015].

To summarize, in our case (waxy cross-linked maize starch) variability in swelling onset and swelling duration could be attributed to the variability between granules in terms of crystallinity/structure, branching of amylopectin, cross linking. This variability comes perhaps from the different positions in the corn, positions on the cob, maturity, intra-granular heterogeneity, etc. These parameters influence the melting of the crystallites and the water diffusion. However, in our case the diffusion seems to not be the limiting phenomenon since the smallest granules do not swell faster than the biggest ones. It could be interesting to introduce variability for water activity curves and tortuosity in mechanistic swelling models such as the one developed by Desam et al. [2020]. This approach could help one determine which of these parameters might potentially explain the swelling kinetics variability. For more complex starches (non-waxy or non-cross-linked) the presented model is perhaps not adapted and additional experimental efforts are required because additional phenomena occur.

## 2.5 Conclusion

A novel individual granule scale model was developed to predict the swelling kinetics of modified waxy maize starch granules under heat treatment. The model parameters were calibrated with data from one ramp rate and hold temperature and validated with data from other cases. From the experiments it is shown that there is granule to granule variability not only in terms of ratio of swelling but also in terms of latency to swell when a critical temperature is reached. These phenomena are independent of the diameter of the granules. For practical time scales we can say the swelling reaction does not initiate below 60 °C. The latency time is random with a characteristic time constant decreasing as temperature is increased. Also the kinetics of the reaction is enhanced at higher temperatures. A granule with high latency time is also shown to have slower swelling rate compared to granules with low latency time.

The rheology of the suspension results from the hydrodynamic interactions and collisions between the granules which is a function of the volume fraction of granules and granule PSD. To design, control, scale up and operate complex processes for liquid food products one needs to leverage simulation techniques such as Computational Fluid Dynamics (fluid flow, heat transfer) and Discrete Element Method (particle evolution and interaction). This granule scale model can represent the commencement of such techniques for multi-scale modelling and simulation of modified starch suspension undergoing thermal treatment.

## 2.6 Acknowledgments

This research has been carried out with funding from European Union as part of EU RESEARCH FRAMEWORK PROGRAMME: H2020 / Marie Skłodowska-Curie Actions ITN MATHEGRAM [813202].

We acknowledge Giana Almeida-Perré and Gabrielle Moulin (UMR-SayFood) for their support and contributions.

## Conclusion (version française)

Un nouveau modèle a été développé pour prédire la cinétique individuelle de gonflement de granules d'amidon de maïs cireux modifiés soumis à un traitement thermique. Les paramètres du modèle ont été calibrés avec les données correspondant à une vitesse de montée en température et à une température de maintien et validés avec les données d'autres cas. A partir des expériences, il est montré qu'il existe une variabilité de granule à granule non seulement en termes de rapport de gonflement (diamètre final/diamètre initial) mais également en termes de temps de latence après atteinte de la température critique. Ces phénomènes sont indépendants du diamètre des granules. En pratique, la réaction de gonflement ne démarre quasiment pas en dessous de 60°C. Le temps de latence est aléatoire avec un temps caractéristique diminuant à mesure que la température augmente. La cinétique de gonflement est également plus rapide à des températures plus élevées. Enfin, un granule ayant un temps de latence élevé s'avère avoir un taux de gonflement plus lent par rapport aux granules ayant un temps de latence faible.

La rhéologie de la suspension résulte des interactions hydrodynamiques et des collisions entre les granules qui est fonction de la fraction volumique des granules et de leur distribution granulométrique. Pour concevoir et contrôler des procédés de traitement de produits alimentaires liquides contenant de l'amidon, il serait intéressant de tirer parti de techniques de simulation telles que la mécanique des fluides numérique (écoulement de fluide, transfert de chaleur) et la méthode des éléments discrets (évolution et interaction des particules). Ce modèle de gonflement à l'échelle des granules peut contribuer à une telle approche de modélisation et de simulation multi-échelles.



## Chapter 3

# Starch granule material properties characterization

In this chapter starch granule material properties, chiefly Young's modulus and Poisson's ratio are characterized experimentally at different degrees of swelling. Native unswollen starch granules are dense and hard in nature while fully swollen starch granules fall in the domain of soft particles such as hydrogels. Material properties are shown to play a critical role in the stress-strain responses [Imole et al., 2016]. Shi et al. [2020] showed that particle-particle cohesion results in different bulk responses based on if the particle is hard or soft in nature. In literature hard particles are typically probed using techniques such as AFM or nano-indentation to decipher the Young's modulus. Soft particle material properties are characterized using techniques such as microfluidics, centrifugal compression, etc. Thus, this chapter is divided into two sections, in the first section 3.1 we characterize the material properties of fully swollen starch granules through bulk rheology and osmotic compression of fully swollen starch suspension. In the second section 3.2 native unswollen starch granule stress-strain curve is characterized through nano-indentation inside a scanning electron microscope to estimate the Young's modulus of native starch.

### 3.1 Determination of the mechanical properties of gelatinized starch granule from bulk suspension characterization

Arnesh Palanisamy<sup>a</sup>, Gabrielle Moulin<sup>a</sup>, Artemio Plana-Fattori<sup>a</sup>, Denis Flick<sup>a</sup>, Marco Ramaioli<sup>a</sup>, Paul Menut<sup>a</sup>

<sup>a</sup> Université Paris Saclay, INRAE, AgroParisTech, UMR SayFood, 91300, Massy, France

#### Abstract

Gelatinized starch granules are soft and deformable particles that are commonly used in food products as texture modifiers. Modelling the flow behaviour of such suspensions during industrial processes requires the knowledge of the mechanical properties of the swollen granules, however, such data is usually lacking because of the difficulties inherent to the determination of mechanical properties of particles that are heterogeneous in terms of size and shape. We investigate here the rheological properties of dense suspensions prepared at different volume fractions and by different means (centrifugation, limited water swelling, osmotic compression) to estimate the mechanical properties of an "averaged" starch granule. Results show that starch granule exhibits a rough surface and behave as frictional particles. We compare the shear modulus value determined assuming either frictionless (previous model) or frictional interactions (as suggested by our results), the latter giving shear modulus lower by about one order of magnitude. This study also allows the first estimate of the starch granule bulk modulus, which value is corresponding to a Poisson ratio of 0.47, close to the maximum value of 0.5. The swollen granule shear modulus is also shown to be temperature independent in the range commonly found in industrial processes (20-90 °C). These results pave the way towards multiscale mechanistic modelling of the flow of starch suspensions, to derive macroscopic rheological properties from the description of the microscopic granule properties.

*Keywords:* Microgel; Shear modulus; Bulk modulus; Thermal effects; Particle Elasticity

This article is accepted for publication in the Journal *Rheologica Acta*

## Détermination des propriétés mécaniques moyennes de granules d'amidon à partir de la caractérisation de suspensions

Arnesh Palanisamy<sup>a</sup>, Gabrielle Moulin<sup>a</sup>, Marco Ramaioli<sup>a</sup>, Paul Menut<sup>a</sup>, Artemio Plana-Fattori<sup>a</sup>, Denis Flick<sup>a</sup>

<sup>a</sup> Université Paris Saclay, INRAE, AgroParisTech, UMR SayFood, 91300, Massy, France

### Résumé

Les granules d'amidon gélatinisé sont des particules molles et déformables qui sont couramment utilisées dans les produits alimentaires comme modificateurs de texture. La modélisation du comportement d'écoulement de ces suspensions au cours des procédés industriels nécessite la connaissance des propriétés mécaniques des granules gonflés. Cependant, ces données font généralement défaut en raison des difficultés inhérentes à la détermination des propriétés mécaniques de particules hétérogènes en termes de taille et de forme. Nous étudions ici les propriétés rhéologiques de suspensions denses préparées à différentes fractions volumiques et par différents moyens (centrifugation, gonflement limité en l'eau, compression osmotique) afin d'estimer les propriétés mécaniques d'un granule d'amidon "moyen". Les résultats montrent que les granules d'amidon présentent une surface rugueuse favorisant le frottement. Nous comparons la valeur du module de cisaillement déterminée en supposant des interactions sans frottement ou avec frottements (comme suggéré par nos résultats), cette dernière hypothèse conduisant à un module de cisaillement inférieur d'environ un ordre de grandeur. Cette étude permet également une estimation du module d'élasticité isostatique des granules d'amidon, dont la valeur correspond à un coefficient de Poisson de 0,47, proche de la valeur maximale de 0,5. Le module de cisaillement des granules gonflés s'avère également indépendant de la température dans la plage couramment rencontrée dans les procédés industriels (20-90 °C). Ces résultats ouvrent la voie à une modélisation mécanistique multi-échelle de l'écoulement des suspensions d'amidon, permettant d'en déduire les propriétés rhéologiques macroscopiques.

*Mots clés:* Microgel ; Module de cisaillement ; Module en vrac ; Effets thermiques ; Élasticité des particules.

### 3.1.1 Introduction

In its native form, starch is found as dense granules in a variety of grains and tubers. After industrial fractionation and in some cases, chemical/thermal treatments, a large variety of starch granules with contrasted properties are obtained. These starch granules that differ in terms of textural properties, or stability against mechanical, Physico-chemical or thermal stresses, are produced for various specific applications such as enhanced oil recovery in oil drilling applications or thickening agents in food products [Ratnayake and Jackson, 2008, Nawaz et al., 2020]. Global starch production is expected to reach around 156 metric tonnes by 2025 [Reportlinker.com, 2020], of this roughly 60% is used for food-based applications and 40% is expected to be used for industrial uses including oil, pharmaceutical, paper, etc.

Thermal treatments are commonly used in food processing and are usually applied to highly hydrated products. Applying a thermal treatment to native starch granules in the presence of excess water results in important modifications of their properties. In their native state, starch granules are solid particles, more or less spherical, in which starch macromolecules (amylopectin and amylose) are densely packed so that these granules only have a very limited water absorption capacity. However, if the temperature exceeded  $\sim 70^\circ\text{C}$ , an important swelling of the particles is very rapidly observed if water is available around the granule. The influx of water is driven by the enthalpic interactions between the hydrogen bonding sites of starch and water [Renzetti et al., 2021]. This process, during which the particle can absorb more than 10 times its mass in water, is called gelatinization. During gelatinization, the volume fraction of the starch particles present in a starch suspension strongly increases, and so does the suspension viscosity.

If the volume fraction of the particles in solution remains very low, i.e. much below the random close packing volume fraction  $\phi_{\text{rcp}}$ , that is the maximum volume fraction that can be reached by solid undeformable particles packed randomly, it behaves as a hard particle suspension at low shear rates [Einstein, 1905, Batchelor, 1977]. However, at high enough starch volume fractions ( $\phi > \phi_{\text{rcp}}$ ), these suspensions form thick pastes (gelatinization is also called starch pasting [Chen et al., 2007]) which exhibit properties that are similar to the ones of dense suspensions of soft microgel particles, with both solid-like and fluid-like properties [Seth et al., 2006]. At low stresses, they behave like elastic solids and deform reversibly under stress. However, once sufficient stress is reached they begin to flow and show the properties of a fluid. The threshold stress at which they begin to flow is called the yield point. Soft particle pastes have a jammed amorphous microstructure that is the source of their rheological behaviour. At volume fractions higher than  $\phi_{\text{rcp}}$ , soft particles start to deform to accommodate more neighbouring particles [Menut et al., 2012, de Aguiar et al., 2018]. Further compression results in particle shrinkage. Therefore, their volume fraction, also called packing fraction, that is estimated from the volume occupied by the particles in the diluted state, can exceed 1 [Seth et al., 2006, Evans and Lips, 1992].

With the advent of particle-based simulation methods, such as Discrete Element Modelling and CFD-DEM, there is significant interest in developing simple methods to characterize material properties such as particle Young's modulus and Poisson's ratio, required as model input. One of the most common contact models used for simulating particles is the Hertzian contact model. This model takes into account the curvature of the spherical surfaces while predicting the interaction forces on the colliding particles. According to this contact model, a

repulsive force exists when the granules overlap and no force exists when they do not overlap [Di Renzo and Di Maio, 2005]. To predict these normal and tangential repulsive forces one needs two parameters namely, Young's modulus and Poisson's ratio. To fully describe suspensions behaviour, lubrication forces need to be integrated, they arise due to the presence of the fluid layers in between particles. The momentum of a granule is imparted to the surrounding fluid and subsequently the other granules, hence leading to transport of momentum, even when granules are not physically in contact with each other. One requires interstitial fluid viscosity, surface roughness, position and velocities of particles for predicting the lubrication forces.

For homogeneous isotropic materials, simple relations exist between the three elastic constants are Young's modulus, the bulk modulus and the shear modulus. These relations allow calculating them all as long as two are known, as they are related by the following equations.

$$K = \frac{E}{3(1 - 2\nu)} \quad (3.1)$$

$$G = \frac{E}{2(1 + \nu)} \quad (3.2)$$

where  $K$ ,  $G$ ,  $E$  and  $\nu$  are respectively the bulk modulus, shear modulus, Young's modulus and Poisson's ratio. These relations could be applied to describe the whole behaviour of dense suspensions, which at a macroscopic scale could be considered homogeneous and isotropic. Individual starch granules, however, are non-spherical particles, and their behaviour might deviate significantly from one of the homogeneous and isotropic particles. Therefore a strategy could be to determine only "averaged" properties, as it is usually done for example for their size determination, done by static light scattering assuming a spherical shape.

Techniques at the particle level exist for deciphering materials properties of individual particle material properties in literature [Villone et al., 2019, Villone and Stone, 2020, Abate et al., 2012, Mohapatra et al., 2017]. Typical techniques include atomic force microscopy (AFM) based on nano-indentation, Brillouin light scattering (BLS), microfluidics, tensiometer. In AFM based techniques a Poisson ratio is assumed and Young's modulus is deduced from resisting force vs displacement data [Kaufman et al., 2017, Aufderhorst-Roberts et al., 2018]. However, these techniques are not straightforward to apply to measure a particle averaged modulus for such a complex system of soft particles with a very high degree of variability in terms of size and shapes. BLS data is used to infer the Poisson's ratio [Mohapatra et al., 2017]. In microfluidic approaches, a particle is compressed through a tapered channel and as pressure is developed by increasing the flow rate, the particle deforms due to the pressure and penetrates further into the channel. The penetration depth is optically observed and Young's modulus is deduced [Villone et al., 2019]. Similarly, tensiometer and microgel based techniques make use of surface tension to generate force for deformation and optical techniques for measuring the deformation [Abate et al., 2012, Villone and Stone, 2020]. However, the applicability of these techniques is not straightforward for non-spherical, poly-disperse, complex suspensions such as starch suspensions. Typical DEM models make the spherical particle assumption, albeit the 'multi-sphere' approach and methods for specific shapes such as super-quadratics exists [Lane et al., 2010, Preece et al., 1999]. For non-spherical particles with no particular shape

features, it is a standard practice to simulate spherical particles with averaged particle properties. One simple methodology to obtain such average particle properties is to infer them from the bulk response of the dense suspensions, which behave macroscopically as homogeneous isotropic materials and then to determine from that an "averaged" properties at the level of the individual particles. Such use of average 'calibration techniques' are also a common feature in powder and dry granular material simulations using DEM [He et al., 2015, Yan et al., 2016, Orefice and Khinast, 2020]. This approach is also useful in 'coarse-graining' simulations where the actual system is too large and one simulates at a mesoscale with larger 'representative particles' instead of actual particle sizes to reduce the computational costs.

In this article, the average mechanical properties of a large population of starch granules are investigated from bulk rheological measurements conducted on dense suspensions. To estimate the average particle shear modulus, the suspension shear modulus was measured. Two extreme hypotheses were considered, namely the fully frictional and the friction-less scenarios, to determine an upper and a lower limit for the particle shear modulus. The likelihood of the two assumptions is critically discussed. Then, we investigate the particles bulk modulus by osmotic compression. Finally, we investigate how particles shear modulus depends on the temperature, in the range 20-90 °C.

### 3.1.2 Materials and methods

Chemically cross-linked waxy maize starch (C\*Tex 06205), provided by Cargil (Baupte, France) was used for the entire study. Waxy maize starch contains more than 99 % amylopectin, and chemical cross-linking prevents the release of macromolecules during gelatinization.

#### True density measurement

The starch particles true density was measured using an air pycnometer (micromeritics AccuPyc 1330). We determined a true density  $\rho_{\text{true, starch}} = 1.321 \pm 0.002$  g/ml (average value from 6 repeats).

#### Centrifugation

In a 2-litre mixing vessel, we introduced 15 grams of starch before the addition of 1 litre of distilled water. The mixture was heated to 90 °C while mixing a 50 rpm using an IKA Eurostar 60 mixer with a 3 blade propeller of diameter 5 cm and held at this temperature for 15 minutes to ensure complete swelling of the starch granules. After letting the suspension cool down to room temperature, it was transferred into centrifuge tubes and centrifuged (SIGMA 3-18KS centrifuge) in the required conditions of rotation speed and duration. The supernatant (excess water layer) was carefully removed and the pellet, which consisted of densely packed swollen starch granules, was recovered for rheological characterization and dry weight measurements to estimate the volume fraction. A combination of centrifugation speeds ranging from 500g to 10000g and centrifugation duration ranging from 15 minutes to 30 minutes resulted in swollen starch suspensions with volume fractions  $\phi$  ranging from 0.447 to 0.552.

### Osmotic compression

22.5 grams of starch were added to 1.5 l of distilled water in a mixing vessel. The mixture was gelatinized at 90 °C as described previously (centrifugation). After letting the suspension cool down to room temperature, it was transferred into a regenerated cellulose dialysis tube with a cut-off of 6-8 kDa (spectra/por 1, diameter 40 mm). The dialysis tube was clipped at both ends and placed for osmotic compression inside a solution of Poly-Ethylene Glycol (PEG, 20 kg.mol<sup>-1</sup>) of known concentration. After osmotic compression, the compressed samples were recovered and subjected to rheological characterization and dry weight measurements to estimate their volume fraction. We used PEG 20kDa concentrations ranging from 0.2% to 5% (wt/wt) and compression times ranging from 2 to 15 days to produce samples with volume fractions  $\phi$  ranging from 0.46 to 1.69.

For the estimation of bulk modulus, we used the same protocol as described above, however, to ensure a constant osmotic pressure (that could decrease with time due to water diffusion from the sample to the PEG bath), the PEG bath was renewed 3 times. To determine the osmotic pressure corresponding to a given PEG concentration, we used the phenomenological one-parameter equation of state proposed by [Cohen et al. \[2009\]](#), which correctly described the behaviour of PEG (and others neutral flexible polymers in good solvents). This equation, based on the sum of a van 't Hoff and a des Cloizeaux terms, include a fitted parameter  $\alpha$ , also called the "crossover index", which is polymer size-dependent and for which we used the value proposed by [Li et al. \[2015\]](#) for PEG 20kDa. In that case, the osmotic compression lasted around 17 days to ensure equilibrium without any degradation or granule softening.

### Limited water swelling

After the addition of a known quantity of starch (ranging from 5 to 25 grams) into 100ml of water in a mixing vessel, the suspension was heated up to 90 °C and held at this temperature for 15 min under constant mixing. The sample was then cooled down to room temperature and recovered for rheological characterization and dry weight measurements. This resulted in starch suspension with volume fractions  $\phi$  ranging from 0.42 to 1.90.

### Dry weight measurement and volume fraction determination

Dry weight measurements were conducted at 100 °C in an oven (Chopin technologies). Prior measurements showed that after 24h at 100 °C the sample had reached a constant weight, therefore all samples were let in the oven for 24h before dry weight measurement. Samples were introduced in an aluminium foil previously weighted, and the weight of the sample was determined before ( $M_1$ ) and after ( $M_2$ ) drying so that the sample dry starch content could be determined as  $S_{\text{dry}} = M_2/M_1$ . Therefore, the starch concentration in the suspension,  $C_s$  (in g of starch per 100g of water) is given by

$$C_s = 100 * \frac{S_{\text{dry}}}{1 - S_{\text{dry}}} \quad (3.3)$$

The corresponding equivalent volume fraction of unswollen starch granules,  $\phi_{ug}$ , is given by

$$\phi_{ug} = \frac{C_s}{\rho_{true,starch}} * \frac{1}{100 + \frac{C_s}{\rho_{true,starch}}} \quad (3.4)$$

With  $\rho_{true,starch}$  the true density of unswollen starch previously determined assuming density for water  $\rho_{water} = 1000 \text{ kg/m}^3$ .

To estimate the volume fraction of swollen granules, we used data from previous microscopic experiments showing that, on average, the starch granule radius (the geometric mean of the Feret diameters) increases 2.35 times when gelatinized in excess of water [Palanisamy et al., 2020, Deslandes et al., 2019]. Thus, assuming that the granules are spherical and the total volume is conserved (volume gained by the starch during swelling is lost by water), one can estimate the volume of the swollen starch granules divided by the volume of the suspension:  $\phi$ , which is also known as the volume fraction. Please note that based on the definition here volume fraction is notional and thus can exceed 1. Similar definitions have been used extensively in the literature for various other suspensions as well [Mattsson et al., 2009].

$$\phi = (2.35^3) * \phi_{ug} \quad (3.5)$$

## Rheology

The rheological measurements were all performed in a Couette cell using an Anton Paar MCR92 rheometer. The characterization of the dense suspensions of swollen starch granules was performed at 20 °C. The mechanical properties were first probed at a constant frequency ( $f = 1 \text{ Hz}$ ) and strain ( $\gamma = 0.01$ ) for 120 seconds, with an acquisition rate of 1 point per second. Then, a frequency sweep was carried out at constant strain  $\gamma = 0.01$ , from  $f = 0.02 \text{ Hz}$  to  $f = 3.5 \text{ Hz}$ . Storage modulus obtained from single point measurements are plotted in figure 3.1. The frequency and loading effects were negligible compared to the volume effects.

The effect of temperature on the rheological properties was also evaluated. A rejuvenation and ageing step was performed before the first measurement, to limit measurements error resulting from the sample history (Cloitre et al. [2000]). Rejuvenation consists of shearing the sample at shear stress greater than the yield stress thus allowing the flow of the sample. Here, the sample was sheared at a shear rate  $\dot{\gamma} = 50 \text{ s}^{-1}$ . The following ageing step consists in holding the sample at rest for 45 minutes. Sedimentation experiments showed the absence of settling in the sample during all the duration of the experiments, which can be attributed to the large volume fraction of the samples (above random loose packing), combined with a low-density difference between the swollen starch granules and the surrounding water. Rheological properties were measured at 20 °C; 40 °C, 60 °C, 80 °C and finally 90 °C, the ramp rate during heating being 2 °C per minute. At each temperature, the rheological properties were measured at constant frequency  $f = 1 \text{ Hz}$  and constant strain  $\gamma = 0.01$  for 120 seconds with an acquisition rate of 1 point per second. For cooling the sample from 90 °C to 20 °C, a ramp rate of 0.4 °C per minute was used, and sample properties were again measured once thermal equilibrium was reached.

### Confocal laser scanning microscopy (3D)

Gelatinized samples obtained by the limited water swelling method and characterized by a particle volume fraction close to 0.4 were observed using a confocal laser scanning microscope (CLSM) (Leica TCS SP8, Germany). 0.5 ml of starch solution was stained using 50  $\mu$ L of Congo Red solution (1% in water, Sigma-Aldrich). Two 250  $\mu$ m thick spacers were used to place the stained solutions on the microscope slides. The solutions were excited with a laser at 488 nm and the emitted fluorescence was detected in the range 497 - 717 nm. The laser was used at 85% of the maximum intensity. Samples were observed with a 40X water objective. The total number of pixels in each picture is 3224 x 3224 and each pixel correspond to 0.09  $\mu$ m. Thus, the length and width of each picture correspond to 290.62  $\mu$ m. A total of 192 scans were performed using 0.422  $\mu$ m step for a total sample height of 80.67  $\mu$ m to generate a stack of images. Each of these 192 images was manually analyzed to count the number of neighbours of some representative granules.

### Bulk modulus measurements through osmotic compression

To measure the bulk modulus of the suspension using osmotic compression, one first needs to establish the time taken for the sample to equilibrate osmotically with the surrounding medium. To do so, we followed the dry weight evolution during osmotic compression, at two different PEG concentrations, and determined the corresponding volume fraction (Table 3.1). After 17 days, the volume fraction tends to reach a plateau. Above 17 days, the increase in volume fraction is very limited, but we observed by rheology a decrease in the sample shear modulus, that could result from starch degradation and granule softening, thus only samples obtained after 17 days will be considered for analysis.

time [days]	$\phi$ -3% PEG20K [wt/wt]	$\phi$ -4% PEG20K [wt/wt]
4	0.76	0.99
9	1.20	1.60
14	1.39	1.67
17	1.45	1.69
21	1.46	1.75
24	1.47	1.75

Table 3.1: Evolution of the sample volume fraction during osmotic compression, at two different PEG concentrations

## 3.1.3 Results and discussion

### Suspension rheology and estimation of the particle shear modulus

We observed that starting from  $\phi \sim 0.4$ , suspensions exhibit a finite value of elastic modulus. By contrast to what is observed in colloidal systems, which are liquid till the random closed packing, suspensions of granular particles can exhibit a finite modulus at volumes fractions much lower, due to the formation of a self-supporting stress-bearing network. The minimum volume fraction at which this network can form is called the random loose packing, its value depends on the shape but also the frictional properties of the particles [Silbert, 2010, Dong et al., 2006]. Starting from the random loose packing, the shear modulus (measured at  $f = 1$  Hz and  $\gamma = 0.01$ ) of dense suspensions of

swollen starch granules strongly increases with volume fraction, as illustrated in figure 3.1. Whatever the method used to prepare dense suspensions, namely centrifugation, osmotic compression or limited water swelling, the data superimposed. Whatever the history associated with each procedure, the final stage that is reached is reproducible in terms of rheological characterization and the granule volume fraction is the key parameter that controls the elastic behaviour of the paste. Even in the case of limited water swelling, for which granule never reached their full swelling capacity due to the limited amount of water (for  $\phi > 1$ ), the properties of the suspension are identical to the one of fully swollen starch granules that were partially dehydrated by compression. Two regimes are observed concerning the elastic modulus dependency toward volume fraction. First, from above the random loose packing to  $\phi \approx 0.7$ , the shear modulus strongly increases with the volume fraction. Then, a transition zone exists for  $0.7 < \phi < 1$ . For volume fraction  $\phi > 1$ , the dependence of shear modulus on volume fraction is much weaker. Insert in Figure 3.1 shows the log-log plot which shows the existence of the two regimes and the power-law dependence of shear modulus with the notional volume fraction of granules. Fitting a power law to these regimes resulted in the following equation

$$G' = \begin{cases} 1600\phi^{3.15} & 0.4 \leq \phi \leq 0.7 \\ 550\phi^{0.53} & 1 \leq \phi \end{cases} \quad (3.6)$$

A similar increase in shear modulus with notional volume fraction has been reported by [Evans and Lips \[1990\]](#), [Abdulmola et al. \[1996\]](#), [Rodriguez-Hernandez et al. \[2006\]](#). The existence of two regimes of shear modulus with volume fraction for swollen starch suspensions is reported in [Evans and Lips \[1992\]](#). Also, for comparison [Evans and Lips \[1992\]](#) reported values of suspension shear modulus around 750 Pa and 1000 Pa at a notional volume fraction of 1, for two different grades of chemically modified maize starches.

Whatever the volume fraction, the elastic modulus of the suspension only show a very weak dependency on the frequency. This is illustrated in the insert of figure 3.1 for 3 different volume fractions achieved via 3 sample preparation methods, in the first, intermediate and second regime. As reported by [Seth et al. \[2006\]](#), soft particle suspension moduli are function of the frequency. [Seth et al. \[2006\]](#) even predicted from simulations  $G_0$  and  $G_\infty$  (storage moduli at low and high frequency). We show from the following data that the relationship of storage moduli with frequency are similar across the volume fractions tested.

For friction-less systems, [Evans and Lips \[1990\]](#) derived an analytical equation that links the suspension shear modulus with the individual granule shear modulus and the average number of neighbouring granules. This model assumes a Hertzian potential (contact model) between granules. The equation, valid for  $\phi_{\text{rcp}} < \phi < 1$ , is as follows:

$$G'_{\text{susp}} = \frac{\phi_{\text{rcp}} n G'_p}{5\pi(1-\nu)} \left( \left( \frac{\phi}{\phi_{\text{rcp}}} \right)^{\frac{1}{3}} \left( 1 - \left( \frac{\phi}{\phi_{\text{rcp}}} \right)^{\frac{-1}{3}} \right)^{\frac{1}{2}} - \frac{8}{3} \left( \frac{\phi}{\phi_{\text{rcp}}} \right)^{\frac{2}{3}} \left( 1 - \left( \frac{\phi}{\phi_{\text{rcp}}} \right)^{\frac{-1}{3}} \right)^{\frac{3}{2}} \right) \quad (3.7)$$

where  $G'_{\text{susp}}$  is the suspension shear modulus,  $\phi_{\text{rcp}}$  is the volume fraction at random close packing and  $n$  is the average number of neighbouring granules respectively.  $\nu$  is the Poisson's ratio of the granule.

Given a granule size distribution one can estimate the  $\phi_{\text{rcp}}$  based on the relationship proposed by [Farr and Groot \[2009\]](#) as previously done in [Shewan and Stokes \[2015a,b\]](#), [Shewan et al. \[2021\]](#). In the system investigated, the

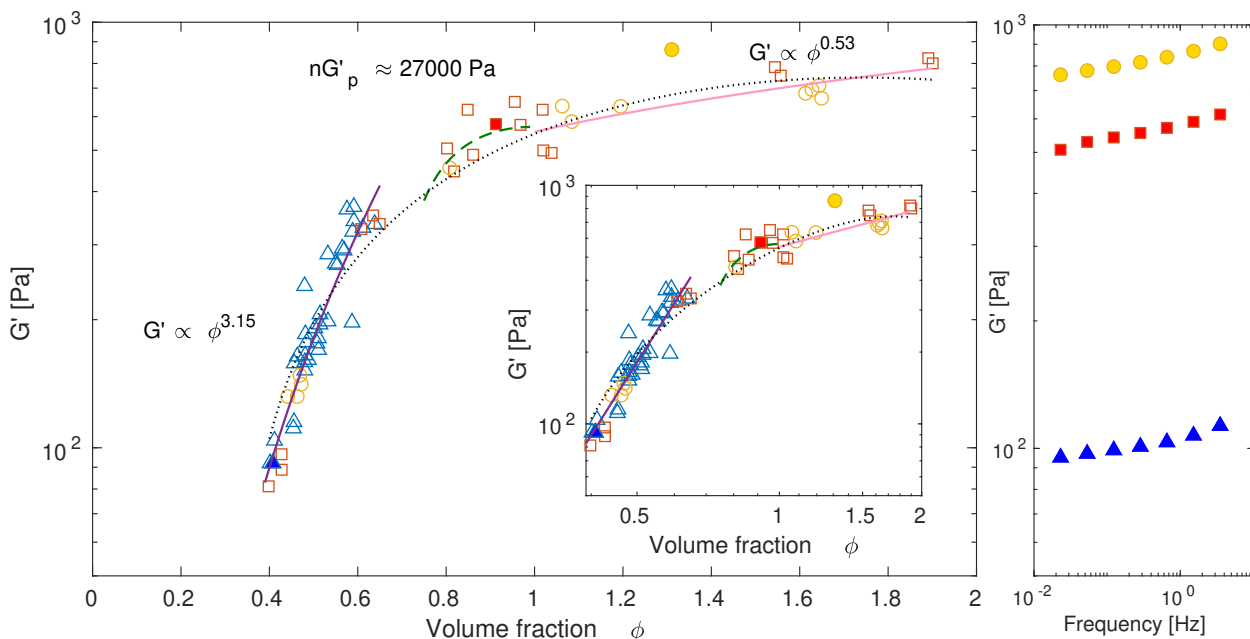


Figure 3.1: Suspension shear modulus as a function of volume fraction. Triangles[ $\Delta$ ], Squares[ $\square$ ], circles[ $\circ$ ] represent samples prepared via centrifugation, limited water swelling and osmotic compression respectively ( $\gamma = 0.01$ ,  $f = 1$  Hz). The solid dotted line represents the polynomial fit of overall experimental data ( $G'_{suspension} = -352\phi^2 + 1229\phi - 330$ ). The purple continuous line represents the power-law fit for volume fractions  $\phi < \phi_{rcp}$ , Green dashed line represents the best fit from the Evans and Lips [1990] model for  $0.8 < \phi < 1$ , Pink continuous line represents the power law fit for volume fractions  $\phi > 1$ .

*Insert:* The same figure in the log-log plot.

*Right-side plot:* Dependence on frequency: volume fraction of three samples prepared via centrifugation, limited water swelling and osmotic compression correspond to 0.4, 0.91, 1.31.

size distribution of Feret diameters of swollen starch granules has been previously determined, it is characterized by a normal distribution with mean = 33.1  $\mu\text{m}$  and standard deviation = 10.7  $\mu\text{m}$ . With this value,  $\phi_{rcp} = 0.68$  was determined. The average number of neighbours for each granule,  $n$ , was estimated using confocal microscopy. This method was previously used for PMMA spheres by van der Vaart et al. [2013] and also allowed to measure the pair correlation function. In fact, they predicted suspension shear moduli at high frequency with Young's modulus obtained from atomic force microscopy and pair correlation function from confocal microscopy.

In figure 3.1 we show the fit of equation 5 for the truncated data in the volume fraction range of  $\phi_{rcp} < \phi < 1$  ( $nG'_p \approx 27000$  Pa). As we can see from equation 5,  $G'_p$  depends on the assumption of the average coordination number  $n$  of each granule. To determine  $n$ , confocal images were acquired on suspensions and the coordination number of 10 different granules was manually counted for each of them, based on the contacts that were observed in different layers.

Figure 3.2 shows the confocal cross-section image of the starch granule suspension at  $\phi = 0.4$ , the maximum fraction that could be reached for which each granule could still be easily distinguished from its neighbours. Here,  $\phi < \phi_{rcp}$  and as  $n$  could depend on  $\phi$  [van Hecke, 2009], the value determined at this volume fraction might differ from the one at  $\phi = 1$ , that should be used to apply the Evans and Lips model. Experimental studies have shown that once particles are in contact, further compression first result in a decrease in the void fraction de Aguiar et al.

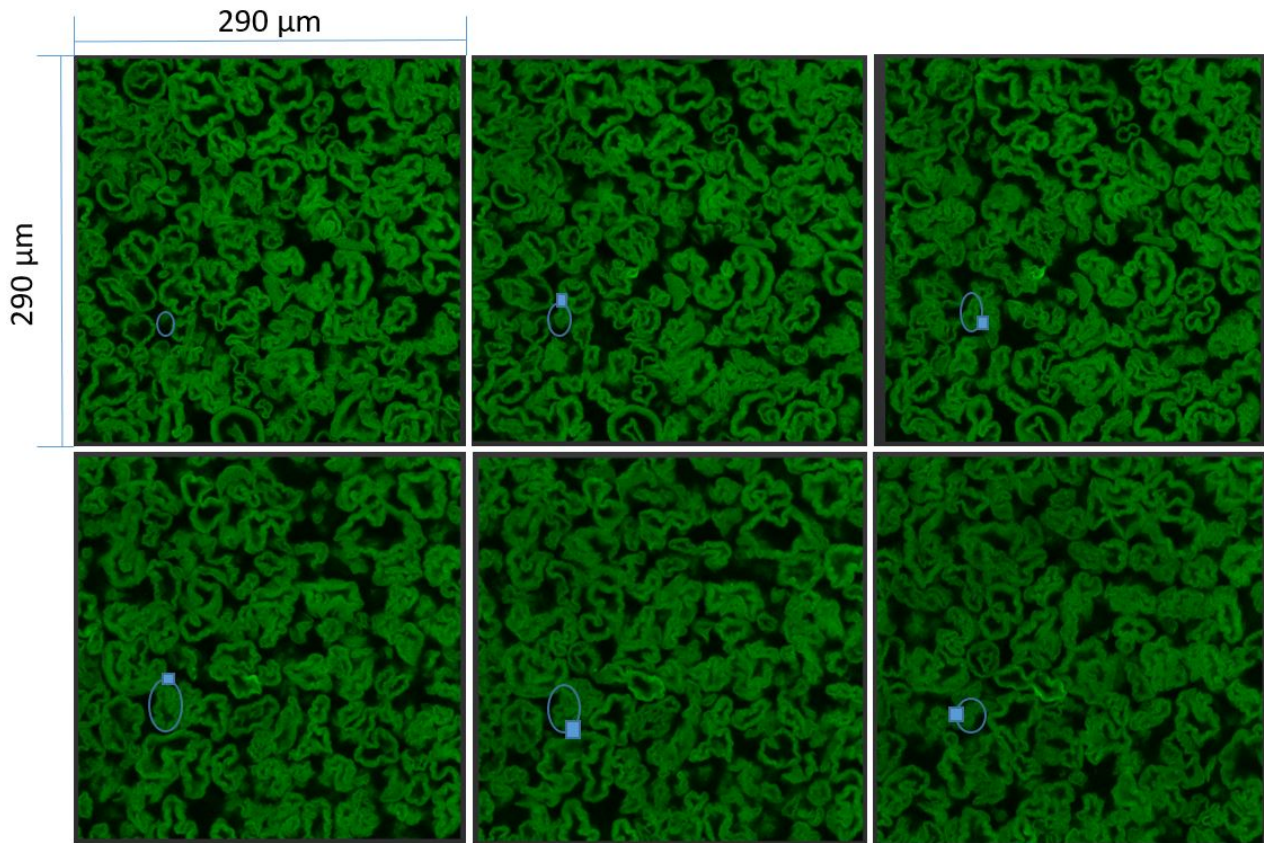


Figure 3.2: Confocal stack images of starch granule suspension. Blue Boxes ( $\square$ ) correspond to the contact of the traced granule with the neighbouring granule. Image slice number starting from left to right [30, 39, 46, 69, 78, 92]. Each slice corresponds to a depth of  $0.422 \mu\text{m}$

[2018] and local deformation at the contact point De Aguiar et al. [2017]. As a result, the increase in coordination number with volume fraction might be limited, especially if friction is present in the system. From the image acquired by confocal microscopy, it is evident that the starch granules are far from being spherical. It should be noted that if the granule seems hollow, this is likely due to the fact that dye (congo red) is adsorbed only on the surface of the granule. In figure 3.2 we tracked one selected granule from its base (top-left image) to its top (bottom-right image). For this selected granule 5 contacts were observed with neighbouring granules (highlighted as blue boxes on the pictures). This analysis was carried out to analyze ten different granules, for which we found coordination numbers varying from 5 (min) to 8 (max).

Therefore, with  $n = (5,8)$  and a Poisson's ratio  $\nu = 0.5$ , values obtained for the particle modulus were between  $G_p \approx 5300 \text{ Pa}$  and  $G_p \approx 3300 \text{ Pa}$ .

However, as seen in the confocal images, the particles are far from being spherical and have hair-like protrusions on the surface. This suggests that friction might be present in the system, which is coherent with the measure of a finite shear modulus at low volume fraction, the hallmark of the system above random loose packing concentration. Assuming a fully frictional case,  $G_p \approx G_{suspension}$  at  $\phi$  around 1, and we obtain  $G_p \approx 550 \text{ Pa}$ .

### Estimation of particle bulk modulus

To estimate the starch granule bulk modulus, we used osmotic compression experiments as previously done by [De Aguiar et al. \[2017\]](#) on model microgels. In general terms, the isotropic compressibility of material of volume  $V$  under a pressure  $P$  is measured by its bulk elastic modulus  $K = -V \frac{dP}{dV}$ . In this study, we do not measure directly the volume of the sample, but instead, we determined  $\phi$ , which is directly proportional to the sample volume through the relation  $\phi = n_p V_d / V$ , where  $n_p$  is the particle's number in the sample,  $V_d$  is the average volume of a fully swollen starch granule in the diluted state, and  $V$  the volume of the entire suspension in the compressed state. The bulk modulus of a gelatinized starch paste, compressed under an osmotic pressure  $\pi$ , can then be written as  $K = -(1/\phi) \frac{d\pi}{d(1/\phi)}$ , or in a more simple way

$$K = \phi \frac{d\pi_{in}}{d\phi} \quad (3.8)$$

where  $\pi$ ,  $\phi$  are the applied osmotic pressure and the starch particle volume fraction in the suspension respectively. In our experiments, the osmotic pressure is directly linked to the PEG content in the water bath, so that osmotic pressures ranging from about 1.8 kPa to about 19 kPa were experimentally reached (Table 3.2)

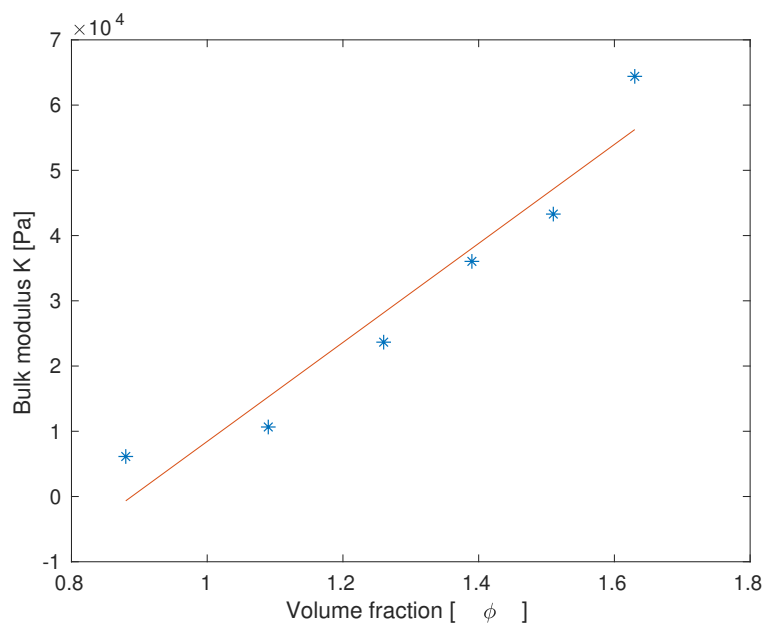


Figure 3.3: Suspension bulk modulus as function of volume fraction. Asterisks[\*] correspond to experimental data.

Using equation 3.8, the estimates for bulk modulus at different volume fractions are shown in figure 3.3. Consistently with [Nikolov et al. \[2020\]](#), a linear relationship between suspension bulk modulus and volume fraction is obtained. The linear trend also agrees well with the experimental results of [Liétor-Santos et al. \[2011\]](#) for microgel particles comprising vinyl pyridine and divinylbenzene. [Nikolov et al. \[2020\]](#) showed that the suspension bulk modulus at  $\phi = 1$  is roughly equal to  $0.8 \times$  particle bulk modulus and that the ratio of the suspension bulk modulus to the particle bulk modulus is independent of volume fraction for  $\phi > 1$ . From the linear fit in figure 3.3, it

PEG conc [wt %]	Osmotic pressure [kPa]	Volume fraction( $\phi$ ) [%]
1	1.8	77
1.5	3.4	99
2	5.4	120
2.5	8.0	139
3	11.0	145
3.5	14.7	158
4	18.9	169

Table 3.2: Equilibrium osmotic pressure and volume fractions

appears that the bulk modulus of the suspension is about 8.4 kPa at  $\phi = 1$ . Therefore, an estimate for starch particle bulk modulus is  $K_{particle} \approx 10.5$  kPa. Using this estimate for bulk modulus and shear modulus of the suspension at  $\phi = 1$ , we obtain a Poisson's ratio of 0.47, which is close to the maximum value of 0.5. By contrast, a Poisson's ratio of 0.33 is obtained if it is calculated using the friction-less spherical particle assumption. Poisson's ratio for hydrogels reported in literature ranged from 0.38 to 0.5 [Mohapatra et al., 2017, Boon and Schurtenberger, 2017]. This methodology to characterize the modulus of particles is complementary to the techniques such as nano-indentation, AFM, etc [Kaufman et al., 2017, Aufderhorst-Roberts et al., 2018]. Such existing alternative techniques are not straightforward to apply to measure a particle averaged modulus for such a complex system of soft particles with a very high degree of variability in terms of size and shapes.

### Suspension material properties with temperature

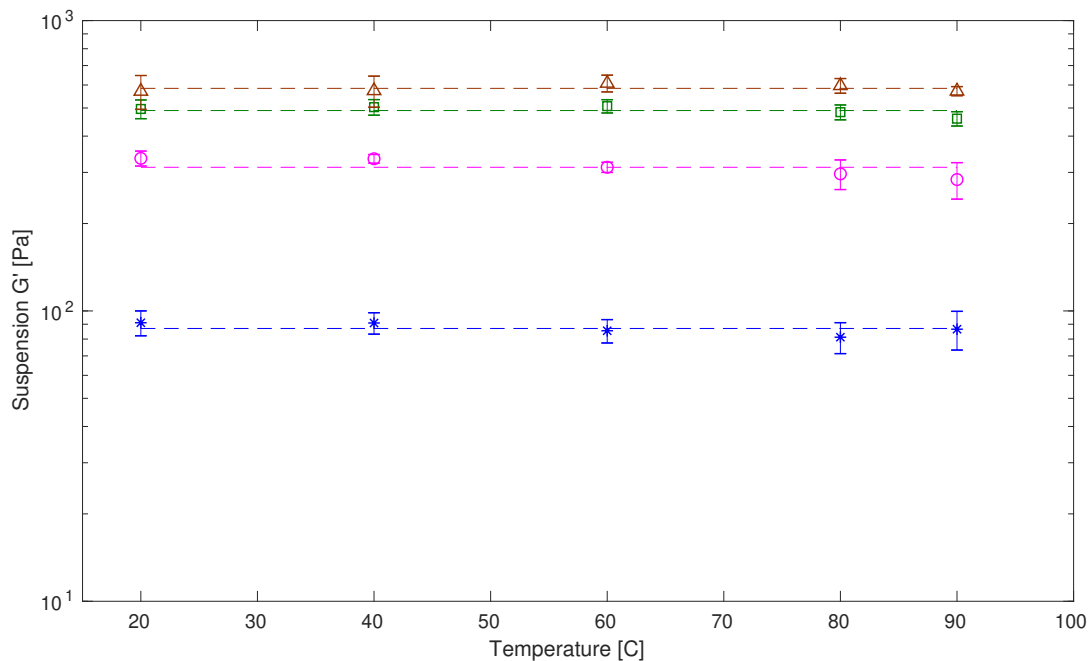


Figure 3.4: Storage modulus of suspension at different temperatures. Asterisks[\*], circles[○], boxes[□] and triangles[△] correspond to volume fractions  $\phi$  of 0.42, 0.63, 0.83 and 1.03 respectively. Error bars correspond to one standard deviation. The dashed line is the mean value of all the measurements across temperatures.

The storage modulus of the suspension was measured at five different temperatures for four different volume fractions. No significant dependence of shear modulus with temperature was observed in the range of temperatures tested. In figure 3.4 the dotted line is the mean of the measurements of storage moduli at all temperatures for a given volume fraction. These dotted lines fall within the error bars for all volume fractions except for  $\phi = 0.63$  at 40 °C. Thus, we conclude that the swollen starch granule material properties are independent of the temperature for the tested range of 20 °C to 90 °C. Such temperature independence of hydrogels is also observed by [Jing et al. \[2021\]](#) for polyvinyl alcohol (PVA), carrageenan and calcium-chloride based particles as long as there is no phase change such as melting.

### 3.1.4 Conclusion

This study focused on the rheological properties of fully gelatinized chemically modified waxy maize starch. We characterized suspension shear modulus and suspension bulk modulus at different particles volume fractions, which was reached thanks to three different and independent techniques: centrifugation of a diluted suspension, osmotic compression of a diluted suspension, and controlled swelling of the granules with a limited amount of water. These different techniques allowed to reach a large range of volume fractions but also gave coherent results showing the results are not technique-dependant. The shear and bulk moduli were determined by rheometry and osmotic compression, respectively. From these macroscopic measurements, we deduced the mechanical properties of an "averaged" swollen granule. We first discussed the equation previously used by [Evans and Lips \[1990\]](#), which can be used to estimate the particle shear modulus from the suspension shear modulus, and required an estimate of the average number of neighbouring granules. This was roughly estimated manually using the layered scans of confocal microscopy. Besides, [Evans and Lips \[1990\]](#) equation is only valid for perfectly spherical friction-less spheres, which is rarely the case in naturally occurring systems such as starch suspensions, this approach could give an upper bound for the particle shear modulus which was deduced to be around 4400 Pa for this starch. For the lower bound, we considered frictional interactions so that the particle shear modulus is nearly identical to the suspension shear modulus at a volume fraction close to 1. From this assumption, an estimate of particle shear modulus of 550 Pa was obtained (figure 3.1). It seems reasonable, notably because of the 'roughness' of the observed granules to consider rather the second hypothesis. Therefore, assuming frictional interactions, the bulk modulus of the particle was deduced to be around 10.5 kPa. Interestingly, the suspension shear modulus, measured at different volume fractions, were found to be independent of temperature, which suggests that starch granules mechanical properties could be temperature independent in the range of temperature investigated here. Finally, in a first approach, for this kind of starch, in a fully swollen state, Young's modulus and Poisson's ratio of the granules are approximately 1.8 kPa and 0.47 respectively. These estimates could find use in research using modelling and simulation techniques such as DEM and CFD-DEM which in turn help in designing process equipment, process intensification, optimization and designing model-based process control. This methodology can be applied to estimate the properties of similar microgel systems and different grades of chemically modified cross-linked waxy maize starches.

### 3.1.5 Acknowledgments

This research has been carried out with funding from European Union as part of EU RESEARCH FRAMEWORK PROGRAMME: H2020 / Marie Skłodowska-Curie Actions ITN MATHEGRAM [813202].

## Conclusion (version française)

Cette étude a porté sur les propriétés rhéologiques de l'amidon de maïs cireux chimiquement modifié et entièrement gélatinisé. Nous avons caractérisé le module de cisaillement de la suspension et son module d'élasticité isostatique à différentes fractions volumiques de particules, ce qui a été obtenu grâce à trois techniques différentes et indépendantes : centrifugation d'une suspension diluée, compression osmotique d'une suspension diluée, et gonflement contrôlé des granules avec une quantité limitée d'eau. Ces différentes techniques ont permis d'atteindre une large gamme de fractions volumiques mais ont également donné des résultats cohérents montrant que les résultats ne dépendent pas de la technique. Les modules de cisaillement et d'élasticité isostatique ont été déterminés respectivement par rhéométrie et par compression osmotique. A partir de ces mesures macroscopiques, nous avons estimé les propriétés mécaniques d'un granule gonflé "moyen". Nous avons d'abord examiné l'équation utilisée par [Evans and Lips \[1990\]](#), qui permet d'estimer le module de cisaillement des particules à partir du module de cisaillement de la suspension, et qui nécessite une estimation du nombre moyen de granules voisins. Ce nombre a été estimé expérimentalement par l'acquisition d'image 2D à des profondeurs croissantes dans des suspensions, par microscopie confocale. L'équation proposée par [Evans and Lips \[1990\]](#) n'est valable que pour des sphères parfaitement sphériques et en l'absence de phénomènes de friction, ce qui est rarement le cas dans les systèmes naturels tels que les suspensions d'amidon. Cette approche peut néanmoins donner une limite supérieure pour le module de cisaillement des particules qui a été estimé à environ 4400 Pa pour cet amidon. Pour la limite inférieure, nous avons considéré l'existence de frottement (absence de glissement) de sorte que le module de cisaillement de la particule peut être considéré comme très proche de celui de la suspension pour une fraction volumique proche de 1. Une estimation du module de cisaillement de la particule de 550 Pa a ainsi été obtenue. Il semble raisonnable, notamment au vu de la "rugosité" des granules observés de considérer plutôt la seconde hypothèse. Le module d'élasticité isostatique de la particule a été estimé à environ 10,5 kPa. Le module de cisaillement de la suspension, mesuré à différentes fractions volumiques, s'est avéré indépendant de la température, ce qui suggère que les propriétés mécaniques des granules d'amidon sont indépendantes de la température dans la gamme de température étudiée ici. En première approche, on peut donc considérer que le module d'Young et le coefficient de Poisson des granules étudiés sont respectivement d'environ 1,8 kPa et 0,47. Ces estimations pourraient être utilisées dans des modélisations DEM ou CFD-DEM de suspensions d'amidon en écoulement soumis à des transferts thermique, pour améliorer la conception et le contrôle d'équipements de traitement de produits amylicés. Cette méthodologie pourrait également être appliquée pour estimer les propriétés d'autres types d'amidon ou de systèmes similaires (comme des microgels).

## 3.2 Estimation of Young's modulus of un-swollen starch granules through nano-indentation

### Abstract

In the previous section the mechanical properties of fully swollen starch granules were investigated. Here, we aim to characterize the Young's modulus of un-swollen individual starch granules using nano-indentation. Typical techniques such as nano-indentation, AFM (Atomic force microscopy), centrifugal compression, micro-fluidic are used to characterize the modulus of particles in literature [Kaufman et al., 2017, Aufderhorst-Roberts et al., 2018, Villone et al., 2019, Nordstrom et al., 2010]. The range of applicability of these techniques is different. Centrifugal compression and micro-fluidic are applicable for soft-particles such as micro-gel suspensions (Young's modulus < 200,000 Pa). However, literature reported values of Young's modulus of 2 GPa warrants the use of techniques such as nano-indentation or AFM [Govedarica et al., 2012]. As the particles are very close to being spherical (aspect ratio of 1.18 as shown from microscope images in Deslandes et al. [2019]), we used a flat punch tip for performing nano-indentation. The choice of a flat punch instead of the traditional pyramidal Berkovich punch stems from the fact that particle slippage during indentation could be avoided in the former compared to the later [Gibson et al., 2015]. Hwang and Shahsavari [2018] recommended the use of flat punches for individual particles or single layered films and pyramidal tip if the sample was compacted (dense material). They further showed through experiments that while probing single particle layered films at small indentation depths the response to the indentations is of particle origin.

*Keywords:* Nano-indentation; Young's modulus; SEM; Starch granule.

## Estimation du module d'Young des granules d'amidon natif non gonflé par nano-indentation

### Résumé

Dans la section précédente, nous avons présenté la caractérisation des propriétés mécaniques des granules d'amidon entièrement gonflés. Ici, nous caractérisons le module d'Young de granules d'amidon individuels non gonflés en utilisant la nano-indentation. Des techniques typiques telles que la nano-indentation, l'AFM (Atomic force microscopy), la compression centrifuge, la micro-fluidique sont utilisées pour caractériser le module des particules dans la littérature : [Kaufman et al., 2017, Aufderhorst-Roberts et al., 2018, Villone et al., 2019, Nordstrom et al., 2010]. Le champ d'application de ces techniques est différent. La compression centrifuge et la microfluidique sont applicables aux particules molles telles que les suspensions de microgels (module d'Young < 200 000 Pa). Cependant, les valeurs du module d'Young de 2 GPa rapportées dans la littérature pour les granules d'amidon natif justifient l'utilisation de techniques telles que la nano-indentation ou l'AFM [Govedarica et al., 2012]. Étant donné que les particules sont très proches de la sphéricité (rapport d'aspect de 1,18 comme le montrent les images de microscopie dans [Deslandes et al., 2019]), une pointe de poinçon plate du nano-indenteur est utilisée. Le choix d'un poinçon plat au lieu du traditionnel poinçon pyramidal de Berkovich s'explique par le fait que le glissement des particules pendant l'indentation a pu être évité grâce à ce type de poinçon [Gibson et al., 2015]. [Hwang and Shahsavari, 2018] ont également suggéré l'utilisation de poinçons plats pour les particules individuelles ou les films, et de poinçons pyramidaux si l'échantillon est constitué d'un empilement dense de particules. Ils ont en outre montré par des expériences que lors du sondage de films de particules à de faibles profondeurs d'indentation, la réponse aux indentations est d'origine particulaire.

*Mots clés:* Nano-indentation ; Module d'Young ; Microscopie électronique à balayage (MEB) ; Granule d'amidon.

### 3.2.1 Materials and Methods

An Alemnis Nano-indenter mounted inside a Scanning Electron Microscope (TESCAN MIRA II) was used to decipher the stress-strain curves. C\*Tex(06205) chemically modified maize starch is sparsely dispersed on a piece cut from a 3-inch silicon wafer attached to the SEM stub as shown in figure 3.5. SEM stub is mounted onto the Alemnis nano-indenter with a 50  $\mu\text{m}$  flat indenter tip and loaded into the SEM. The nano-indenter is rotated to 80° to the normal as shown in the figure 3.6 where the normal direction corresponds to the SEM beam source.

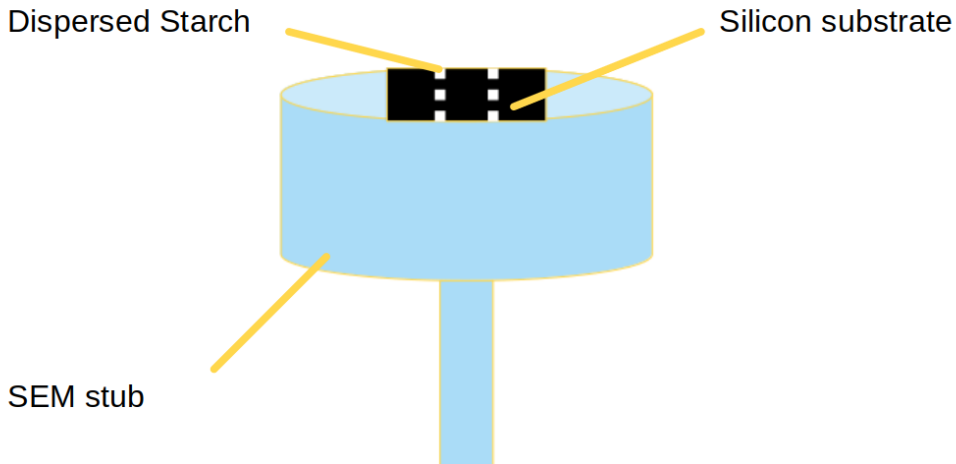


Figure 3.5: Dispersed starch on silicon substrate mounted on a SEM stub.

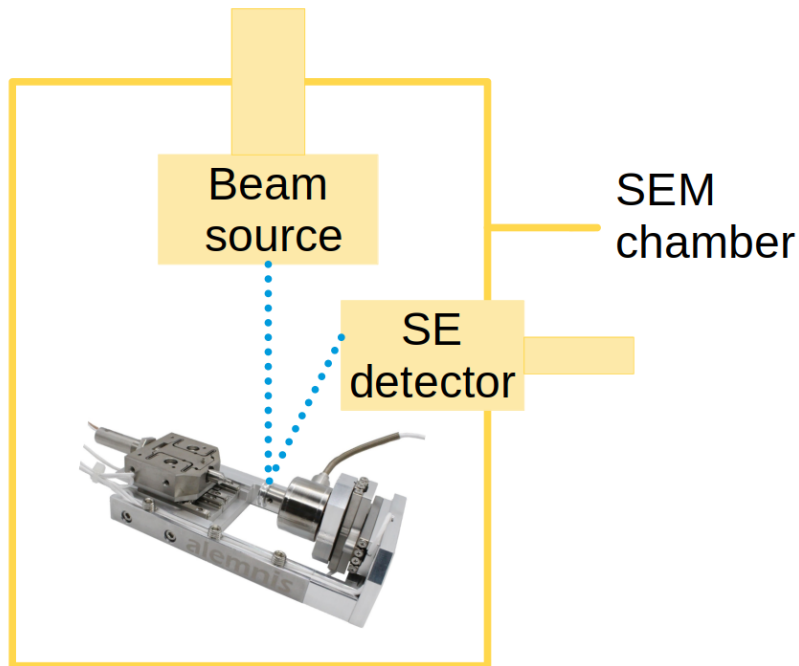


Figure 3.6: Nano-indenter alignment inside the SEM chamber

The chamber is brought under vacuum and subsequently, the electron beam is switched on to start imaging the sample. 5 kV accelerating voltage along with a probe current of 15 is used. The units of probe current are in arbitrarily defined microscopy units. SEM is operated under the Secondary electron mode. The secondary electron detector is located at  $55^\circ$  to the normal (Source of the electron beam). A typical SEM image of the sample is shown in figure 3.10. After obtaining a satisfactory SEM image of the sample, the indenter tip is lowered towards an individual particle slowly. The load sensor used could measure a maximum force of up to 500 mN. The program has 5 steps: approach, loading, hold, unloading and retreat. The approach step is ended when the load force detected by the sensor is greater than 0.5 mN. The speed at which the indenter is lowered/lifted in the approach/retreat step is  $4\text{E-}07$  m/s. Target indentation displacement is 700 nm which roughly corresponds to 7% of the diameter of the particle. Loading-unloading speed is  $2.33\text{E-}8$  m/s. Once the probe reached the desired indentation depth (700 nm in this case), the program switches to the hold step, where the indenter tip is held for 5 sec. After 5 seconds the probe is lifted in the unloading step slowly and further at a faster pace in the retreat step. During all these steps the load is constantly recorded at a sampling rate of 40 points per second. The nanoindentation steps have been summarized in table 3.3

Step	Velocity [m/s]	End condition
1	$4\text{e-}7$	Load > 0.5 mN
2	$2.33\text{e-}8$	Indentation depth = 700 nm
3	0	hold time = 5 s
4	$-2.33\text{e-}8$	Indentation depth = 0 nm
5	$-4\text{e-}7$	–NA–

Table 3.3: Indentation program

### 3.2.2 Results and discussion

Typically Young's modulus is estimated from the force-displacement data from techniques such as nano-indentation or AFM using two models: (1) the Oliver-Pharr model or (2) the Hertz model [Oliver and Pharr, 1992, Hertz, 1896]. The Oliver-Pharr method is widely accepted in the field of nano-indentation since its proposal. This method requires one to have accurate information of the contact area between the tip and the sample surface to get reliable estimates of Young's modulus [Yan et al., 2012]. The Berkovich pyramidal tip is one of the most frequently used tips in nano-indentation. The contact area of the indenter tip with the sample is estimated based on the geometry given an indentation depth using a polynomial equation in terms of indentation depth. The unloading part of the curve is fit to Sneddon's equation [Sneddon, 1965]. The equation is valid only in the elastic limit and the basis for using the unloading part is that the initial part of the unloading curve is mostly due to the elastic response of the system. The phenomena of pile up and sink in (figure 3.7) is related to the under and overestimation of the contact area between the indenter tip and the sample [Yan et al., 2012]. The reasons for pile up and sink-in could be due to the adhesive or cohesive forces in the sample.

On the other hand, the Hertzian model has been applied extensively in the literature for particles, especially when they are close to being spherical [Hwang and Shahsavari, 2018, Perkins et al., 2007, Joly-Pottuz et al., 2015]. Hertz model is based on the purely elastic response on the particles and is known to be valid for spherical particles

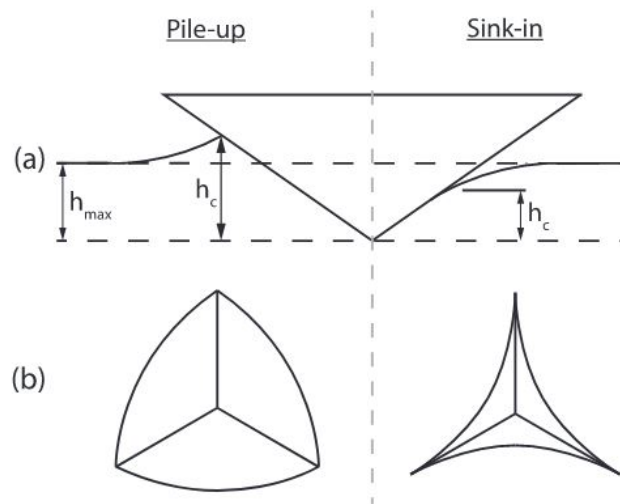


Figure 3.7: Illustration of pile-up and sink-in material behaviour at maximum indentation depth (a) side profile of indentation, (b) geometry of projected contact areas for each case. Courtesy: [Hardiman et al., 2016]

in the initial part of loading curve in the force vs displacement plot as shown in figure 3.8.

Figure 3.8 shows a schematic force displacement curves for a typical nano-indentation test with loading curve starting at the origin and unloading curve with an intercept on the x-axis. Another major difference between the two methods is that for Oliver-Pharr method, the data from initial part of the unloading curve is used where as for the Hertz method, the data from initial part of the loading curve is used.

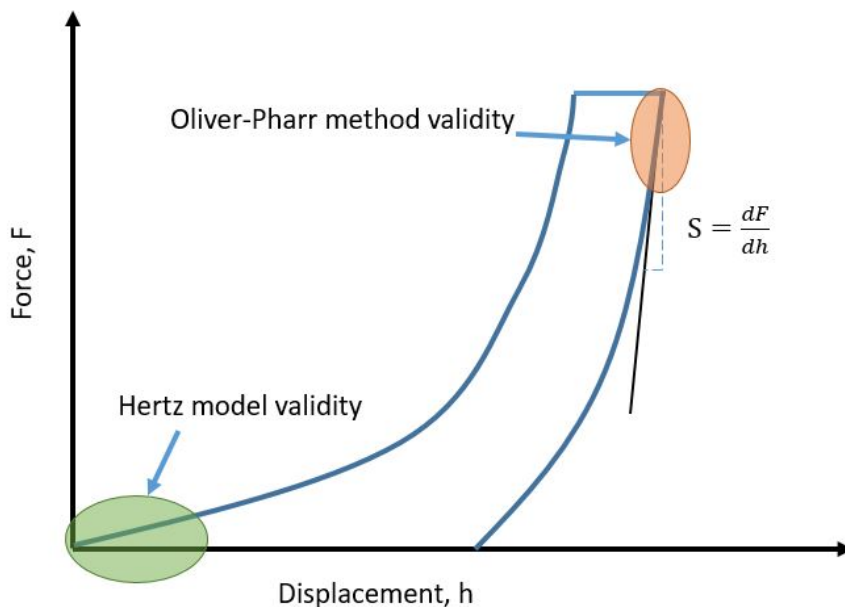


Figure 3.8: Schematic of load-displacement curve for an instrumented nanoindentation test

The model equation for Oliver-Pharr method is as follows.

$$E_r = \frac{\sqrt{\pi}}{2} \frac{S}{\sqrt{A_p}} \quad (3.9)$$

where,  $S$  is the slope at the initial point of the unloading curve as shown in figure 3.8,  $A_p$  is the area of contact of the indenter tip with the particle.

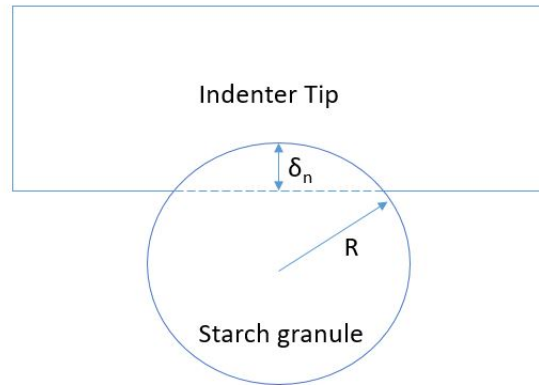


Figure 3.9: Particle indentation depth illustration

As previously mentioned accurate determination of  $A_p$  is essential. In the current experimental setup, it is not feasible. Thus, we make an estimate using the spherical elastic particle assumption. This is given as follows

$$A_p = \pi R \delta_n \quad (3.10)$$

Another method to measure Young's modulus is using the Hertz model. The indentation force as a function of indentation depth  $h$  is given by the following equation 3.11 according to the Hertz theory.

$$F = \frac{4}{3} R^{0.5} E_r \delta_n^{1.5} \quad (3.11)$$

where  $E_r$  is the reduced elastic modulus,  $R$  is the initial radius of the particle,  $\delta_n$  is the length of particle deformation due to indentation in the normal direction to the indenter tip as shown in figure 3.9.

Further, the reduced elastic modulus  $E_r$  is given by the following equation 3.12

$$\frac{1}{E_r} = \frac{1 - \nu_p^2}{E_p} + \frac{1 - \nu_i^2}{E_i} \quad (3.12)$$

where,  $\nu_p$  is the Poisson's ratio of the particle,  $\nu_i$  is the Poisson's ratio of the indenter material,  $E_p$  is Young's modulus of the particle,

$E_i$  is Young's modulus of the indenter material.

The indenter tip is made of diamond ( $E_i = 1047$  GPa), thus we can neglect the second term in equation 3.12 to make the following simplification.

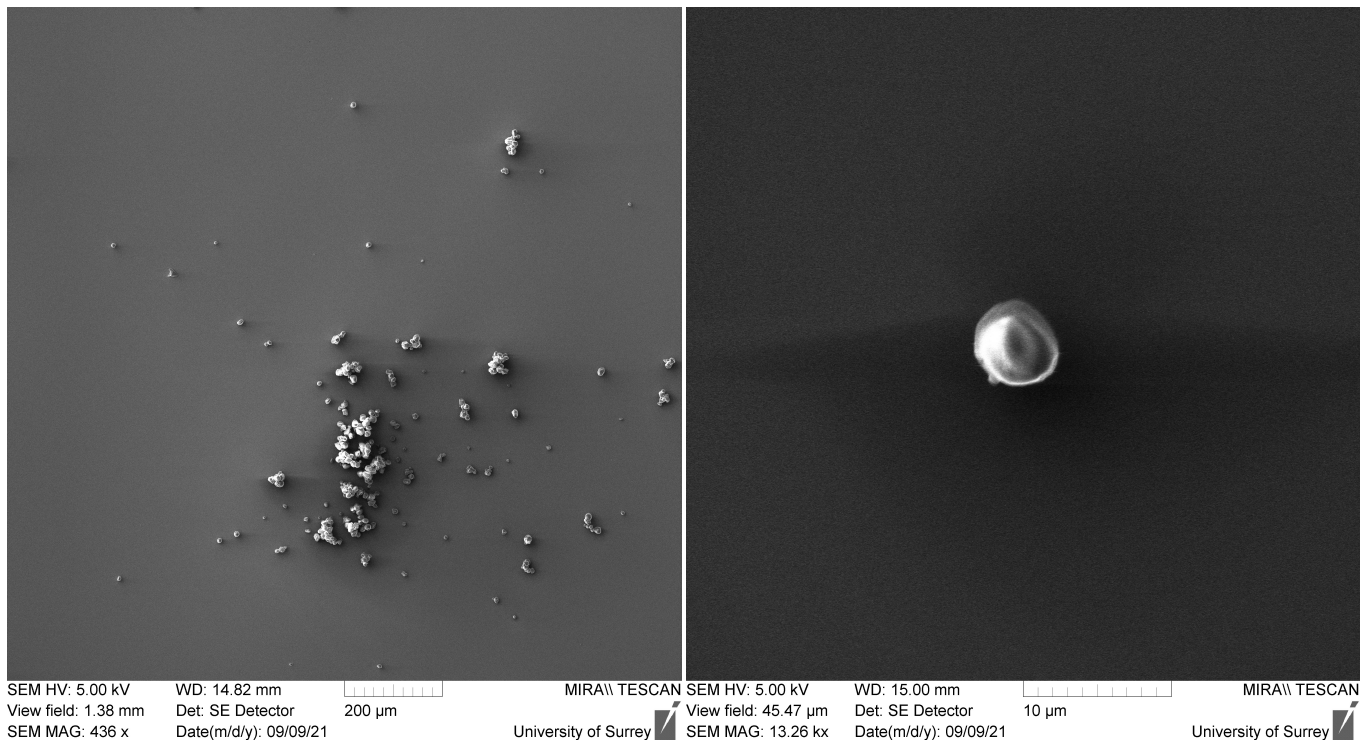
$$\frac{1}{E_r} \simeq \frac{1 - \nu_p^2}{E_p} \quad (3.13)$$

Furthermore, compliance adjustment to the measured force due to the silicon substrate is neglected using a similar argument that silicone Young's modulus is  $\simeq 100$  GPa, which is 2 orders of magnitude higher than expected Young's modulus of starch. In the plot of force vs displacement<sup>1.5</sup> of the loading curve, the slope of the linear fit is  $\frac{4}{3}R^{0.5}E_r$ .

In this work, we have used both methodologies to estimate Young's modulus.

### 3.2.3 Raw data and images

SEM images of native (dry) starch particles dispersed on a silicon substrate are shown in figure 3.10a. Most of the starch granules are found adhering to another granule and forming clusters. However, we could find individual particles as shown in figure 3.10b. Once individual particles have been identified by SEM, the nano-indenter tip is brought closer towards one of them to perform indentation.



(a) SEM image of dispersed starch granules

(b) SEM image of individual starch granule

Figure 3.10: SEM images of starch

Typical nano-indentation results in force vs displacement data. However, one must take into account the

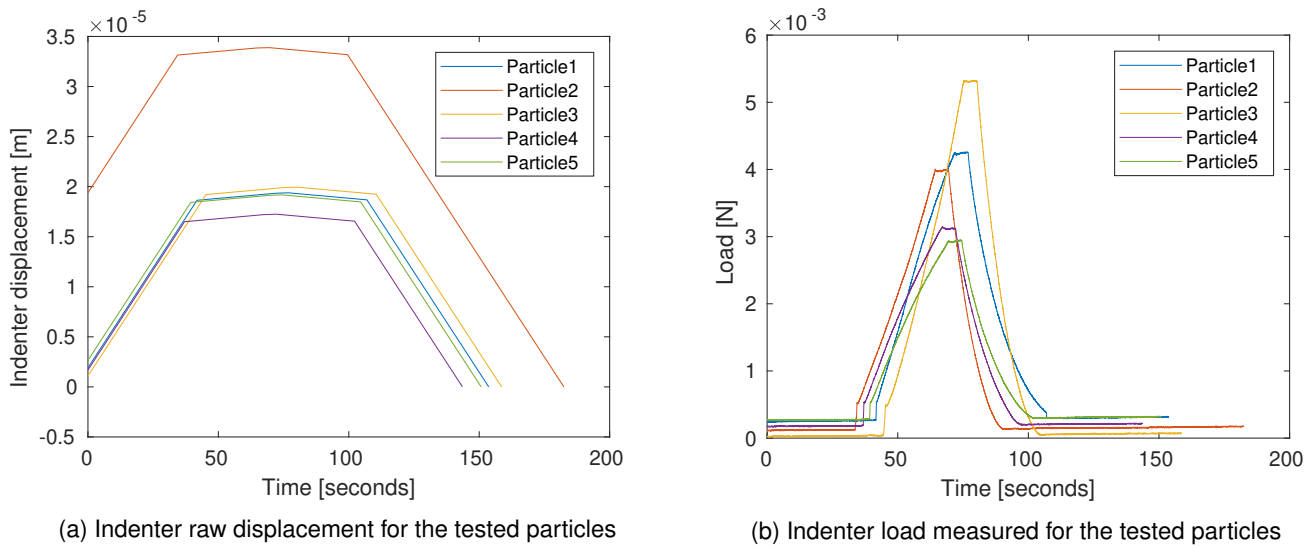


Figure 3.11: Raw data from the indenter

instrument deformation and correct the raw displacement. This is commonly called the compliance correction and the pre-factors are given by the manufacturer and depends on the load sensor that is used. The load compliance for the instrument and load sensor that is used is  $4.203 \text{ E-}6 \text{ m/N}$ . The correction equation is as follows:

$$\delta_n = displacement - load * frame\ compliance \tag{3.14}$$

Similarly, A small residual load is detected by the sensor even when there is no contact of the indenter tip with the particle. This residual load is subtract from the measured load.

Figure 3.11 shows the raw data as measured during indentation of particles. Some trials resulted in particle breakage, these data were excluded here.

Figure 3.12 shows the SEM images at different stages of nano-indentation of particle 3 with a  $50 \mu\text{m}$  flat tip. As one can see the particles are close to being spherical and due to the instrument geometric configuration it was not possible to view the particles during the compression phase. However, we could see that the particle shape does not change significantly before and after indentation.

### 3.2.4 Young’s modulus calculation

As mentioned previously, the Hertz model is applicable in the initial parts of the loading curve and the Oliver-Pharr method is applied to the initial part of the unloading curve. Figure 3.13 shows the stress-strain curves of 5 particles tested.

Figure 3.14 shows the initial part of the loading curve. 100 data points are considered to fit the Hertzian model. As we can see except for particle 2 the model closely matches the experimental data. Large asperities on particle 2 and 3 at the indentation point could be a possible reason for the discrepancy of the experimental loading curve with the Hertzian model.

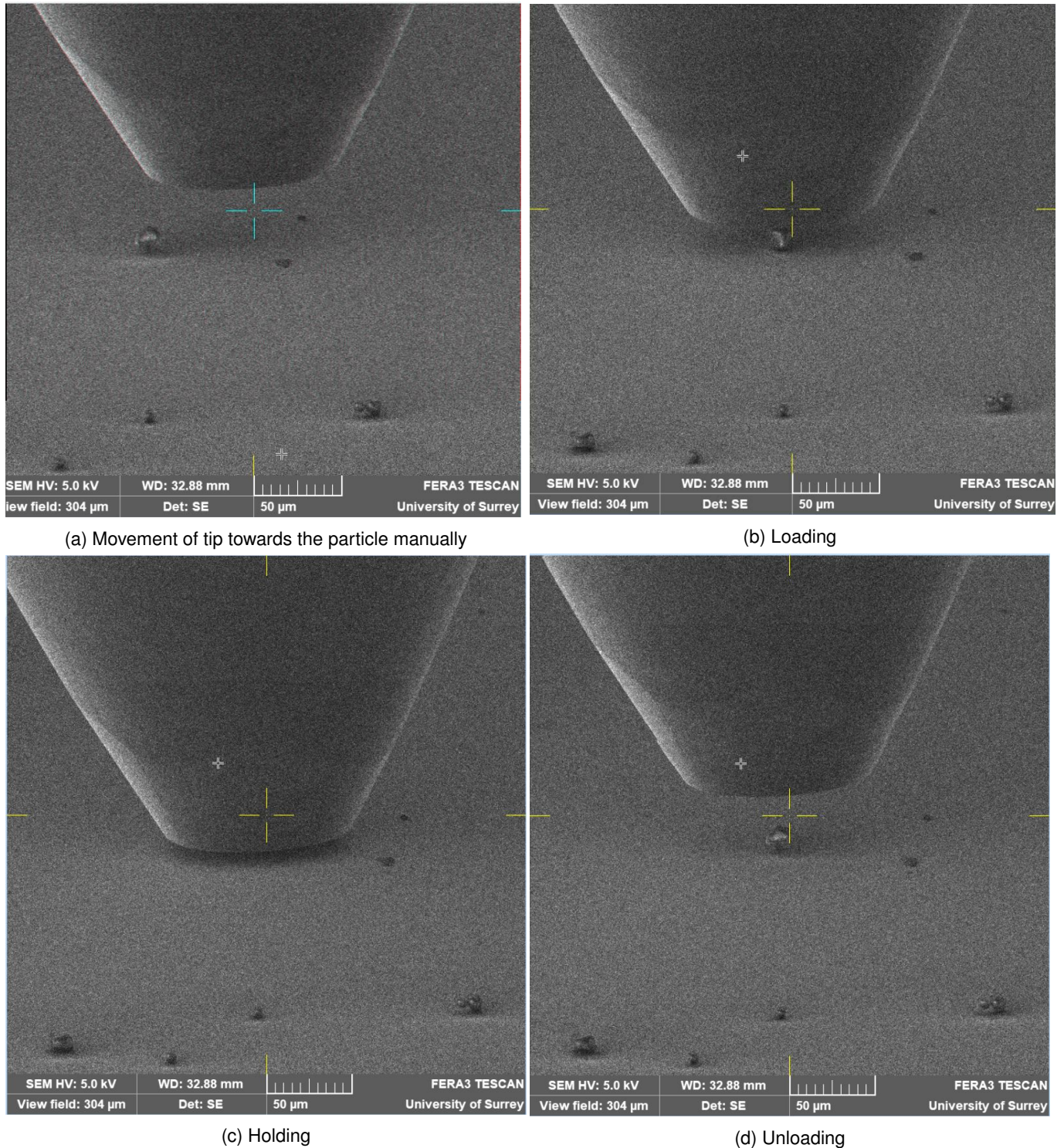


Figure 3.12: SEM imaging during nano-indentation.

Figure 3.15 shows the initial part of the unloading curve. 100 data points are considered to fit a linear model. As we can see the linear model closely matches the experimental data.

Table 3.4 summarizes the parameters obtained by applying the Hertzian and Oliver-Pharr method respectively. The diameter of the particle is obtained by processing the SEM images obtained before indentation, and assumed

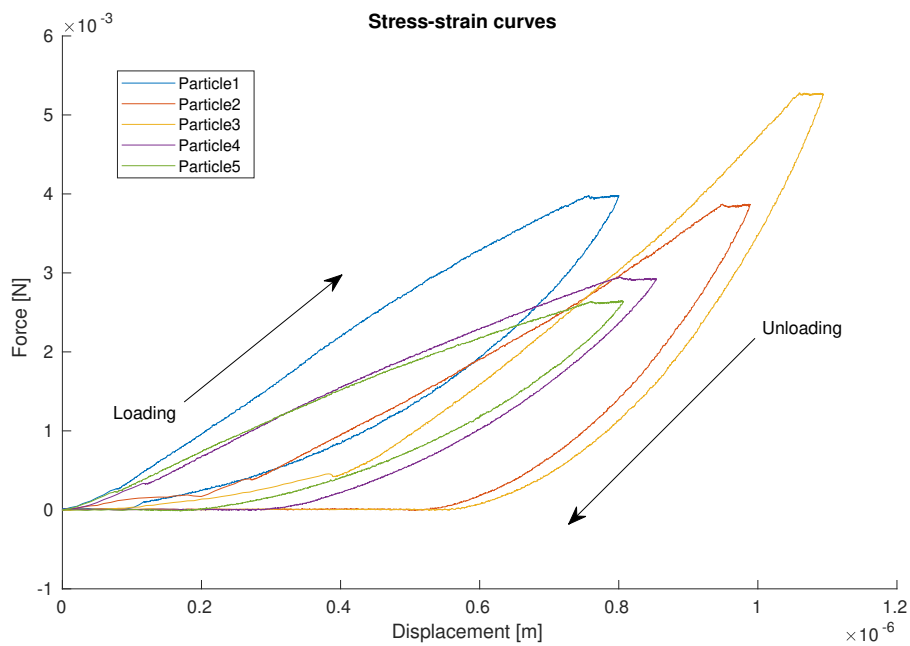


Figure 3.13: Stress-strain curve obtained via nano-indentation.

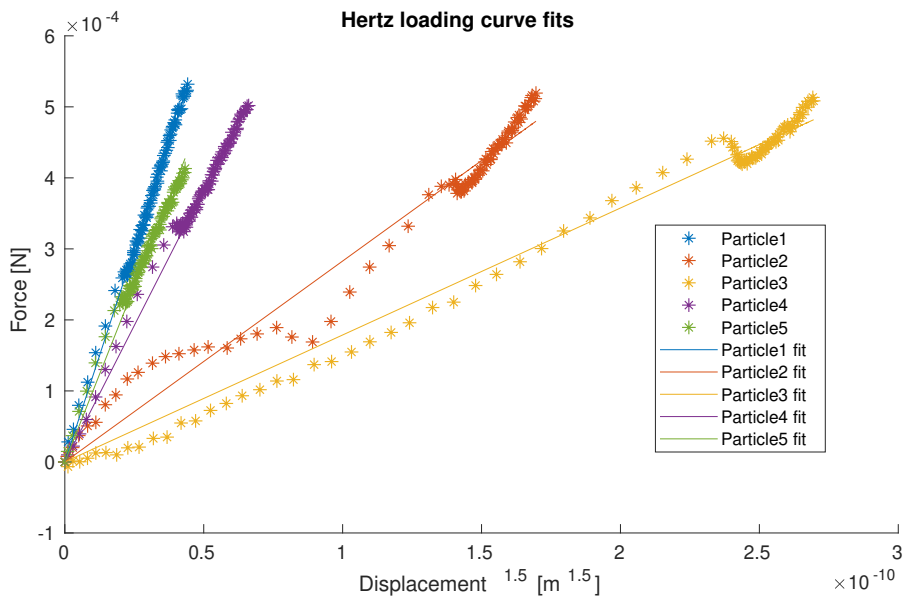


Figure 3.14: Initial portions of the loading curve and Hertzian model fits.

to be equal to the Feret diameter. The analysis resulted in an averaged reduced modulus value of  $2.15 \pm 1.51$  GPa and  $2.95 \pm 0.72$  GPa respectively for Hertz and Oliver-Pharr models. As explained previously, particles 2 and 3 have poor fits with the Hertz model possibly due to asperities on the particle. Excluding these two particles results in an estimate of  $3.16 \pm 0.86$  GPa and  $2.68 \pm 0.82$  GPa respectively for Hertz and Oliver-Pharr models that are coarsely in agreement with each other. Such a comparison between Hertz and Oliver-Pharr is also made by [Joly-Pottuz et al. \[2015\]](#) for alumina nano-particles obtaining same modulus irrespective of the method used for that system. The

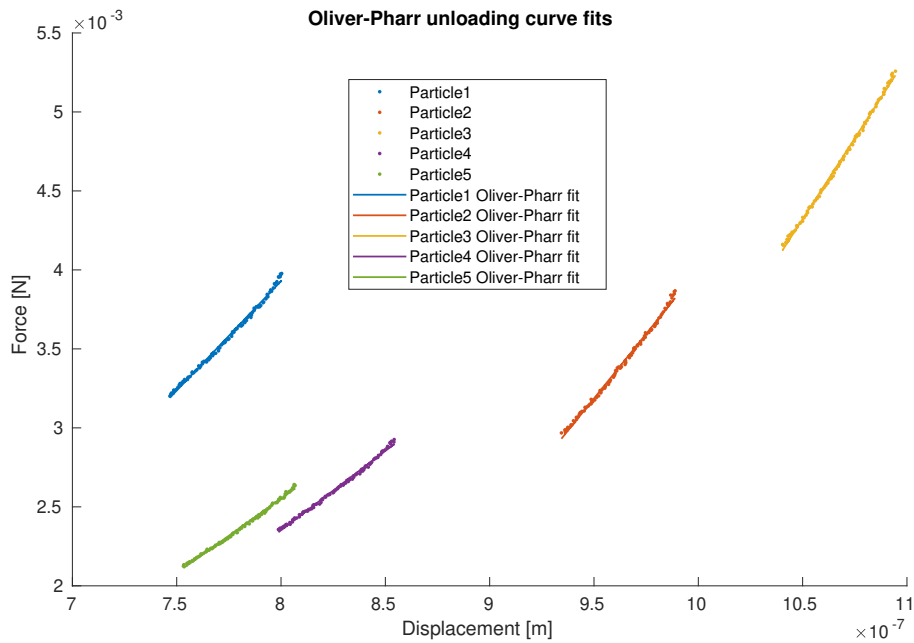


Figure 3.15: Initial portions of the unloading curves and linear fits for applying Oliver-Pharr method.

small difference in Young’s modulus estimates in this work compared to no difference in estimates in works of [Joly-Pottuz et al. \[2015\]](#) can be attributed to two reasons. Firstly their particles were perfectly spherical and secondly, they also had optical techniques to better estimate the contact area between indenter tip and particle  $A_p$ .

		Particle 1	Particle 2	Particle 3	Particle 4	Particle 5
	Diameter [ $\mu\text{m}$ ]	9.50	14.92	14.63	10.68	13.52
Hertzian model	coefficient [ $\text{Nm}^{-1.5}$ ]	$1.20 \times 10^7$	$2.83 \times 10^6$	$1.79 \times 10^6$	$7.68 \times 10^6$	$9.87 \times 10^6$
	fit $R^2$	0.996	0.967	0.990	0.992	0.978
	$E_r$ [GPa]	4.13	0.78	0.50	2.49	2.85
Oliver-Pharr method	Slope [ $\text{Nm}^{-1}$ ]	$1.39 \times 10^4$	$1.63 \times 10^4$	$2.05 \times 10^4$	$1 \times 10^4$	$0.94 \times 10^4$
	Linear model fit $R^2$	0.994	0.996	0.998	0.995	0.995
	$E_r$ [GPa]	3.61	3.05	3.66	2.39	2.05

Table 3.4: Data summary of Hertz and Oliver-Pharr fits to the data.

### 3.2.5 Conclusion

Native un-swollen starch granule material properties are deciphered through nano-indentation. This study resulted in the stress-strain curves during loading and unloading phases. The SEM imaging technique is used to estimate the diameter of the nano-indented particles. Oliver-Pharr method and Hertzian contact mechanics model are applied to the unloading and loading curves to estimate the Young’s modulus of 5 granules. Native starch granule Young’s modulus is estimated to be around  $\approx 3$  GPa which is six orders of magnitude higher than the Young’s modulus of fully swollen starch particles determined in section 3.1 ( $\approx 1.8$  kPa). Such a large variation in material properties as a function of gelatinization has profound implications on the rheology of starch suspensions as will be discussed in chapter 4. Knowledge of evolution of Young’s modulus as function of swelling degree is quintessential for robust and

accurate simulations. Starch granule material property characterization at partial gelatinization degree is challenging owing to multiple reasons principally the heterogeneity associated with the swelling degree of granules for a given time-temperature history. Future work envisaging methods such as microfluidics could aid in characterizing the material properties at the intermediate degree of swelling. Hence, an equation linking swelling degree to material properties such as Young's modulus of starch granules can be deduced which in turn serve as inputs to model rheology of suspensions as discussed in chapter 4.

## Conclusion (version française)

Les propriétés mécaniques des granules d'amidon natif non gélatinisés ont été déterminées par nano-indentation. Cette étude a permis d'établir les courbes de contrainte-déformation pendant les phases de chargement et de déchargement. La technique d'imagerie SEM est utilisée pour estimer le diamètre des particules nano-indentées. La méthode d'Oliver-Pharr et le modèle de mécanique de contact de Hertz sont appliqués aux courbes de déchargement et de chargement pour estimer le module d'Young de 5 granules. Le module d'Young des granules d'amidon natif est estimé à environ  $\approx 3$  GPa, ce qui est six ordres de grandeur plus élevé que le module d'Young des particules d'amidon entièrement gonflées déterminé dans la section 3.1 ( $\approx 1,8$  kPa). Une variation aussi importante des propriétés mécanique au cours de la gélatinisation a des implications profondes sur la rhéologie des suspensions d'amidon, comme nous le verrons au chapitre 4. La caractérisation des propriétés mécaniques des granules d'amidon à un degré de gélatinisation intermédiaire (gélatinisation partielle) est difficile pour de multiples raisons, principalement du fait de l'hétérogénéité associée au degré de gonflement des granules pour un historique temps-température donné. Des travaux futurs envisageant des méthodes telles que la microfluidique pourraient aider à caractériser les propriétés aux degrés intermédiaires de gonflement. Avec de telles données, une équation reliant le degré de gonflement aux propriétés mécaniques telles que le module de Young des granules d'amidon peut être déduite, qui à son tour peut servir d'entrée pour modéliser la rhéologie des suspensions, comme discuté dans le chapitre 4.



## Chapter 4

# DEM simulations of starch suspensions

In this chapter, we use Discrete Element method (DEM) simulations to probe and understand the granule-granule interactions of starch suspensions. This chapter is divided into two sections. In the first section 4.1 swelling on particles in the stationary domain is considered. Hertzian contact model is coupled with swelling model discussed in chapter 2. The jamming indicators and the granule size dispersion is monitored as the swelling proceeds during the temperature treatment of the domain. No lubrication forces are considered in this section as particle-particle contact forces are dominant factors during the jamming transitions. In the second section DEM simulations with periodic boundary conditions are performed to compute the viscosity of a fully swollen starch granule suspension. The lubrication contact model is used to account for the forces on the particles due to squeezing, shearing and pumping of fluid between particles. Hertzian contact model is used to model the repulsive forces when particles come in contact with each other. The granule properties deciphered in chapter 2 & 3 are used for the simulations. In NEMD simulations one imposes a shear rate profile on the system and measure the stress responses. The off-diagonal component ( $\sigma_{xy}$ ) of the stress tensor (proportional to momentum flux) is used to calculate the suspension viscosity. Simulation data are compared with experimentally obtained flow curves. Soft-particle shear-thinning is reproduced and the origin of shear-thinning is attributed to soft particle contacts.

## 4.1 Transient DEM simulation of starch granule suspension undergoing thermal treatment

Arnesh Palanisamy<sup>a</sup>, Artemio Plana-Fattori<sup>a</sup>, Paul Menut<sup>a</sup>, Marco Ramaioli<sup>a</sup>, Denis Flick<sup>a</sup>

<sup>a</sup> Université Paris Saclay, INRAE, AgroParisTech, UMR SayFood, 91300, Massy, France

### Abstract

During hydrothermal treatment of starch suspension, the starch granules swell with kinetics depending on temperature evolution. Variability of swelling characteristics between starch granules was also observed. A semi-mechanistic and semi-stochastic model for individual starch granule swelling was developed and coupled with a discrete element (DEM) model. The DEM model takes into account the normal elastic forces exerted between the granules when they come in contact and optimally occupy the available volume. The evolution of particle volume fractions, size dispersion, the fraction of overlap volume and elastic energy per unit volume were analysed in the case of chemically modified waxy maize starch. It appears that for this particular starch all the jamming indicators increase rapidly for a volume fraction of about 65%

*Keywords:* Discrete Element Modeling(DEM); Starch Granule; Starch swelling; Gelatinization; MATLAB

This article was published in the conference proceedings of *Foodsim 2020*

## Simulation DEM transitoire d'une suspension de granules d'amidon subissant un traitement thermique

Arnesh Palanisamy<sup>a</sup>, Artemio Plana-Fattori<sup>a</sup>, Paul Menut<sup>a</sup>, Marco Ramaioli<sup>a</sup>, Denis Flick<sup>a</sup>

<sup>a</sup> Université Paris Saclay, INRAE, AgroParisTech, UMR SayFood, 91300, Massy, France

### Résumé

Lors du traitement hydrothermal d'une suspension d'amidon, les granules d'amidon gonflent avec une cinétique qui est fonction de l'évolution de la température. Une variabilité de cette cinétique a été observée entre granules. Un modèle semi-mécanistique comportant une part stochastique a été développé pour prédire le gonflement individuel des granules d'amidon. Il a été couplé à un modèle d'interactions entre particules par la méthode des éléments discrets (DEM). Le modèle DEM prend en compte les forces élastiques normales exercées entre les granules lorsqu'ils entrent en contact et occupent de manière optimale le volume disponible. Les évolutions de la fraction volumique occupée par les particules, de la dispersion granulométrique, du chevauchement entre particules et de l'énergie élastique par unité de volume ont été analysées dans le cas d'un amidon de maïs cireux chimiquement modifié. Il apparaît que pour cet amidon particulier tous les indicateurs d'encombrement augmentent rapidement pour une fraction volumique d'environ 65%.

*Mots clés:* Modélisation par éléments discrets(DEM); Granule d'amidon; Gonflement de l'amidon; Gélatinisation; MATLAB

### 4.1.1 Introduction

Starch is predominant food reserve in plant and provides for 70-80% of calories consumed by humans worldwide from various sources (Bertolini 2009). Hence it has been a perennial subject of research for decades. Starch undergoes the process known as gelatinization when heated in the presence of water. Gelatinization is the process in which starch granules undergo an irreversible chemical transformation when subjected to thermomechanical treatment in the presence of water. Starch granules are semi-crystalline with concentric rings of crystalline and amorphous phases (Ratnayake and Jackson 2008). Gelatinization on the microscopic scale corresponds to melting of crystallites, loss of birefringence, increase in size (swelling), leaching of amylose into the continuous phase and sometimes rupture of the granular structure (Atwell 1988; Biliarderis 1992). Starch majorly consists of amylose and amylopectin. The composition of these two polymers with alpha glucose as a monomer, vary according to the source of starch. This, in turn, has consequences on the physical properties and gelatinization behaviour of starch (Banks et al. 1974; Hoover 2001; Srichuwong et al. 2005; Visser et al. 1997). The expected range for these transitions is between 60 and 70 °C (Slade and Levine, 1995). The evolution of viscosity during gelatinization is also influenced by the process parameters such as concentration, shear rate, thermal history, pH and presence of other ingredients (Thomas and Atwell 1999). For high amylopectin cereal starches such as waxy maize starch, the granules tend to hydrate with ease, swell rapidly and rupture to a great extent which results in loss of paste viscosity. The rupture of the granules can be avoided by chemically modifying the starch. This involves the introduction of functional groups into the starch molecules, resulting in markedly altered physicochemical properties (Ashogbon and Akintayo 2014). Waxy maize starch is used in a wide variety of applications in the food industry owing to its stability (Tattiyakul and Rao 2000)

During gelatinization, the starch granules undergo swelling and viscosity of the suspension increases multi-fold. Thus it is important to understand this phenomenon both in terms of process equipment design perspective as well as novel product development. Hence, over the years researchers have been modelling starch gelatinization and swelling as kinetic phenomena with various rate equations with respect to metrics such as the median diameter of the granule population. These models ranged from simple first-order rate equation to Nth order, Diffusional, Phase boundary and Avrami-Erofeev type rate equations (Kubota et al. 1979; Okechukwu and Rao 1995; Lagarrigue et al. 2008; Krüger et al. 2003 and Malumba et al. 2013). These were all at the population scale, recently we (preprint submitted to Food structure) suggested first-order reaction kinetics at the granule scale with a random delay time.

One functional property of gelatinized starch is the texture improvement by increasing apparent viscosity. A starch suspension can be postulated as a non-colloidal suspension of soft (elastic) spheres. The apparent viscosity of such a suspension depends on the ratio between the actual volume fraction of particles and its maximum value ( $\phi_{rcp}$ ) also called random close packing density. Farr et al. (2009) proposed a novel algorithm to determine  $\phi_{rcp}$  for a suspension of polydisperse spheres. They presented a simple but accurate approximation for the random close packing density of hard spheres of any size distribution based upon a mapping onto a one-dimensional problem. To validate the same, they carried out extensive simulations for mixtures of elastic spheres with hydrodynamic friction. In subsequent work, Farr (2013) compared the algorithm with slower direct numeric simulations and showed good agreement between them. Various algorithms exist for such direct numerical simulations and chief among them is

Lubachevski-Stillinger (1990) algorithm in which spheres at a low volume fraction are placed in a box with periodic boundary conditions by random sequential addition. The particles are randomised with initial velocities and their radius are increased proportionally to initial radius. This algorithm takes into account three input parameters: the number of spheres, the initial volume fraction  $\phi_{\text{init}}$  and the ratio  $\delta$  of the radial growth. A similar algorithm is used in this work for DEM simulations, however, the rate of increase of radius is governed by the swelling kinetics for a specific type of chemically modified maize starch.

## 4.1.2 Methods

### Swelling model

We have described the granules swelling kinetics at the individual granule scale using a semi-mechanistic model in a separate work under review for publishing in food structure journal. According to microscopy observation of modified waxy maize starch granules during heating in the presence of water, variability in swelling kinetics from granule to granule was observed. Each granule has a specific delay time associated with the onset of swelling. Also, the granules which begin to swell at later instant tend to swell slower compared to the granules which begin to swell earlier for a given time-temperature profile. No swelling was observed below  $T_{\text{min}} = 60^\circ\text{C}$ . The higher the temperature, the lower the delay time and the faster the diameter increases. These phenomena were cast mathematically as below. The reader is advised to refer the pre-print submitted by us to food structure for further details regarding the same. The earlier work describes in detail the Kinetic model for swelling of individual starch granules in a suspension. In this work, we make use of the already developed kinetic model and couple it with the DEM model for prediction of suspension material properties such as volume fraction. In the subsequent future works, one would like to simulate and predict the transient rheology such complex fluids for better design and operation of industrial-scale food processing equipment. However, in the interest of the readers and completeness, we touch briefly on the concepts and terms of the kinetic model we make use of in the present work.

A parameter called "difficulty of swelling"  $\alpha \in [0, 1]$  was introduced. For a granule,  $\alpha$  is selected at random from a uniform distribution.

For a constant temperature, for example,  $T_{\text{ref}} = 62^\circ\text{C}$ , the onset delay time follows an exponential distribution

$$\ln(1 - \alpha) = -\frac{t_{\text{onset}}}{\tau_{\text{ref}}} \quad (4.1)$$

where  $\tau_{\text{ref}}$  is the characteristic latency time at  $T_{\text{ref}}$ . For variable temperature, the time delay in onset of swelling  $t_{\text{onset}}$  is given by solving equation 4.1.

$$\ln(1 - \alpha) = -\int_0^{t_{\text{onset}}} \frac{1}{\tau} dt \quad (4.2)$$

$$\tau = \max\left(0, \left(\frac{T_{\text{ref}} - T_{\text{min}}}{T - T_{\text{min}}}\right)\right) \tau_{\text{ref}} \quad (4.3)$$

Non dimensional diameter  $S$  is given by the equation 4.4.

$$S(t) = \frac{D(t) - D_i}{D_f - D_i} \quad (4.4)$$

The reaction kinetics is given by equation 4.5 after the time delay  $t_{\text{onset}}$  is overcome.

$$\frac{dS}{dt} = K(1 - S) \quad (4.5)$$

$$K = K_{\text{ref}}(1 - \alpha)^{0.5} \left( \frac{T - T_{\text{min}}}{T_{\text{ref}} - T_{\text{min}}} \right)^2 \quad (4.6)$$

where  $K_{\text{ref}}$  is the rate constant at  $T_{\text{ref}}$  for a granule which has no difficulty to swell ( $\alpha = 0$ ).

For the chemically modified maize starch that was studied the following parameter values were estimated;  $\tau_{\text{ref}} = 190\text{s}$ , and  $K_{\text{ref}} = 0.0023\text{s}^{-1}$ . From the above set of equations, one can describe the swelling kinetics of this starch. The same has been used for the DEM simulations in this work. The following assumptions regarding the starch granules population were made. Initial diameters and swelling ratio are from a random normal distribution.

$$D_i \subset \mathcal{N}(14.77 \mu\text{m}, 4.44 \mu\text{m}),$$

$$D_f/D_i \subset \mathcal{N}(2.34, 0.33),$$

### DEM model

For Discrete Element Modelling of the starch granules during swelling, the following assumptions are made.

- All the granules are spherical and have the same Young's modulus.
- No tangential forces are considered.
- No gravity force on the particles are considered.
- The particles are considered Non-Brownian.
- No Lubrication forces are considered.
- Periodic boundary conditions are applied.

To determine a realistic initial state(position and radius) of a total number  $I$  of unswollen granules in a cubic box, a stepwise Monte-Carlo procedure was applied:

- For the granule of index  $i$  (among  $I$ ),  $\alpha$  is chosen as  $\alpha_i = (i - 1/2)/I$  (uniform distribution).
- Similarly  $D_0$  and  $D_f/D_0$  are randomly chosen from  $\mathcal{N}(14.77 \mu\text{m}, 4.44 \mu\text{m})$  and  $\mathcal{N}(2.34, 0.33)$ .
- Then the location of the granule in the simulations box is determined by choosing randomly  $x, y$  and  $z$  coordinates. If there is an overlap with the previously placed granule, a new location is proposed for granule  $i$ . This approach is guaranteed to work as initially the volume occupied by the granules is low compared to the total volume of the box and hence granule insertion in the cubic domain is fairly straightforward by this trial and error method.

Such an approach has been already been used by Luding and Bauer [2010] to model particle swelling and evolution of pressure during swelling for various particle properties.

After deposition of the required number of granules inside the simulation box, The transient swelling of granules is undertaken. At this instant where transient swelling is undertaken is the initial time  $t = 0$  seconds. For every granule, if the criteria of time delay in onset are met, then new radii are calculated using the kinetics of swelling as per equation 4.5 and 4.6.

The normal Hertzian force due to overlap of the spherical granules is calculated based on the following equations (Di Renzo and Di Maio 2005)

$$F_n = -\frac{4}{3}E^* \sqrt{R_{12}}(\delta_n)^{1.5} \quad (4.7)$$

$$E^* = \frac{E}{1 - \nu^2} \quad (4.8)$$

$$R_{12} = \frac{R_1 R_2}{R_1 + R_2} \quad (4.9)$$

Here,  $E$  and  $\nu$  are the young's modulus and Poisson's ratio of granules respectively.  $R_1$  and  $R_2$  correspond to radii of granules 1 and 2 respectively. Also,  $\delta_n$  is the overlap distance between the two spheres.

Thus, new particle positions are calculated based on timestep using Newton's equations of motion. Each particle radius is increased at every time step according to equations 4.5 and 4.6. As particles grow and overlap the normal force due to overlap is calculated and repulsive force begins to originate between particles. The coordinates of the particles are updated after calculation of this repulsive force due to overlap. The particles move away from each other and the force exists until the overlap exists. The time step for DEM simulations was  $10ms$ . The timescales of the swelling are much lower compared to the timescales of force resolution, this ensures that particles do not overlap excessively causing the particles to experience large forces. For each particle, a list of neighbour lists is maintained, whose centres are within cut off distance. The contacts are searched for within these neighbour particles to reduce the computational time. The neighbour lists are updated periodically. The contacts are deemed to be active when the distance between two-particle centres is less than the sum of their radii.

### 4.1.3 Results

The simulation was performed for a single ramp rate of  $5^\circ C/min$  from  $60^\circ C$  to  $80^\circ C$  in 4 minutes. The overall computation time required for the entire simulation was about 2 hours on a single core work station. The entire program was scripted in MATLAB. Figure 4.1 shows the granules contours at a cross-section of the simulation box. The dotted lines represent the actual granule diameter and continuous lines are the intersection of the granule with the cross-section plane. The cross at the centre of the granule indicates that the granule is yet to swell and dotted lines take over when the granule starts to swell. The notation for the same is to mimic the Maltese cross observed on the un-swollen starch granules when observed through polarised light under a microscope and the disappearance of the same when swollen. This phenomenon is called the loss of birefringence during gelatinization. For the simulation 200 granules(l) were inserted in a cubic box of length 0.2 mm. The initial volume fraction  $\phi_0 = 5.1\%$

(when  $S = 0$  for all the granules) and  $\phi_{\max} = 71.5\%$  at the end of 4 minutes of simulation (when mean value of  $S = 0.983$ , signifying almost complete swelling). The Young's modulus was taken as 10000 Pa for unswollen as well as for swollen granules. Parallel experimental work is underway to estimate this parameter more precisely.

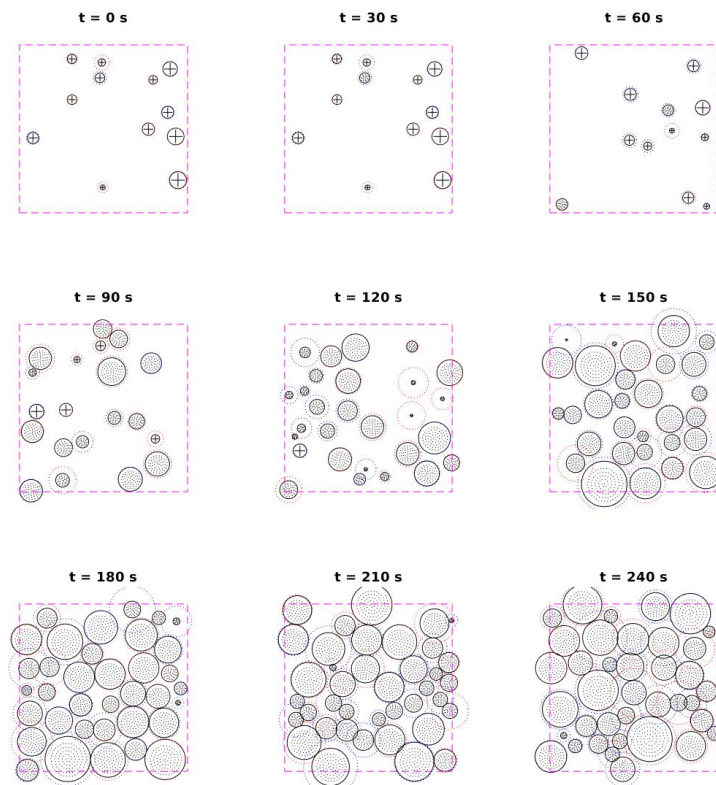
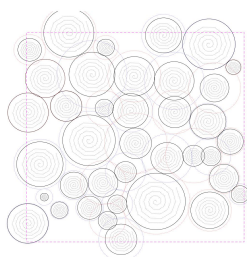
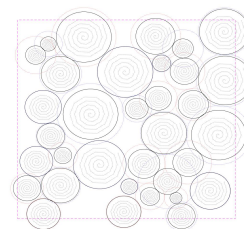


Figure 4.1: Granules contours at every 30 seconds



(a) Run 1 completely swollen state



(b) Run 2 completely swollen state

Figure 4.2: Contour comparison of different runs

Figure 4.1 shows the cross-section of the box every 30 seconds. We observe that at the initial instances when the granules are yet to swell there is the low volume fraction of granules and subsequently there is no movement of the grains as there are no forces acting (no gravity, no Brownian agitation, zero initial velocity). However, at the later

instances when the granules come in contact with each other and Hertzian interaction forces act, the granules push each other and move freely in the system such that Hertzian interaction energy remains close to zero. This is quite notable for times between 90 seconds and 150 seconds. At later instances when granule volume fraction reaches close to  $\phi_{rcp}$  the granules cannot move freely but they reorient optimally to minimize the energy in the system. Since the insertion of particles and the swelling characteristics are random we compare the contours of two different runs at the fully swollen state in Figure 4.2.

In Figure 4.3 we can see the time evolution of different parameters. Temperature is linearly increased from 60 °C to 80 °C as depicted in figure 4.3a. In figure 4.3b we see the total number of granules which began to swell plotted as a function of time. Note that the total number of granules used for the simulation is 200 and all begin to swell after 200 seconds. In figure 4.3c, we see the mean radius of the starch granule population evolving with time. In figure 4.3d, we see the volume fraction of granules increase with time as the granules are swelling. The mean radius is increased by a factor of 2.34 the volume of the granules rises by a factor of 12.8. Figure 4.3e depicts the size dispersion among the granule population. Since there is variability in the onset of swelling initially the dispersion increases as some granules begin to swell and the ratio of largest granule to smallest granule increases, but as time progresses other granules also catch up as they begin to swell and hence the dispersion decreases. However, the final dispersion is higher than the initial level as the ratio of swelling is also random and as expected the variability is higher after swelling compared to initial unswollen granules.

In figure 4.4 we have the ratio of volume overlap and Hertzian interaction energy in the function of time(left) and volume fraction of the granules(right). We calculated  $\phi_{rcp}$  based on the chart provided by [Farr and Groot \[2009\]](#). for the starch granule population at the end of the simulation( $t=4\text{min}$ , mean value of  $S = 0.983$ ). The same has been overlayed in the plots to compare with the DEM simulations.

Interestingly since the starch granules are soft spheres the increase in interaction energy is slower compared to hard spheres and hence the algorithm proposed by [Farr and Groot \[2009\]](#) which predicts the  $\phi_{rcp}$  for hard poly-disperse spheres gives a lower value compared to the DEM simulations reported in this work. Through these simulations, we can study the dynamic evolution of particle and bulk properties of the system during the swelling of the chemically modified starch granules.

#### 4.1.4 Conclusion

In this study, we have demonstrated the modelling of starch granule suspension evolution during gelatinization using DEM. The earlier developed kinetic model for individual starch granule swelling was coupled to the DEM model resulting in the transient DEM simulation of the suspension. This is particularly interesting as the macro scale properties such as volume fraction are obtained by modelling the granule level details. Using this approach one can get the size evolution as a function of time and also the interaction parameters such as elastic Hertzian energy as a function of time. From this study, we see that since the granules are soft spheres the increase in jamming indicators occur at a volume fractions greater than the prediction based on an analytical solution for hard spheres. This is of physical significance since a multi-fold increase in suspension viscosity occurs near this jamming transition. Thus, having an accurate prediction of such phenomena is critical for the process of equipment design

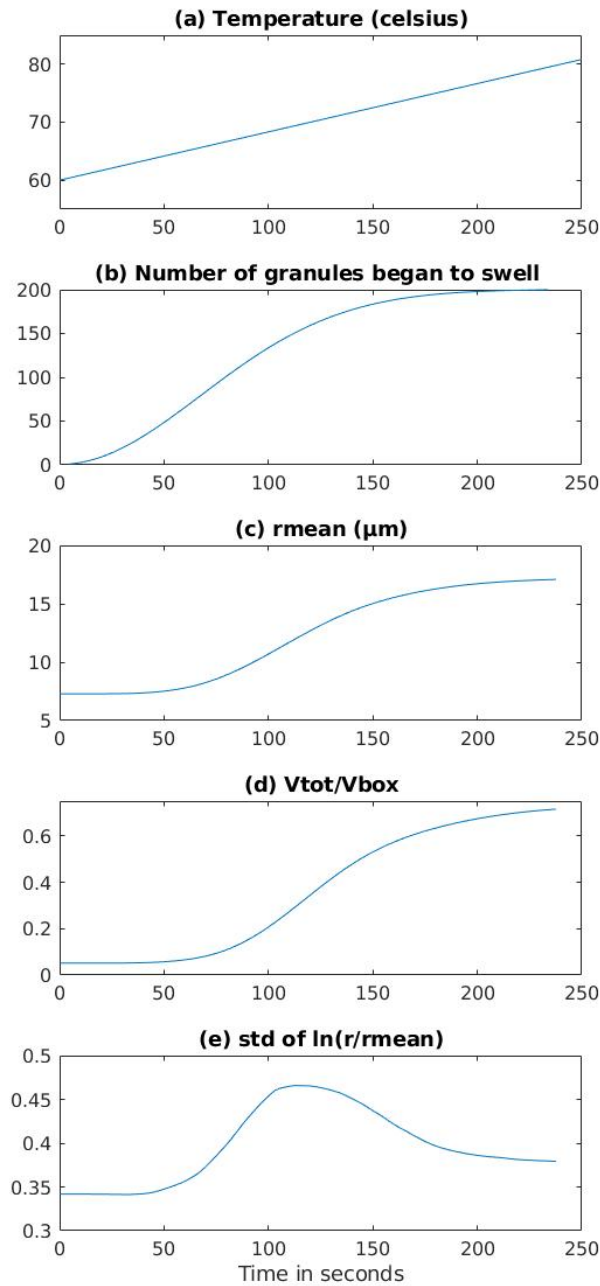


Figure 4.3: Time evolutions of parameters

and optimal operation. Going forward in the future works, one should be in principle able to predict the rheology of such complex material. Transient DEM with evolving particulate sizes and properties could also be coupled with computational fluid dynamics using multiscale modelling approaches to study flow, heat transfer and starch-based product transportation inside heat-treatment equipment.

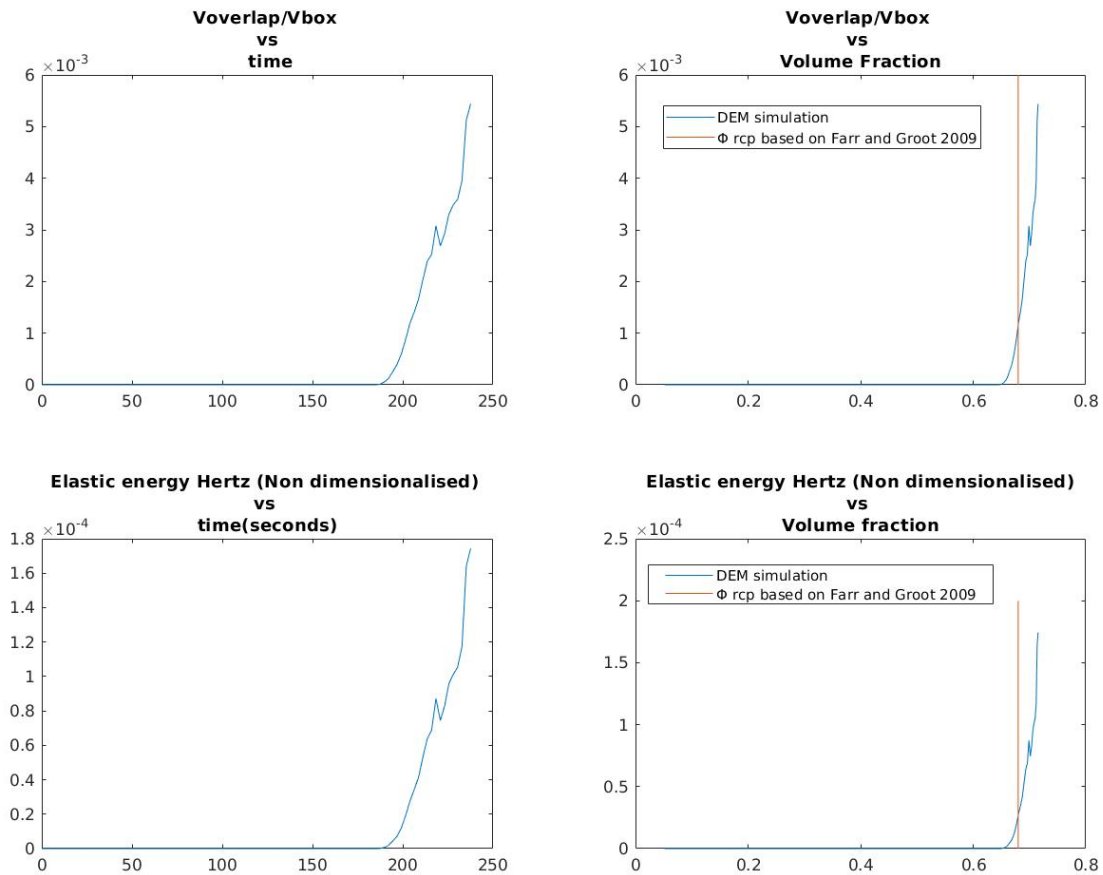


Figure 4.4: Interactions energy vs volume fraction

#### 4.1.5 Future work

- Estimate experimentally Young's modulus vs gelatinization degree which is characterized by parameter  $S$ . Incorporate the same in the model.
- Include tangential forces, lubrication forces and other effects as deemed necessary.
- Study the influence of the box size on the results.
- Perform shear flow simulations for the same system and capture the viscosity evolution of the suspension.

#### Acknowledgements

This research has been carried out with funding from European Union as part of EU RESEARCH FRAMEWORK PROGRAMME: H2020 / Marie Skłodowska-Curie Actions ITN [813202].

## Conclusion (version française)

Dans cette étude, nous avons modélisé l'évolution d'une suspension de granules d'amidon au cours de la gélatinisation à l'aide de la méthode des éléments discrets (DEM). Le modèle cinétique développé précédemment pour le gonflement individuel des granules d'amidon a été couplé à un modèle DEM, ce qui a permis une simulation transitoire d'une suspension d'amidon en cours de chauffage. Ceci permet d'obtenir l'évolution de propriétés à l'échelle macroscopique à partir des mécanismes ayant lieu à l'échelle des granules. En utilisant cette approche, on peut ainsi obtenir l'évolution de la distribution de tailles ainsi que les paramètres d'interaction tels que l'énergie hertzienne élastique en fonction du temps. L'étude montre que puisque les granules sont des sphères molles, l'augmentation des indicateurs d'encombrement se produit à des fractions volumiques supérieures à la prédiction basée sur une solution analytique pour des sphères dures. Ceci est d'une importance pratique puisqu'une augmentation très forte de la viscosité de la suspension se produit lorsque la fraction volumique se rapproche de la valeur critique de blocage. Ainsi, avoir une prédiction précise de tels phénomènes est essentiel pour la conception et le fonctionnement optimal d'équipement de traitement thermique de produits contenant de l'amidon. Des travaux futurs devraient permettre de prédire par ce type d'approche (DEM) la rhéologie de suspensions d'amidon. Le couplage avec de la mécanique des fluides numérique (CFD) est également envisageable pour développer des simulations multi-échelles plus réalistes des phénomènes ayant lieu au sein des équipements.

## 4.2 Shear flow DEM simulations of fully swollen starch granule suspension

### Abstract

In this section, the simple shear flow of a starch suspension is simulated using the Discrete Element Method (DEM), taking into account direct particle-particle contacts and short-range hydrodynamic lubrication forces. This class of simulations are called Non-Equilibrium molecular dynamics simulations with periodic boundary conditions. The resulting stress responses matrix is used to compute the viscosity of the suspension. In these simulations, the implicit assumption regarding the continuous phase is that the fluid velocity gradient is linear and equal to the domain deformation rate. This fluid velocity is used to calculate the Stokes forces on particles. The granule properties such as population size distribution, Young's modulus, Poisson's ratio of fully swollen starch granules is obtained from the studies of chapter 2 and chapter 3. Suspension viscosity predictions from simulations and experiments are compared. Both simulations and experiments show shear-thinning beyond a critical volume fraction and shear rate. Simulations show that shear-thinning could be attributed to the soft particles contacts. It is also shown through experiments that a critical shear-stress is required for the onset of soft particle contacts in the suspension.

*Keywords:* Starch granule; Discrete element method(DEM); Suspension Viscosity; Rheometry, Soft-particle.

## **Simulations DEM du flux de cisaillement d'une suspension de granules d'amidon entièrement gonflés**

### **Résumé**

Dans cette section, l'écoulement de cisaillement simple d'une suspension d'amidon est simulé à l'aide de la méthode des éléments discrets (DEM), en tenant compte des contacts directs entre particules et des forces de lubrification hydrodynamiques à courte portée. Cette catégorie de simulations est appelée simulations de dynamique moléculaire hors équilibre avec des conditions limites périodiques. La matrice des réponses aux contraintes qui en résulte est utilisée pour calculer la viscosité de la suspension. Dans ces simulations, l'hypothèse implicite concernant la phase continue est que le gradient de vitesse du fluide est linéaire et égal à la vitesse de déformation du domaine. Cette vitesse du fluide est utilisée pour calculer les forces de Stokes sur les particules. Les propriétés des granules telles que la distribution de la taille de la population, le module de Young, le coefficient de Poisson des granules d'amidon complètement gonflés sont obtenues à partir des études des chapitres 2 et 3. Les prédictions de la viscosité de la suspension à partir des simulations et des expériences sont comparées. Les simulations et les expériences montrent un comportement rhéo-fluidifiant au-delà d'une contrainte critique. Les simulations montrent que l'amincissement par cisaillement pourrait être attribué aux contacts mous des particules.

*Mots clés:* Granule d'amidon ; Méthode des éléments discrets (DEM) ; Viscosité de la suspension ; Rhéométrie, Particules molles.

### 4.2.1 Introduction.

Discrete element method [Cundall and Strack, 1979] simulations are carried out using particle simulation package LIGGGHTS [Kloss and Goniva, 2011], an open-source package developed based on LAMMPS [Plimpton, 1995] adapted to simulating granular materials. DEM is a particle-based method in which Newton's equations of motion for each particle are solved with a predetermined timestep. The positions, velocities and forces of all particles are tracked over a period of time. Various algorithms exist for numerically integrating Newton's equations which can be broadly classified into (i) one step algorithms, (ii) Multi-step algorithms, (iii) Predictor–corrector algorithms [Kruggel-Emden et al., 2008]. In this study, the Velocity-Verlet algorithm is used which is a one-step algorithm. This algorithm provides a numerical solution to the following second-order equation.

$$m \frac{d^2 x_i}{dt^2} = F_i \quad (4.10a)$$

$$m \frac{d\omega_i}{dt} = \Gamma_i \quad (4.10b)$$

where  $x_i$  is the position of particle  $i$ ,  $\omega_i$  is the angular velocity of particle  $i$ ,  $m$  is the mass of the particle subjected to a total force  $F_i$  and total torque  $\Gamma_i$  across a time period  $dt$ . The total force acting on the particle at a given instant is the sum of direct particle/particle forces (contact), indirect particle/particle forces via the fluid (lubrication), fluid/particle Stokes forces (drag) and body forces such as gravity. Contact models are the definitions ingrained in the code to define deterministically the way particles interact when they are in close proximity to another particle or walls. Standard techniques based on Rayleigh timestep are used to determine the maximum cut off timestep [O'Sullivan and Bray, 2004]. Equations 4.10a and 4.10b represent a system of  $6N$  equations where  $N$  is the number of particles.  $3N$  equations for force balance in the 3 dimensions and  $3N$  equations for balancing the torque in 3 dimensions. The particle sizes as discussed in chapter 2 is roughly in the range of 10 to 60  $\mu\text{m}$ . The highest studied shear rate is  $100 \text{ s}^{-1}$ . The Reynolds number ( $Re = \rho_f R^2 \dot{\gamma} / \mu_f$ ) for  $\dot{\gamma} = 100 \text{ s}^{-1}$  and such a size range results in  $\approx O(10^{-1} - 10^{-3})$ . This shows that particle inertia is not dominant for such a system. Here,  $R$  is the radius of the particle,  $\rho_f$  is the mass density of the fluid,  $\dot{\gamma}$  is the shear rate imposed on the suspension and  $\mu_f$  is the viscosity of the suspending Newtonian fluid.

The equations could be rewritten in the matrix form as follows. Here, we split the contributions to force ( $F_{total}$ ), torque ( $\Gamma_{total}$ ) and stresslet ( $G_{total}$ ) as arising due to contacts and hydrodynamics. Stresslet is a function that represents the symmetric first moment of the surface stress of a body in a flowing fluid.

$$\begin{bmatrix} F_{total} \\ \Gamma_{total} \\ G_{total} \end{bmatrix} = \begin{bmatrix} F_H \\ \Gamma_H \\ G_H \end{bmatrix} + \begin{bmatrix} F_c \\ \Gamma_C \\ 0 \end{bmatrix} \quad (4.11)$$

Further, hydrodynamic interactions could be split into Stokes forces and lubrication forces. The models used for these simulations are Hertzian for contact and near-field approximation of lubrication with fast lubrication dynamics popularly known as Ball-Melrose-Kumar model [Ball and Melrose, 1997, Kumar and Higdon, 2010]. The

Ball-Melrose-Kumar approximation is computationally less intensive compared to solving for the actual Stokes equations. Hertzian contact model is available in the standard release of LIGGGHTS. Fast lubrication dynamics corresponds to the Stokes forces and the near-field approximations of pairwise lubrication interactions between particles immersed in a fluid. Lubrication model files are written as per their implementation in the LAMMPS release. The governing equation of the Hertzian model is as follows

$$F_{n,Hertz} = k_n \delta_n n_{ij} \quad (4.12)$$

where,  $\delta_n = c_{ij} - R_1 - R_2$  is the overlap distance between two contacting particles

$c_{ij}$  is the centre to centre distance of particle i and j,

$$k_n = \frac{4}{3} Y^* \sqrt{R^* \delta_n},$$

$n_{ij}$  is the unit vector connecting the centre of particle 1 to centre of particle 2,

$Y^*$  is the reduced Young's modulus given by  $\frac{1}{Y^*} = \frac{1-\nu_1^2}{Y_1} + \frac{1-\nu_2^2}{Y_2}$  and

$R^*$  is the radius of curvature of the contact given by  $\frac{1}{R^*} = \frac{1}{R_1} + \frac{1}{R_2}$

The force in the normal direction is given by equation 4.12. Here,  $R_1, R_2, \nu_1, \nu_2, Y_1$  and  $Y_2$  are the radius, Poisson's ratio and Young's modulus of the colliding particles, respectively. The dissipation component in the Hertzian model is neglected here as, in the case of suspensions, the primary mode of dissipation is due to lubrication and Stokes forces [Ness and Sun \[2016\]](#). Similarly, the tangential component of the Hertz contact model is given by equation 4.13

$$F_{t,Hertz} = \min(k_t \delta_t t_{ij}, \mu_p F_{n,Hertz}) \quad (4.13)$$

where,  $\delta_t$  is the tangential overlap and is calculated via a summation of the relative tangential motion during the whole contact.

$t_{ij}$  is the unit vector in the tangential direction.

$$k_t = 8G^* \sqrt{R^* \delta_n},$$

$\mu_p$  is the Coulomb friction coefficient.

$G^*$  is the reduced shear modulus given by  $\frac{1}{G^*} = \frac{2(2-\nu_1)(1+\nu_1)}{Y_1} + \frac{2(2-\nu_2)(1+\nu_2)}{Y_2}$

Since water is a Newtonian fluid with a constant viscosity  $\mu_f$ , the velocity field imposed on the fluid can be written as follows

$$U^\infty(r) = \omega^\infty \times r + E^\infty \cdot r \quad (4.14)$$

Where,  $\omega^\infty$  is the angular velocity vector

$E^\infty$  is the rate of strain tensor.

For simple shear flows in xy direction with a shear rate  $\dot{\gamma}$ , we have

$$\omega^\infty = \begin{bmatrix} 0 \\ 0 \\ -\frac{\dot{\gamma}}{2} \end{bmatrix} \quad (4.15)$$

$$E^\infty = \begin{bmatrix} 0 & \frac{\dot{\gamma}}{2} & 0 \\ \frac{\dot{\gamma}}{2} & 0 & 0 \\ 0 & 0 & 0 \end{bmatrix} \quad (4.16)$$

Thus, we could write the force( $F$ ), torque( $\Gamma$ ) and stresslet( $G$ ) terms due to hydrodynamics in the matrix force with the grand resistance matrix as follows.

$$\begin{bmatrix} F_H \\ \Gamma_H \\ G_H \end{bmatrix} = -(R^{Stokes} + R^{lub}) \cdot \begin{bmatrix} U - U^\infty \\ \omega - \omega^\infty \\ -E^\infty \end{bmatrix} \quad (4.17)$$

Here,  $R^{Stokes}$  is the diagonal matrix giving Stokes drag forces and torques.  $R^{lub}$  is a sparse matrix giving near-field lubrication interactions. The Stokes forces are implemented using the Fast-Lubrication Dynamics approximation as described in Kumar and Higdon [2010]. The elements of the resistance matrix  $R^{lub}$ , consists of various pairwise interaction parameters which depend on the inter-particle gap and radius ratios of the interacting particles. We follow the approach of Mari et al. [2014] and only consider the squeeze, shear and pump modes of Ball-Melrose-Kumar [Ball and Melrose, 1997, Kumar and Higdon, 2010] and neglect the twist mode of interactions. Illustration 4.5 represents pictographically the different modes of hydrodynamic interactions between two-suspended particles in a fluid. In the next paragraphs, the lubrication model terms are further described in detail.

The normal and tangential pair-wise lubrication interactions force [Kim and Karrila, 2013, Ball and Melrose, 1997] are given by the following equations.

$$F_{Lubrication} = -a_{sq}6\pi\mu_f(v_i - v_j) \cdot n_{ij}n_{ij} - a_{sh}6\pi\mu_f(v_i - v_j) \cdot (I - n_{ij}n_{ij}) \quad (4.18)$$

$$\Gamma_{Lubrication} = -a_{pu}\pi\mu_f(R_1 + R_2)^3(\omega_i - \omega_j) \cdot (I - n_{ij}n_{ij}) - \frac{R_1 + R_2}{2}(n_{ij} \times F_{Lubrication}) \quad (4.19)$$

Here, coefficients  $a_{sq}, a_{sh}$  and  $a_{pu}$  corresponds to squeeze, shear and pump pair-wise resistance terms due to the fluid between the particles. These different motions could be visualized as shown in the illustration 4.5.

Analytical solutions for  $a_{sq}, a_{sh}$  and  $a_{pu}$  for spherical particles in the vicinity are used as derived in [Kim and Karrila, 2013].

$$a_{sq} = \frac{\beta^2}{(1 + \beta)^2} \frac{(R_1 + R_2)}{2} \frac{(R_1 + R_2)}{2h} + \frac{1 + 7\beta + \beta^2}{5(1 + \beta)^3} \frac{(R_1 + R_2)}{2} \ln\left(\frac{R_1 + R_2}{2h}\right) + \frac{1 + 18\beta - 29\beta^2 + 18\beta^3 + \beta^4}{21(1 + \beta)^4} \frac{(R_1 + R_2)}{2} \frac{(R_1 + R_2)}{2h} \ln\left(\frac{R_1 + R_2}{2h}\right) \quad (4.20a)$$

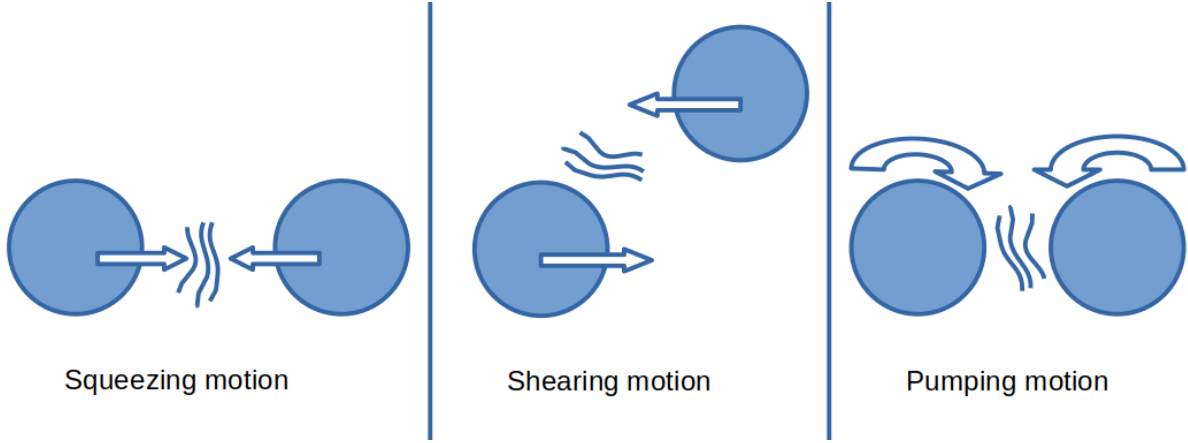


Figure 4.5: Different modes of near field lubrication interactions on particles in a suspension.

$$a_{sh} = 4\beta \frac{2 + \beta + 2\beta^2}{15(1 + \beta)^3} \frac{(R_1 + R_2)}{2} \ln\left(\frac{(R_1 + R_2)}{2h}\right) + 4 \frac{16 - 45\beta + 58\beta^2 - 45\beta^3 + 16\beta^4}{375(1 + \beta)^4} \left(\frac{(R_1 + R_2)}{2}\right) \frac{(R_1 + R_2)}{2h} \ln\left(\frac{(R_1 + R_2)}{2h}\right) \quad (4.20b)$$

$$a_{pu} = \beta \frac{4 + \beta}{10(1 + \beta)^2} \ln\left(\frac{(R_1 + R_2)}{2h}\right) + \frac{32 - 33\beta + 83\beta^2 + 43\beta^3}{250(1 + \beta)^3} \frac{(R_1 + R_2)}{2h} \ln\left(\frac{(R_1 + R_2)}{2h}\right) \quad (4.20c)$$

where,  $h$  is the surface to surface distance between particles 1 and 2 given by  $h = |n_{12}| - (R_1 + R_2)$

$n_{12}$  is the centre-centre vector between particle 1 and 2,

$\beta = R_2/R_1$  is the ratio of the particle radii.

The terms in equation 4.20a, 4.20b and 4.20c diverge as particles come in contact with each other as  $h \rightarrow 0$ . This is true for perfectly smooth spherical particles. However, as shown in the images of chapters 2 & 3, we see that the particles have asperities. Thus, following the approach of [Ness and Sun \[2016\]](#) one can limit the value of pairwise lubrication forces by limiting the minimum value of  $h$  to say  $0.01 \times$  average diameters of the interacting particles which typically corresponds to the asperity length scale of the particles. In mathematical terms, it could be written as 4.21.

$$h_{corrected} = \max(0.01 * (R_1 + R_2), h) \quad (4.21)$$

The bulk stress on the systems is calculated from the particle force and velocity data. It could be decomposed into contributions due to the particle-particle contacts, hydrodynamic interaction and velocity fluctuations. The stress computed through such a summation from individual particles is called virial stress.

$$\sigma^H = \frac{1}{V} \sum_i \sum_{i \neq j} r_{ij} F_H^{ij} \quad (4.22a)$$

$$\sigma^C = \frac{1}{V} \sum_i \sum_{i \neq j} r_{ij} F_C^{ij} \quad (4.22b)$$

$$\sigma^V = \frac{1}{V} \sum_i m_i v_i' v_i' \quad (4.22c)$$

$$\sigma_{suspension} = \sigma^C + \sigma^H + \sigma^V \quad (4.22d)$$

Here,  $V$  is the total volume of the sheared suspension,  $v_i'$  is the particle velocity after the mean streaming velocity (velocity of the surrounding fluid) is subtracted. Under simple shear flow, the relevant diagonal element of the stress tensor (say  $\sigma_{xy}$ ) is used for computing the viscosity of the suspension. Viscosity is calculated using the equation 4.23.

$$\mu_{suspension} = \frac{\sigma_{xy}}{\dot{\gamma}} \quad (4.23)$$

## 4.2.2 Materials and methods

### Shear flow simulations

Poly-disperse particles with 6 discrete classes of fully swollen particles mimicking the PSD obtained after complete swelling in chapter 2 is considered. i.e.  $D_f \subset \mathcal{N}(34.24 \mu\text{m}, 11.31 \mu\text{m})$ . The Young's modulus (1.8 kPa) and Poisson's ratio (0.47) of particles for the Hertzian model are taken from the characterization experiments of chapter 3. Granule density is assumed to be the same as that of water. Coulomb friction coefficient ( $\mu_p$ ) is assumed to be 1. A tri-clinic box of dimensions [0.001 m, 0.001 m, 0.001 m] in x,y and z directions is considered. The viscosity of water (0.001 Pa.s) at 20 °C is taken as the viscosity of the suspending medium. 10 realisations with the same particle size distribution (PSD) but with different initial positions of particles are sheared to get the flow curves (Viscosity vs shear rate) to compare with experimental data. The timestep used in the simulation is either  $10^{-7}$  or  $5 \times 10^{-7}$  seconds depending on shear rate. Flow curves generated from both experiments and simulations were compared and were in coarse agreement provided necessary corrections to take into account the non-sphericity of starch granules. Soft particle-particle contacts are shown to be the origin of shear-thinning in simulations.

LIGGGHTS-PUBLIC 3.8.0 DEM code is used to simulate the shear flow of particles. The lubrication contact model is implemented via a newly written fix file. The lubrication code implementation is similar in implementation to lubricate/poly pair-style in LAMMPS [Plimpton, 1995]. The implementation codes are attached in Appendix C. Fast lubrication dynamics terms are used to enforce the Stokes forces on particles.

As mentioned in chapter 2 and also in prior works [Deslandes et al., 2019], each starch granule has an aspect ratio defined as the ratio of minimum and maximum Feret diameter. Feret diameter is defined as the length of granule measured along a specified direction.

$$Asp = \frac{\max(\text{Feret diameters})}{\min(\text{Feret diameters})} \quad (4.24)$$

The probability distribution function for the aspect ratio of fully swollen granules is depicted in figure 4.6. The

average aspect ratio of fully swollen granules is 1.3 [Deslandes et al., 2019].

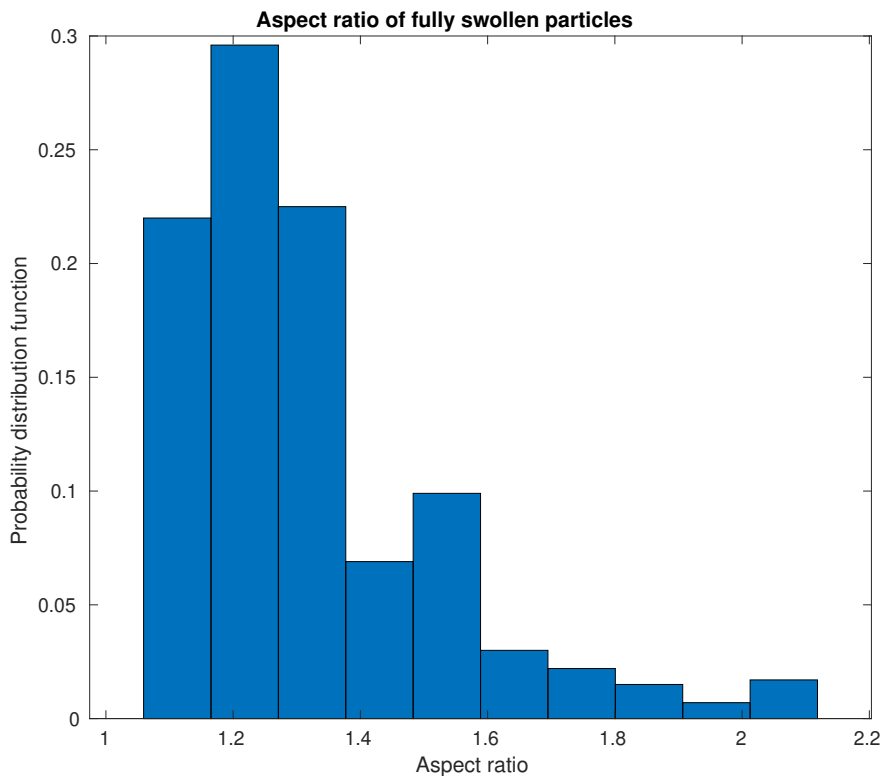


Figure 4.6: Aspect ratio

Maximum Feret diameter ( $M$ , equation 2.1) of particles are used to define the diameter of the simulated particles. Six discrete particle sizes with weights defined by the number distribution are used to mimic the poly-dispersity of fully swollen starch granule population size distribution. Figure 4.8 shows the six discrete particle sizes used to mimic the poly-dispersity of the fully swollen starch suspensions. Material properties used in the simulation are summarized in table 4.1.

The maximum Feret diameter was used because two ellipsoid particles can come in contact, especially if they rotate since the centre to centre distance becomes lower than half the sum of the maximum diameters (Figure 4.7). We assume that hydrodynamic forces (Stokes, lubrication) can rather be approximate with the circumscribed sphere diameter than the inscribed one. Considering that granules are ellipsoids and the view angle by the microscope is random, the volume of a granule is on average equal to one circumscribed sphere divided by the aspect ratio power 1.5.

A triclinic simulation box of length 0.001 m in each of  $x$ ,  $y$  and  $z$  directions is considered. Lees-Edwards boundary conditions are imposed with a constant box deformation shear rate. For each shear rate and volume fraction of particles, 10 simulations with different initial particle positions in the domain are performed to generate repeatability statistics. Five particle volume fractions ( $\phi$ ) are considered. On the basis of the circumscribed spheres the studied values were 35%, 40%, 45%, 52% and 55% but on the base of the ellipsoid granules the volume fractions were 23%, 26%, 30%, 34% and 36%. For each volume fraction of particles in the simulation domain, five shear rates

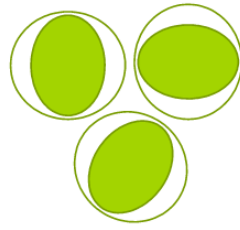


Figure 4.7: Particle contacts of ellipsoidal particles.

Property	Value
Young's modulus [Pa]	1800
Poisson's ratio	0.47
$h_{min}$	0.01*(radius)
$h_{max}$	0.1*(radius)
Fluid viscosity [Pa.s]	$10^{-3}$

Table 4.1: Granule material properties used in the simulation.

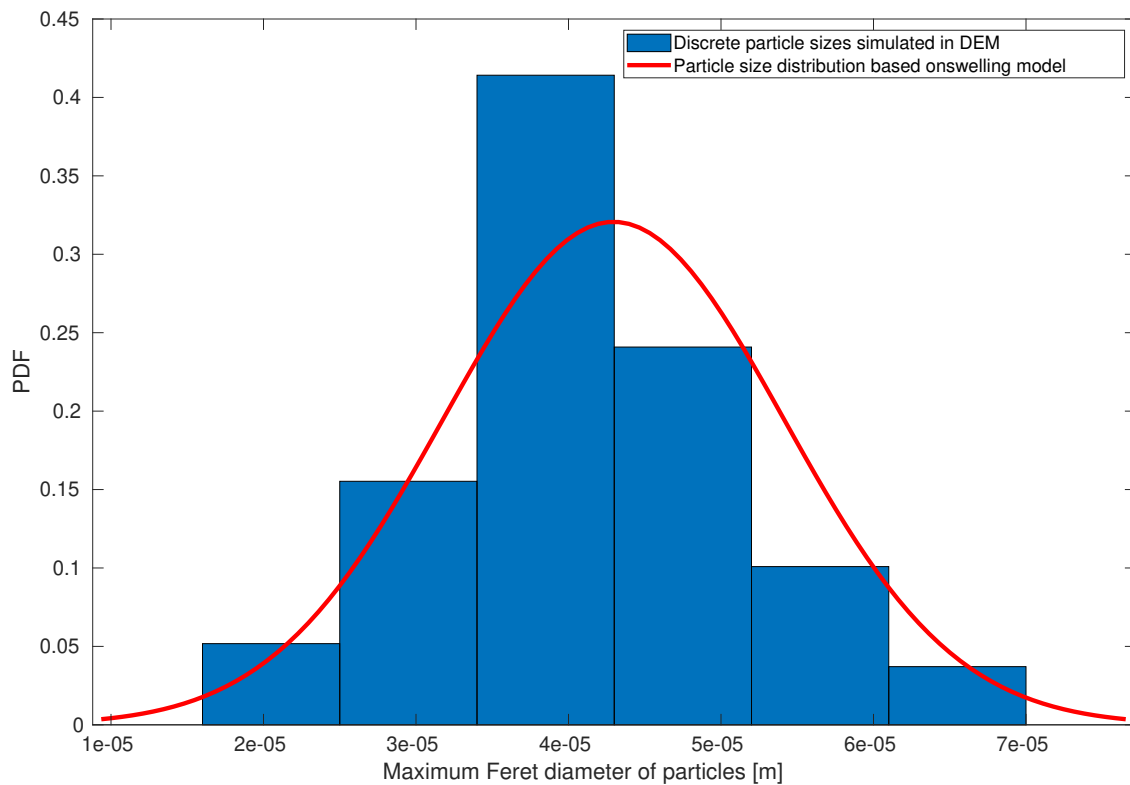


Figure 4.8: Discretization of particle size distribution in simulations.

are simulated (table 4.2). Virial stresses are calculated at every 100 timesteps and particle data such as positions, velocity, angular velocity, forces are stored in vtk files for every 50000 timesteps. The entire simulation is run for 500000 timesteps.

shear rate [ $s^{-1}$ ]	time step[s]
1	5e-7
5	1e-7
10	1e-7
50	1e-7
100	1e-7

Table 4.2: Simulations summary.

The three virial stresses contributions as defined in equation 4.22 are analysed. It is shown that the stresses reach a steady-state value and the average value of stresses for the last 100000 timesteps are considered to compute the viscosity using equation 4.23. The viscosity thus obtained through simulations are compared with the experimental viscosity measurements.

## Experiments

This section describes the experimental procedure used to obtain the flow curves that could be used to compare with the simulation results. We use a similar procedure to the one described in chapter 2 to estimate the volume fraction  $\phi$  of the suspension. A known quantity of starch (wn grams) is added to 100 ml of demineralized water in a beaker with a magnetic pellet. The summary of the samples prepared is listed in table 4.3. The suspension is heated to 90 °C under constant stirring of the magnetic pellet at 250 rpm (revolutions per minute). The suspension is held at 90 °C for 15 minutes to ensure complete swelling of the granules. The suspension is allowed to cool to room temperature. The suspension flow curves are measured inside a Couette rheometer at 20 °C. The flow curve program used is presented in the table 4.4. The data points collected during the flow-curve measurement are log-spaced. The tested suspension sample is weighted in a dry mass-measurement foil and placed inside an oven at 100 °C for 24 hours. The sample dry mass is measured and using the procedure mentioned in 3.1.2, the volume fraction ( $\phi$ ) of the suspension is calculated which is summarized in table 4.3

Sample	wn [g]	Volume fraction ( $\phi$ )[%]
1	2	17
2	2.5	22
3	3	26
4	3.25	28
5	4	34
6	6	49
7	7.5	61

Table 4.3: Summary of samples tested for flow-curves

Step	Shear rate [ $s^{-1}$ ]
1	1 to 500
2	500 to 1
3	1 to 500
4	500 to 1

Table 4.4: Rheometer program to measure flow-curves

### 4.2.3 Results and discussion

Although shear-thinning in starch suspensions has been observed for a long [Chamberlain et al., 1999], the origin of shear-thinning in starch suspensions at the granule level is not well understood. However, soft particle suspensions were shown by several authors [Silva et al., 2021, Voudouris et al., 2012, Chatté et al., 2018, Seth et al., 2011] to display shear thinning behaviour.

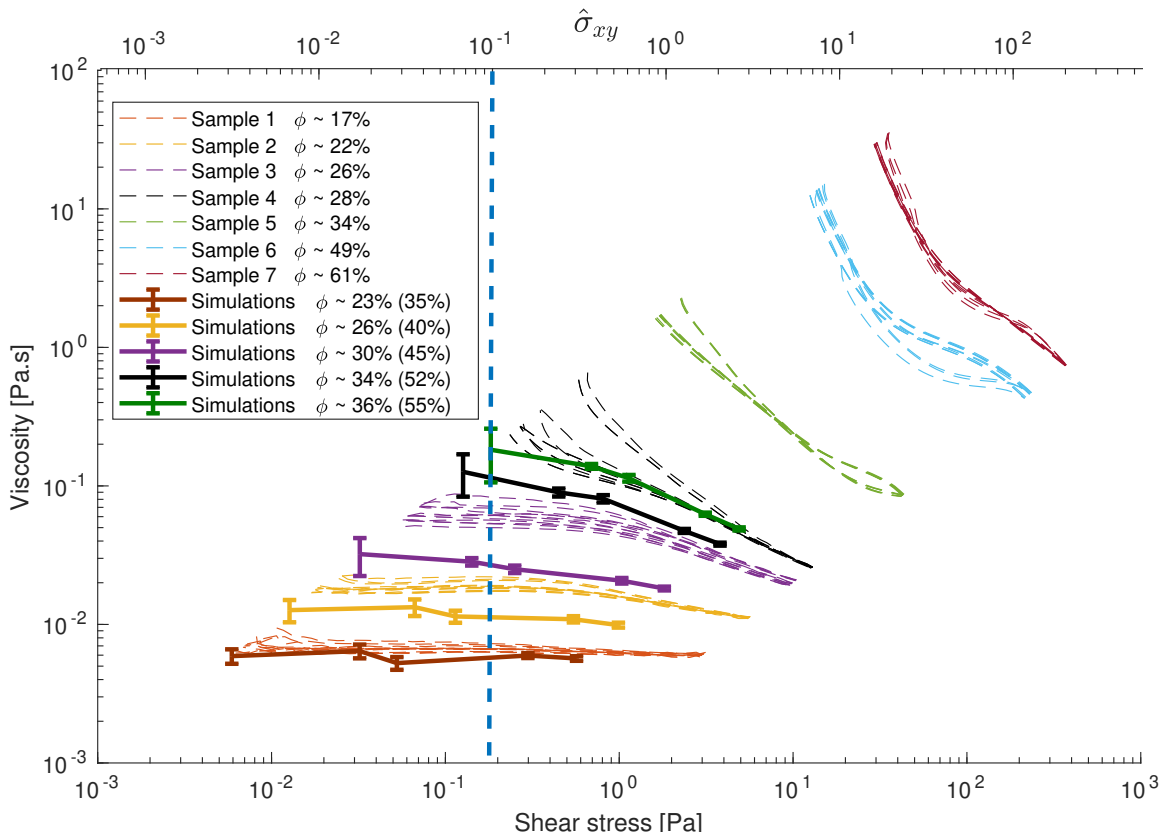


Figure 4.9: Newtonian to shear thinning transition of fully swollen starch suspensions.

Figure 4.9 shows the experimentally measured viscosity with the shear stress at different volume fractions. Experiments show low shear Newtonian visco-plateau (for shear stress  $< 0.5$  Pa), followed by shear thinning beyond this critical shear stress. Samples 1 shows a completely Newtonian curve while samples 2 and 3 show Newtonian to shear-thinning transition. DEM simulation results from 4.2.3 are also shown in figure 4.9 which also confirms the existence of the a critical shear stress for onset of shear-thinning. Figure 4.9 contains a secondary x-axis on top of the figure with a non-dimensional shear stress defined based on equations 4.32 and 4.33. Blue vertical line separates the hard particle and soft particle regime as defined by the inequality 4.34.

#### Krieger-Dougherty and Ellis model fits

The apparent volume fractions for samples 1,2 and 3 are estimated using Krieger-Dougherty equation 4.25 [Krieger and Dougherty, 1959]. Farr and Groot [2009] method is used to estimate the parameter  $\phi_m$  in the Krieger-Dougherty equation as 0.68.

$$\mu_{suspension} = \mu_{fluid} * \left(1 - \frac{\phi}{\phi_m}\right)^{-2.5\phi_m} \quad (4.25)$$

Sample No	Low shear viscosity [mPa.s]	$\phi_{viscosity}$ [%]	$\phi_{dry\ weight}$ [%]
1	8	48	17
2	21	57	22
3	61	62	26

Table 4.5: Volume fraction estimates using viscosity data and krieger-Dougherty equation

Table 4.5 summarizes the volume fraction as estimated using the krieger-Dougherty equation and compares it with the volume fraction using dry mass measurements as detailed in section 3.1.2. There are significant differences in the estimates obtained using the two methods. This could be attributed to the non-sphericity and the roughness of particles.

Reiner and Leaderman [1960] proposed the Ellis model for fluids transitioning from Newtonian at low shear stress to shear-thinning at high shear stress. Ellis model equation is given by equation 4.26:

$$\frac{\mu_0(\phi)}{\mu_{suspension}(\phi)} - 1 = \left(\frac{\tau}{\tau_c}\right)^{m_e} \quad (4.26)$$

where,  $\mu_{suspension}$  is the viscosity of the fluid at given shear stress  $\tau$ ,  
 $\mu_0$  is the Newtonian viscosity of the fluid,  
 $\tau_c$  is the critical shear stress characterizing the transition to shear thinning,  
 $m_e$  is the flow index of Ellis model.

Sample No	$\tau_c$ [Pa]	$m_e$	Adjusted R-squared
2	8	0.53	0.725
3	4	1.16	0.848

Table 4.6: Ellis model fit summary

Table 4.6 summarizes the Ellis model fits with the Newtonian viscosity in table 4.5 for samples 1 to 3. MATLAB function fitlm is used to perform the fits. Fits on sample 1 and sample 1 resulted in critical stress  $\tau_c$  values of 8 and 4 Pa respectively.

### DEM Shear flow simulations

Figure 4.10 shows the comparison of flow curves obtained through simulations and experiments. The average value of viscosities obtained from 10 different runs are plotted with error bars representing the standard deviation of runs. The numerical results presented in Figure 4.10 are therefore obtained from 250 different simulations. Effect of particle size on the simulation results is discussed in Appendix D.

For the simulations, the indicated volume fraction is based on the estimated average ellipsoid volume (in bracket is the volume fraction corresponding to the circumscribed spheres). At low volume fractions, the response is almost

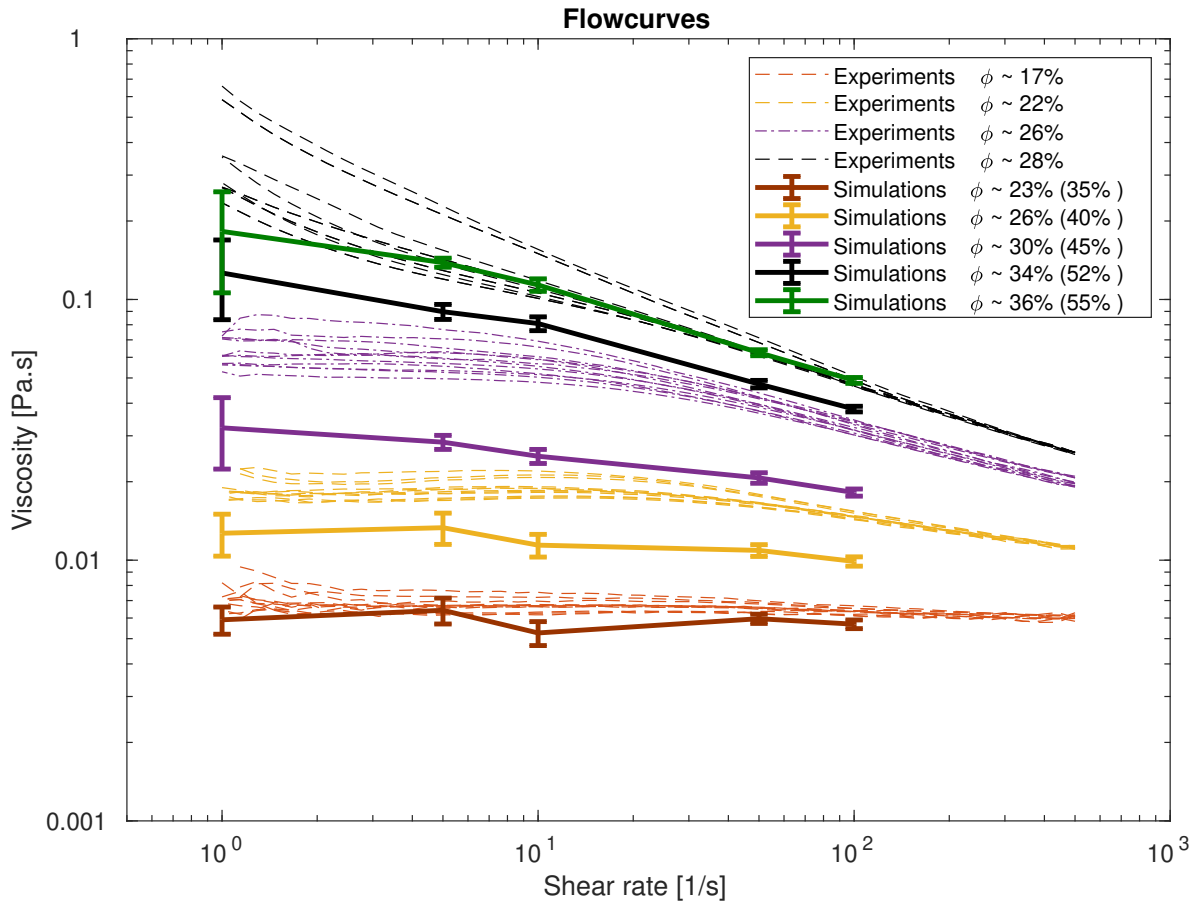


Figure 4.10: Flow-curves of fully swollen starch granules.

Newtonian, however, the Newtonian viscosity is volume fraction dependent and increases with particle concentration similar to hard particle suspensions and predicted by the Krieger-Dougherty equation. Experimental curves show some hysteresis for increasing and decreasing shear rates albeit the variation is minimal in comparison to the effect of volume fraction of particles.

From experimentally measured maximum and minimum Feret diameters, the geometric mean Feret diameter can be calculated based on equation 2.1.

$$D = \sqrt{Mm} \tag{4.27}$$

Where M is the maximum Feret diameter and m is the minimum Feret diameter

The aspect ratio (*asp*) of a particle is defined as the ratio of minimum and maximum Feret diameter of the granule.

$$asp = \frac{M}{m} \tag{4.28}$$

The total volume occupied by the circumscribed sphere of ellipsoidal particles is given by

$$V_{circumscribed\ sphere} = \frac{\pi M^3}{6} = \frac{\pi D^3 asp^{1.5}}{6} \quad (4.29)$$

The volume of ellipsoidal particle which is used to estimate the experimental volume fraction is

$$V_{particle\ ellipsoid} = \frac{\pi D^3}{6} \quad (4.30)$$

When considering the volume fraction based on ellipsoid granules, the order of magnitude of apparent viscosity seems to be in better agreement with the experimental measurements if circumscribed spheres (value in the bracket in figure 4.10) are considered than with volume fraction based on ellipsoid volume. Equation 4.31 is used to convert the volume fraction of spherical simulated particles to the ellipsoidal particles in experiments. This is in accordance with literature results for hard particles that viscosity increases with the aspect ratio of particles for the same particle volume fraction [Tapia et al., 2017].

$$\phi_{experimental} = \frac{\phi_{simulation}}{asp^{1.5}} \quad (4.31)$$

Shewan and Stokes [2015b] showed experimentally that above particle Young's modulus of 185 kPa the suspension behaves like a hard particle suspension for stresses in the range of 0.1 Pa to 10 Pa. Soft particle rheology is realised below this limit, which is the case for fully swollen starch suspensions. The limit is expected to be a function of the applied stress in the system as this leads to the deformation of the particles. Indeed, there seems to exist a critical volume fraction and shear rate combination that results in critical shear stress at which the onset of shear-thinning is observed as shown in figure 4.9. These features are replicated in the simulations as well.

Figure 4.7 shows the circumscribed circles of the particles for ellipsoids. The actual volume of a granule (in green) is lower than the one of the circumscribed sphere.

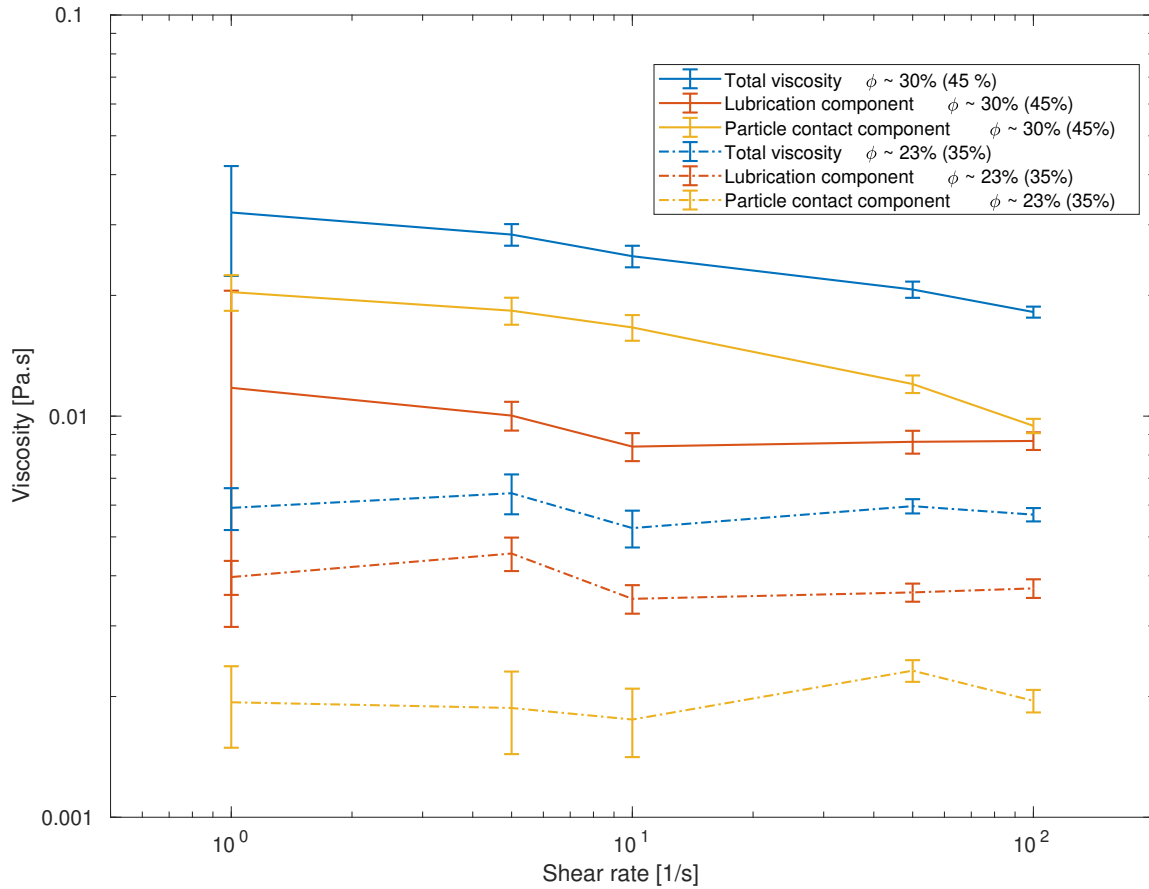


Figure 4.11: Shear dependency of lubrication and contact contributions to virial stresses at  $\phi \approx 30\%$  (45%) and  $\phi \approx 23\%$  (35%).

	Shear rate [ $s^{-1}$ ]	1	5	10	50	100
$\phi = 23\%$ (35%)	Lubrication [%]	67	71	67	61	65
	Contact [%]	33	29	33	39	34
$\phi = 30\%$ (45%)	Lubrication [%]	37	35	34	42	48
	Contact [%]	63	65	66	58	52

Table 4.7: Contribution of lubrication and contact forces to the viscosity of suspension.

Figure 4.11 shows that the lubrication and contact contributions to the total viscosity of the suspension at two different volume fractions  $\phi \approx 30\%$ (45%) and  $23\%$ (35%). At both, the volume fractions the lubrication contribution to viscosity is shear rate independent. At high volume fraction ( $\phi \approx 30\%$ (45%)) the contact contribution is significant as also shown in table 4.7. The contact contribution is shear-thinning thus leading to overall shear-thinning in the viscosity of the suspension. At a lower volume fraction ( $\phi \approx 23\%$ (35%)) the lubrication contribution is dominant and secondly, the contact contribution is shear independent. Thus, we can conclude that onset of the contacts is at the origin of shear-thinning at high volume fractions.

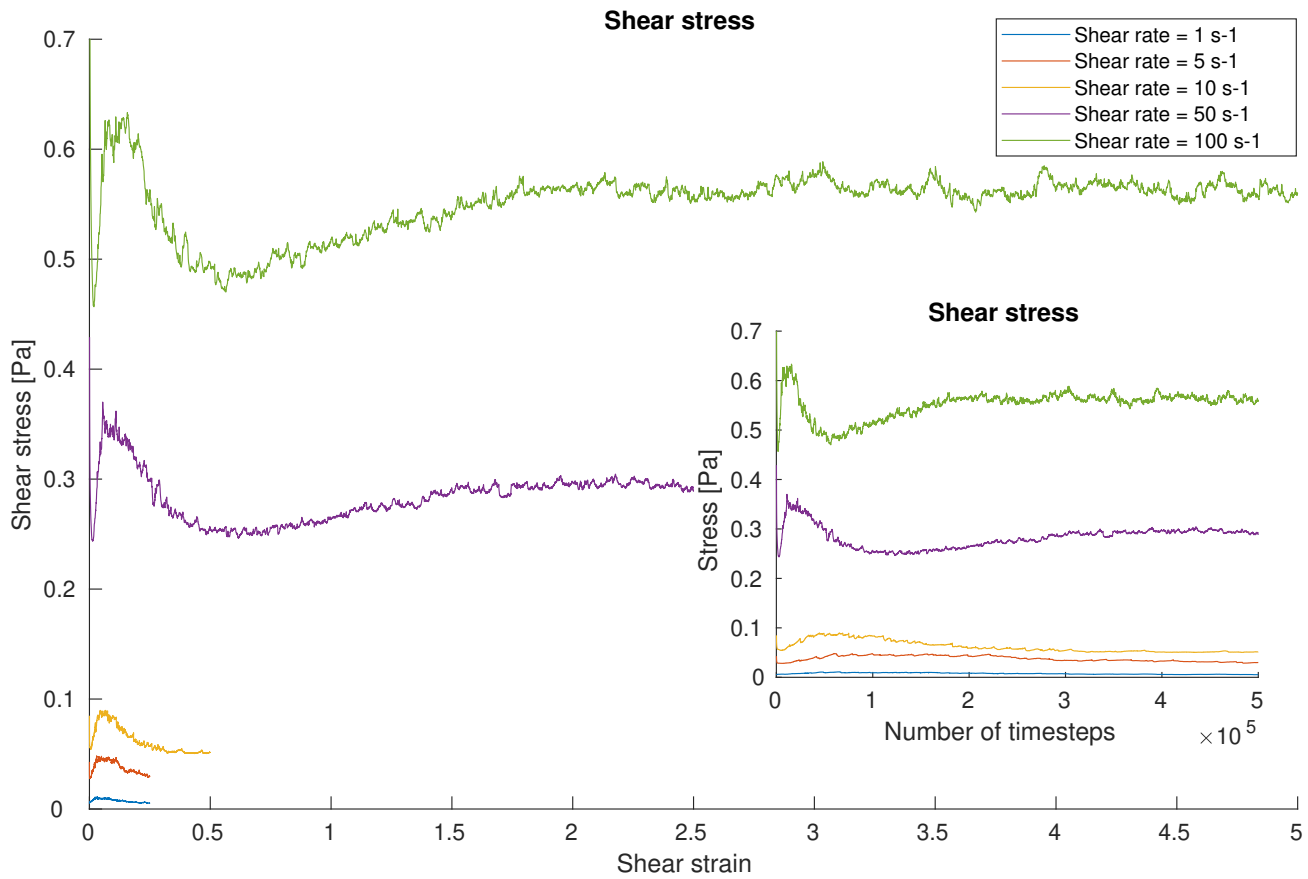


Figure 4.12: Shear stress evolution with shear strain for  $\phi \approx 23\%$ (35%) (Insert: Shear stress evolution with number of timesteps)

Figure 4.12 shows the average shear stress evolution with shear strain and in the insert the average shear stress evolution with timesteps for 10 simulations. As seen in the shear stress vs shear strain plot, there is an initial rearrangement in the system which leads to peak and the system reaches steady state value and the average value of the last 1000 timesteps are used to calculate the viscosity of the suspension.

### Differentiating hard particle and soft particle rheology

In the previous section 4.2.3, it was shown that soft particle contacts are at the origin of shear-thinning in fully swollen soft starch suspensions. Native un-swollen corn starch suspensions are shown to be Newtonian or shear-thickening. [Ness and Sun \[2016\]](#) showed through DEM simulations that frictional particle contacts are at the origin of the shear thickening for such suspensions. Thus, differentiating soft particle rheology and hard particle rheology helps one to predict if the rheology of the suspension is shear thinning or shear thickening.

We define non-dimensional shear stress re-scaled with particle Young's modulus( $E_p$ ).

$$\hat{\sigma}_{xy} = \frac{\mu_{suspension}(\phi) \dot{\gamma}_{local}}{E_p} \quad (4.32)$$

where  $\dot{\gamma}_{local}$  is the shear rate at the surface of the particle.

$E_p$  is Young's modulus of the particle.

Vázquez-Quesada et al. [2016] through DEM simulations showed that the local shear rate at the inter-particle gap can be 3 to 4 orders of magnitude higher than the global shear rate. The local shear is a function of relative velocity between colliding particles and interparticle gaps. Thus, here we make the following simplifying assumption in equation 4.33.

$$\gamma_{local} = 10^3 \times \gamma_{global} \quad (4.33)$$

Further, an assumption can be made that soft particle rheology is realised when the shear stress on the surface of the particle is greater than 10% of Young's modulus of the particle ( $E_p$ ). The choice of 10% bodes well with the rheological data as shown in figure 4.9. This results in the following inequality 4.34 to predict the onset of soft particle rheology.

$$\mu_{suspension}(\phi) \dot{\gamma}_{global} > 10^{-4} E_p \quad (4.34)$$

Thus, the shear rate at which the soft particle rheology is realized is drastically different for native starch and fully swollen starch. For the system of Shewan and Stokes [2015b] this inequality predicts that soft particle rheology is realised at shear stresses greater than 18 Pa for particles with Young's modulus of 185 kPa. As mentioned previously, Shewan and Stokes [2015b] found hard particle suspension rheology for this system in the range of 0.1 Pa to 10 Pa. This inequality predicts well the transition from Newtonian to soft particle rheology for fully swollen starch in water suspensions as well as shown in figure 4.9. A schematic representation of the rheology of suspensions with Non-dimensional shear stress vs relative viscosity is shown in figure 4.13.

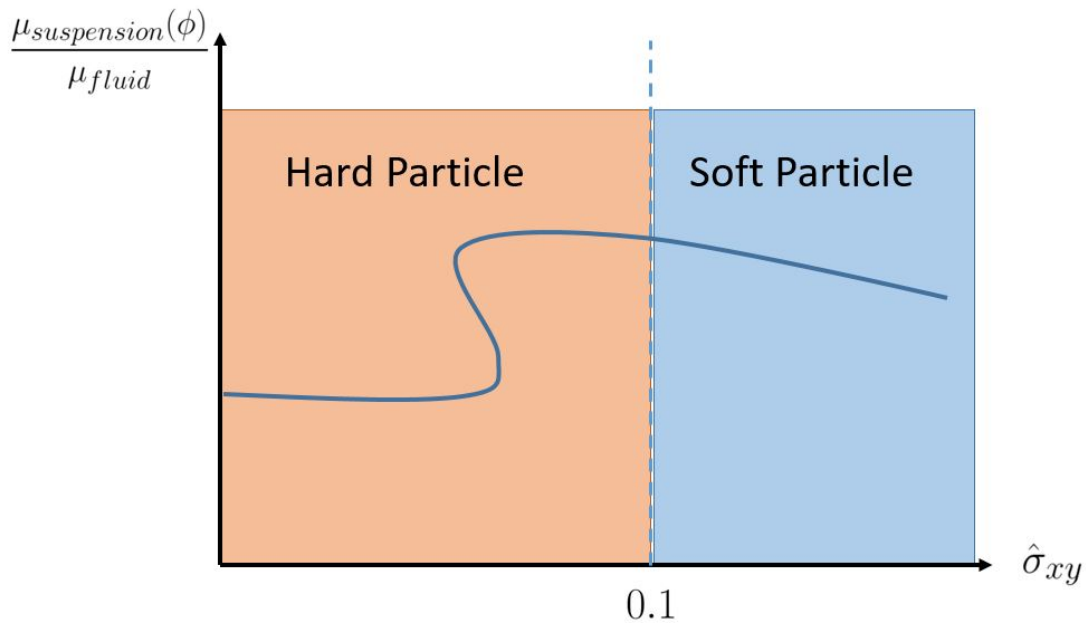


Figure 4.13: Scheme illustrating the different rheology in hard particle and soft particle limits

#### 4.2.4 Conclusion

Shear-thinning of starch suspensions has been reproduced in simulations. The origin of shear-thinning is shown to be soft particle contacts. To take into account the non-sphericity of the granules (average aspect ratio = 1.3), we considered that particles interact as their circumscribed spheres: maximum Feret diameter was used for the equivalent spherical particles. This way, the order of magnitude of the apparent viscosities was in coarse agreement with the measurements. The scaling of shear-thinning also matches the experimental data. In a first approach, the effect of granule-granule interactions on the viscosity of the shear-thinning suspensions are captured.

On another hand, with the same approach, [Ness and Sun \[2016\]](#) showed that frictional particle contacts are at the heart of shear-thickening in hard particle suspensions. Together, this gives one the confidence to model starch swelling and rheology evolution as it transitions from hard particle to soft particle rheology during gelatinization. The shortcoming of this method is that the rheology of the suspension cannot be simulated at high volume fractions because of the simplification of the particle shape.

Future work is necessary to quantify the effect of parameters such as particle Young's modulus, continuum phase viscosity, etc. Further to decipher particle shape effects, non-spherical particles shapes such as elongated ellipsoids could be used in simulations. Improved Hertz contact model applicable at higher deformations can be used to improve the robustness of the simulations.

## Conclusion (version française)

Le caractère rhéofluidifiant des suspensions d'amidon gélatinisé a été reproduit dans des simulations de contacts entre particules molles. Pour tenir compte de la non-sphéricité des granules (facteur d'aspect moyen=1,3), nous avons considéré que les particules interagissent comme leurs sphères circonscrites : le diamètre maximum de Ferret a été utilisé pour les particules sphériques équivalentes mais leur volume a été considéré comme celui d'ellipsoïdes (pour la détermination de la fraction volumique). De cette façon, l'ordre de grandeur des viscosités apparentes est en assez bon accord avec les mesures. Le modèle prédit également assez bien les contraintes de cisaillement à partir desquels le caractère rhéofluidiant apparaît. En première approche, l'effet des interactions granule-granule sur la viscosité de la suspension a donc été.

Avec la même approche, [Ness and Sun \[2016\]](#) ont montré que les contacts frictionnels des particules sont au cœur du caractère rhéoépaississant dans les suspensions de particules dures. On peut donc a priori utiliser ce type de modèle pour simuler des configurations où une suspension d'amidon gélatinisé sous cisaillement passant de particules dures à des particules molles. L'inconvénient de cette méthode est que la rhéologie de la suspension ne peut pas être simulée à des fractions volumiques élevées à cause de la simplification de la forme des granules.

Des travaux futurs sont nécessaires pour déchiffrer l'effet de paramètres tels que le module de Young des particules, la viscosité de la phase continue, etc. Pour mieux comprendre les effets de la forme des particules, des particules non sphériques telles que des ellipsoïdes allongés pourraient être utilisées dans les simulations. Un modèle de contact de Hertz amélioré, applicable à des déformations plus importantes, peut être utilisé pour améliorer la robustesse des simulations.



## Chapter 5

# Multiscale modelling of flow, heat transfer and swelling during thermo-mechanical treatment of starch suspensions

Arnesh Palanisamy<sup>a</sup>, Marco Ramaioli<sup>a</sup>, Paul Menut<sup>a</sup>, Artemio Plana-Fattori<sup>a</sup>, Denis Flick<sup>a</sup>

<sup>a</sup> Université Paris Saclay, INRAE, AgroParisTech, UMR SayFood, 91300, Massy, France

### Abstract

During thermal treatment of starch-based liquid food products, many coupled phenomena occur at different scales. Heat transfer affects local temperature evolution, which determines starch transformation (swelling and eventually amylose release and/or granules breakage). This transformation modifies the rheology, which in turn affects the fluid flow and heat transfer. This two-way coupling of flow, transfer and transformation was previously simulated in heat exchangers by Computational Fluid Dynamics (CFD), through purely Eulerian or Eulerian/Lagrangian approaches, assuming that the starch granules follow locally the fluid velocity. Moreover, the transformation was only characterized by a deterministic model for the mean particle size evolution (swelling). The present work takes into account directly the trajectory and the swelling of each starch granule in interaction with the surrounding fluid through an approach combining CFD with Discrete Element Method (DEM) simulations. Due to lubrication forces, the granules tend to avoid one another and when they come in contact, an elastic rebound is assumed. This approach is applied here to a waxy maize starch suspension during heating in a Couette rheometer. A shear-induced random walk of the particles is observed. Swelling first occurs near the heated wall, then swollen granules migrate toward zones of lower solid fraction. This multiscale model (rheometer scale: 1 mm, starch granule scale: 10  $\mu\text{m}$ ) can be used for the analysis of such rheometry tests in which the sample cannot be assumed as homogeneous.

*Keywords:* Starch granule, Swelling kinetics, DEM, CFD, Modelling

This article was published in the Journal *Food structure*

<https://doi.org/10.1016/j.foostr.2021.100211>

## Chapitre 5

# Modélisation multi-échelle de l'écoulement, du transfert de chaleur et du gonflement lors du traitement thermomécanique de suspensions d'amidon.

Arnesh Palanisamy<sup>a</sup>, François Deslandes<sup>b</sup>, Marco Ramaioli<sup>a</sup>, Paul Menut<sup>a</sup>, Artemio Plana-Fattori<sup>a</sup>, Denis Flick<sup>a</sup>

<sup>a</sup> Université Paris Saclay, INRAE, AgroParisTech, UMR SayFood, 91300, Massy, France

### Résumé

Lors du traitement thermique des produits alimentaires liquides à base d'amidon, de nombreux phénomènes couplés se produisent à différentes échelles. Le transfert de chaleur affecte l'évolution locale de la température, qui détermine la transformation de l'amidon (gonflement et éventuellement libération d'amylose et/ou rupture des granules). Cette transformation modifie la rhéologie, qui à son tour affecte l'écoulement du fluide et le transfert de chaleur. Ce couplage bidirectionnel entre écoulement, transferts et transformation a été précédemment simulé dans des échangeurs de chaleur par la mécanique des fluides numérique (Computational Fluid Dynamics:CFD), par des approches purement eulériennes ou eulériennes/lagrangiennes, en supposant que les granules d'amidon suivent localement la vitesse du fluide. De plus, la transformation n'a été caractérisée que par un modèle déterministe de l'évolution de la taille moyenne des particules (gonflement). La nouvelle approche proposée ici prend en compte directement la trajectoire et le gonflement de chaque granule d'amidon en interaction avec le fluide environnant à travers une approche combinant des simulations CFD avec la méthode des éléments discrets (DEM). En raison des forces de lubrification, les granules ont tendance à s'éviter et lorsqu'ils entrent en contact on considère un choc parfaitement élastique. Cette approche est appliquée ici à une suspension d'amidon de maïs cireux lors d'un chauffage dans un rhéomètre de Couette. On observe une marche aléatoire des particules induite par le cisaillement. Le gonflement se produit d'abord près de la paroi chauffée, puis les granules gonflés migrent vers les zones de fraction solide inférieure. Ce modèle multi-échelle (échelle du rhéomètre : 1 mm, échelle des grains d'amidon : 10  $\mu\text{m}$ ) peut être utilisé pour l'analyse de tels tests de rhéométrie dans lesquels l'échantillon ne peut être supposé homogène.

*Mots clés:* Granule d'amidon; Cinétique de gonflement; DEM; CFD; Modélisation

## 5.1 Introduction

Starch is one of the most abundantly available naturally occurring biopolymers on earth. It is predominantly found in grains and tubers and is the source of 70-80 % of the calories consumed by humans worldwide in various forms of food products [Bertolini, 2010]. Starch also finds many applications apart from food in industries such as bio-medical, packaging, paper, textile and pharmaceutical industries. Starch in its native form occurs as granules which consists of two polysaccharides, amylose and amylopectin. Both amylose and amylopectin have  $\alpha$ -glucose as the monomer but differ in the way they are bonded. Amylose has  $\alpha(1-4)$  bonds and is linear whereas amylopectin has  $\alpha(1-6)$  bonds and is highly branched. The granule structure, molecular weight distribution, degree of amylopectin branching and the ratio of amylose to amylopectin varies according to the botanical origin of the starch granule. This, in turn, can have drastic consequences in the physical and chemical properties of the granules such as rheology and gelatinization behaviour [Banks et al., 1974, Hoover, 2001, Srichuwong et al., 2005, Visser et al., 1997]. Some kinds of starch are chemically modified to have enhanced structural and functional properties of the starch granules [Debnath et al., 2013, Alcázar-Alay and Meireles, 2015]. By 2025, the world starch production is projected to be around 156 million metric tons, including native and modified starches [Reportlinker.com, 2020]. As a result starch has been in the past, a subject of perennial research interest for researchers from diverse backgrounds and will be in the near future as well.

Gelatinization is the process in which starch granules undergo an irreversible transformation when subjected to thermomechanical treatment in the presence of water. During this process, starch granules swell by imbibing water and the overall viscosity of the suspension increases. It is also sometimes referred to as starch pasting in literature. Starch granules are semi-crystalline with concentric rings of crystalline and amorphous phases [Ratnayake and Jackson, 2008]. On the microscopic scale, the process corresponds to the melting of crystallites, loss of birefringence, leaching of amylose into the continuous phase and sometimes rupture of the granular structure [Atwell, 1988, Biliarderis, 1992]. The evolution of viscosity during gelatinization is also influenced by the process parameters such as concentration, shear rate, thermal history, pH and presence of other ingredients [Thomas and Atwell, 1999, Malumba et al., 2018]. For high amylopectin cereal starches, such as waxy maize starch, the granules tend to hydrate with ease, swell rapidly and rupture to a great extent which results in loss of paste viscosity. As starch is used as a viscosity enhancer in many food applications such as in ketchup and also in non-food applications such as enhanced oil recovery in oil drilling, the rupture of the granules which leads to loss in suspension viscosity should be avoided, this can be avoided by chemically modifying the starch.

### 5.1.1 Coupling starch swelling, flow and heat transfer

It is of particular interest to understand the coupled evolution of temperature, starch gelatinization (notably swelling) and rheology in heat exchangers. Pioneer work was done in this field by Yang and Rao [1998] and more recently by Plana-Fattori et al. [2013] and Plana-Fattori et al. [2016]. In these studies, the rheology of partially gelatinized suspension is related to the temperature evolution directly [Yang and Rao, 1998] or via a swelling kinetic model where the parameters of this model are estimated empirically. Then fluid flow and heat transfer are studied after

solving the governing equations in interaction with the rheology/swelling model. The simulations were in relatively good agreement with some experimental measurement. However, these studies had several limitations: the size distribution of the granules was ignored (only average diameter evolution was considered), the variability from a granule to another in terms of swelling was ignored, the granules followed exactly the fluid flow, inside a fluid parcel (on a given trajectory) all the granules were assumed to have the same behaviour. It is known that particles migrate towards a region of lower shear rate, lower volume fraction and lower viscosity [Shauly et al., 2000]. It is also known, that even without a gradient of these variables, there is shear-induced self-diffusion of the particles due to elastic collisions and lubrication interaction [Foss and Brady, 1999]. This is well documented in literature [Eckstein et al., 1977, Leighton and Acrivos, 1987, Breedveld et al., 1998, Phillips et al., 1992]. Shear induced self diffusivity is proportional to the shear rate and to the squared particle radius. The proportionality parameter depends on the particle volume fraction ( $\phi$ ) and different correlations were proposed (linear or quadratic). Eckstein et al. [1977] found that this parameters increases almost linearly from 0 to 0.02 when the volume fraction rises from 0 to 0.2. This general trend was confirmed by Breedveld et al. [1998] who compared different studies. Inertial effect can also be involved depending on the particle Reynolds number. Also, particle migratory self-diffusion can induce an increase of momentum and heat transfer, in other words, this phenomenon can increase the apparent viscosity and conductivity.

The main question we would like to answer in this study is, are these various granular phenomena of appreciable importance in the case of starch suspension subjected to fluid flow and heat transfer? To answer this question, an approach combining Computational Fluid Dynamics (CFD) and the Discrete Element Method (DEM) is here proposed, similar to one implemented in Qian et al. [2014] for simulating granular filters. One specificity is that the suspension evolves because of the starch granule swelling. We apply this modelling approach to the case of a small gap Couette rheometer during fast heating of the external cylinder. In this case, we also have shear and heat transfer with momentum and energy exchanges between fluid and particles, possible particle migration and self-diffusion (random walk) but the fluid flow is simpler than in a heat exchanger.

### 5.1.2 Starch swelling modelling

Many models exist in the literature to predict the average degree of swelling depending on the thermal history of a given starch suspension [Lagarrigue et al., 2008, Malumba et al., 2013, Plana-Fattori et al., 2016]. More recently, Desam et al. [2018a,b, 2020] proposed a mechanistic model based on the Flory-Rehner theories, for the starch swelling of various grades. However, this deals at the population level assuming same model parameters for all granules and hence, does not take into account the inter-granule variability. The inter-granule variability has biological origins and the alternating crystalline and amorphous phase of the starch granule is bound to slightly vary even among starch granules from the same plant. Thus, modelling the average behavior may not be sufficient to understand some mechanisms such as granule migration during thermal processing in presence of high velocity and temperature gradients. Therefore, in our previous work we have described the granules swelling kinetics at the individual granule scale using a semi-mechanistic model [Palanisamy et al., 2020] for modified waxy maize starch. According to the microscopic observation of starch granules during heating in the presence of water, we observed

variability in swelling kinetics from granule to granule. Each granule has a specific delay time associated with the onset of swelling. Also, the granules which began to swell at a later instant tended to swell slower compared to the granules which began to swell earlier for a given time-temperature profile. Below a minimal temperature, no swelling was observed. Experiments showed that high temperatures resulted in lower delay time and faster increase in granule diameter. These phenomena were cast mathematically in a model [Palanisamy et al., 2020]. Nayouf et al. [2003] indicated that the volume fraction of granule can be estimated if the mean granule size can be accurately determined. As discussed in the next section, volume fraction of starch is a critical parameter used in the closure relations for predicting viscosity in mixture models. This inter granular level kinetic model of starch granule swelling is coupled here, with a CFD-DEM model for prediction of fluid flow, heat transfer and granule trajectories.

### 5.1.3 Starch suspension rheology

As discussed in the previous sections, starch has many different varieties and is used as a viscosity enhancer in various fields. Rheology measurements are generally carried out at a constant temperature and after complete gelatinization. However, having the evolution of rheology during gelatinization is quintessential for robust process design and can be of interest to design control strategies as well. This is done notably with the Brabender farinograph method to characterize different starches before processing. This method involves measuring the torque required to move the impeller at a predetermined rpm while measuring the temperature of the sample independently throughout the gelatinization process. However, this method does not allow measuring directly the usual rheological material functions but gives only an indication of the viscosity in arbitrary Brabender units [Eliasson, 2004]. To carry out Couette rheometry of starch suspensions during heating, at a rate comparable to the industrial processes (around  $1\text{ }^{\circ}\text{C}/\text{s}$ ), Lagarrigue [2002] developed a high heating/cooling rate rheometer. She took into account (via a thermal model) the thermal gradient in the rheometer gap and was able to propose a model predicting the rheology of the starch suspension as a function of its thermal history.

The properties of starch vary based on its botanical origin and processing it has undergone. Hence, suspension rheology also varies widely, it can be either shear thinning or shear thickening depending on the variety and concentrations [Plana-Fattori et al., 2016, Crawford et al., 2013]. Origins of such varied behaviour of starch suspensions can be deciphered by leveraging the literature existing on viscosity predictions of broad class of materials known as non-brownian particulate suspensions.

Researchers over the years have developed two methods of modelling the suspension rheology namely, two-fluid model and mixture model [Vollebregt et al., 2010]. In a two-fluid model the conservation equations are written for both particle phase and the fluid phase with the interaction terms between the phases. In the mixture approach, the suspension is modelled as an equivalent single phase. Both two-fluid model and mixture model regard the liquid and solid phases as interpenetrating continua.

The **two-fluid model** is obtained by averaging the equations of motion over the liquid and the particle phases. This results in a set of equations with a closure problem as it contains a number of indeterminate terms which are not related to the averaged variables but associated with the details in the microscopic length scale. Multiple methods exist for coming up with this closure problem. Two of which are effective medium theory and fully resolved

CFD-DEM simulation. The latter is an Eulerian-Lagrangian method which is computationally expensive. Effective medium theory approach is favourable for thermodynamic and computational point of view. The indeterminate terms of the two-fluid model are represented by the effective stress tensors of the phases and interaction force exchanged by the phases. The expressions for the effective stress tensors and fluid-particle interaction forces are important as they indicate the origins of these terms.

According to [Jamshidi et al. \[2019\]](#), the liquid effective stress tensor is the sum of four terms. The first is the product of the liquid viscosity( $\mu$ ), the liquid volume fraction ( $1-\phi$ ) and the mean liquid shear rate ( $\dot{\gamma}$ ). The fourth term is similar to Reynolds stress and becomes important in turbulent case. The second and third terms together are called the 'particle-particle stress'. The 'particle-presence stress' takes notably into account that the presence of particles distort the fluid streamlines and generate larger local velocity gradients, which increase viscous dissipation. This occurs even if the particles follow the liquid i.e. with zero slip velocity with the surrounding fluid. For dense mixtures, it considers also lubrication films between a significant number of particles in which viscous dissipation occurs.

For non-Brownian, neutrally buoyant, spherical particles dispersed in a Newtonian fluid in laminar flow and low volume fractions (typically  $\phi < 0.05$ ), [Jamshidi et al. \[2019\]](#) recovered the expression obtained by [Einstein \[1905\]](#) for the part of the 'particle-presence stress' due to streamline distortion (in this derivation the lubrication interactions are neglected). [Jamshidi et al. \[2019\]](#) further claim that the approach often used in two-fluid modelling for the fluid/fluid interaction, which considers only the first term of the liquid effective stress tensor is incorrect and should be avoided notably because it predicts a decrease in effective viscosity as the solid concentration rises.

For dense suspensions and soft particle pastes, besides fluid/fluid interactions, a critical point is how to treat the particle/fluid and particle/particle interactions [[Vollebregt et al., 2010](#), [Van der Sman and Vollebregt, 2012](#)]. In particular, shear induced diffusion is a phenomenon of main importance. It has been shown that particle-particle interaction leads to osmotic pressure of the suspension as derived by [Seth et al. \[2011\]](#). These authors studied through simulations the variation of osmotic pressure and suspension shear modulus as a function of the particle properties. It was shown that gradient in osmotic pressure of a suspension contributes to the shear induced particle migration [[Vollebregt et al., 2010](#)]. Further [Van der Sman and Vollebregt \[2012\]](#) went on to define an effective granular temperature based on osmotic pressure for sheared suspensions.

In the **mixture approach**, the suspension is considered like a single phase with an apparent viscosity also called suspension viscosity. The latter includes not only the effect of streamlines distortion due to the simple presence of the particles but also the particle/particle and fluid/particle interactions. Analytical and empirical correlations were proposed (e.g. [Batchelor and Green \[1972\]](#)). The four most important factors that dictate a suspension viscosity are (a) suspending medium's viscosity, (b) granule volume fraction, (c) granule deformability, and (d) imposed shear rate [[Chen et al., 2007](#)]. Granules deformability (granule's Young's modulus) is of particular importance for large volume fractions when particle-particle interactions becomes predominant [[Li et al., 2020](#), [Evans and Lips, 1990](#)]. The governing momentum equation for the mixture can also be obtained by adding the two momentum equations of the two-fluid approach, this allows also developing approximate expressions for the suspension viscosity [[Jamshidi et al., 2019](#)].

For concentrated suspensions, when fluid/fluid interactions becomes negligible compared to contact and lubrication forces, DEM simulations can also predict the rheology including shear-thickening [Ness and Sun, 2016].

Despite these efforts to understand how rheology evolution is connected to the transformation of the starch suspension during heating, there is no unequivocal single answer to explain or model all the experimentally observed phenomena.

## 5.2 Modelling

### 5.2.1 Starch swelling modelling

The previously developed individual starch granule swelling model [Palanisamy et al., 2020] is presented briefly here. In this study we use chemically stabilized cross-linked waxy maize starch (C\*Tex 06205), provided by Cargil (Baupte, France). This has a  $D_{10}$  greater than  $8 \mu\text{m}$  and thus is non-colloidal in nature.

For a constant reference temperature  $T_{\text{ref}}$ , the onset delay time  $t_{\text{onset}}$  follows an exponential distribution for which the cumulative distribution function is:  $1 - e^{-t_{\text{onset}}/\tau_{\text{ref}}}$ , where  $\tau_{\text{ref}}$  is the characteristic latency time at  $T_{\text{ref}}$ . To traduce this, a parameter  $\alpha$  called ‘difficulty of swelling’ was introduced. For each granule,  $\alpha$  is selected at random from uniform distribution in the range [0, 1]. This way, for constant temperature  $T_{\text{ref}}$ , the delay time  $t_{\text{onset}}$  follows:

$$t_{\text{onset}} = -\tau_{\text{ref}} \cdot \ln(1 - \alpha) \quad (5.1)$$

Regarding the swelling onset, equation 5.1 arises from an experiment carried out a constant temperature of  $62 \text{ }^\circ\text{C}$  during one hour [Palanisamy et al., 2020].

For variable temperature, the time delay in onset of swelling is given by solving equations 5.2 and 5.3, which means that the delay in onset of swelling is higher at lower temperatures that at higher temperatures.

$$\ln(1 - \alpha) = - \int_0^{t_{\text{onset}}} \frac{dt}{\tau} \quad (5.2)$$

$$\tau = \max \left( 0, \left( \frac{T_{\text{ref}} - T_{\text{min}}}{T - T_{\text{min}}} \right) \right) \tau_{\text{ref}} \quad (5.3)$$

Dimensionless diameter  $S$  is given by

$$S(t) = \frac{D(t) - D_i}{D_f - D_i} \quad (5.4)$$

where  $D(t)$  is the diameter at an instant  $t$ ,  $D_i$  is the initial diameter of the granule,  $D_f$  is the final diameter of the granule.

After the delay time  $t_{\text{onset}}$  is overcome, the swelling kinetics is given by:

$$\frac{dS}{dt} = K(1 - S) \quad (5.5)$$

with

$$K = K_{\text{ref}}(1 - \alpha)^{0.5} \left( \frac{T - T_{\text{min}}}{T_{\text{ref}} - T_{\text{min}}} \right)^2 \quad (5.6)$$

where  $K_{\text{ref}}$  is the rate constant at  $T_{\text{ref}}$  for a granule which has no difficulty to swell ( $\alpha = 0$ ).

For chemically stabilized cross-linked waxy maize starch (C\*Tex 06205) provided by Cargill (Baupte, France) the following parameters were estimated:  $T_{\text{min}} = 60 \text{ }^\circ\text{C}$ ,  $\tau_{\text{ref}} = 190 \text{ s}$  and  $K_{\text{ref}} = 0.0023 \text{ s}^{-1}$  at  $T_{\text{ref}} = 62 \text{ }^\circ\text{C}$ . From the above equations, one can describe the swelling kinetics of these starch granules.

The following assumptions regarding the starch population were made. Initial diameters and swelling ratio are from a random normal distribution:  $D_i \subset \mathcal{N}(14.77\mu\text{m}, 4.44\mu\text{m})$ ,  $D_f/D_i \subset \mathcal{N}(2.34, 0.33)$ .

The details and experimental basis of this swelling model for individual starch granules of cross-linked waxy maize starch were presented in previous work [Deslandes et al., 2019, Palanisamy et al., 2020]. The model was validated by microscopic observation for different temperature ramps (up to  $90 \text{ }^\circ\text{C}$ ) and also by comparing size distribution obtained by Malvern mastersizer after different non-linear heat treatments. These model parameters should be re-calibrated for other waxy cross-linked starches and the model should be modified for other types of starches and is not applicable if the granule ruptures.

## 5.2.2 CFD-DEM modelling

A two-phase modelling approach is used as by Jamshidi et al. [2019] except that the solid phase (starch granules) is not treated as a continuous phase but as a discrete one: each particle is characterized by its centre position and velocity. This approach is similar to the one used by Qian et al. [2014].

An Eulerian approach is used for solving flow and heat transfer of the continuous fluid (in this case pure water). In each representative elementary volume (REV) there are a number of solid particles (in this case starch granules).

For the fluid phase, in a general case, the momentum equation holds:

$$(1 - \phi)\rho_f \frac{\partial \vec{v}_f}{\partial t} + (1 - \phi)\rho_f \vec{v}_f \cdot \vec{\nabla} \vec{v}_f = -\vec{\nabla} \cdot \vec{\bar{S}} + (1 - \phi)\rho_f \vec{g} + \overrightarrow{f_{p \rightarrow f}} \quad (5.7)$$

where  $\overrightarrow{f_{p \rightarrow f}}$  is the sum of the forces exerted on the fluid by the particles per unit volume (notably drag forces), and  $\vec{\bar{S}}$  is the fluid effective stress tensor.

For non-Brownian, neutrally bouyant, spherical particles dispersed in a Newtonian fluid in laminar flow and low volume (typically  $\phi < 0.05$ ), Jamshidi et al. [2019] obtained the following approximation.

$$\vec{\bar{S}} = p\vec{\bar{I}} - (1 + 2.5\phi)\mu\vec{\bar{\gamma}} \quad (5.8)$$

where  $\vec{\bar{\gamma}}$  is twice the deformation rate tensor. we can use the deformation rate tensor of the fluid because particle velocity rapidly tends to the surrounding fluid velocity (gradient of the mean particle velocity is close to the fluid velocity gradient).

In the gap of a Couette rheometer only the variations in radial directions are considered; taking a small gap, i.e.  $(R_e - R_i) \ll R_e$ , a Cartesian approximation can be used. The radial position in the gap is referred as  $x$  (unit vector  $\vec{u}_x$ ). On the internal wall  $x = 0$ , on the external wall  $x = e$ . The flow direction is referred as  $y$ .

For the fluid, only momentum balance in  $y$  direction is considered and only the shear stress  $\tau_{xy}$  is involved. Fluid velocity is assumed to be in  $y$  direction (unit vector  $\vec{u}_y$ ) its magnitude is referred as  $v_f$ ; hence:

$$(1 - \phi)\rho_f \frac{\partial v_f}{\partial t} + \frac{\partial \tau_{xy}}{\partial x} = f_{y,p \rightarrow f} \quad (5.9)$$

where  $f_{y,p \rightarrow f}$  is the sum of the forces exerted on the fluid by the particles located in the REV per unit volume in  $y$  direction. Since there is no variation in pressure nor in fluid velocity in  $y$  direction, the convective term of momentum and the pressure gradient term vanish.

In this equation  $\tau_{xy}$  accounts for the fluid/fluid interaction. Therefore, this term should take into account the increased viscous dissipation due the distortion of the streamlines caused by the simple presence of the particles. According to equation 5.8 Jamshidi et al. [2019], for dilute suspensions, it can be approximated by Einstein's correlation. Unfortunately, as per our knowledge, there is no available expression for higher volume fraction, which only integrates the additional stress due to streamlines distortion. As a case in point, the correlation of Batchelor and Green [1972] applies for higher volume fractions but includes lubrication interactions as well which are here directly calculated in the DEM part of the model. Thus, we intend to use Einstein [1905] expression for the effective viscosity even though it certainly underestimate the additional stress due to streamline distortion for intermediate solid volume fractions of  $0.05 < \phi < 0.3$ . At least, this relation (equation 5.11) takes into account that higher the particle volume fraction, the more the streamline are distorted, which increases viscous dissipation.

$$\tau_{xy} = -\mu_e(T_f, \phi) \frac{\partial v_f}{\partial x} \quad (5.10)$$

$$\mu_e(T, \phi) = \mu(T_f) \cdot (1 + 2.5\phi) \quad (5.11)$$

The energy balance for the fluid is :

$$(1 - \phi)\rho_f C_{pf} \frac{\partial T_f}{\partial t} + \frac{\partial q}{\partial x} = Q_{p \rightarrow f} + Q_{diss} \quad (5.12)$$

where

$$q = -\lambda \frac{\partial T_f}{\partial x} \quad (5.13)$$

where  $Q_{p \rightarrow f}$  is the sum of the heat fluxes from the particles to the fluid and  $Q_{diss}$  is the viscous dissipation of mechanical energy into heat due to the viscous forces.

$$Q_{diss} = \mu_e(T_f, \phi) \left( \frac{\partial v_f}{\partial x} \right)^2 \quad (5.14)$$

The external wall has zero velocity and imposed temperature evolution, say

$$x = e : v_f = 0 \text{ and } T_f = T_{e(t)}.$$

The internal wall has a given velocity, this corresponds to a strain controlled rheometer (constant global shear rate):

$$x = 0 : v_f = v_i = \dot{\gamma} \cdot e$$

The internal wall is also characterized by a given thermal inertia per unit surface ( $\frac{m_{iw}C_{p,iw}}{A_{iw}}$ ):

$$x = 0 : \frac{m_{iw}C_{p,iw}}{A_{iw}} \frac{dT_{iw}}{dt} = \lambda \frac{\partial T_f}{\partial x}$$

Periodic boundary conditions apply in  $y$  and  $z$  direction.

The trajectory of each particle of index  $i$  is given by :

$$m_i \frac{d^2 \vec{x}_i}{dt^2} = \vec{F}_{f \rightarrow i} + \sum_j \vec{F}_{j \rightarrow i} \quad (5.15)$$

with  $\vec{F}_{f \rightarrow i} = 6\pi\mu r_i (v_f \cdot \vec{u}_y - \vec{v}_i)$  (Stokes viscous drag force). Here,  $v_f$  is the fluid velocity interpolated at particle centre position  $\vec{x}_i$  (piecewise linear velocity profile is considered) and  $r_i$  is the radius of granule  $i$ .

The maximal observed particle/fluid relative velocity was about 1 mm/s in our case, the maximal granule diameter is around 50  $\mu\text{m}$ , and the lowest liquid viscosity is 0.32 mPa.s. Therefore, Reynolds number was always lower than 0.15, inertial effect is negligible and Stokes law is applicable. Therefore we can write that

$$F_{p \rightarrow f} = - \sum_{i \in REV} \frac{\vec{F}_{f \rightarrow i}}{V_{REV}} \cdot \vec{u}_y \quad (5.16)$$

Lubrication forces in the normal direction are expressed by the following expression. Only the first-order normal force is considered, a more detailed lubrication interaction [Kim and Karrila, 2013] will be integrated in further work.

$$\vec{F}_{j \rightarrow i} = 6\pi\mu r_i \frac{\beta^2}{(1 + \beta)^3} \frac{r_i + r_j}{h_{i,j,eff}} ((\vec{v}_i - \vec{v}_j) \cdot \vec{n}_{ij}) \vec{n}_{ij} \quad (5.17)$$

$$\vec{x}_{ij} = \vec{x}_j - \vec{x}_i$$

$$d_{ij} = |\vec{x}_{ij}|$$

$$\vec{n}_{ij} = \vec{x}_{ij} / d_{ij}$$

$$h_{ij} = d_{ij} - (r_i + r_j)$$

$\vec{n}_{ij}$  is the centre to centre unit vector and  $h_{ij}$  is the surface to surface distance.

$$h_{i,j,eff} = \max(h_{ij}, 0.005(r_i + r_j))$$

$$\beta = r_j / r_i$$

No gravity, no Brownian or repulsive forces were considered.

If two particles come in contact ( $h_{ij} < 0$ ) an instantaneous elastic rebound is assumed. Friction between particles are assumed negligible, this assumption should be reconsidered, especially for high volume fraction, since starch granules cannot be considered as smooth spheres. They exchange momentum  $\vec{P}$  in the normal direction  $\vec{n}_{ij}$  given by:

$$\vec{P}_{j \rightarrow i} = \frac{2m_i m_j}{m_i + m_j} ((\vec{v}_j - \vec{v}_i) \cdot \vec{n}_{ij}) \vec{n}_{ij} \quad (5.18)$$

$$m_i \delta \vec{v}_i = \vec{P}_{j \rightarrow i}; \quad m_j \delta \vec{v}_j = \vec{P}_{i \rightarrow j} \quad (5.19)$$

where  $\delta\vec{v}_i$  and  $\delta\vec{v}_j$  are the difference in velocities before and after the collision for particles  $i$  and  $j$  which are applied during next time step.

Elastic rebound was assumed on the internal and external walls ( $x = 0$  and  $x = e$ ). Periodic boundary conditions were assumed in  $y$  and  $z$  direction for both the particle and fluid phases.

Seth et al. [2006] have used a similar approach of elastohydrodynamic lubrication for microgels. However, they have used Hertzian contact model when particles touch each other in place of the instantaneous shocks in the model presented here. In their case with a high concentration suspension, a detailed contact model was essential because the volume fraction was higher than the random close packing fraction. In our case, the maximum volume fraction is about 30 %, much lower than the random close packing value of 68 % which was determined for our poly-disperse suspension using the methodology given in Farr and Groot [2009]. Thus, the current approach (instantaneous elastic collision) seems a valid approximation.

The temperature evolution of each particle is given by:

$$m_i C_{pp} \frac{dT_i}{dt} = Q_{f \rightarrow i} + Q_{ld} \quad (5.20)$$

with  $Q_{f \rightarrow i} = 4\pi r_i^2 h(T_f - T_i)$ ,  $h = Nu \frac{\lambda}{2r_i}$  and  $Nu \approx 2$ . Here,  $Q_{ld}$  is the dissipation term for the lubrication forces and drag. The same is calculated using the following expression:

$$Q_{ld} = \frac{1}{2} \sum_j [\vec{F}_{j \rightarrow i} \cdot (\vec{v}_i - \vec{v}_j)] + \vec{F}_{f \rightarrow i} \cdot (v_f \vec{u}_y - \vec{v}_i) \quad (5.21)$$

Initially the granules are randomly distributed, the fluid and particle velocity varies linearly in the gap and the temperature is uniform and equal to the minimal swelling temperature (60 °C)

Elsewhere researchers have often used fabric tensor to quantify anisotropy [Ness and Sun, 2016, Barreto et al., 2009]. However, fabric tensor is typically used for the cases of quasi-static systems and we have a dynamic system with almost no true contacts. This is why we consider ‘quasi-contact’ when the centre-centre distance between particle  $i$  and  $j$  is less than  $1.2(r_i + r_j)$  where  $r_i$  and  $r_j$  are the radius of granules  $i$  and  $j$ . There exists two definitions of fabric tensor and multiple definitions for the fabric deviator. Here, we follow the definitions as reported in Barreto et al. [2009]. They are as follows

$$\Omega_{ij} = \frac{1}{N_c} \sum_{k=1}^{N_c} n_i^k n_j^k \quad (5.22)$$

where  $N_c$  is the total number of quasi-contacts and  $n_i^k$  denotes the component of the normalized centre to centre vector in direction  $i$  for the  $k$ -th quasi-contact.

Thus, we have the fabric tensor which is a  $3 \times 3$  matrix. The eigenvectors give the dominant directions of these quasi-contacts. The eigenvalues ( $\Omega_1, \Omega_2 < \Omega_1, \Omega_3 < \Omega_2$ ) are called major, intermediate and minor magnitudes of the fabric tensor. In an isotropic situation  $\Omega_1 = \Omega_2 = \Omega_3$ . The deviator fabric is defined by the following equation as reported in Barreto et al. [2009]. The higher its value the more the configuration is anisotropic.

$$\Omega_d = \frac{1}{\sqrt{2}} [(\Omega_1 - \Omega_2)^2 + (\Omega_2 - \Omega_3)^2 + (\Omega_1 - \Omega_3)^2]^{0.5} \quad (5.23)$$

### 5.2.3 Numerical solving

The simulated domain was of 1 mm in  $x$ -direction ( $R_e - R_i$  of the Couette rheometer) and 200  $\mu\text{m}$  in the two other directions.

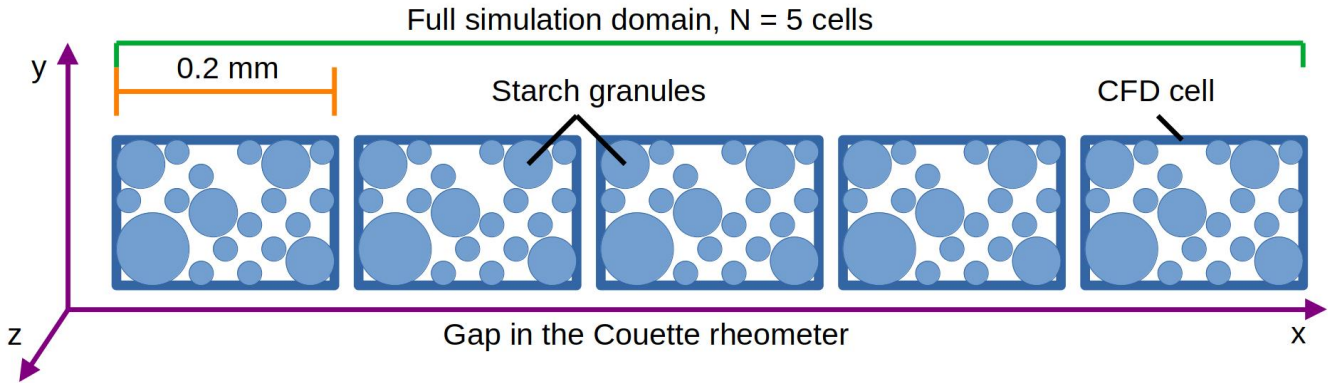


Figure 5.1: Simulation domain

Particle centroid method is used for coupling the DEM to the CFD. As the name suggested the entire particle is assigned to a particular cell based on the location of the centroid of the particle. This method is known to be accurate only when the fluid cell size is significantly larger than the diameter of the particle. Thus, the fluid equations were solved with the finite volume method with  $N = 5$  cells and initially 100 granules in each cell as a compromise. Also, if  $N$  is too low, the fluid velocity and temperature profile are not accurately represented and if  $N$  is too high, the number of granules in each cell becomes too low to be representative. To ensure periodic condition in  $y$  and  $z$  direction, for each particle at position  $(x, y, z)$  inside the domain, 4 mirror particles (same radius and velocity) were considered at  $(x, y + \Delta y, z)$ ,  $(x, y - \Delta y, z)$ ,  $(x, y, z + \Delta z)$  and  $(x, y, z - \Delta z)$ .

First, for each granule, its initial radius ( $r_0$ ), its maximum swelling ratio ( $r_{max}/r_0$ ) and its difficulty of swelling ( $\alpha$ ) are chosen from the distributions as defined in section 5.2.1. Then its position is randomly chosen to avoid any overlap. This is ensured by checking for overlap at every step and if overlap occurs a new position is chosen until there is no overlap. This methodology works as the initial volume fraction of the granules ( $\phi$ ) is very low.

At each time step, the swelling of each granule is calculated (according to the temperature history of the granule and difficulty of the swelling parameter) in order to re-evaluate its radius and mass. All the different forces and heat fluxes are then estimated. Finally, the velocities, temperatures (fluid and particles) and particle positions are actualized by an explicit first order scheme. Fluid velocity is assumed to be in  $y$  direction. Particle positions and velocities are calculated in 3D.

The maximum time step is dictated by the characteristic Stokes time ( $\rho r^2/\mu$ );  $\Delta t = 10^{-5}$  s was chosen (smallest granules having radius of about 3  $\mu\text{m}$ ). The code was implemented in Matlab [MATLAB, 2018]. For the fluid

(Eulerian part), the velocity and the temperature profiles were considered as piecewise linear and an explicit first order scheme was used.

The presented results correspond mainly to one simulation of  $N = 5$  cubic cells with a side length of 0.2 mm each. In each cell, 100 granules were initially randomly located. This allows comparing what happens with the granules depending on their initial position in the gap. The average shear rate was of  $10 \text{ s}^{-1}$  (internal wall velocity 10 mm/s). The precise results depend on the initial position and radius of the granules, four sets of random initial conditions were simulated. The results were comparable and the reported analyze (trends, dominant phenomena, etc..) applies also for the other runs. A comparison between two runs for the evolution of some key variables is presented and the variability of some parameter between the four runs is also presented.

The simulation duration was of 1 min, during which the external wall temperature increased linearly from 60 to 90 °C. The mean volume fraction was initially 2.6 % and 30.0 % at the end of the simulation. If all the granules were completely swollen the volume fraction would have been 32.8 %, so on average, 91 % of the possible swelling is achieved after 1 min of heating.

The liquid properties are those of pure water:

$$C_p = 4180 \text{ J.K}^{-1} . \text{kg}^{-1}$$

$$\lambda_f = 0.6 \text{ W.m}^{-1} . \text{K}^{-1}$$

$$\mu = 2.414 \cdot 10^{-5} \cdot 10^{(247.8/(T_f+133))} \text{ Pa.s where } T_f \text{ is in } ^\circ\text{C}.$$

The starch gelatinization enthalpy was neglected. In fact, the enthalpy of gelatinization is less than 10 kJ per kg of dry starch [Desam et al., 2018a, Li et al., 2020], which corresponds to 0.3 kJ per kg of suspension. This is negligible compared to the sensible heat increase from 60 to 90 °C, which is about 125 kJ per kg of suspension.

## 5.2.4 Results and discussion

Figure 5.2 a presents at 5 different instants the temperature profile of the fluid vs position in the gap. Similarly, Figure 5.2b shows the temperature profile of the 500 granules and of surrounding fluid vs position in the gap at a time of 30 s from the start of simulation. The temperature of the particles is always very close to the local fluid temperature as shown in Figure 5.2b. Figure 5.2c shows the temperature difference between the granule and the surrounding fluid. The pattern observed is an artifact and is due to the approximations arising due to the finite elements of the CFD cells. The maximum temperature difference observed is around 0.02 °C. This is always the case irrespective of the time. This can be explained by the very short characteristic time to reach thermal equilibrium. If we consider the energy balance of one particle (taking into account only the heat exchange with the fluid):  $m_p C_{pp} \frac{dT_i}{dt} = hS(T_f - T_i)$ .

A characteristic time appears as follows:  $t_{th} = m_p C_{pp} / (h.S)$ , where  $S$  is the surface area of the particle and  $h$  is obtained considering  $Nu = 2$ . This results in a  $t_{th}$  which is less than 1 ms. The profile is nearly linear, the external/internal temperature difference reaches about 5 °C. The viscous dissipation of mechanical energy into heat is negligible compared to the conductive heat flux even at the end of the simulation. From Figure b (presented later) it appears that the dissipation is less than  $0.2 \text{ W/m}^3$ , this is much lower than the sensible heat increase of the fluid whose temperature increases by  $\Delta T = 30 \text{ } ^\circ\text{C}$  in  $\Delta t = 60 \text{ s}$ . In our case,  $\rho_f C_{pf} \Delta T / \Delta t$  is about  $2 \cdot 10^6 \text{ W/m}^3$ .

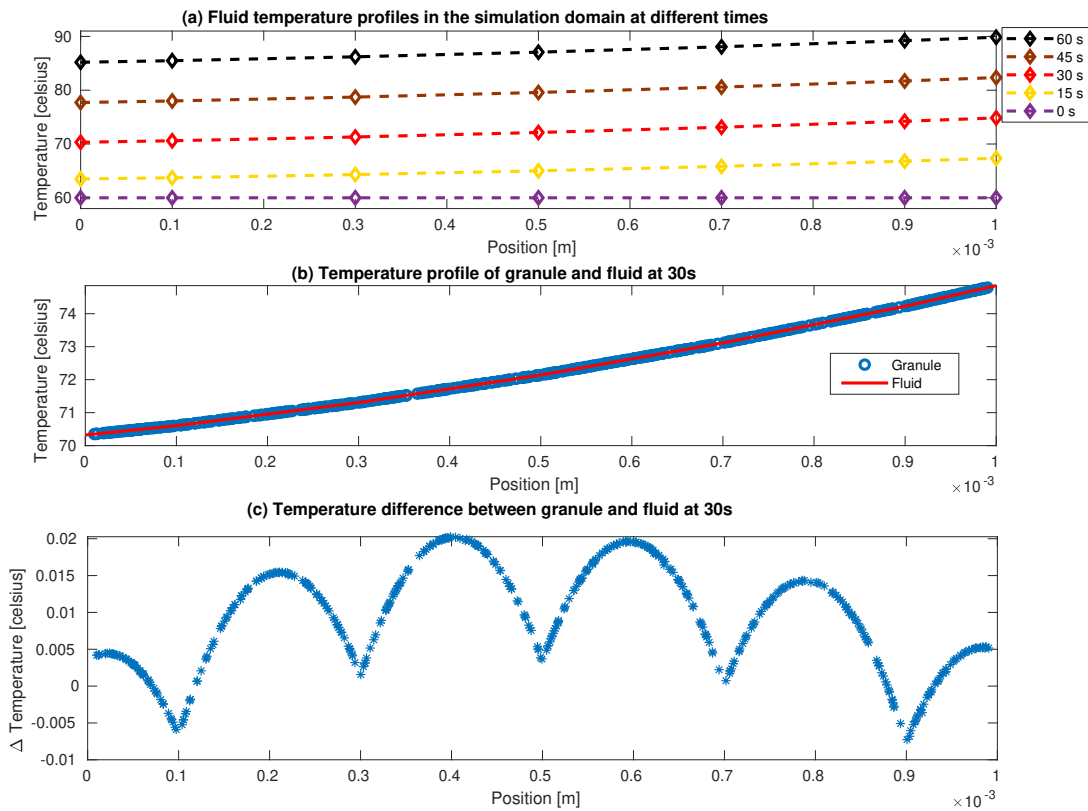


Figure 5.2: Temperature of granules and fluid

Figure 5.3 presents at 9 different time instants, the fluid and particles velocity profiles ( $v_y$  vs  $x$ ). Cumulative particle density is superimposed, i.e. the fraction of particles whose centre is at a position lower than  $x$ . For a uniform distribution, this line would correspond to a straight line. From this we can see that near the wall there is a region where particles are absent and this region increases slightly as the swelling increases. This is arising due to the wall effects as there exists a minimum distance of particle radius between the centre of the particle and the wall (around  $20 \mu\text{m}$ ).

At a given time, since the curvature is ignored, the shear stress is almost constant throughout the gap, i.e. versus  $x$  in a quasi steady state approximation. This is not exactly true since the particles are growing and moving during the time, but it should apply on average. Therefore, if we assume that the shear stress is almost the same across the rheometer gap, at the beginning of the simulation, one could expect a higher velocity gradient near the heated wall where the viscosity of the continuous phase is lower. This effect is observed at  $t = 15 \text{ s}$ , the local shear rate varies monotonically between  $9.8 \text{ s}^{-1}$  to  $10.2 \text{ s}^{-1}$  from internal to an external wall. However, this variation is very small because of the limited temperature difference. At the later instances when granules swell first near the external wall, the opposite effect is expected because the suspension viscosity will be higher due to the increased volume fraction of the granules. A lower shear rate is effectively observed near the heated wall ( $10.7 \text{ s}^{-1}$ ) than near the internal wall ( $12.2 \text{ s}^{-1}$ ) at  $t = 45 \text{ s}$ . But in the same time, the particle density decreases near the wall. This explains that the velocity gradient is higher than the average one ( $10 \text{ s}^{-1}$ ) near the wall and reaches its minimum value ( $8 \text{ s}^{-1}$ )

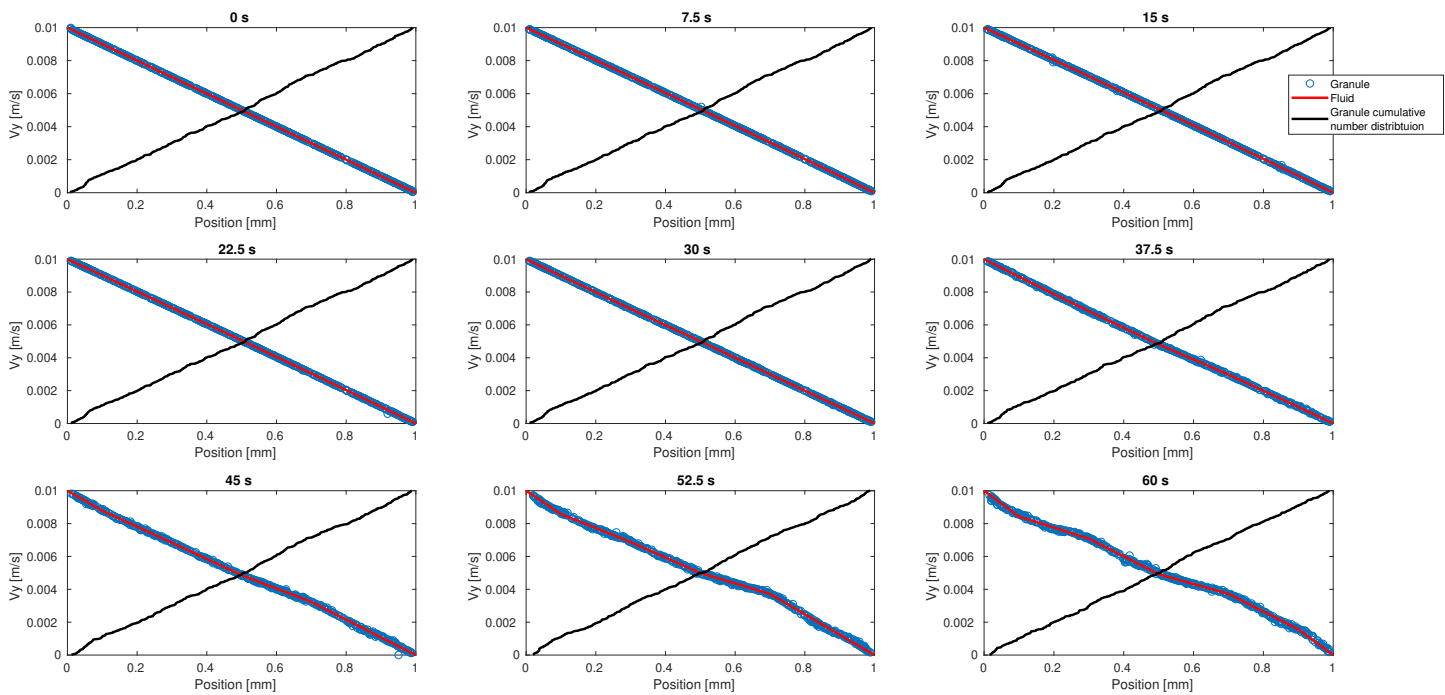


Figure 5.3: velocity of granules and fluid

near the centre of the gap. This phenomenon of depletion of particles near the wall and subsequent higher shear rate is discussed in Coussot [2016]. In addition, the interaction between a particle and the smooth wall generates no friction contrary to the interaction between particles. This highlights that the boundary effects are not completely negligible even for a low ratio of particle diameter to gap width, which is about 4 % in our case. In future works the impact of wall lubrication forces and friction forces can be interesting to investigate. It is also observed that the particle velocity fluctuations increase with time. This is because the granules swell and occupy more volume and they interact more and more in a random manner.

Figure 5.4, shows a  $xy$  section (at middle  $z$  position) of the gap at 9 different instants. The granule swelling begins significantly after about 30 s. As we expected a higher degree of swelling is observed near the external heated wall (right side of the graphs) but the difference through the gap appears small, perhaps because of the particle movements. It should be noted that the swelling model was developed by observing a very dilute suspension without any motion or collision and here, we employ the same in presence of particle interactions, these interactions could modify the swelling kinetics. This should be investigated further. In the figure 5.4 at 60 s, we see a small grouping of particles.

Figure 5.5 shows some parameters evolution as the simulation progresses. Here we show two runs of the simulation with different initial properties(radius, swelling difficulty) and positions of the starch granules (reference case at left). Figure 5.5a shows the evolution of fluid temperature at the internal and external walls and in the middle of the gap. There is a time lag for the temperature rise from external to internal wall of about 10 s. Figure 5.5b presents the evolution of the mean granule radius over the entire gap, only for the internal cell and only for the

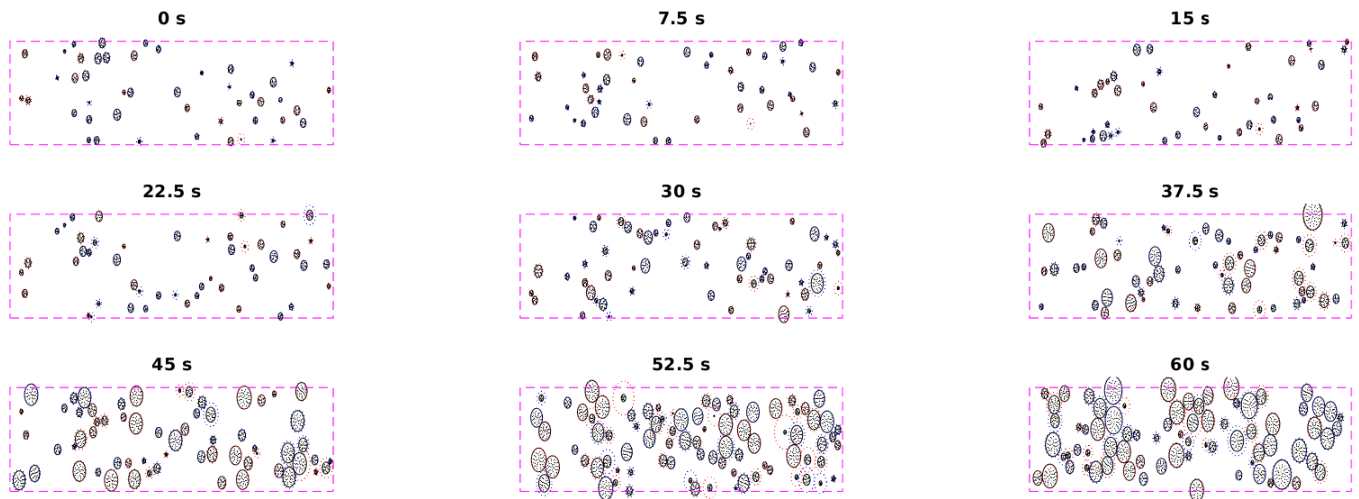


Figure 5.4: xy cross section of the simulation domain

external cell. The granules begin to swell significantly near the external heated wall when its temperature reaches around 70 °C. Similar to the temperature, there is also a time delay for granule swelling from the external to the internal wall. Figure 5.5c presents the evolution of the mean particle volume fraction  $\phi$  over all the gap, the internal cell and the outer cell. These time series are directly related to those of granules radius. Near the heated external wall, the volume fraction reaches a plateau whereas the mean value over the gap and the value near the internal (colder) wall are still increasing at the end of heating time of 1 min. Figure 5.5d shows the evolution of the wall shear stress. Shear stress first decreases slightly because when the temperature is increased, liquid viscosity decreases. But when the volume fraction reaches about 10 %, the shear stress increases significantly. The swelling effect then becomes predominant compared to liquid viscosity decrease. This stress is mainly due to the viscous friction between the fluid layers (represented here by the 5 cells). This friction is proportional to the effective viscosity which increases with the particles volume fraction. Another contribution of global stress is due to the movement of the particle relative to the fluid because of the lubrication forces and the collisions. For example, one particle located near the internal wall with a high velocity in the  $y$ -direction can move toward a more external zone, and then via the Stokes forces, it will communicate some momentum (in the  $y$ -direction) to this new fluid layer. Alternatively, it can also interact with slower particles of this layer. For a given run, the shear stress on the internal and external wall are almost equal at a given time. Random collisions can explain these fluctuations and the small differences between internal and external values. Nevertheless, averagely constant shear stress across the gap seems ensured.

From figure 5.5, it can be observed that the temperature evolution is the same for the two runs. The mean radius and volume fraction evolutions over the whole gap are slightly different between the two runs. This can be explained by a small difference in initial volume fraction (run 1: 2.6 % ; run 2: 2.9 %) as well as differences in swelling difficulty and swelling ratio which are randomly chosen. When we observe the internal or external cells, there are more fluctuations because of the random walk of the particles. The most important difference between the two runs is observed for the shear stress ( $\tau_{xy}$ ). Initially the time series are almost the same, but when swelling

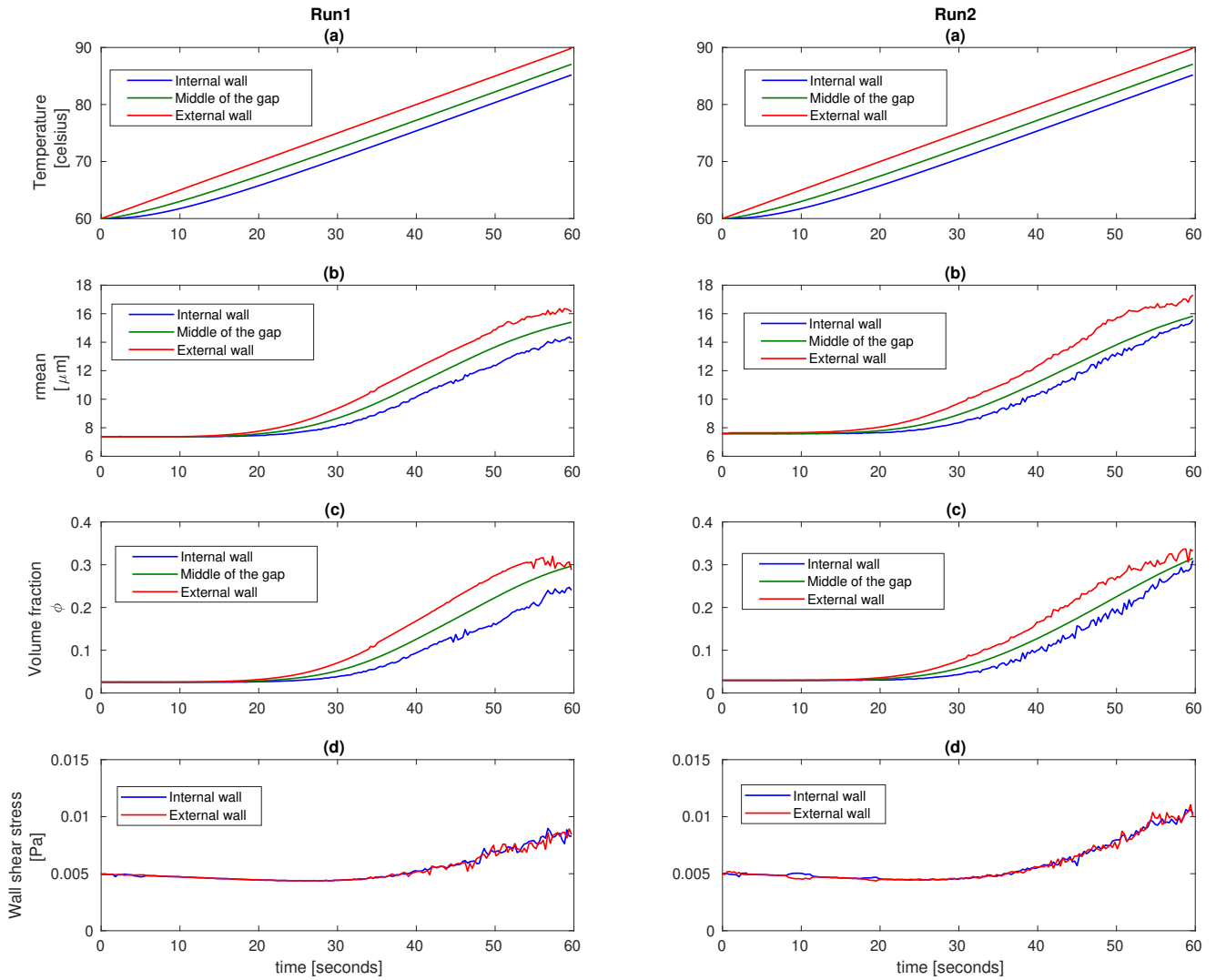


Figure 5.5: Time evolution of suspension parameters at different regions of the simulation domain

becomes significant ( $t > 30$  s) the shear stress becomes higher for run 2. This can be explained by a slightly higher volume fraction (at the end of simulation run1: 30 %, run2: 32 %) this leads to a higher effective viscosity but also to an increase of particle/particle interactions (collisions and lubrication).

Table 5.1: Variability between runs

	$\phi_{initial}(\%)$	$\phi_{final}(\%)$	$T_{iwfinal}$ ( $^{\circ}C$ )	$\tau_{xyfinal}^*$ ( $mPa$ )	$D_{rwfinal}^*$ ( $\mu m^2/s$ )	$\Omega_{d,final}^*$	$d_{nn,final}$ ( $\mu m$ )
run1	2.6	30.0	85.20	8.1	79	0.060	31.2
run2	2.9	31.5	85.20	9.9	76	0.065	31.9
run3	2.5	24.5	85.20	7.3	56	0.073	30.9
run4	2.7	30.2	85.20	8.7	82	0.067	31.2
mean	2.7	29.1	85.20	8.5	73	0.066	31.3
std	0.2	3.1	< 0.01	1.1	12	0.005	0.4

\* average for  $55 \text{ s} < t < 60 \text{ s}$

Table 5.1 presents the variability of some parameters between the four runs (some of them will be presented later). The variability is mainly linked to the range of initial volume fraction. For example run 3 has the lowest initial value of  $\phi$  and logically the shear stress and the random walk diffusivity ( $D_{rw}$ ) are also the lowest. Variability could be reduced by increasing box sizes in  $y$  and  $z$  direction. To compare easier different runs, the particle properties could be fixed and only the initial position could be varied. To obtain precise quantitative values, average over large number of simulations could be taken. Nevertheless the trends are the same and the phenomena analyzed of run 1 applies also to the other runs. In the following only results for run 1 are presented.

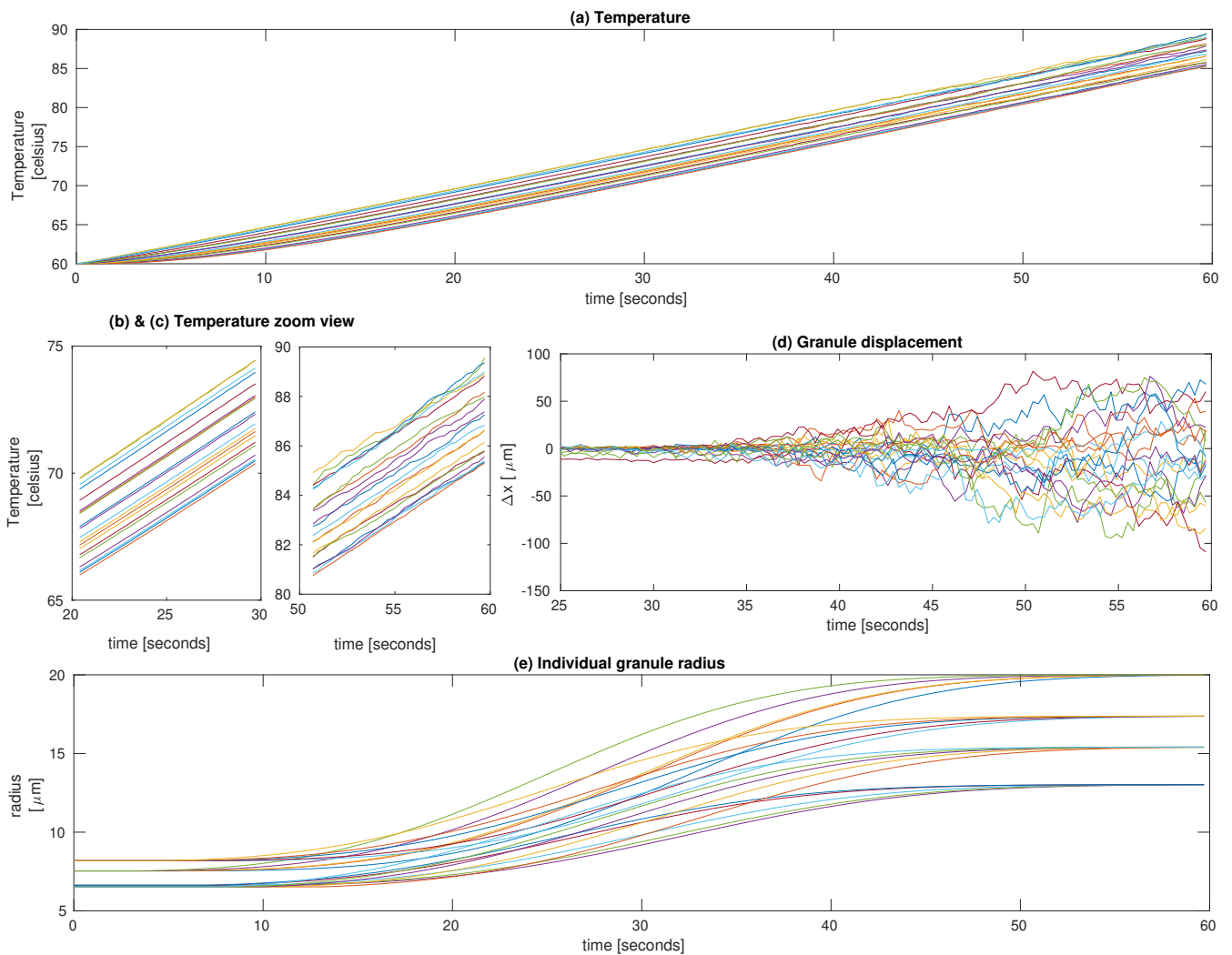


Figure 5.6: Sample granule properties evolution during simulation

To illustrate the movement of the particles inside the gap, Figure 5.6d presents the time evolution of the  $x$ -displacement of 20 particles (initially 4 particles in each of the 5 cells). At the beginning of the simulation, the granules are small, they interact only weakly by lubrication forces; random walk of low amplitude is observed. After about 40 s, when the volume fraction reaches about 10 % (see Fig 5c), the grain grain interactions induce a

random walk movement which becomes more significant and the displacement sometimes exceed 100  $\mu\text{m}$ , which is not negligible compared to the gap width. Figure 5.6a presents the temperature evolution of these particles. In the beginning, the particle temperatures increase smoothly but when a random walk becomes significant, small fluctuations appear as can be observed in the zoom view in figure 5.6b and 5.6c. This means that the particle moves randomly between layers of different temperatures (more or less close to the heating wall). When a particle moves towards a cold layer, heat is transferred from this particle to the fluid. This participates in heat transfer from the external to the internal wall. Figure 5.6e presents the radius evolution of these 20 particles. Initially, the four tracked particles in a cell have the same radius and the difficulty to swell as the four particles in the other cells to see the influence of the initial position in the gap of identical granules. As expected, the particles close to the heating wall begin to swell earlier and faster.

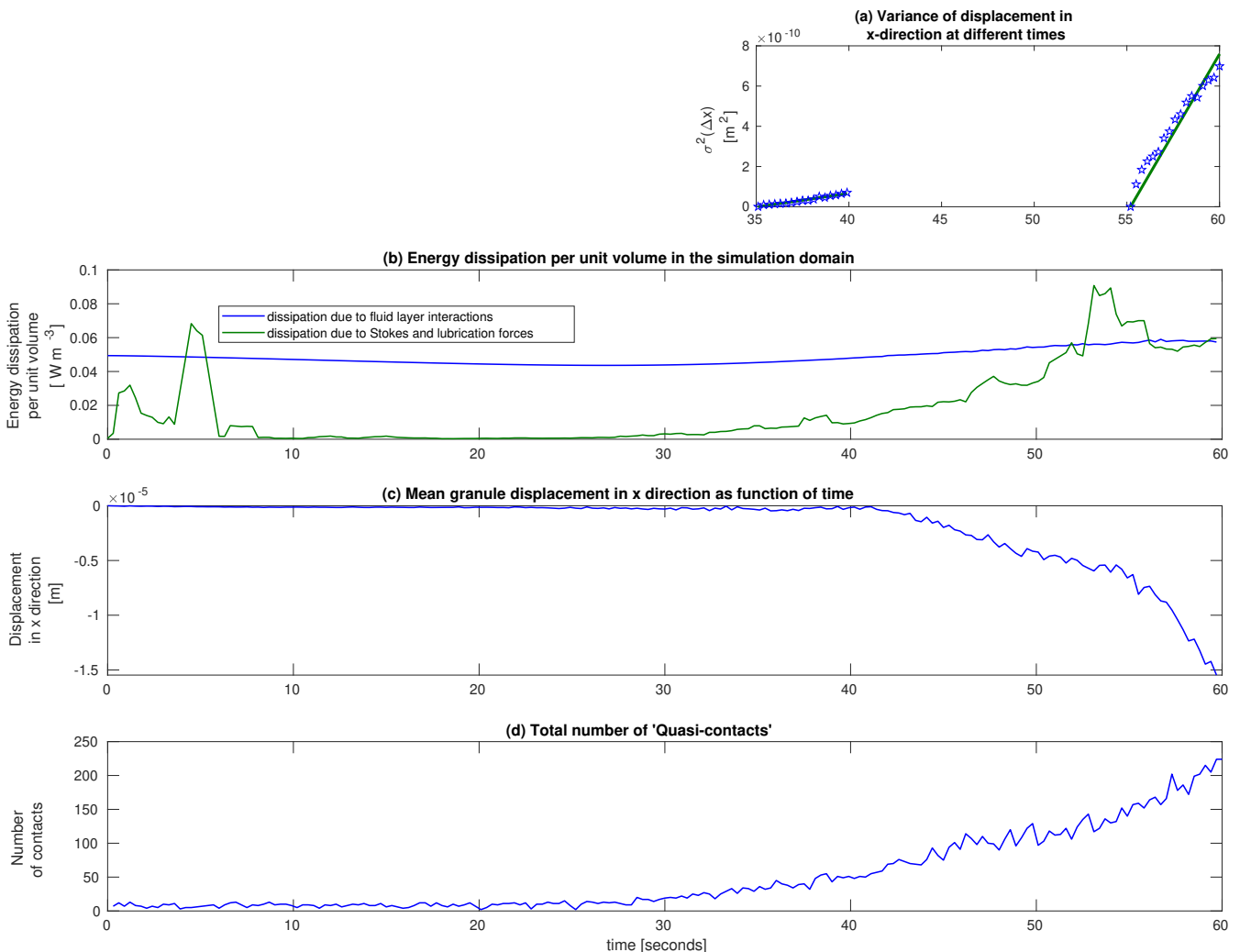


Figure 5.7: Granule population properties evolution with time

Figure 5.7a presents the variance of displacement ( $\sigma^2$ ) in  $x$ -direction of all the particles respectively from 35 to

40 s ( $\phi \approx 10\%$ ) and from 55 to 60 s ( $\phi \approx 30\%$ ). For one-dimensional random walk it is expected that  $\sigma^2 \approx 2D_{rw}t$  where  $D_{rw}$  is the self-diffusivity of the particles. Different formulas are given in [Leighton and Acrivos \[1987\]](#), in a first approach the findings of [Eckstein et al. \[1977\]](#) can be used.

$$\frac{D_{rw}}{r^2\dot{\gamma}} \approx \frac{\phi}{10} \quad (5.24)$$

In our case  $\dot{\gamma} = 10 \text{ s}^{-1}$ ; when  $\phi \approx 10\%$  most of the granules are unswollen, mean radius is about  $7 \mu\text{m}$  and when  $\phi \approx 30\%$  mean radius is about  $17 \mu\text{m}$ , based on this formula the self-diffusivity is expected to be around  $4.9 \cdot 10^{-12} \text{ m}^2/\text{s}$  and  $8.7 \cdot 10^{-11} \text{ m}^2/\text{s}$  respectively. This is close to our estimates of  $D_{rw}$ , which is  $5 \cdot 10^{-12}$  and  $1 \cdot 10^{-10} \text{ m}^2/\text{s}$  for these periods respectively (values obtained by linear regression). This is much higher than the Brownian diffusivity of the particles due to the thermal agitation (collisions of the water molecules on the granules)  $D_B = \frac{k_B T}{6\pi\mu r} \approx 5 \cdot 10^{-14} \text{ m}^2\text{s}^{-1}$ .

The self-diffusivity due to the random walk of the particles is notably a function of the volume fraction (as shown here) and of the shear rate as shown in the literature [[Leighton and Acrivos, 1987](#)]. Its value can be interesting to analyze in other situations, like heat treatment of starch suspension. For example, for a tubular heat exchanger (tube radius  $R_t$ , residence time  $t_r$ ), it can reasonably be assumed that the particles follow the fluid flow only if  $\sqrt{D_{rw}t_r} \ll R_t$ .

As explained earlier, the random walk of the particles participates to heat transfer. It is expected that the apparent conductivity is increased by about  $\phi\rho_p C_{pp} D_{rw}$ . The order of magnitude of this additional conductivity (about  $10^{-4} \text{ W}\cdot\text{m}^{-1}\cdot\text{K}^{-1}$ ) is however low compared to the ordinary conductivity of water (about  $0.6 \text{ W}\cdot\text{m}^{-1}\cdot\text{K}^{-1}$ ). When this kind of heat transfer is switched off ( $Nu = 0$ ) there is almost no difference ( $< 0.15 \text{ }^\circ\text{C}$ ) in the heating rate of the internal wall.

To identify the part of the friction due to particle random walk, Figure 5.7b presents the evolution of the dissipation due to viscous friction between layers of fluid and the dissipation due to lubrication and drag forces (per unit volume:  $\text{W}\cdot\text{m}^{-3}$ ). The total dissipation is the product of the wall shear stress and the global shear rate. So this figure illustrates how the shear stress and similarly the mixture apparent viscosity evolve and which part is due to fluid/fluid interaction and particle/particle/fluid interactions. The fluid/fluid interaction first decreases because the liquid viscosity decreases when temperature rises. Then it increases because the solid volume fraction increases which enhances the distortion of the fluid streamlines. The particle/particle/fluid interaction (lubrication and drag) is first very low ( $t < 30 \text{ s}$ ) except at the simulation starting. Initially, due to the random localisation, some particles are very close to another, this leads to some collisions. Then the lubrication forces tend these particles to move away from each other. When the volume fraction becomes significant ( $t > 30 \text{ s}$ ) and the particles moves randomly across the gap, the particle/particle interaction increases significantly the friction, or in other terms, the mixture apparent viscosity.

At the end of the simulation ( $\phi \approx 0.30$ ), the two contributions are of the same order. This highlights the importance of particle random walk in the rheology evolution of a starch suspension.

As shown previously, swelling begins near the heated wall. In addition to the random walk, a global particle migration from the zone of highest volume fraction (near the heated wall) towards zones of lower volume fraction

(near the internal wall) is expected.

Figure 5.7c shows the mean displacement in the  $x$ -direction of the granules initially located in the cell near the heated wall vs time. The phenomenon starts effectively with the swelling but it remains small: only about 15  $\mu\text{m}$ . Part of this displacement is simply due to the fact that the centre of the particles is at least one radius from the wall. This is on average 7  $\mu\text{m}$  initially and 17  $\mu\text{m}$  once the granules are swollen. Another part is due to diffusion in the direction opposite to the volume fraction gradient, but this gradient remains weak (Fig5c). It would be interesting in further work to relate particle migration to gradients in osmotic pressure as proposed by [Vollebregt et al. \[2010\]](#) but this is not easy in our case due to the heterogeneity across the gap. Thus, we can see that the granule migration towards the internal walls is significant only when the granules begin to swell. The temperature gradient and velocity gradients, which exist initially, do not lead to any significant diffusion unless the granules begin to swell.

The figure 5.7d shows the number of quasi contacts defined by the criteria that centre to centre distance between particles is less than  $1.2 \times (r_i + r_j)$ . Initially when the starch granules are in an unswollen state the number of quasi-contacts are too low to determine the fabric tensor. When this number exceeded 100, the fabric deviator was found to be less than 0.1. At the end of the simulation, the fabric tensor is as follows

$$\Omega_{ij,run1} = \begin{bmatrix} 0.3549 & -0.0009 & -0.0027 \\ -0.0009 & 0.3151 & -0.0025 \\ -0.0027 & -0.0025 & 0.3300 \end{bmatrix} \quad (5.25)$$

and the fabric deviator,  $\Omega_{d,run1} = 0.060$ .

One can see very faint anisotropy based on these metrics in the system as the non-diagonal elements are very smaller than the unity. For perfect isotropy, all the non-diagonal elements are equal to zero.

The quadratic mean velocity components of the particles (relative to the fluid) in  $x$ ,  $y$  and  $z$ -direction at the end of the simulation are respectively 0.097, 0.096 and 0.050 mm/s. Particle agitation is anisotropic, this can be explained by the particular direction of shear (in the velocity gradient only the term  $\frac{\partial v_y}{\partial x} \neq 0$ ). This finding is coherent with the results of [Breedveld et al. \[1998\]](#) which found that the self diffusivity was 1.7 higher in the velocity gradient direction than in the other direction. A characteristic distance before direction change (like mean free path before the collision) can be obtained by dividing  $2D_{rw}$  by the quadratic mean velocity. The order of magnitude is of some microns at the end of the simulation.

In figure 5.8a the pair correlation function or otherwise known as radial distribution function, which represents the probability of finding another particle at a given distance from the centre of a representative particle. Initially the particles have a low volume fraction and hence the pair correlation function is fairly flat. At the end of the simulation particle swelling and increase in volume fractions lead to a peak at around 45  $\mu\text{m}$ .

Figure 5.8b shows the cumulative distribution of the centre to the centre distance to the nearest neighbour at the beginning and the end of the simulation. The centre to centre average distance increases from 25.7  $\mu\text{m}$  (initial random positioning) to 31.2  $\mu\text{m}$  at the end of the simulation. The particles tend to increase their mutual distance, by the swelling effect and by the lubrication forces. However, the final value is far from the maximal possible distance (hexagonal arrangement) :  $2^{1/6}(V_{box}/I)^{1/3} = 48 \mu\text{m}$  in our case. It was mentioned previously that the particles

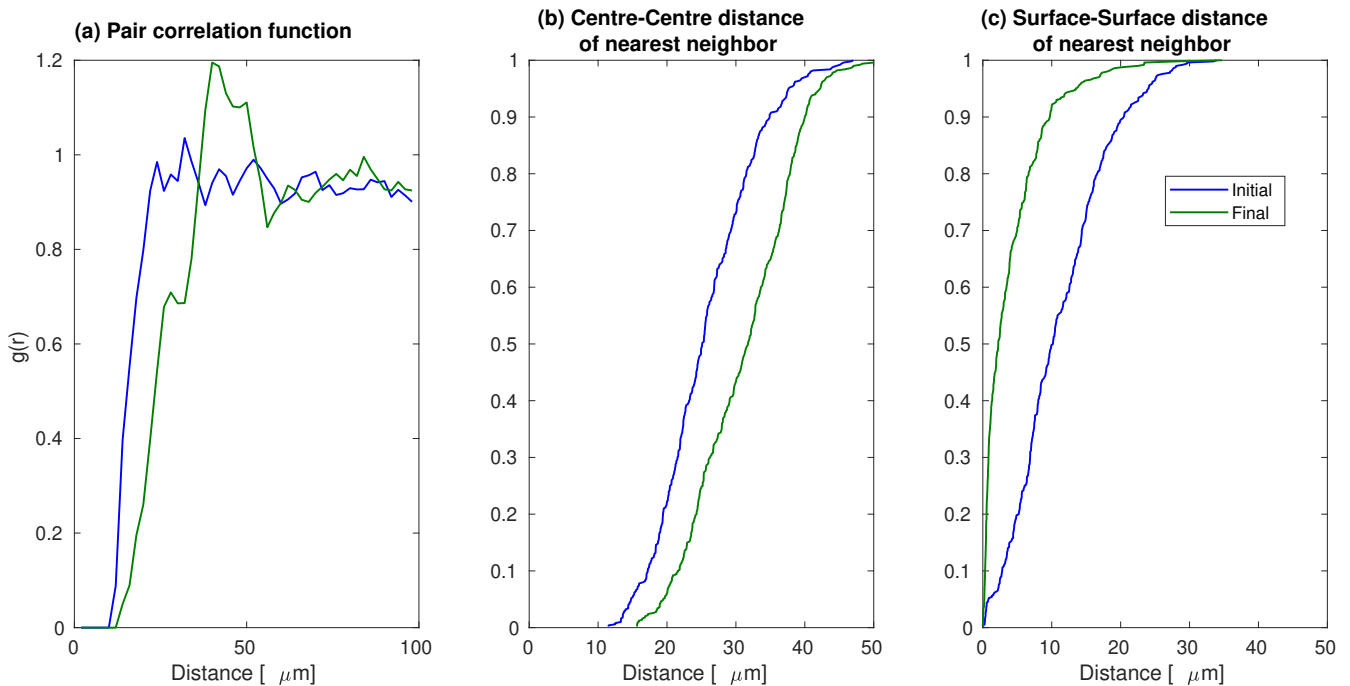


Figure 5.8: cumulative distributions of distance from neighbors

velocity fluctuations are not isotropic. Indeed, alignment in  $y$ -direction could reduce friction (diminish dissipation) as expected from the minimal entropy production principle proposed by Prigogine [Prigogine, 1978]. From the visual observation of Figure 5.4, such trends are not obvious even at the final instant, two zones orientated in the  $y$ -direction of lower particle density seem to be present. Therefore, to quantify possible heterogeneity/anisotropy of particles repartition in addition to the fabric tensor discussed previously, the position of the nearest neighbour of all the particles were analyzed. The root mean squared average distance to the closest neighbour of each particle in  $x$ ,  $y$  and  $z$  directions at the end of the simulation are respectively 19.1, 17.5 and 18.8 μm. This indicates a small trend toward alignment in the  $y$ -direction (lower  $y$ -direction distance, higher  $x$ -direction distance). Isothermal simulations at different shear rates (not presented here) indicate that the alignment trend increases with the shear rate which could imply shear thinning. This has to be confirmed by further work. Figure 5.8c shows the distribution of the surface to the surface distance to the closest neighbour. The mean distance decreases from 11.1 to 4.0 μm as expected since the volume fraction increases from 2.6 to 30 %. For about 35 % of the particles, the closet neighbour is at less than 1μm at the end of the simulation.

### 5.3 Conclusion

Starch granules swelling inside a heated Couette rheometer is simulated using a CFD-DEM model with a kinetic model for granule swelling. One can see, as expected that the sample is not uniform across the rheometer gap and the same has been quantified through various parameters. The velocity profile is not always linear except at the start of the simulation. The particle temperature is very close to the temperature of the nearby fluid always. It is also showed that random walk of the particles (self diffusivity) arising due to the lubrication force is significant. There is

a small migration of particles from the outer walls to the inner cells. The transport of heat by particles is negligible compared to heat transfer by the fluid.

A small anisotropy exists in the direction of shear for the position of the particles in the system. This study was limited to a volume fraction of about 30 % whereas volume fraction up to 70 % are common in processing. For higher volume fraction, thermal effects are still expected to be negligible. However, the particle-particle and particle-fluid interaction will dominate the fluid-fluid interaction. The lubrication/drag interactions and contact frictions will gain prominence; thus, warranting a pure DEM approach by neglecting the fluid phase at  $\phi$  close to  $\phi_{rcp}$ . This model should be enhanced, to account for the shear-thinning behaviour which is experimentally observed for gelatinized starch suspensions of intermediate solid volume fraction. Further work could integrate full lubrication terms along with angular velocity components as well as lubrication forces between the walls and particles. In conclusion, this work gives insights into the important phenomena that one needs to consider during thermo-mechanical treatment of starch suspensions.

## 5.4 Acknowledgments

This research has been carried out with funding from European Union as part of EU RESEARCH FRAMEWORK PROGRAMME: H2020 / Marie Skłodowska-Curie Actions ITN MATHEGRAM [813202]. We acknowledge and thank the organizers of the conference Dr. Ruud Vandersman and Dr. Duynhoven John Van. We thank the participants of the conference for their comments, suggestions and inputs. [Palanisamy \[2021\]](#) is the conference presentation corresponding to this article.

## Conclusion (version française)

La gélatinisation de l'amidon à l'intérieur d'un rhéomètre de Couette chauffé a été simulé à l'aide d'un modèle CFD-DEM couplé à un modèle cinétique de gonflement des granules. On peut voir, comme prévu, que l'échantillon n'est pas uniforme à travers l'entrefer du rhéomètre. Le profil de vitesse n'est pas toujours linéaire sauf au début de la simulation. La température des particules est toujours très proche de la température du fluide voisin. Il est également montré que la marche aléatoire des particules (diffusivité) résultant des forces de lubrification est significative. De plus, il y a une légère migration globale de particules de la paroi externe chauffée vers l'intérieur. Le transport de chaleur par les particules est négligeable par rapport au transfert de chaleur par le fluide.

Une légère anisotropie existe dans la direction du cisaillement pour la position des particules dans le système (léger effet d'alignement). Cette étude s'est limitée à une fraction volumique d'environ 30% alors que des fractions volumiques allant jusqu'à 70% sont courantes dans la pratique. Pour une fraction volumique plus élevée, les effets thermiques devraient toujours être négligeables. Cependant, l'interaction particule-particule et particule-fluide dominera l'interaction fluide-fluide. Les interactions lubrification/traînée et les frottements de contact prendront de l'importance ; ceci justifierait une approche DEM (sans couplage CFD) en négligeant la phase fluide.

Ce modèle devrait être amélioré, pour tenir compte du comportement rhéofluidifiant qui est observé expérimentalement pour les suspensions d'amidon gélatinisé de fraction volumique intermédiaire. De futurs travaux pourraient intégrer des termes de lubrification plus complets, la rotation des particules ainsi que des forces de lubrification entre les parois et les particules. En conclusion, ce travail donne un aperçu des phénomènes importants que l'on doit considérer lors du traitement thermomécanique des suspensions d'amidon.

# Chapter 6

## General conclusion and outlooks

### 6.1 Take away from this thesis (Everything that remains)

The objective of this thesis was to decipher the impact of temperature and thermal history on the physical properties of starch granule suspensions, most notably rheology. Experiments and simulations were carried out for a chemically modified waxy-maize starch. The impact of volume fraction of solids on the rheology of suspension has been known since the works of [Einstein \[1905\]](#). Later, advanced empirical models to predict the viscosity of suspension such as Maron-Pierce-Quemada has shown the importance of the knowledge of the random close packing volume fraction of solid-phase  $\phi_{rcp}$  [Maron and Pierce \[1956\]](#), [Quemada \[1977\]](#). [Farr and Groot \[2009\]](#) proposed a method that could be used to predict the  $\phi_{rcp}$  given the poly-dispersity. Thus, accurately capturing the evolution of the solid phase properties such as particle size distribution for starch in water suspension is quintessential for deciphering rheology. Given the ambivalence of starch in industrial applications as a viscosity enhancer, there exist previous works on modelling starch swelling albeit with limited resolution capturing only the mean particle size evolution given time-temperature history. In a first approach, we propose (for the studied starch) a kinetic model for starch swelling in water at the inter-granular resolution allowing the prediction of the complete size distribution.

Starch granule material properties are expected to change during the swelling process. It is a known phenomenon that un-swollen corn starch in water suspensions are shear-thickening at large volume fraction. [Ness and Sun \[2016\]](#) showed that the onset of frictional contacts are at the origin of shear-thickening and one can in theory tune the granule material properties to modify the range (shear rate and volume fraction) at which shear thickening occurs through simulations. [Shewan and Stokes \[2015b\]](#) has shown experimentally that if the granule Young's modulus is greater than 185 kPa, the suspension could be considered hard particle suspension. We showed through experimental characterization such as bulk rheology and osmotic compression that the average swollen starch Young's modulus is around 1.8 kPa (for the studied starch). Nano-indentation coupled with scanning electron microscope was used to estimate that Young's modulus of native unswollen maize starch is around 2 GPa. Thus, this shows that starch suspension transitions from hard particle suspension (when unswollen) to soft particle suspension (when fully swollen) along with a large increase in solid phase volume fraction. It was also shown that shear modulus of suspension is independent of temperature for fully swollen starch in water suspension in the range of 20 °C to 90 °C. Thus, it could be inferred that starch granule material properties change drastically during temperature-induced swelling but properties of fully swollen starch granule modulus are independent of temperature in this range.

Partially swollen or fully swollen chemically modified waxy maize starch at certain volume fractions and shear rates are shown to exhibit shear-thinning behaviour [Plana-Fattori et al. \[2016\]](#). Unlike shear-thickening there is no

equivocal answer to the origin of shear-thinning in suspensions. Some are listed as follows:

- [Chatté et al. \[2018\]](#) proposed the excluded volume effect when particles come in contact with each other. They suggested that the hair-like projection on the particle surfaces could lead to soft contact called 'lubricated contacts' leading to shear thinning behaviour. If the core of the particle is hard, this could lead to frictional contact as shown by [Ness and Sun \[2016\]](#) and lead to shear-thickening after shear-thinning.
- [Vázquez-Quesada et al. \[2016\]](#) proposed the hypothesis that continuous phase could break down and is shear-thinning at very high shear rates at the interparticle gaps. They showed that the shear rate experienced by the interstitial fluid particles can be 3 orders of magnitude greater than the global shear rate.
- [Lobry et al. \[2019\]](#) proposed a variable friction model and showed shear-thinning through simulations. They argued that particle friction decreases as the normal force at the contact points increases. [More and Ardekani \[2020\]](#) went on a step further and added the plasticity of contacts arising due to the asperities on the surface of the particles. The asperities are modelled as a concentric ring on the particle.

However, for chemically modified waxy maize starch in the water system, the origin of shear-thinning is shown to be soft particle contacts. This is shown through a combination of experiments and simulations. Through rheological experiments of fully swollen starch granule suspensions, the transition from Newtonian to shear-thinning is shown. This transition is dependent on volume fraction and shear rate. This transition was also captured through DEM simulations and with similar scaling of viscosity with shear rate albeit with a small discrepancy arising due to non-sphericity of particles. Through DEM simulations we infer that soft particle contacts are the origin of the shear-thinning in this system.

Finally, all the four elements (DEM, CFD, Heat transfer and Starch swelling) are combined to decipher the important phenomena occurring during starch gelatinization inside a heating Couette rheometer. It is shown that the suspension could not be assumed homogeneous even in the case of a small gap Couette rheometer. It was shown that the granule closely follows the temperature of the surrounding fluid. There exists a random walk of particles due to particle-particle interactions originating from lubrication and particle-particle collisions. The contribution of random walk of particles to the momentum transfer is not negligible. There is a net movement of particles due to the volume fraction gradient created due to temperature difference and swelling of particles.

This thesis thus lays its emphasis on including the granular contribution in the understanding of different phenomena occurring during heat treatment of starch suspensions (swelling, change in mechanical properties, contact and lubrication interactions) and their consequences at a macroscopic scale notably in terms of rheology.

## 6.2 Future prospects

The methods utilized in this thesis could be applied or extended to other similar systems with increasing complexity such as starch with amylose release, polymer suspensions, apple/vegetable puree, etc.

### **6.2.1 Starch swelling**

The kinetic model for starch swelling developed in chapter 2 is only applicable to chemically modified waxy-maize starch which does not rupture at the later stages of swelling. For other types of natural occurring starches, the approach needs to be modified and redeveloped. Through experiments, it was shown that there is a delay associated with the onset of swelling. The intra-granular mechanism responsible for this variable delay in swelling is still to be investigated. Secondly, the kinetic swelling model makes the simplification of spherical particles. As shown from the optical and confocal images this is not true. A kinetic swelling model that captures the non-sphericity of the particles would be of interest as it is known that non-sphericity has a great influence on the rheology of suspensions [Tapia et al. \[2017\]](#).

### **6.2.2 Methods to characterize materials**

In chapter 3, Young's modulus of fully swollen waxy maize starch particle and of native unswollen starch is measured. For the partially swollen case, the relation of Young's modulus with the swelling degree is yet to be deciphered. Partially swelling the granule is also challenging to begin with. Other techniques such as microfluidics need to be envisaged to measure Young's modulus of partially swollen granules.

### **6.2.3 DEM shear flow simulations**

In chapter 4, DEM simulations successfully replicated shear-thinning observed in experiments. However, the major limitation is the use of spherical particles in simulations whereas the actual particles are far from being spherical. Thus, the simulated volume fractions had to be adjusted to compare with experiments. DEM shear flow simulations with non-spherical particles could address this drawback.

### **6.2.4 Coupling simulations**

Finally, a fully coupled simulation at a larger scale(heat exchanger) with complex geometries could be envisioned. This exercise is computational prohibitive currently. With the availability of higher computation resources through cloud computing and improved algorithms, it might be feasible in the future. Then this data could be used to generate a reduced-order model useful for process optimization and control.

## **6.3 Final word**

We have come to the end of this manuscript. I would like to end it by saying, I have learned and experienced much more than what could be written in a thesis manuscript. After three years of working on this theme, I am still as enthusiastic as I was on day one. There is still a lot to be understood about the rheology of suspensions and starch. My thesis was multi-faceted which required me to interact with multiple personnel who are experts in their respective domains. All thanks to the strong team at the laboratories and advisors who welcomed me with open arms, I could say that I leave with a lot more than I started with and thoroughly enjoyed working on this subject.

I cannot say enough how lucky and privileged I feel to have been able to be supervised in the way I was. I have been very lucky throughout this work. All my advisors guided me smartly and patiently corrected me multiple times with not a hint of frustration on their faces. Finally, I thank my family for supporting and enduring the circumstances that were thrown at them during the testing times of the global pandemic.

## Conclusion générale et perspectives (résumé en français)

Ce que nous pouvons retenir principalement de cette thèse est que les études précédentes portant sur les écoulements (rhéologie), les transferts et les transformations dans les suspensions d'amidon considéraient le gonflement moyen d'une population de granules et la suspension comme une phase unique. L'objectif global de la thèse était de proposer une approche expérimentale et de modélisation prenant en compte le gonflement à l'échelle individuelle et les différentes interactions granule/granule et granule/fluide.

Pour cela, nous avons proposé un modèle cinétique de gonflement tenant compte d'une variabilité entre granules dont les paramètres ont été identifiés expérimentalement pour un amidon de maïs cireux modifié. Puis nous avons caractérisé (pour ce type d'amidon) les propriétés mécaniques des granules à l'état natif et complètement gonflé. Ceci permet de rendre compte du passage, lors de la gélatinisation, d'une suspension relativement diluée de particules dures à une suspension dense de particules molles.

Des simulations par la méthode des éléments discrets (DEM) à permis de montrer l'importance du caractère 'mou' des particules sur la fraction volumique critique et sur la rhéologie. Il a notamment été constaté expérimentalement un caractère rhéofluidifiant dans certaines conditions de cisaillement et de fraction volumique qui a pu être reproduit par simulation.

Un exemple de couplage entre écoulement, transfert et transformation (gélatinisation d'une suspension d'amidon dans un rhéomètre de Couette chauffant à petit entrefer) a été traitée par une approche couplée CFD-DEM. Il a notamment été mis en évidence un mouvement aléatoire des granules du fait des collisions et des forces de lubrifications qui a rôle non-négligeable sur les transferts de quantité de mouvement (rhéologie).

Les méthodes utilisées dans cette thèse pourraient être appliquées ou étendues à d'autres systèmes similaires tels que de l'amidon avec libération d'amylose, des suspensions de polymères, des purées de fruits ou de légumes.

En ce qui concerne le modèle de gonflement développé au chapitre 2, il n'est applicable qu'à de l'amidon cireux chimiquement modifié qui ne se rompt pas aux stades ultérieurs du gonflement ; pour d'autres types d'amidons l'approche doit être modifiée et réaménagée. Les expériences ont montré qu'il y a un retard au gonflement variable d'un grain à un autre ; l'origine de cette variabilité reste à établir. Enfin, le modèle assimile les granules à des sphères ce qui n'est pas vraiment le cas d'après les observations microscopiques. Or la non-sphéricité à une influence importante sur la rhéologie de suspensions denses. Un modèle plus adapté (e.g. granules ellipsoïdes) pourrait être développé.

En ce qui concerne la caractérisation des propriétés mécaniques des granules, elles ont été déterminées pour des granules natifs et entièrement gonflés, les cas intermédiaires restent à être investigués. Des techniques telles que la microfluidique pourraient y contribuer

En ce qui concerne la simulation d'écoulement de cisaillement par DEM, le caractère rhéofluidifiant a pu être reproduit. Néanmoins, la limitation majeure est l'utilisation de particules sphériques dans les simulations alors que c'est loin d'être le cas en réalité. Ainsi, les fractions volumiques simulées ont dû être ajustées pour être en accord avec les mesures. Des simulations DEM avec des particules non sphériques pourraient remédier à cet inconvénient.

Pour ce qui est des simulations couplant écoulement, transferts et transformation par CFD-DEM; de telles

simulations entièrement couplée à plus grande échelle (échangeur de chaleur) avec des géométries complexes pourrait être envisagées mais restent prohibitives en temps de calcul sur de simples PC. L'accès à des ressources informatiques de calcul intensif pourrait permettre de simuler de façon plus réaliste des procédés industriels de traitement de produits amylacés.

## Appendix A

# Appendix: Transient DEM simulation of starch swelling (MATLAB script)

```
clear all; close all; clc
D=200e-6*[1,1,1]; D_2=D/2; Vbox=D(1)*D(2)*D(3);
Vmax=0.001;
l=200; tmax=4*60; dt=0.005; dts=tmax/100; dtg=tmax/8.05;
dtsmall = 0.00001;
dtlarge = 0.005;
dt = dtlarge;
dtV=20*dt; criV=2; % list of neighbors
r0mean=14.77e-6/2; r0sig=4.44e-6/2; %  $D > 2*(r0mean+3r0sig)*(rf_r0mean+3*rf_r0sig)$ 
mean_vol= pi/6*(16.16e-6^3); phi0=l*mean_vol/Vbox
rf_r0mean=2.34; rf_r0sig=0.33 ;
rho=1000; mu=1e-5;
g=0*9.81;
Brow=0% 1e-14 %  $N*s^{0.5}$ 
Stokes=0;
cLub=0; cco=1; % cLub around 40 to approx theor. law between  $h/r=0.1$  and  $0.7$ 
K=1e-5; %  $N/m$ 
Es0=10000; % Pa  $Estar=E/(1-nu)$ 
cH=sqrt(16/9);
cHEs0=cH*Es0;
nTmax=2; tT=[0,6*60]; Tt=[60,90]; %  $T$  vs  $t$  (above  $Tmin$ ) ( $tTmax > tmax$ )
Tmin=60; Tref=62; tauref=190 % 190;
Kref=0.0023 % 0.0023; % swelling model parameters

rng(1); % rng('shuffle'); initialize random
r0=min(max(r0mean+randn(l,1)*r0sig,0.25*r0mean),3*r0mean); r=r0;
rf_r0=rf_r0mean+min(max(randn(l,1),-2),2)*rf_r0sig;
alpha = ([1:l]-0.5)/l;
```

```

S=zeros(1,1); nV=zeros(1,1); jV=zeros(1,1); F=zeros(1,3); v=zeros(1,3);
Es=Es0*ones(1,1); % all the granules have the same renormalised Young's modulus
t_oscH=2*pi*sqrt(rho*2*pi/3*r0mean^2/Es0)
t_oscK=2*pi*sqrt(rho*2*pi/3*r0mean^3/K)

for i=1:l
    ok=0; i=i
    while ok==0 % while new i intersect previous j propose new position
        x(i,:)=rand(1,3).*D;
        ok=1;
        for j=1:i-1
            xij=x(j,:)-x(i,:);
            xij=xij-D.*(xij>D_2)+D.*(xij<-D_2);
            if xij*xij' < (r(i)+r(j))^2; ok=0 ;end
        end
    end
end
end

t=0; tonset_int=0; nT=1; ng=0; tg=0; ns=0; ts=0; ion=0; tV=0;

while t<tmax
    mass=rho*4/3*pi*r.^3; %rho_dm = rho_w
    invm=1./mass*[1,1,1];
    rmax=max(r);

    if (ts-t)<0.1;
        dt = dtsmall;
    end
    if t>ts
        ts=ts+dts; ns=ns+1; rs(:,ns)=r; xs(:, :, ns)=x; vs(:, :, ns)=v;
        dt = dtlarge;
        rmean(ns)=mean(r);
        siglog(ns)=std(log(r/rmean(ns)));
        Vtot(ns)=4*pi/3*sum(r.^3);
        Voverl(ns)=0;% overlap volume
        EeK(ns)=0; % elastic energy Hook
    end
end

```

```

EeH(ns)=0; % id Hertz
for i=2:l-1
    for m=1:nV(i)
        j=jV(i,m);
        xij=x(j,:)-x(i,:);
        xij=xij-D.*(xij>D_2)+D.*(xij<=-D_2);
        dij=sqrt(xij*xij'); sumr=r(i)+r(j);
        if dij<sumr
            ri_d=r(i)/dij; rj_d=r(j)/dij;
            xi_d=0.5*(1+ri_d^2-rj_d^2); xj_d=1-xi_d;
            cosi=xi_d/ri_d; cosj=xj_d/rj_d;
            Vi=pi/3*r(i)^3*(1-cosi)*(2-(1+cosi)*cosi);
            Vj=pi/3*r(j)^3*(1-cosj)*(2-(1+cosj)*cosj);
            Voverl(ns)=Voverl(ns)+Vi+Vj;
            EeK(ns)=EeK(ns)+0.5*K*(sumr-dij)^2;
            EeH(ns)=EeH(ns)+cH/(1/Es(i)+1/Es(j))*(sumr-dij)^2.5/2.5/sqrt(1/r(i)+1/r(j)
                );
        end
    end
end % overlap volume
end % data output

if t>tT(nT+1); nT=nT+1; end; % swelling
T=Tt(nT)+(Tt(nT+1)-Tt(nT))*(t-tT(nT))/(tT(nT+1)-tT(nT));
tonset_int=tonset_int+(T-Tmin)/(Tref-Tmin)/tauref*dt;
if ion<l & tonset_int> -log(1-alpha(ion+1)); ion=ion+1; tonset(ion)=t; end;
for i=1:ion % for all the granules which began to swell
    S(i)=S(i)+ Kref*sqrt(1-alpha(i))*((T-Tmin)/(Tref-Tmin))^2*(1-S(i))*dt;
    r(i)=r0(i)*(1+(rf_r0(i)-1)*S(i));
end

if t>tV % update of neighbor list (V=voisin)
    tV=tV+dtV; nV=zeros(l,1); % nbr of neighbors of i
    dmax2=(criV*2*rmax)^2;
    for i=2:l
        for j=1:i-1
            xij=x(j,:)-x(i,:);

```

```

xij=xij-D.*(xij>D_2)+D.*(xij<=-D_2);
if xij*xij' < dmax2
    nV(i)=nV(i)+1; jV(i,nV(i))=j;
    nV(j)=nV(j)+1; jV(j,nV(j))=i;
end
end
end
end

for i=1:l
    F(i,:) = mass(i) * [0,0,-g] - Stokes * 6 * pi * mu * r(i) * v(i,:) ...
        + (rand(1,3) - [0.5,0.5,0.5]) * Brow / sqrt(dt);
    for m=1:nV(i)
        j=jV(i,m);
        xij=x(j,:)-x(i,:);
        xij=xij-D.*(xij>D_2)+D.*(xij<=-D_2);
        dij=sqrt(xij*xij'); sumr=r(i)+r(j);
        if dij < sumr
            % Fij=K*(sumr-dij)*xij/dij;
            % Fij=cHEs0*(sumr-dij)^1.5/sqrt(1/r(i)+1/r(j))*xij/dij; % Hertz E uniform
            Fij=cH/(1/Es(i)+1/Es(j))*(sumr-dij)^1.5/sqrt(1/r(i)+1/r(j))*xij/dij; % Hertz
            Ei ~= Ej
            F(j,:)=F(j,)+Fij;
            F(i,:)=F(i,)-Fij;
        % else
        % if cLub>0
        % hmr=1/(1/r(i)+1/r(j)); % harmonic mean of ri and rj
        % gapco = cco*hmr; % gapco = gapcut off
        % if (dij-sumr)< gapco
        % Fij=cLub*mu*(1-(dij-sumr)/gapco)^2*(v(i)-v(j))*(xij/dij)*hmr;
        % F(j,:)=F(j,)+Fij;
        % F(i,:)=F(i,)-Fij;
        % end
        % end
        % end
    end
end % fin boucle j

```

```

end % fin boucle i

t=t+dt
x=x+v*dt;
for m=1:3; x(:,m)=x(:,m)-(x(:,m)>D(m))*D(m)+(x(:,m)<0)*D(m); end ;
v=v+F.*invm*dt;
V=sqrt(sum(v.*v,2));
v=(min(1,Vmax./V)*ones(1,3)).*v;
if t>tg
    ng=ng+1; tg=tg+dtg;
    figure(1); subplot(3,3,ng);
    npart=vertsection(l,x,r,D,ion);
    drawnow;
end;
end % fin boucle en temps

figure(2); plot3(x(:,1),x(:,2),x(:,3),'O');

tsave=([1:ns]-1)*dts;

figure(3)
subplot(3,3,1); plot(tsave,rmean*1e6); title('rmean_\mu_m')
subplot(3,3,2); plot(tsave,Vtot/Vbox); title('Vtot/Vbox')
subplot(3,3,3); plot(tsave,Voverl/Vbox); title('Voverlap/Vbox')
subplot(3,3,4); plot(tsave,siglog); title('std_of_ln(r/rmean)') %
subplot(3,3,5); plot(tsave,EeK/Vbox); title('elastic_energy_Hook_cts_K') % J/m3=Pa
subplot(3,3,6); plot(tsave,EeH/Vbox); title('elastic_energy_Hertz') %J%

function n=vertsection(l,x,r,D,ion) % plot vert mid-section and returns the nb of
    intersected particules
hold on; n=0; J=50;
for i=1:l
    dymoy=x(i,2)-D(2)/2;
    if abs(dymoy)<r(i)
        n=n+1;
        rs=sqrt(r(i)^2-(x(i,2)-D(2)/2)^2);

```

```
for j=1:J+1
    xx(j)=x(i,1)+cos(2*pi*j/J)*r(i);zz(j)=x(i,3)+sin(2*pi*j/J)*r(i);
    xxs(j)=x(i,1)+cos(2*pi*j/J)*rs;zzs(j)=x(i,3)+sin(2*pi*j/J)*rs;
    xxr(j)=x(i,1)+cos(10*pi*j/J)*rs*(j/1.2/J);z zr(j)=x(i,3)+sin(10*pi*j/J)*rs*(j
        /1.2/J);
end
if (i<ion)
plot(xxs,zzs,'k',xxr,z zr,'k:');axis([-0.1*D(1),1.1*D(1),-0.1*D(3),1.1*D(3)])
else
plot(xxs,zzs,'k')
plot([max(xxr),min(xxr)],[x(i,3),x(i,3)],'k-');
plot([x(i,1),x(i,1)],[max(z zr),min(z zr)],'k-');
axis([-0.1*D(1),1.1*D(1),-0.1*D(3),1.1*D(3)])
end
if dymoy>0;
    plot(xx,zz,'r:');
else
    plot(xx,zz,'b:');
end
end
end;
plot([0,D(1),D(1),0,0],[0,0,D(2),D(2),0], 'm--');
hold off;
```

## Appendix B

# Appendix: Thermo-mechanical treatment of starch suspensions in small gap Couette rheometer (MATLAB)

```
% rheo    swelling in the gap of a rheometer
%        Fn lubrication from kim and karila .
%        no Ft, no rotation/torque, no contact forces)
% tau_Stokes = (2/9)rÂš/nu ~ 2e-5 s (r=10Âµm)
% tau_therm_part = rÂšrho.cp/3/k ~ 2e-3 s
% tau_therm_cond = dXÂš/(k/(rho*cp)) = ~ 0.2 s (dX=0.2mm)
% dtV < 1/gamma_dot =0.01 s for dt=1e-5 dtv<1000.dt here dtv=20*dt

clear all; close all; clc
D=[1e-3, 2e-4, 2e-4], D_2=0.5*D;
D2=D(2),D2_2=D2/2; D3=D(3),D3_2=D3/2; pi6=pi*6;
Vbox=D(1)*D(2)*D(3); Slat=D(2)*D(3);
vext=0;vint=0.01; % gamma_dot=vint/D(1)=10 1/s
vmax=vint/10;
xsimin=0.01;
mou=0;

N=5; dX=D(1)/N; dX_2=dX/2; nmid=ceil(N/2);
lc=100; l=N*lc;
lplot=20; tmax=60;
dt=0.00001; dts=tmax/200; dtg=tmax/8.001
dtV=20*dt; criV=2; % list of neighbors
dV=dX*D(2)*D(3); mcpint=7000*500*0.001*Slat; %rhometal*cpmatal*e*dY*DZ
```

```

r0mean=14.77e-6/2; r0sig=4.44e-6/2; %  $D > 2*(r0mean+3r0sig) *(rf_r0mean+3*rf_r0sig)$ 
mean_vol= pi/6*(16.16e-6^3); phi0=l*mean_vol/Vbox;
rf_r0mean=2.34; rf_r0sig=0.33 ;
rho=1000; k=0.6; cp=4180 %  $Cp_{grain}=Cp_{liq}$ 
Nu=2; piNuk2=2*pi*Nu*k; %
Stokes=6 %
%  $phimax=0.7$ ;
Fmax=rho*mean_vol*r0mean/ dt / dt/1000;

nTmax=2;tT=[0,tmax,1.5*tmax]; Tt=[60,90,90]; %  $T$  vs  $t$  (above  $Tmin$ ) ( $tTmax > tmax$ )
% Achtung
Tmin=60; Tref=62; tauref=190 % 190;
Kref=0.0023 %0.0023; % random swelling Arnesht model

r=zeros(l,1); rf_r0=zeros(l,1); alpha=zeros(l,1); S=zeros(l,1);
F=zeros(l,3); vfi=zeros(l,3); T=zeros(l,1); Qf=zeros(l,1); Qp=zeros(l,1);
nV=zeros(l,1); jV=zeros(l,1); pi6mur=zeros(l,1);
in=zeros(N,1); Qv=zeros(N,1);
vectX(1)=0;
for n=1:N; vectX(n+1)=(n-0.5)*dX;end;
vectX(N+2)=D(1);

rng(10); % initialize random
for ic=1:lc % same particles in the N cells
    r_ic=min(max(r0mean+randn*r0sig,0.25*r0mean),r0mean+2*r0sig);
    rf_r0_ic=rf_r0mean+min(max(randn,-2),2)*rf_r0sig;
    alpha_ic = (ic-0.5)/lc;
    for n=1:N
        i=(ic-1)*N+n
        r(i)=r_ic;
        rf_r0(i)=rf_r0_ic;
        alpha(i)=alpha_ic;
        ok=0;
        while ok==0 % while new i intersect previous j propose new position
            x(i,1)=dX*(n-1)+rand*dX;
            x(i,2)=rand*D(2); x(i,3)=rand*D(3);
            ok=1;
        end
    end
end

```

```

    if x(i,1)<0 | x(i,1)>D(1); ok=0; end;
    for j=1:i-1
        xij=x(j,:)-x(i,:);
        xij=xij-D.*(xij>D_2)+D.*(xij<-D_2);
        if xij*xij' < (r(i)+r(j))^2; ok=0 ;end
    end
end
end
end
r0=r;
for n=1:N; vf(n)=vint+(vext-vint)*(n-0.5)/N; Tf(n)=Tt(1); end;
Tint=Tt(1);

for i=1:l
    v(i,1)=0; v(i,3)=0;
    v(i,2)=vint+(vext-vint)*x(i,1)/D(1);
    T(i)=Tt(1);
end;

t=0;tonset_int=zeros(l); nT=1; ng=0; tg=0; ns=0; ts=0; tV=0;
phin=ones(N,1)*phi0; choc=0; Voverl=zeros(1,200);

while t<tmax      %state var: r,T,x,v, Tf, Tint, vf(scalar)
    V=4/3*pi*r.^3;
    mass=rho*V;      %rho_dm = rho_w
    rmax=max(r);

    if t>tT(nT+1); nT=nT+1; end; %
    Text=Tt(nT)+(Tt(nT+1)-Tt(nT))*(t-tT(nT))/(tT(nT+1)-tT(nT));

    if t>tV % update of neighbor list (V=voisin)
        tV=tV+dtV; nV=zeros(l,1);% nbr of neighbors of i of lower index
        dmax2=(criV*2*rmax)^2;
        for i=2:l
            for j=1:i-1
                xij=x(j,:)-x(i,:);
                xij(2)=xij(2)-D2*(xij(2)>D2_2)+D2*(xij(2)<-D2_2);
            end
        end
    end
end

```

```

    xij(3)=xij(3)-D3*(xij(3)>D3_2)+D3*(xij(3)<=-D3_2);
    if xij*xij' < dmax2
        nV(i)=nV(i)+1; jV(i,nV(i))=j;
    end
end
end
end

ln=zeros(N,1); Ffn=zeros(N,3); Qfn=zeros(N,1); Vn=zeros(N,1);
vn=zeros(N,1); Tn=zeros(N,1); F=zeros(l,3); Qp=zeros(l,1);
for i=1:l
    nn=ceil(x(i,1)/dX-0.5); prop=(x(i,1)-(nn-0.5)*dX)/dX;
    if nn==0
        vfi(i,:)=[0,1,0]*(vint+(vf(1)-vint)*x(i,1)/dX_2);
        Tfi=Tint+(Tf(1)-Tint)*x(i,1)/dX_2;
    elseif nn==N
        vfi(i,:)=[0,1,0]*(vf(N)+(vext-vf(N))*prop*2);
        Tfi=Tf(N)+(Text-Tf(N))*prop*2;
    else
        vfi(i,:)=[0,1,0]*(vf(nn)+(vf(nn+1)-vf(nn))*prop);
        Tfi=Tf(nn)+(Tf(nn+1)-Tf(nn))*prop;
    end
    mui=2.414e-5*10^(247.8/(Tfi+133));
    pi6mur(i)=pi6*mui*r(i);
    n=ceil(x(i,1)/dX);
    ln(n)=ln(n)+1; in(n,ln(n))=i;
    Vn(n)=Vn(n)+V(i);
    vn(n)=vn(n)+v(i,2);
    Tn(n)=Tn(n)+T(i);
    Ffi=pi6mur(i)*(vfi(i,:)-v(i,:));
    Qp(i)=Qp(i)+Ffi*(vfi(i,:)-v(i,:))';
    Qf(i)=piNuk2*r(i)*(Tfi-T(i));
    Ffn(n,:)=Ffn(n,)+Ffi;
    Qfn(n)=Qfn(n)+Qf(i);
    for m=1:nV(i)
        j=jV(i,m);
        xij=x(j,:)-x(i,:);
    end
end
end
end

```

```

xij(2)=xij(2)-D2*(xij(2)>D2_2)+D2*(xij(2)<=-D2_2);
xij(3)=xij(3)-D3*(xij(3)>D3_2)+D3*(xij(3)<=-D3_2);
dij=sqrt(xij*xij'); nij=xij/dij; sumr=r(i)+r(j); h=dij-sumr; xsi=2*h/sumr;
if xsi<0
    if t>ts
        ri_d=r(i)/dij;rj_d=r(j)/dij;
        xi_d=0.5*(1+ri_d^2-rj_d^2);xj_d=1-xi_d;
        cosi=xi_d/ri_d; cosj=xj_d/rj_d;
        Vi=pi/3*r(i)^3*(1-cosi)*(2-(1+cosi)*cosi);
        Vj=pi/3*r(j)^3*(1-cosj)*(2-(1+cosj)*cosj);
        Voverl(ns+1)=Voverl(ns+1)+Vi+Vj;
    end
    x(i,:)=x(i,:)+0.5*h*nij;x(j,:)=x(j,:)-0.5*h*nij; % suppress overlap, new in
        rheoL12
    vij=v(j,:)-v(i,:);
    vijn=vij*nij';
    if vijn<0
        choc=choc+1;
        P=(1-mou/2)*2*vijn*mass(i)*mass(j)/(mass(i)+mass(j))*nij;
        F(i,:)=F(i, :)+P/dt;
        F(j,:)=F(j, :)-P/dt;
    end;
    elseif xsi<1
        xsi=max(xsi,xsimin);
        vij=v(j,:)-v(i,:);
        beta=r(j)/r(i);
        Fji=pi*6*mu(i)*2*beta^2/(1+beta)^3/xsi*vij*nij'*nij;
        F(i,:)=F(i, :)+Fji;
        F(j,:)=F(j, :)-Fji;
        Qp(i)=Qp(i)+0.5*Fji*vij';
        Qp(j)=Qp(j)+0.5*Fji*vij';
    end
end % fin boucle j
end % fin boucle i
nFmax=0;
% normF=sqrt(sum(F.*F,2))+1e-15;
% F=min(1,Fmax./normF)*[1,1,1].*F;

```

```

for i=1:l
    normFi=sqrt(F(i,:) *F(i,:) ');
    if normFi>Fmax
        nFmax=nFmax+1;
        F(i,:)=F(i,:) *Fmax/normFi;
    end;
end;
vn=vn./(ln+1e-5); Tn=Tn./(ln+1e-5);

QL(1)=Slat*k*(Tint-Tf(1))/dX_2; % L left of cell n
QL(N+1)=Slat*k*(Tf(N)-Text)/dX_2;
for n=2:N; QL(n)=Slat*k*(Tf(n-1)-Tf(n))/dX; end

phin=Vn/dV;
for n=1:N; eta(n)=(1+2.5*phin(n)); mu(n)=2.414e-5*10^(247.8/(Tf(n)+133)); end
phinL(1)=phin(1); phinL(N+1)=phin(N); TfL(1)=Tint; TfL(N+1)=Text;
for n=2:N; phinL(n)=0.5*(phin(n-1)+phin(n)); TfL(n)=0.5*(Tf(n-1)+Tf(n)); end
for n=1:N+1; etaL(n)=(1+2.5*phinL(n)); muL(n)=2.414e-5*10^(247.8/(TfL(n)+133)); end
% eta relative viscosity

FvL(1)=Slat*muL(1)*etaL(1)*(vint-vf(1))/dX_2;
FvL(N+1)=Slat*muL(N+1)*etaL(N+1)*(vf(N)-vext)/dX_2;
for n=2:N; FvL(n)=Slat*muL(n)*etaL(n)*(vf(n-1)-vf(n))/dX; end

Qv(1)=dV*mu(1)*eta(1)*((vint-0.5*(vf(1)+vf(2)))/dX)^2;
Qv(N)=dV*mu(N)*eta(N)*((vext-0.5*(vf(N)+vf(N-1)))/dX)^2;
for n=2:N-1; Qv(n)=dV*mu(n)*eta(n)*((vf(n+1)-vf(n-1))/2/dX)^2; end

if t>ts
    t
    nFmax/l
    ts=ts+dts; ns=ns+1;
    rs(:,ns)=r; xs(:,ns)=x; Xs(:,ns)=xs(:,1,ns)-xs(:,1,1); vs(:,ns)=v; Ts(:,ns)=T
    ;
    Tfs(1,ns)=Tint; vfs(1,ns)=vint; phis(1,ns)=phin(1); lns(1,ns)=ln(1);
    vns(1,ns)=1.5*vn(1)-0.5*vn(2); Tns(1,ns)=1.5*Tn(1)-0.5*Tn(2); % extrapolated
    mus(1,ns)=muL(1); muetas(1,ns)=muL(1)*etaL(1); % plateau

```

```

for n=1:N
    Tfs(n+1,ns)=Tf(n); vfs(n+1,ns)=vf(n); phis(n+1,ns)=phin(n); lns(n+1,ns)=ln(n);
    vns(n+1,ns)=vn(n); Tns(n+1,ns)=Tn(n);
    mus(n+1,ns)=mu(n); muetas(n+1,ns)=mu(n)*eta(n);
end
Tfs(N+2,ns)=Text; vfs(N+2,ns)=vext; phis(N+2,ns)=phin(N); lns(N+2,ns)=ln(N);
vns(N+2,ns)=1.5*vn(N)-0.5*vn(N-1); Tns(N+2,ns)=1.5*Tn(N)-0.5*Tn(N-1);
mus(N+2,ns)=muL(N+1); muetas(N+2,ns)=muL(N+1)*etaL(N+1);
rmean(ns)=mean(r);
Vtot(ns)=sum(V);
tau_w(ns)=FvL(1)/Slat;
Qvtot(ns)=sum(Qv);
Qptot(ns)=sum(Qp);
chocs(ns)=choc/dts/1000; choc=0;
Ecinx(ns)=0; Eciny(ns)=0; Ecinz(ns)=0;
for i=1:l;
    Ecinx(ns)=Ecinx(ns)+0.5*mass(i)*v(i,1)*v(i,1);
    Eciny(ns)=Eciny(ns)+0.5*mass(i)*v(i,2)*v(i,2);
    Ecinz(ns)=Ecinz(ns)+0.5*mass(i)*v(i,3)*v(i,3);
end;
sig2x(ns)=0; sig2z(ns)=0;
for ic=1:lc
    i=(ic-1)*N+nmid;
    sig2x(ns)=sig2x(ns)+(x(i,1)-xs(i,1,1))^2;
    sig2z(ns)=sig2z(ns)+min([(x(i,3)-xs(i,3,1))^2,(x(i,3)+D3-xs(i,3,1))^2,...
        (x(i,3)-D3-xs(i,3,1))^2]);
end;
sig2x(ns)=sig2x(ns)/lc; sig2z(ns)=sig2z(ns)/lc;
end % data output

t=t+dt;
for i=1:l
    tonset_int(i)=tonset_int(i)+(T(i)-Tmin)/(Tref-Tmin)/tauref*dt;
    if tonset_int(i)> -log(1-alpha(i));
        S(i)=S(i)+Kref*sqrt(1-alpha(i))*((T(i)-Tmin)/(Tref-Tmin))^2*(1-S(i))*dt;
        r(i)=r0(i)*(1+(rf_r0(i)-1)*S(i));
    end

```

```

end
for n=1:N;
    Tf(n)=Tf(n)+(QL(n)-QL(n+1)-Qfn(n)+Qv(n))/(dV-Vn(n))/rho/cp*dt;
    vf(n)=vf(n)+(FvL(n)-FvL(n+1)-Ffn(n,2))/(dV-Vn(n))/rho*dt;
end
Tint=Tint-QL(1)/mcpint*dt;
T=T+(Qf+Qp)/mass/cp*dt;

tau=(mass./pi6mur)*[1 1 1];
expdt_tau=exp(-dt./tau);
veq=vfi+F./(pi6mur*[1 1 1]);
x=x+veq*dt+(veq-v).*tau.*expdt_tau;
v=veq+expdt_tau.*(v-veq);
% normv=sqrt(sum(v.*v,2))+1e-15;
% v=(min(1,vmax./normv)*ones(1,3)).*v;

for m=2:3; x(:,m)=x(:,m)-(x(:,m)>D(m))*D(m)+(x(:,m)<0)*D(m); end;
for i=1:l % rebond Ãlatsique sur les parois
    if x(i,1)<r(i); x(i,1)=r(i); v(i,1)=abs(v(i,1)); end;
    if x(i,1)>D(1)-r(i); x(i,1)=D(1)-r(i); v(i,1)=-abs(v(i,1)); end;
end;

if t>tg
    ng=ng+1; tg=tg+dtg;
    figure(1); subplot(3,3,ng);
    plot(x(:,1),v(:,2),'o');
    figure(2); subplot(3,3,ng);
    plot(x(:,1),F(:,1),'o');
    figure(3); subplot(3,3,ng);
    plot(x(:,1),T,'o');

    figure(4); subplot(3,3,ng); axis off;
    hold on; n=0; J=50;
    for i=1:l
        dz=x(i,3)-D(3)/2;
        if abs(dz)<r(i)
            n=n+1;

```

```

rsec=sqrt(r(i)^2-dz^2);
for j=1:J+1
    xx(j)=x(i,1)+cos(2*pi*j/J)*r(i);yy(j)=x(i,2)+sin(2*pi*j/J)*r(i);
    xxs(j)=x(i,1)+cos(2*pi*j/J)*rsec; yys(j)=x(i,2)+sin(2*pi*j/J)*rsec;
    xxr(j)=x(i,1)+cos(10*pi*j/J)*rsec*(j/1.2/J); yyr(j)=x(i,2)+sin(10*pi*j/J)*
        rsec*(j/1.2/J);
end
plot(xxs, yys, 'k', xxr, yyr, 'k:'); axis([-0.1*D(1), 1.1*D(1), -0.1*D(3), 1.1*D(3)])
; axis off
if dz>0; plot(xx, yy, 'r:'); else plot(xx, yy, 'b:'); end
end
end;
plot([0, D(1), D(1), 0, 0], [0, 0, D(2), D(2), 0], 'm--');
hold off;

figure(5); plot3(x(:,1), x(:,2), x(:,3), 'O'); axis on;

if t>dt
    tsave=( [1:ns]-1)*dts;
    figure(6);
    subplot(3,1,1); plot(tsave, Xs(1:lplot, :));
    subplot(3,1,2); plot(tsave, rs(1:lplot, :));
    subplot(3,1,3); plot(tsave, Ts(1:lplot, :));

    figure(7)
    nsaff=round(linspace(1, ns, 11));
    subplot(4,2,1); plot(vectX, vfs(:, nsaff)); title('vf')
    subplot(4,2,2); plot(vectX, vns(:, nsaff)); title('v_pmean')
    subplot(4,2,3); plot(vectX, Tfs(:, nsaff)); title('Tf')
    subplot(4,2,4); plot(vectX, Tns(:, nsaff)); title('T_pmean')
    subplot(4,2,5); plot(vectX, phis(:, nsaff)); title('phi')
    subplot(4,2,6); plot(vectX, lns(:, nsaff)/dV*N/1e9); title('part/mm3')
    subplot(4,2,7); plot(vectX, mus(:, nsaff)); title('Ât')
    subplot(4,2,8); plot(vectX, muetas(:, nsaff)); title('Ât_susp')

    figure(8);
    subplot(4,3,1); plot(tsave, rmean*1e6); title('rmean_Âtm')

```

```

    subplot(4,3,2); plot(tsave, Vtot/Vbox); title('Vtot/Vbox')
    subplot(4,3,3); plot(tsave, tau_w); title('tau_w')
    subplot(4,3,4); plot(tsave, chocs); title('chocs/ms')
    subplot(4,3,5); plot(tsave, Qvtot); title('Qvf/f_(W)')
    subplot(4,3,6); plot(tsave, Qptot); title('Qvp/f_(W)')
    subplot(4,3,7); plot(tsave, Ecinx); title('Ecinx(J)')
    subplot(4,3,8); plot(tsave, Eciny); title('Eciny(J)')
    subplot(4,3,9); plot(tsave, Ecinz); title('Ecinz(J)')
    subplot(4,3,10); plot(tsave, Voverl(1:ns) ./ Vtot); title('Voverlap')
    subplot(4,3,11); plot(tsave, sig2x); title('sig2x')
    subplot(4,3,12); plot(tsave, sig2z); title('sig2z')

end
drawnow;
save data_Einstein
end;
end % fin boucle en temps

save data_Einstein_fin

dijmin=zeros(1,1); xijmin=zeros(1,3); nijmin=zeros(1,3); nearest=zeros(1,1);
for i=1:l
    dijmin(i)=D(1);
    for j=1:l
        if i~=j
            xij=x(j,:)-x(i,:);
            xij(2)=xij(2)-D2*(xij(2)>D2_2)+D2*(xij(2)<=-D2_2);
            xij(3)=xij(3)-D3*(xij(3)>D3_2)+D3*(xij(3)<=-D3_2);
            dij=sqrt(xij*xij');
            if dij<dijmin(i)
                xijmin(i,:)=xij;
                dijmin(i)=dij;
                nijmin(i,:)=xij/dij;
                nearest(i)=j;
            end
        end
    end
end
end

```

```
end
dm=mean(dijmin)
dijsort=sort(dijmin);
figure(9);
subplot(2,3,1); plot(xijmin(:,1),xijmin(:,2),'o');axis(2*dm*[-1 1 -1 1]);title('xy')
;
subplot(2,3,2); plot(xijmin(:,1),xijmin(:,3),'o');axis(2*dm*[-1 1 -1 1]);title('xz')
;
subplot(2,3,3); plot(xijmin(:,2),xijmin(:,3),'o');axis(2*dm*[-1 1 -1 1]);title('yz')
;
subplot(2,3,4); plot3(xijmin(:,1),xijmin(:,2),xijmin(:,3),'O');
subplot(2,3,5); plot(dijsort,[1:l]/l);
subplot(2,3,6); plot(nijmin(:,2),dijmin,'o');
sigmaxijminx=sqrt(mean(xijmin(:,1).*xijmin(:,1)))
sigmaxijminy=sqrt(mean(xijmin(:,2).*xijmin(:,2)))
sigmaxijminz=sqrt(mean(xijmin(:,3).*xijmin(:,3)))
tau_w_mean=mean(tau_w(100:200))
Qvf_mean=mean(Qvtot(100:200))
Qvp_mean=mean(Qptot(100:200))
```



# Appendix C

## Appendix: LIGGGHTS files

### C.1 Lubrication contact model

Lubrication contact model is implemented as a fixes with a header file and main c++ file. The files can be accessed through the following github repository link along with relevant documentation test cases.

*[https://github.com/arneshp/DEM/tree/master/Lubrication\\_model](https://github.com/arneshp/DEM/tree/master/Lubrication_model)*

### C.2 Swelling model

Particle growth kinetics following the swelling model of chemically modified waxy-maize starch described in chapter 2 is implemented in LIGGGHTS via a fix files. The files can be accessed through the following github repository link along with relevant documentation and test cases.

*[https://github.com/arneshp/DEM/tree/master/Swelling\\_model](https://github.com/arneshp/DEM/tree/master/Swelling_model)*

### C.3 Variable Young's modulus based on swelling degree

Particle Young's modulus is varied through a given implicit function of swelling degree via new normal contact model implementation in LIGGGHTS. The files can be accessed through the following github repository link along with relevant documentation and test cases.

*[https://github.com/arneshp/DEM/tree/master/variable\\_youngs\\_modulus](https://github.com/arneshp/DEM/tree/master/variable_youngs_modulus)*



# Appendix D

## Appendix: Effect of particle size on DEM shear flow simulations

The sensitivity of particle size distribution on the viscosity predictions of DEM shear-flow simulations discussed in chapter 4.2 is discussed in detail here. The Box dimensions ( [0.001 m, 0.001 m, 0.001 m] ) is maintained constant and the particle sizes are increased 10 fold while maintaining the same particle volume fractions.

As discussed in chapter 4.2 the lubrication and Stokes forces on the particles are considered.

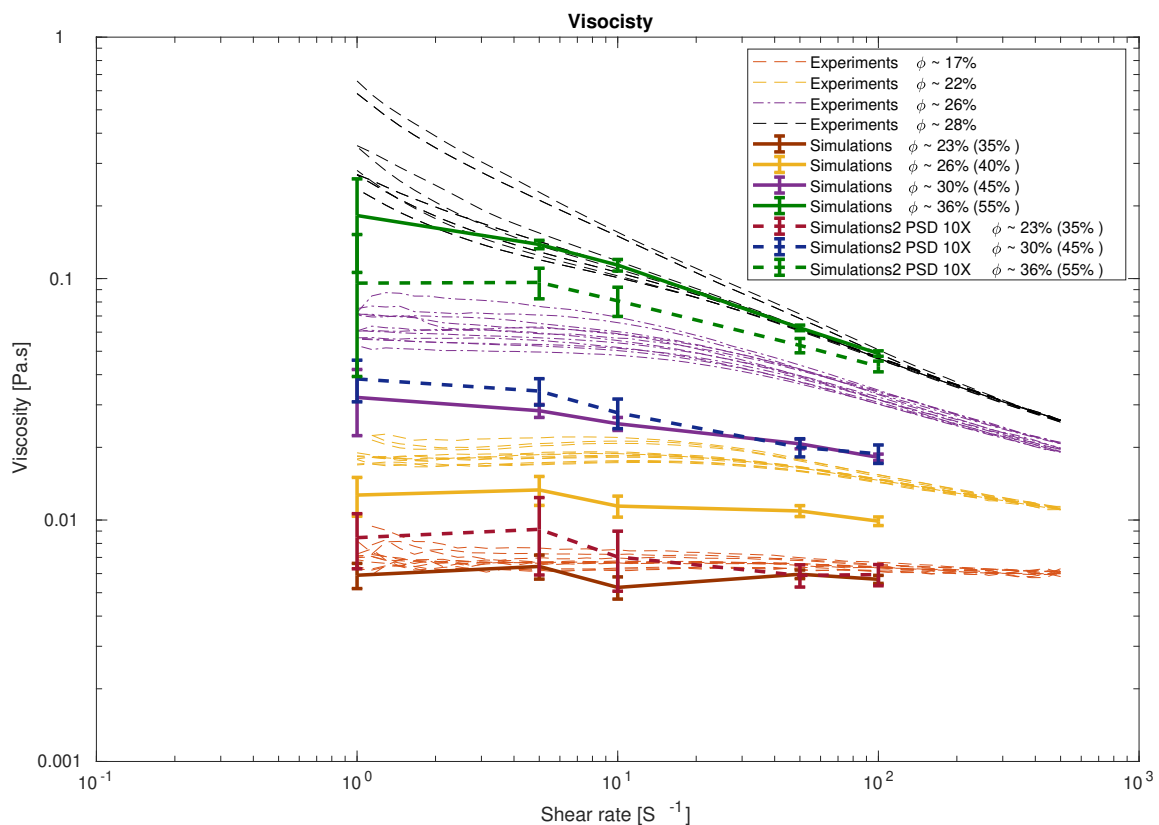


Figure D.1: Impact of Particle size distribution on Flow-curves of fully swollen starch granules.

It is observed that the size of the error bars have increased. This is due to increase in the ratio of particle size relative to box dimensions. As the particle sizes increased the viscosity of the suspension increased at low volume fraction and decreased at high volume fractions. This could be attributed to the dominance of lubrication forces at low volume fractions and particle-particle contacts at high volume fractions.



# Appendix E

## Bibliography

- A. R. Abate, L. Han, L. Jin, Z. Suo, and D. A. Weitz. Measuring the elastic modulus of microgels using microdrops. *Soft Matter*, 8(39):10032–10035, 2012.
- N. Abdulmola, M. Hember, R. Richardson, and E. Morris. Effect of xanthan on the small-deformation rheology of crosslinked and uncrosslinked waxy maize starch. *Carbohydrate Polymers*, 31(1-2):65–78, 1996.
- S. C. Alcázar-Alay and M. A. A. Meireles. Physicochemical properties, modifications and applications of starches from different botanical sources. *Food Science and Technology*, 35(2):215–236, 2015.
- G. Almeida, A. Plana-Fattori, G. Moulin, C. Michon, and D. Flick. Observing and modeling the evolution of starch granules size distribution. In 6. *International Symposium on Delivery of Functionality in Complex Food Systems. Physically-Inspired Approaches from the Nanoscale to the Microscale*, 2015.
- F. Alobaid and B. Epple. Improvement, validation and application of cfd/dem model to dense gas–solid flow in a fluidized bed. *Particuology*, 11(5):514–526, 2013.
- B. Andreotti, Y. Forterre, and O. Pouliquen. *Granular media: between fluid and solid*. Cambridge University Press, 2013.
- J. Anuntagool, G. Alvarez, and D. Flick. Predictive model for viscosity development of modified rice starch suspension under unsteady temperature change. *Journal of Food Engineering*, 209:45–51, 2017.
- A. O. Ashogbon and E. T. Akintayo. Recent trend in the physical and chemical modification of starches from different botanical sources: A review. *Starch-Stärke*, 66(1-2):41–57, 2014.
- W. Atwell. The terminology and methodology associated with basic starch phenomena. *Cereal Foods World*, 33: 306–311, 1988.
- A. Aufderhorst-Roberts, D. Baker, R. J. Foster, O. Cayre, J. Mattsson, and S. D. Connell. Nanoscale mechanics of microgel particles. *Nanoscale*, 10(34):16050–16061, 2018.
- E. Bagley and D. Christianson. Swelling capacity of starch and its relationship to suspension viscosity-effect of cooking time, temperature and concentration. *Journal of Texture Studies*, 13(1):115–126, 1982.
- A. Bakshi and R. Singh. Kinetics of water diffusion and starch gelatinization during rice parboiling. *Journal of Food Science*, 45:1387–1392, 1980a.
- A. S. Bakshi and R. P. Singh. Kinetics of water diffusion and starch gelatinization during rice parboiling. *Journal of Food Science*, 45(5):1387–1392, 1980b.

- R. Ball and J. R. Melrose. A simulation technique for many spheres in quasi-static motion under frame-invariant pair drag and brownian forces. *Physica A: Statistical Mechanics and its Applications*, 247(1-4):444–472, 1997.
- W. Banks, C. Greenwood, and D. Muir. Studies on starches of high amylose content. part 17. a review of current concepts. *Starch-Stärke*, 26(9):289–300, 1974.
- D. Barreto, C. O'Sullivan, and L. Zdravkovic. Quantifying the evolution of soil fabric under different stress paths. 1145:181–184, 2009.
- G. Batchelor. The effect of brownian motion on the bulk stress in a suspension of spherical particles. *Journal of Fluid Mechanics*, 83(1):97–117, 1977.
- G. Batchelor and J. Green. The determination of the bulk stress in a suspension of spherical particles to order  $c^2$ . *Journal of Fluid Mechanics*, 56(3):401–427, 1972.
- C. Bertolini, A. *Trends in starch applications. Starches: Characterization, Properties, and Applications*. Taylor and Francis Group, LLC, Abingdon, 2010.
- C. Biliaderis. Structures and phase transitions of starch polymers-r.h walter (ed.). *Polysaccharide association structures in food, Marcel Dekker, Inc, New York*, 29(47):57–168, 1998.
- C. G. Biliaderis and D. J. Prokopowich. Effect of polyhydroxy compounds on structure formation in waxy maize starch gels: a calorimetric study. *Carbohydrate Polymers*, 23(3):193–202, 1994.
- C. Biliaderis. Structure and phase transitions of starch in food system. *Food Technol.*, 46:98–109, 1992.
- J. Blanshard. Physicochemical aspects of starch gelatinization. In *Proceedings*, 1979.
- A. Blennow, A. M. Bay-Smidt, and R. Bauer. Amylopectin aggregation as a function of starch phosphate content studied by size exclusion chromatography and on-line refractive index and light scattering. *International Journal of Biological Macromolecules*, 28(5):409–420, 2001.
- T. Y. Bogracheva, P. Cairns, T. Noel, S. Hulleman, T. Wang, V. Morris, S. Ring, and C. Hedley. The effect of mutant genes at the *r*, *rb*, *rug3*, *rug4*, *rug5* and *lam* loci on the granular structure and physico-chemical properties of pea seed starch. *Carbohydrate Polymers*, 39(4):303–314, 1999.
- N. Boon and P. Schurtenberger. Swelling of micro-hydrogels with a crosslinker gradient. *Physical Chemistry Chemical Physics*, 19(35):23740–23746, 2017.
- V. Breedveld, D. van den Ende, A. Tripathi, and A. Acrivos. The measurement of the shear-induced particle and fluid tracer diffusivities in concentrated suspensions by a novel method. *Journal of Fluid Mechanics*, 375:297–318, 1998.
- A. Briffaz, C. Mestres, F. Matencio, B. Pons, and M. Dornier. Modelling starch phase transitions and water uptake of rice kernels during cooking. *Journal of Cereal Science*, 58(3):387–392, 2013.

- A. Briffaz, P. Bohuon, J.-M. Méot, M. Dornier, and C. Mestres. Modelling of water transport and swelling associated with starch gelatinization during rice cooking. *Journal of food engineering*, 121:143–151, 2014.
- C. Cai and C. Wei. In situ observation of crystallinity disruption patterns during starch gelatinization. *Carbohydrate polymers*, 92(1):469–478, 2013.
- E. Chamberlain, M. Rao, and C. Cohen. Shear thinning and antithixotropic behavior of a heated cross-linked waxy maize starch dispersion. *International Journal of Food Properties*, 2(1):63–77, 1999.
- S.-M. Chang and L.-C. Liu. Retrogradation of rice starches studied by differential scanning calorimetry and influence of sugars, nacl and lipids. *Journal of Food Science*, 56(2):564–566, 1991.
- E. Chantoiseau, A. Plana-Fattori, C. Doursat, and D. Flick. Coupling fluid flow, heat transfer and thermal denaturation-aggregation of beta-lactoglobulin using an eulerian/lagrangian approach. *Journal of Food Engineering*, 113(2):234–244, 2012.
- M. Chapwanya and N. Misra. A soft condensed matter approach towards mathematical modelling of mass transport and swelling in food grains. *Journal of Food Engineering*, 145:37–44, 2015.
- G. Chatté, J. Comtet, A. Niguès, L. Bocquet, A. Siria, G. Ducouret, F. Lequeux, N. Lenoir, G. Ovarlez, and A. Colin. Shear thinning in non-brownian suspensions. *Soft matter*, 14(6):879–893, 2018.
- B. Chaudhuri, F. J. Muzzio, and M. S. Tomassone. Modeling of heat transfer in granular flow in rotating vessels. *Chemical Engineering Science*, 61(19):6348–6360, 2006.
- G. Chen, O. H. Campanella, and S. Purkayastha. A dynamic model of crosslinked corn starch granules swelling during thermal processing. *Journal of Food Engineering*, 81(2):500–507, 2007.
- S. Chialvo and S. Sundaresan. A modified kinetic theory for frictional granular flows in dense and dilute regimes. *Physics of Fluids*, 25(7):070603, 2013.
- S.-G. Choi and W. L. Kerr. Swelling characteristics of native and chemically modified wheat starches as a function of heating temperature and time. *Starch-Stärke*, 56(5):181–189, 2004.
- M. Cloitre, R. Borrega, and L. Leibler. Rheological aging and rejuvenation in microgel pastes. *Physical Review Letters*, 85(22):4819, 2000.
- J. Cohen, R. Podgornik, P. L. Hansen, and V. Parsegian. A phenomenological one-parameter equation of state for osmotic pressures of peg and other neutral flexible polymers in good solvents. *The Journal of Physical Chemistry B*, 113(12):3709–3714, 2009.
- P. Coussot. *Rheophysics*. Springer, 2016.
- P. Coussot and C. Ancey. Rheophysical classification of concentrated suspensions and granular pastes. *Physical Review E*, 59(4):4445, 1999.

- N. C. Crawford, L. B. Popp, K. E. Johns, L. M. Caire, B. N. Peterson, and M. W. Liberatore. Shear thickening of corn starch suspensions: Does concentration matter? *Journal of colloid and interface science*, 396:83–89, 2013.
- L. Cui, S. Dong, J. Zhang, and P. Liu. Starch granule size distribution and morphogenesis in maize ('zea mays' l.) grains with different endosperm types. *Australian Journal of Crop Science*, 8(11):1560–1565, 2014.
- P. A. Cundall and O. D. Strack. A discrete numerical model for granular assemblies. *geotechnique*, 29(1):47–65, 1979.
- I. B. De Aguiar, T. Van de Laar, M. Meireles, A. Bouchoux, J. Sprakel, and K. Schroën. Deswelling and deformation of microgels in concentrated packings. *Scientific Reports*, 7(1):1–11, 2017.
- I. B. de Aguiar, K. Schroën, M. Meireles, and A. Bouchoux. Compressive resistance of granular-scale microgels: From loose to dense packing. *Colloids and Surfaces A: Physicochemical and Engineering Aspects*, 553:406–416, 2018.
- M. R. Debet and M. J. Gidley. Three classes of starch granule swelling: Influence of surface proteins and lipids. *Carbohydrate Polymers*, 64(3):452–465, 2006.
- S. Debnath, V. Gayathri, and M. Niranjan Babu. Chemically modified starches and their applications in pharmacy. *International Journal of Research in Pharmaceutical and Nano Sciences*, 2(3):332–344, 2013.
- G. P. Desam, J. Li, G. Chen, O. Campanella, and G. Narsimhan. A mechanistic model for swelling kinetics of waxy maize starch suspension. *Journal of Food Engineering*, 222:237–249, 2018a.
- G. P. Desam, J. Li, G. Chen, O. Campanella, and G. Narsimhan. Prediction of swelling behavior of crosslinked maize starch suspensions. *Carbohydrate polymers*, 199:331–340, 2018b.
- G. P. Desam, J. Li, G. Chen, O. Campanella, and G. Narsimhan. Swelling kinetics of rice and potato starch suspensions. *Journal of Food Process Engineering*, 43(4):e13353, 2020.
- F. Deslandes, A. Plana-Fattori, G. Almeida, G. Moulin, C. Doursat, and D. Flick. Estimation of individual starch granule swelling under hydro-thermal treatment. *Food Structure*, 22:100125, 2019.
- A. Di Renzo and F. P. Di Maio. An improved integral non-linear model for the contact of particles in distinct element simulations. *Chemical engineering science*, 60(5):1303–1312, 2005.
- K. D. Dolan and J. F. Steffe. Modeling rheological behavior of gelatinizing starch solutions using mixer viscometry data. *Journal of Texture Studies*, 21(3):265–294, 1990.
- A. Donald, T. Waigh, P. Jenkins, M. Gidley, M. Debet, and A. Smith. Internal structure of starch granules revealed by scattering studies. *Proceedings of an International Conference sponsored by the Food Chemistry Group of the Royal Society of Chemistry in association with the Institute of Food Science and Technology Research Subject Group held April 15-17, 1996, University of Cambridge, U.K. Edited by P.J. Frazier, P. Richmond, and A.M. Donald*, 1997.

- A. Donald et al. Understanding starch structure and functionality. *Starch in food: Structure, function and applications*, pages 156–184, 2004.
- K. Dong, R. Yang, R. Zou, and A. Yu. Role of interparticle forces in the formation of random loose packing. *Physical review letters*, 96(14):145505, 2006.
- J.-L. Doublier, G. Llamas, and M. Le Meur. A rheological investigation of cereal starch pastes and gels. effect of pasting procedures. *Carbohydrate Polymers*, 7(4):251–275, 1987.
- E. C. Eckstein, D. G. Bailey, and A. H. Shapiro. Self-diffusion of particles in shear flow of a suspension. *J. Fluid Mech*, 79(1):191–208, 1977.
- A. Einstein. *Eine neue bestimmung der moleküldimensionen*. PhD thesis, ETH Zurich, 1905.
- A.-C. Eliasson. *Starch in food: Structure, function and applications*. CRC press, 2004.
- I. Evans and A. Lips. Viscoelasticity of gelatinized starch dispersions. *Journal of Texture Studies*, 23(1):69–86, 1992.
- I. D. Evans and A. Lips. Concentration dependence of the linear elastic behaviour of model microgel dispersions. *Journal of the Chemical Society, Faraday Transactions*, 86(20):3413–3417, 1990.
- R. S. Farr and R. D. Groot. Close packing density of polydisperse hard spheres. *The Journal of chemical physics*, 131(24):244104, 2009.
- D. R. Foss and J. F. Brady. Self-diffusion in sheared suspensions by dynamic simulation. *Journal of fluid mechanics*, 401:243–274, 1999.
- H. Fredriksson, J. Silverio, R. Andersson, A.-C. Eliasson, and P. Åman. The influence of amylose and amylopectin characteristics on gelatinization and retrogradation properties of different starches. *Carbohydrate polymers*, 35(3-4):119–134, 1998.
- M. Fukuoka, K.-i. Ohta, and H. Watanabe. Determination of the terminal extent of starch gelatinization in a limited water system by dsc. *Journal of Food Engineering*, 53(1):39–42, 2002.
- R. F. Gibson, H.-K. Jang, S. Simkhada, Q. Yu, H.-I. Kim, and J. Suhr. Use of nanoindentation, finite element simulations, and a combined experimental/numerical approach to characterize elastic moduli of individual porous silica particles. *Particulate Science and Technology*, 33(2):213–218, 2015.
- S. Golshan, R. Sotudeh-Gharebagh, R. Zarghami, N. Mostoufi, B. Blais, and J. Kuipers. Review and implementation of cfd-dem applied to chemical process systems. *Chemical Engineering Science*, 221:115646, 2020.
- B. Govedarica, I. Ilić, S. Srčić, et al. The use of single particle mechanical properties for predicting the compressibility of pharmaceutical materials. *Powder technology*, 225:43–51, 2012.
- C. Greenwood. Observations on the structure of the starch granule. In *Proceedings*, 1979.

- G. Guo, D. S. Jackson, R. A. Graybosch, and A. M. Parkhurst. Asian salted noodle quality: Impact of amylose content adjustments using waxy wheat flour. *Cereal Chemistry*, 80(4):437–445, 2003.
- M. Hardiman, T. J. Vaughan, and C. T. McCarthy. The effects of pile-up, viscoelasticity and hydrostatic stress on polymer matrix nanoindentation. *Polymer Testing*, 52:157–166, 2016.
- Y. He, Z. Wang, T. Evans, A. Yu, and R. Yang. Dem study of the mechanical strength of iron ore compacts. *International Journal of Mineral Processing*, 142:73–81, 2015.
- H. Hertz. *Miscellaneous papers*. Macmillan, 1896.
- B. E. Hickman, S. Janaswamy, and Y. Yao. Properties of starch subjected to partial gelatinization and  $\beta$ -amylolysis. *Journal of Agricultural and Food Chemistry*, 57(2):666–674, 2008.
- S. Hizukuri. Polymodal distribution of the chain lengths of amylopectins, and its significance. *Carbohydr. Res.*, 147:342–347, 1986.
- S. Hizukuri. Starch: analytical aspects. *FOOD SCIENCE AND TECHNOLOGY-NEW YORK-MARCEL DEKKER-*, pages 347–430, 1996.
- R. Hoover. Composition, molecular structure, and physicochemical properties of tuber and root starches: a review. *Carbohydrate polymers*, 45(3):253–267, 2001.
- S. H. Hwang and R. Shahsavari. Intrinsic size effect in scaffolded porous calcium silicate particles and mechanical behavior of their self-assembled ensembles. *ACS applied materials & interfaces*, 10(1):890–899, 2018.
- K. l'anson, M. Miles, V. Morris, L. Besford, D. Jarvis, and R. Marsh. The effects of added sugars on the retrogradation of wheat starch gels. *Journal of Cereal Science*, 11(3):243–248, 1990.
- O. I. Imole, M. Paulick, V. Magnanimo, M. Morgeneyer, B. E. C. Montes, M. Ramaioli, A. Kwade, and S. Luding. Slow stress relaxation behavior of cohesive powders. *Powder technology*, 293:82–93, 2016.
- R. Jamshidi, P. Angeli, and L. Mazzei. On the closure problem of the effective stress in the eulerian-eulerian and mixture modeling approaches for the simulation of liquid-particle suspensions. *Physics of Fluids*, 31(1):013302, 2019.
- M. Jean. The non-smooth contact dynamics method. *Computer methods in applied mechanics and engineering*, 177(3-4):235–257, 1999.
- M. Jean and J. J. Moreau. Unilaterality and dry friction in the dynamics of rigid body collections. In *1st Contact Mechanics International Symposium*, pages 31–48, 1992.
- H. Jing, J. Shi, P. Guoab, S. Guan, H. Fu, and W. Cui. Hydrogels based on physically cross-linked network with high mechanical property and recasting ability. *Colloids and Surfaces A: Physicochemical and Engineering Aspects*, 611:125805, 2021.

- P. C. Johnson and R. Jackson. Frictional–collisional constitutive relations for granular materials, with application to plane shearing. *Journal of fluid Mechanics*, 176:67–93, 1987.
- L. Joly-Pottuz, E. Calvié, J. Réthoré, S. Meille, C. Esnouf, J. Chevalier, and K. Masenelli-Varlot. Mechanical properties of nanoparticles: Characterization by in situ nanoindentation inside a transmission electron microscope. *Handbook of Mechanical Nanostructuring*, pages 163–180, 2015.
- M. Kanitz and J. Grabe. The influence of the void fraction on the particle migration: A coupled computational fluid dynamics–discrete element method study about drag force correlations. *International Journal for Numerical and Analytical Methods in Geomechanics*, 45(1):45–63, 2021.
- G. Kaufman, S. Mukhopadhyay, Y. Rokhlenko, S. Nejati, R. Boltyanskiy, Y. Choo, M. Loewenberg, and C. O. Osuji. Highly stiff yet elastic microcapsules incorporating cellulose nanofibrils. *Soft Matter*, 13(15):2733–2737, 2017.
- B. Khandelwal, A. Brar, A. Contractor, A. Mehrotra, A. Koul, B. Prakash, I. Agarwal, K. Arora, K. Upadhayaya, K. Sharma, M. Mahajan, M. Agarwal, P. Chand, R. Verma, R. Verma, R. Prahar, R. Sindhu, S. Gupta, S. Dogra, S. Sachdeva, S. Badhwar, V. Pathak, V. Sarda, V. Verma, and V. Gupta. *NCERT Chemistry class 12 part-2*. National Council of Education Research and Training, INDIA, 2020.
- S. Kim and S. J. Karrila. *Microhydrodynamics: principles and selected applications*. Courier Corporation, 2013.
- C. Kloss and C. Goniva. Liggghts–open source discrete element simulations of granular materials based on lammps. *supplemental proceedings: materials fabrication, properties, characterization, and modeling*, 2:781–788, 2011.
- K. Kohyama and K. Nishinari. Effect of soluble sugars on gelatinization and retrogradation of sweet potato starch. *Journal of Agricultural and Food Chemistry*, 39(8):1406–1410, 1991.
- J. Kokini, L.-S. Lai, and L. L. Chedid. Effect of starch structure on starch rheological properties. *Food Technology*, 46:124–139, 1992.
- I. M. Krieger and T. J. Dougherty. A mechanism for non-newtonian flow in suspensions of rigid spheres. *Transactions of the Society of Rheology*, 3(1):137–152, 1959.
- A. Krüger, C. Ferrero, and N. E. Zaritzky. Modelling corn starch swelling in batch systems: effect of sucrose and hydrocolloids. *Journal of Food Engineering*, 58(2):125–133, 2003.
- H. Kruggel-Emden, M. Sturm, S. Wirtz, and V. Scherer. Selection of an appropriate time integration scheme for the discrete element method (dem). *Computers & Chemical Engineering*, 32(10):2263–2279, 2008.
- K. Kubota, Y. Hosokawa, K. Suzuki, and H. Hosaka. Studies on the gelatinization rate of rice and potato starches. *Journal of Food Science*, 44(5):1394–1397, 1979. doi: 10.1111/j.1365-2621.1979.tb06446.x.
- A. Kumar and J. J. Higdon. Origins of the anomalous stress behavior in charged colloidal suspensions under shear. *Physical Review E*, 82(5):051401, 2010.

- S. Lagarrigue. *Modélisation de l'évolution du comportement à l'écoulement de suspensions d'amidon soumises à des cinétiques rapides de température et de cisaillement*. PhD thesis, Paris, Institut national d'agronomie de Paris Grignon, 2002.
- S. Lagarrigue, G. Alvarez, G. Cuvelier, and D. Flick. Swelling kinetics of waxy maize and maize starches at high temperatures and heating rates. *Carbohydrate Polymers*, 73(1):148–155, 2008.
- J. E. Lane, P. T. Metzger, and R. A. Wilkinson. A review of discrete element method (dem) particle shapes and size distributions for lunar soil. *NASA STI*, 2010.
- A. E. Leach. *Food Inspection and Analysis: For the Use of Public Analysts, Health Officers, Sanitary Chemists, and Food Economists*. John Wiley, 1913.
- D. Leighton and A. Acrivos. The shear-induced migration of particles in concentrated suspensions. *Journal of Fluid Mechanics*, 181:415–439, 1987.
- J. Li and D. Mason. A computational investigation of transient heat transfer in pneumatic transport of granular particles. *Powder Technology*, 112(3):273–282, 2000.
- J. Li, M. Turesson, C. A. Haglund, B. Cabane, and M. Skepö. Equation of state of peg/peo in good solvent. comparison between a one-parameter eos and experiments. *Polymer*, 80:205–213, 2015.
- J. Li, G. P. Desam, V. Narsimhan, and G. Narsimhan. Methodology to predict the time-dependent storage modulus of starch suspensions during heating. *Food Hydrocolloids*, page 106463, 2020.
- J. J. Liétor-Santos, B. Sierra-Martín, and A. Fernández-Nieves. Bulk and shear moduli of compressed microgel suspensions. *Physical Review E*, 84(6):060402, 2011.
- L. Lobry, E. Lemaire, F. Blanc, S. Gallier, and F. Peters. Shear thinning in non-brownian suspensions explained by variable friction between particles. *Journal of Fluid Mechanics*, 860:682–710, 2019.
- S. Luding and E. Bauer. Evolution of swelling pressure of cohesive-frictional, rough and elasto-plastic granulates. In *Geomechanics and Geotechnics: From Micro to Macro, (IS-Shanghai Conference Proceedings, 10.-12, 2010)*.
- D. Lund and K. J. Lorenz. Influence of time, temperature, moisture, ingredients, and processing conditions on starch gelatinization. *C R C Critical Reviews in Food Science and Nutrition*, 20(4):249–273, 1984.
- P. Malumba, C. Massaux, C. Deroanne, T. Masimango, and F. Béra. Influence of drying temperature on functional properties of wet-milled starch granules. *Carbohydrate polymers*, 75(2):299–306, 2009.
- P. Malumba, N. Jacquet, G. Delimme, F. Lefebvre, and F. Béra. The swelling behaviour of wheat starch granules during isothermal and non-isothermal treatments. *Journal of Food Engineering*, 114(2):199–206, 2013.
- P. Malumba, L. Doran, S. Danthine, C. Blecker, and F. Béra. The effect of heating rates on functional properties of wheat and potato starch-water systems. *LWT*, 88:196–202, 2018.

- D. J. Manners. Recent developments in our understanding of amylopectin structure. *Carbohydrate Polymers*, 11(2): 87–112, 1989.
- R. Mari, R. Seto, J. F. Morris, and M. M. Denn. Shear thickening, frictionless and frictional rheologies in non-brownian suspensions. *Journal of Rheology*, 58(6):1693–1724, 2014.
- S. H. Maron and P. E. Pierce. Application of ree-eyring generalized flow theory to suspensions of spherical particles. *Journal of colloid science*, 11(1):80–95, 1956.
- MATLAB. *version 9.4.0.813654 (R2018a)*. The MathWorks Inc., Natick, Massachusetts, 2018.
- J. Mattsson, H. M. Wyss, A. Fernandez-Nieves, K. Miyazaki, Z. Hu, D. R. Reichman, and D. A. Weitz. Soft colloids make strong glasses. *Nature*, 462(7269):83–86, 2009.
- P. Menut, S. Seiffert, J. Sprakel, and D. A. Weitz. Does size matter? elasticity of compressed suspensions of colloidal-and granular-scale microgels. *Soft Matter*, 8(1):156–164, 2012.
- M. J. Miles, V. J. Morris, P. D. Orford, and S. G. Ring. The roles of amylose and amylopectin in the gelation and retrogradation of starch. *Carbohydrate research*, 135(2):271–281, 1985.
- H. Mohapatra, T. M. Kruger, T. I. Lansakara, A. V. Tivanski, and L. L. Stevens. Core and surface microgel mechanics are differentially sensitive to alternative crosslinking concentrations. *Soft matter*, 13(34):5684–5695, 2017.
- R. V. More and A. M. Ardekani. Effect of roughness on the rheology of concentrated non-brownian suspensions: A numerical study. *Journal of Rheology*, 64(1):67–80, 2020.
- H. Nawaz, R. Waheed, M. Nawaz, and D. Shahwar. Physical and chemical modifications in starch structure and reactivity. *Chemical properties of starch*, Chapter:13, 2020.
- M. Nayouf, C. Loisel, and J. Doublier. Effect of thermomechanical treatment on the rheological properties of crosslinked waxy corn starch. *Journal of Food Engineering*, 59:209–219, 2003.
- C. Ness and J. Sun. Shear thickening regimes of dense non-brownian suspensions. *Soft matter*, 12(3):914–924, 2016.
- S. V. Nikolov, A. Fernandez-Nieves, and A. Alexeev. Behavior and mechanics of dense microgel suspensions. *Proceedings of the National Academy of Sciences*, 117(44):27096–27103, 2020.
- K. N. Nordstrom, E. Verneuil, W. G. Ellenbroek, T. C. Lubensky, J. P. Gollub, and D. J. Durian. Centrifugal compression of soft particle packings: Theory and experiment. *Physical Review E*, 82(4):041403, 2010.
- H. R. Norouzi, R. Zarghami, R. Sotudeh-Gharebagh, and N. Mostoufi. *Coupled CFD-DEM modeling: formulation, implementation and application to multiphase flows*. John Wiley & Sons, 2016.
- P. E. Okechukwu and A. Rao, M. Influence of granule size on viscosity of cornstarch suspension. *Journal of Texture Studies*, 26(5):501–516, 1995.

- P. E. Okechukwu and A. Rao, M. Kinetics of cowpea starch gelatinization based on granule swelling. *Starch-Stärke*, 48(2):43–47, 1996.
- W. C. Oliver and G. M. Pharr. An improved technique for determining hardness and elastic modulus using load and displacement sensing indentation experiments. *Journal of materials research*, 7(6):1564–1583, 1992.
- L. Orefice and J. G. Khinast. A novel framework for a rational, fully-automatised calibration routine for dem models of cohesive powders. *Powder Technology*, 361:687–703, 2020.
- C. O’Sullivan and J. D. Bray. Selecting a suitable time step for discrete element simulations that use the central difference time integration scheme. *Engineering Computations*, 2004.
- O. K. Ozturk and P. S. Takhar. Water transport in starchy foods: Experimental and mathematical aspects. *Trends in Food Science & Technology*, 78:11–24, 2018.
- A. Palanisamy. Multiscale modelling of flow, heat transfer and transformation during thermal treatment of starch suspensions-oral presentation. July 2021. doi: 10.5281/zenodo.5068054. URL <https://doi.org/10.5281/zenodo.5068054>.
- A. Palanisamy, F. Deslandes, M. Ramaioli, P. Menut, A. Plana-Fattori, and D. Flick. Kinetic modelling of individual starch granules swelling. *Food Structure*, page 100150, 2020.
- A. Papadopoulou, J. J. Gillissen, H. J. Wilson, M. K. Tiwari, and S. Balabani. On the shear thinning of non-brownian suspensions: Friction or adhesion? *Journal of Non-Newtonian Fluid Mechanics*, 281:104298, 2020.
- M. Peleg. An empirical model for the description of moisture sorption curves. *Journal of Food science*, 53(4): 1216–1217, 1988.
- Z. Peng, E. Doroodchi, C. Luo, and B. Moghtaderi. Influence of void fraction calculation on fidelity of cfd-dem simulation of gas-solid bubbling fluidized beds. *AIChE Journal*, 60(6):2000–2018, 2014.
- M. Perkins, S. J. Ebbens, S. Hayes, C. J. Roberts, C. E. Madden, S. Y. Luk, and N. Patel. Elastic modulus measurements from individual lactose particles using atomic force microscopy. *International journal of pharmaceutics*, 332(1-2):168–175, 2007.
- R. J. Phillips, R. C. Armstrong, R. A. Brown, A. L. Graham, and J. R. Abbott. A constitutive equation for concentrated suspensions that accounts for shear-induced particle migration. *Physics of Fluids A: Fluid Dynamics*, 4(1):30–40, 1992.
- E. Pilling and A. M. Smith. Growth ring formation in the starch granules of potato tubers. *Plant Physiology*, 132(1): 365–371, 2003.
- A. Plana-Fattori, E. Chantoiseau, C. Doursat, and D. Flick. An eulerian–lagrangian approach for coupling fluid flow, heat transfer and liquid food product transformation. *Computers & chemical engineering*, 52:286–298, 2013.

- A. Plana-Fattori, D. Flick, F. Ducept, C. Doursat, C. Michon, and S. Mezdoor. A deterministic approach for predicting the transformation of starch suspensions in tubular heat exchangers. *Journal of Food Engineering*, 171:28–36, 2016.
- S. Plimpton. Lammps sandia. [www.lammps.sandia.gov](http://www.lammps.sandia.gov), 1995.
- D. S. Preece, R. P. Jensen, E. D. Perkins, J. R. Williams, et al. Sand production modeling using superquadric discrete elements and coupling of fluid flow and particle motion. In *Vail Rocks 1999, The 37th US Symposium on Rock Mechanics (USRMS)*. American Rock Mechanics Association, 1999.
- I. Prigogine. Time, structure, and fluctuations. *Science*, 201(4358):777–785, 1978.
- F. Qian, N. Huang, J. Lu, and Y. Han. Cfd–dem simulation of the filtration performance for fibrous media based on the mimic structure. *Computers & chemical engineering*, 71:478–488, 2014.
- D. Quemada. Rheology of concentrated disperse systems and minimum energy dissipation principle. *Rheologica Acta*, 16(1):82–94, 1977.
- C. Ramirez-Aragón, J. Ordieres-Meré, F. Alba-Elías, and A. González-Marcos. Comparison of cohesive models in edem and liggghts for simulating powder compaction. *Materials*, 11(11):2341, 2018.
- M. Rao and J. Tattiyakul. Granule size and rheological behavior of heated tapioca starch dispersions. *Carbohydrate Polymers*, 38(2):123–132, 1999.
- W. S. Ratnayake and D. S. Jackson. Starch gelatinization. *Advances in Food and Nutrition Research*, 55:221–268, 2008.
- M. Reiner and H. Leaderman. Deformation, strain, and flow. *Physics Today*, 13(9):47, 1960.
- S. Renzetti, I. A. van den Hoek, and R. G. van der Sman. Mechanisms controlling wheat starch gelatinization and pasting behaviour in presence of sugars and sugar replacers: Role of hydrogen bonding and plasticizer molar volume. *Food Hydrocolloids*, 119:106880, 2021.
- Reportlinker.com. Global starch industry. *GLOBE NEWSWIRE*, New York, 2020. URL <https://www.globenewswire.com/news-release/2020/02/25/1989936/0/en/Global-Starch-Industry.html>.
- A. Rodriguez-Hernandez, S. Durand, C. Garnier, A. Tecante, and J. L. Doublier. Rheology-structure properties of waxy maize starch–gellan mixtures. *Food Hydrocolloids*, 20(8):1223–1230, 2006.
- A. Sarko and H.-C. Wu. The crystal structures of a-, b-and c-polymorphs of amylose and starch. *Starch-Stärke*, 30(3):73–78, 1978.
- J. R. Seth, M. Cloitre, and R. T. Bonnecaze. Elastic properties of soft particle pastes. *Journal of rheology*, 50(3): 353–376, 2006.
- J. R. Seth, L. Mohan, C. Locatelli-Champagne, M. Cloitre, and R. T. Bonnecaze. A micromechanical model to predict the flow of soft particle glasses. *Nature materials*, 10(11):838–843, 2011.

- A. Shauly, A. Wachs, and A. Nir. Shear-induced particle resuspension in settling polydisperse concentrated suspension. *International journal of multiphase flow*, 26(1):1–15, 2000.
- H. M. Shewan and J. R. Stokes. Analytically predicting the viscosity of hard sphere suspensions from the particle size distribution. *Journal of Non-Newtonian Fluid Mechanics*, 222:72–81, 2015a.
- H. M. Shewan and J. R. Stokes. Viscosity of soft spherical micro-hydrogel suspensions. *Journal of colloid and interface science*, 442:75–81, 2015b.
- H. M. Shewan, G. E. Yakubov, M. R. Bonilla, and J. R. Stokes. Viscoelasticity of non-colloidal hydrogel particle suspensions at the liquid–solid transition. *Soft Matter*, 17(19):5073–5083, 2021.
- H. Shi, S. Roy, T. Weinhart, V. Magnanimo, and S. Luding. Steady state rheology of homogeneous and inhomogeneous cohesive granular materials. *Granular matter*, 22(1):1–20, 2020.
- L. E. Silbert. Jamming of frictional spheres and random loose packing. *Soft Matter*, 6(13):2918–2924, 2010.
- D. P. Silva, R. C. Coelho, M. M. T. da Gama, and N. A. Araújo. Effect of particle deformability on shear thinning in a 3d channel. *arXiv preprint arXiv:2101.06981*, 2021.
- J. Singh, L. Kaur, and O. McCarthy. Factors influencing the physico-chemical, morphological, thermal and rheological properties of some chemically modified starches for food applications—a review. *Food Hydrocolloids*, 21(1):1–22, 2007.
- L. Slade and H. Levine. A food polymer science approach to structure-property relationships in aqueous food systems: Non-equilibrium behavior of carbohydrate-water systems. In *Water Relationships in Foods*, pages 29–101. Springer, 1991.
- L. Slade and H. Levine. Glass transitions and water-food structure interactions. In *Advances in Food and Nutrition Research*, volume 38, pages 103–269. Elsevier, 1995.
- A. M. Smith, K. Denyer, and C. Martin. The synthesis of the starch granule. *Annual review of plant biology*, 48(1):67–87, 1997.
- I. N. Sneddon. The relation between load and penetration in the axisymmetric boussinesq problem for a punch of arbitrary profile. *International journal of engineering science*, 3(1):47–57, 1965.
- S. Srichuwong, T. C. Sunarti, T. Mishima, N. Isono, and M. Hisamatsu. Starches from different botanical sources ii: Contribution of starch structure to swelling and pasting properties. *Carbohydrate Polymers*, 62(1):25–34, 2005.
- P. Steeneken. Rheological properties of aqueous suspensions of swollen starch granules. *Carbohydrate Polymers*, 11(1):23–42, 1989.
- J. F. Steffe. *Rheological methods in food process engineering*. Freeman press, 1996.
- J. J. Stickel and R. L. Powell. Fluid mechanics and rheology of dense suspensions. *Annu. Rev. Fluid Mech.*, 37:129–149, 2005.

- U. Suzuki, K. Kubota, M. Omichi, and H. Hosaka. Kinetic studies on cooking of rice. *Journal of Food Science*, 41: 1180–1183, 1976.
- A. S. Szczesniak. Classification of textural characteristics a. *Journal of Food Science*, 28(4):385–389, 1963.
- F. Tapia, S. Shaikh, J. E. Butler, O. Pouliquen, and É. Guazzelli. Rheology of concentrated suspensions of non-colloidal rigid fibres. *Journal of Fluid Mechanics*, 827, 2017.
- J. Tattiyakul and A. Rao, M. Rheological behavior of cross-linked waxy maize starch dispersions during and after heating. *Carbohydrate Polymers*, 43(3):215–222, 2000.
- G. I. Taylor. The viscosity of a fluid containing small drops of another fluid. *Proceedings of the Royal Society of London. Series A, Containing Papers of a Mathematical and Physical Character*, 138(834):41–48, 1932.
- I. J. Tetlow. Understanding storage starch biosynthesis in plants: a means to quality improvement. *Botany*, 84(8): 1167–1185, 2006.
- D. Thomas and W. Atwell. Eagan press handbook series: Starches. st. paul, minnesota, usa eagan press., 1999.
- O. Trubell. Occurrence and varieties of starch. *Chemistry and Industry of Starch*, pages 1–9, 1944.
- R. Van der Sman and H. Vollebregt. Effective temperature for sheared suspensions: A route towards closures for migration in bidisperse suspension. *Advances in colloid and interface science*, 185:1–13, 2012.
- K. van der Vaart, Y. Rahmani, R. Zargar, Z. Hu, D. Bonn, and P. Schall. Rheology of concentrated soft and hard-sphere suspensions. *Journal of Rheology*, 57(4):1195–1209, 2013.
- M. van Hecke. Jamming of soft particles: geometry, mechanics, scaling and isostaticity. *Journal of Physics: Condensed Matter*, 22(3):033101, 2009.
- A. Vázquez-Quesada, R. I. Tanner, and M. Ellero. Shear thinning of noncolloidal suspensions. *Physical review letters*, 117(10):108001, 2016. doi: 10.1103/PhysRevLett.117.108001.
- M. M. Villone and H. A. Stone. Rotating tensiometer for the measurement of the elastic modulus of deformable particles. *Physical Review Fluids*, 5(8):083606, 2020.
- M. M. Villone, J. K. Nunes, Y. Li, H. A. Stone, and P. L. Maffettone. Design of a microfluidic device for the measurement of the elastic modulus of deformable particles. *Soft matter*, 15(5):880–889, 2019.
- R. G. Visser, L. C. Suurs, P. Steeneken, and E. Jacobsen. Some physicochemical properties of amylose-free potato starch. *Starch-Stärke*, 49(11):443–448, 1997.
- T. T. Vo, S. Nezamabadi, P. Mutabaruka, J.-Y. Delenne, and F. Radjai. Additive rheology of complex granular flows. *Nature communications*, 11(1):1–8, 2020.
- H. Vollebregt, R. Van Der Sman, and R. Boom. Suspension flow modelling in particle migration and microfiltration. *Soft Matter*, 6(24):6052–6064, 2010.

- P. Voudouris, B. van der Zanden, D. Florea, Z. Fahimi, and H. Wyss. Shear thinning in soft particle suspensions. In *APS March Meeting Abstracts*, volume 2012, pages P51–006, 2012.
- A. Vázquez-Quesada, R. Tanner, and M. Ellero. Shear thinning of noncolloidal suspensions. *Physical Review Letters*, 117, 08 2016. doi: 10.1103/PhysRevLett.117.108001.
- S. Wang, K. Luo, C. Hu, and J. Fan. Particle-scale investigation of heat transfer and erosion characteristics in a three-dimensional circulating fluidized bed. *Industrial & Engineering Chemistry Research*, 57(19):6774–6789, 2018.
- H. Watanabe, M. Fukuoka, A. Tomiya, and T. Mihori. A new non-fickian diffusion model for water migration in starchy food during cooking. *Journal of Food Engineering*, 49(1):1–6, 2001.
- H. Watanabe, Y. Yahata, M. Fukuoka, T. Sakiyama, and T. Mihori. The thermodynamic basis for the relative water demand model that describes non-fickian water diffusion in starchy foods. *Journal of food engineering*, 83(2): 130–135, 2007.
- W. Wood, F. Psychophysical studies on the consistency of liquid foods. *Rheology and Texture of Food Stuffs, SCI Monograph*, 27:40–49, 1968.
- W. Yan, C. L. Pun, and G. P. Simon. Conditions of applying oliver–pharr method to the nanoindentation of particles in composites. *Composites Science and Technology*, 72(10):1147–1152, 2012.
- Z. Yan, S. K. Wilkinson, E. H. Stitt, and M. Marigo. Investigating mixing and segregation using discrete element modelling (dem) in the freeman ft4 rheometer. *International journal of pharmaceutics*, 513(1-2):38–48, 2016.
- H. Yang, W and A. Rao, M. Numerical study of parameters affecting broken heating curve. *Journal of food engineering*, 37(1):43–61, 1998.
- J. Zhou, A. Yu, and M. Horio. Finite element modeling of the transient heat conduction between colliding particles. *Chemical Engineering Journal*, 139(3):510–516, 2008.
- Z. Zhou, A. Yu, and P. Zulli. Particle scale study of heat transfer in packed and bubbling fluidized beds. *AIChE Journal*, 55(4):868–884, 2009.
- Z. Zhou, S. Kuang, K. Chu, and A. Yu. Discrete particle simulation of particle–fluid flow: model formulations and their applicability. *Journal of Fluid Mechanics*, 661:482–510, 2010.
- H. Zobel. Starch: sources, production, and properties in starch hydrolysis product: worldwide technology, production, and applications, 1992.
- H. Zobel, S. Young, and L. Rocca. Starch gelatinization: An x-ray diffraction study. *Cereal Chem*, 65(6):443–446, 1988.
- H. F. Zobel and A. Stephen. Starch: structure, analysis, and application. *FOOD SCIENCE AND TECHNOLOGY-NEW YORK-MARCEL DEKKER*, pages 19–19, 1995.